Alma Mater Studiorum · Università di Bologna

**SCUOLA DI SCIENZE**
**Corso di Laurea in Astrofisica e Cosmologia**
**Dipartimento di Fisica e Astronomia**

# THE THICKNESS OF THE GASEOUS LAYER IN DISK GALAXIES

**Tesi di Laurea Magistrale**

**Candidato:**
**Giuliano Iorio**

**Relatore:**
**Chiar.mo Prof.**
**Filippo Fraternali**

**Sessione II**
**Anno Accademico 2013/2014**

To me

# Contents

**Sommario**

La componente gassosa delle galassie a disco è comunemente approssimata come un disco infinitamente sottile (Begeman, 1987). Questa approssimazione può ritenersi valida nelle regioni più interne delle galassie dove lo strato gassoso è confinato all'interno del disco stellare. In regioni più esterne il potenziale è dominato dalla dark matter (DM), la cui distribuzione è meno concentrata rispetto alla materia stellare. In queste regioni, lo spessore del disco gassoso può raggiungere valori per cui l'approssimazione di disco sottile potrebbe non essere più valida. Assumendo che il mezzo interstellare (ISM) sia composto da gas isotermo e isotropo in equilibrio idrostatico, possiamo stimare la sua distribuzione verticale come:

$$\rho_{\rm gas}(R,Z) = \rho_{\rm gas}(R,0)\ {\rm Exp}\left[-\frac{\Phi(R,Z)-\Phi(R,0)}{\sigma_z^2}\right]$$

Dalla precedente equazione è evidente che il profilo verticale del gas dipende sia dal potenziale galattico ($\Phi$) e quindi dalla distribuzione di materia, sia dalla dispersione di velocità del gas ($\sigma_z$). Essendo l'ISM composto prevalentemente da idrogeno (70 %), la sua distribuzione può essere tracciata dall'emissione dell'HI a 21 cm. Essa è diffusa lungo tutto il disco galattico ben oltre i confini del disco luminoso, ed è quindi ideale per studiare la dinamica e la cinematica galattica. La nostra analisi teorica ha mostrato che l'altezza scala dell'idrogeno gassoso ad un certo raggio è fortemente legata alla componente di massa dominate: nelle parti centrali, dove domina la materia barionica, il disco gassoso incrementa il suo spessore esponenzialmente con una lunghezza scala pari al doppio di quella del disco stellare; dalle zone intermedie fino alla fine del disco, il profilo verticale del gas è influenzato dalla distribuzione di DM. In queste zone lo spessore del disco gassoso cresce con il raggio in maniera circa lineare. Tale fenomeno viene definito *gas flaring*. Anche la dispersione di velocità ha una sua fondamentale importanza: più è elevata più lo spessore del disco gassoso può assumere valori notevoli. Nel caso estremo in cui essa decresca molto rapidamente con il raggio, è possibile che lo spessore del disco gassoso si mantenga circa costante. Quindi lo studio dei flaring galattici può essere un utile strumento per approfondire e completare lo studio della dinamica e della cinematica delle galassie a disco. La stima diretta della distribuzione verticale del gas è possibile solamente in galassie viste ad alta inclinazione (edge-on). Purtroppo questo tipo di galassie soffre di alcune limitazioni osservative: la stima dello spessore del disco gassoso può essere distorta e influenzata dalla presenza di warp lungo la linea di vista, inoltre in questi oggetti è difficile stimare correttamente la dispersione di velocità del gas. Lo scopo principale di questa tesi è la ricerca di una nuova tecnica per poter stimare il profilo vertical del gas in galassie con inclinazione intermedia ($i \sim 50° - 70°$). La nostra analisi ha evidenziato che, in presenza di uno disco gassoso spesso, l'emissione a 21 cm presenta delle oscillazioni azimutali dipendenti dalla distribuzione dell'idrogeno atomico. Più lo strato è

spesso, più questo effetto è evidente. In linea di principio è quindi possibile utilizzare questa firma osservativa per stimare la distribuzione di densità intrinseca del gas. Il modello di analisi proposto è risultato capace di dare ottimi risultati in galassie simulate. Purtroppo approfondite analisi hanno mostrato che questo metodo è invece difficilmente estendibile a osservazioni di galassie reali. Le altezze scala previste producono oscillazioni del segnale troppo piccole rispetto ad altre asimmetrie azimutali osservabili nel disco. Queste ultime possono essere causate da: rumore osservativo, stima sbagliata dei parametri galattici e disomogeneità intrinseche (per esempio dovute a bracci a spirale). Questa previsione è stata confermata dallo studio del disco gassoso della galassia NGC2403.

# Capitolo 1

# Introduction

In this chapter we introduce the main topics of this work: the vertical density profile of the neutral gas in disk galaxies. In sec. 1.1 we briefly discuss the presence of vertical gas in galaxies., while in sec. 1.2 we show the fundamental link between the HI emission and the density of the gas. In sec. 1.3 we summarize previous studies of the vertical distribution of the gas and the related results. Finally, in sec. 1.4 we briefly expose the aim of this work.

## 1.1 HI in disk galaxies

Hydrogen is the most abundant element in the Universe: it is located in stars, in the ISM (interstellar medium) and in the IGM (intergalactic medium). The gas of the ISM constitutes the galactic reservoir to form stars. Indeed, galaxies can be divided in two big groups: early type galaxies are almost gas free and dominated by red and old stars, while late type galaxies have a large amount of cold gas that are currently using to form stars. Early type galaxies also contain a consistent amount of gas but it is too hot and diffuse to be efficiently cooled and condensed into stars. In this thesis, we focus on late-type disk galaxies, rich of cold gas. As previously mentioned, the ISM is dominated by hydrogen that can be present in various thermal phases (Wolfire et al., 1995):

- Hot: in this phase the hydrogen is totally ionized and very hot ($T \geq 10^6$ K) and diffuse ($n \leq 10^{-2}$ p/cm$^3$). This temperature can be reached as a consequence of a SN explosion or in the diffuse corona around galaxies.

- Warm: in this phase the temperature ranges from 6000°-10000° K and the density is about 0.1-1 p/cm$^3$. The hydrogen can be both ionized (HII), by radiation from young stars (HII regions) and neutral (WNM), heated by background radiation fields.

- Cold: At temperatures of the order 10°-100° K the hydrogen is all neutral (CNM).

- Molecular: in the most extreme ranges of temperature (T $\leq 50^{\circ}$ K) and density (n $\geq 10^2$ p/cm$^3$) the hydrogen is found in molecular form. The collapse of the so-called molecular clouds is the first phase of star formation.

Both HII and $H_2$ are strongly related to star forming regions, while HI is more uniformly diffused in the all galaxy. Moreover, the neutral atomic gas is detected well beyond the optical disk of a typical galaxy and this allows us to extend the studies of the dynamics and kinematics of the galaxies at very large radii. For instance, the first HI studies of external galaxies (Bosma, 1978) showed that the rotational velocity remains constant also at radii where the luminous matter drops and one would expect to see a keplerian decline. This evidence led astronomers to postulate that the visible galaxy should be imbedded in a halo of unknown and undetectable "Dark Matter (DM). HI observations became a unique tool to study the hidden properties of the Dark Matter halos. Of particular relevance for this thesis, the vertical profile of the gas is one of the few ways to constrain the flattening of the DM halos (e.g. Olling 1996; Sicking 1997).

#### HI line emission

As already mentioned, the gaseous disks of galaxies are mostly composed by neutral Hydrogen, some in the Cold phase, some in Warm phase. In these physical conditions all the neutral Hydrogen is in the ground state, so no electonics transitions can occur. However, van de Hulst (1944) theoretically predict a HI emission line due to the interaction between the spin of the electron $\vec{S}$ and the angular momentum of the proton $\vec{I}$. We can introduce the hyperfine quantum number $\vec{F} = \vec{I} + \vec{S}$: in case of parallel I and J, F=1, otherwise F=0. The difference of energy from F= to F=0 leads to an emission line at 21 cm ($\nu \sim$1420 Mhz) with a Einstein coefficient of $2.9 \cdot 10^{-15}$s$^{-1}$. This line is strongly forbidden, but the large amount of HI in the ISM allows us to detect it easily in the Milky Way and nearby galaxies. In 1951 both Even & Purcell and Muller & Oort confirmed with radio observations the prediction of van de Hulst and started to use HI to study the Milky Way.

## 1.2 Physical properties inferred from observations

In this section we use the theory of the interaction between matter and radiation (appendix A) to link the density of the gas with the HI line emission. The optical depth ($\tau$) of an HI region is defined as:

$$\mathrm{d}\tau_\nu = \sigma_\nu \mathrm{n_H ds} = \sigma_\nu \mathrm{dN_H} \tag{1.1}$$

where $\sigma_\nu$ is the cross section of the interaction of the hydrogen with the radiation (see app. 1.2), $n_H$ is the hydrogen particle density and $N_H$ is the column density along a line of sight (los):

$$N_H = \int_{los} n_H ds$$

If one defines the opacity in terms of observed emission, it is possible to directly evaluate the hydrogen column density. The opacity is a measure of the energy loss (absorbed and/or scattered) by the emission crossing a medium. We consider a 21 cm emission line with intensity $I(\nu)$ $\left[\frac{erg}{cm^2\ sterad\ s\ Hz}\right]$ and normalized profile $\phi_\nu d\nu$ (eq. A.7) crossing the gas layer of a galaxy. It can interact with the hydrogen atoms in three ways:

- Absorption: the emission can be absorbed by a atom with F=0 to reach the upper level (F=1). The rate of transition per unit mean intensity at frequency $\nu_{ul}$ is the Einstein coefficient $B_{lu}$.
- stimulated emission: the emission can stimulate an atom in the F=1 leve to decay to the ground state emitting a new photon at the same frequencies. This not a real loss of photons, but for our purpose we consider it as a negative absorption. As above, the Einstein coefficient is $B_{ul}$.
- scattering: a photon can be scattered, the treatment of this phenomena is not trivial but it has a lower importance with respect of the above cases and it can be neglected.

Considering the Einstein coefficients the number of transition $\eta$ per unit time, frequency, solid angle and volume is

$$\begin{aligned} \eta_{lu} &= n_l\ B_{lu}\ \frac{1}{4\pi}\ \phi(\nu)\ I(\nu)\ dt\ d\nu\ d\Omega\ dV \\ \eta_{ul} &= -n_u\ B_{ul}\ \frac{1}{4\pi}\ \phi(\nu)\ I(\nu)\ dt\ d\nu\ d\Omega\ dV \end{aligned} \tag{1.2}$$

where $n_u$ and $n_l$ are the particle density of the hydrogen respectively on the upper (F=1) and ground (F=0) levels, such that $n_H=n_u + n_l$. If every transition involves an energy $E=h\nu_{ul}$ the net infinitesimal energy loss is (dV=dA ds):

$$dE = -(n_l\ B_{lu} - n_u\ B_{ul})\ h\ \nu_{ul}\ \frac{1}{4\pi}\ \phi(\nu)\ I(\nu)\ dt\ d\nu\ d\Omega\ dA\ ds \tag{1.3}$$

The definition of the intensity is energy per unit of second, area, solid angle and frequencies:

$$dI = \frac{dE}{dA\ dt\ d\nu\ d\Omega} \tag{1.4}$$

Using eq. 1.4 in eq: 1.3 we obtain:

$$dI = -\frac{h\nu_{ul}}{4\pi}\phi(\nu)\ (n_l B_{ul} - n_u B_{lu})\ I(\nu) ds \tag{1.5}$$

Comparing eq. 1.5 with the transport equation (A.1) we can find a new definition for the optical depth (eq. 1.1):

$$\mathrm{d}\tau = \alpha_\nu \mathrm{ds} = \frac{\mathrm{h}\nu_{ul}}{4\pi}\phi(\nu)(n_l B_{lu} - n_u B_{ul})\mathrm{ds} \tag{1.6}$$

Using the definition of spin temperature ($T_s$ eq. A.11) and the relations of eqs. A.19 and A.21 in eq. 1.5, we can write:

$$\mathrm{d}\tau = \frac{3c^2}{32\pi\nu_{ul}^2}\phi(\nu)\mathrm{n}_u \left(\mathrm{Exp}\left(-\frac{h\nu_{ul}}{kT_s}\right) - 1\right)\mathrm{ds} \tag{1.7}$$

The energy involved in the hyperfine transition is so low ($\mathrm{h}\nu_{ul} \sim 9.41 \cdot 10^{18}$ erg) that the condition $\mathrm{h}\nu << T_s$ is always fulfilled, thus we can approximate the exponential in the r.h.s as a taylor series. Integrating eq. 1.7 along the los we obtain:

$$\tau_\nu = \frac{3\mathrm{h}c^2}{32\pi k\nu_{ul}}\frac{A_{ul}}{T_s}\phi(\nu)\int n\mathrm{ds} = \frac{3\mathrm{h}c^2}{32\pi k\nu_{ul}}\frac{A_{ul}}{T_s}\phi(\nu)\mathrm{N_H} \tag{1.8}$$

where we have implicitly assumed that the line profile and the spin temperature are constant along the los. The emission profile $\phi(\nu)$ can be broaden by different mechanisms such as natural quantum broadening and/or thermic and turbulent broadening. The last two can be called "Doppler broadening, because the profile $\phi(\nu)$ is due to the different velocities of the hydrogen atoms along the line of sight. The "Doppler broadening is dominant with respect the other mechanism, thus it is useful to operate a change of variables from frequency to velocity: $\phi(\nu) = \phi(V)\frac{dV}{d\nu}$. Using the doppler relation $\frac{dV}{d\nu} = \frac{c}{\nu_{ul}}$, eq. 1.8 becomes:

$$\tau_v = \frac{3hc^3}{32\pi k\nu_{ul}^2}\frac{A_{ul}}{T_s}\phi(V)\mathrm{N_H} = 5.51 \cdot 10^{-14}\frac{\phi(V)\mathrm{N_H}}{T_s} \tag{1.9}$$

Finally, integrating on V both the r.h.s and the l.h.s we obtain:

$$\mathrm{N_H} = 1.823 \cdot 10^{18}\int T_s\tau_v\frac{\mathrm{dV}}{\mathrm{km/s}} \tag{1.10}$$

In the case of a gaussian profile $\tau_v = \tau_0 e^{\frac{(v-v_0)^2}{2\sigma^2}}$ and it is possible to evaluate the optical depth at peak line:

$$\tau_0 = 0.22\left(\frac{\mathrm{N_H}}{10^{21}\mathrm{cm}^{-2}}\right)\left(\frac{T_s}{100\mathrm{K}}\right)^{-1}\left(\frac{\sigma}{10\mathrm{km/s}}\right)^{-1}$$

where $\sigma$ is the velocity dispersion of the HI. The transition between an optically thin and thick regime is roughly $\tau \approx 1$, thus both the physical conditions of the WNM ($T_s \approx 2700K$ from eq. A.27) and the CNM ($T_s \approx 100K$) assure that the neutral disks of spiral galaxies are optically thin for column densities lower than $10^{22}\mathrm{cm}^{-2}$, which is generally a value rarely found in observations.

### 1.2.1 HI column density

Since $T_s$ and $\tau_v$ are not known a-priori, eq. 1.10 is not easy to compare with the observational data. Therefore, in this section we change eq. 1.10 to obtain a direct relation between the column density and the emission of the HI layer. We introduce the useful concept of "Brightness Temperature (BT), as the temperature that a Black Body should have to emit the same brightness $I$ of a given galactic source. In the radio domain we can use the Rayleigh approximation of the Black-Body emission law and write:

$$T = I\frac{c^2}{2k\nu^2} \tag{1.11}$$

Of course, $T$ is a physical temperature only if the emitting source is a blackbody, otherwise it is only a way to measure the brightness. Using the definition of $T$ we can rewrite the transport equation (eq. A.6) as:

$$T_B = T_r e^{-\tau} + T_s(1 - e^{-\tau}) \tag{1.12}$$

where $T_B$ is the total BT of an observed source and $T_r$ is the BT of the background radiation, therefore the BT of the HI emission line will be $T_l = T_B - T_r$. Subtracting $T_r$ on both sides of eq. 1.11 we can write:

$$T_l = (T_s - T_r)(1 - e^{-\tau}) \tag{1.13}$$

Finally, using eq. 1.13 in eq. 1.10 and the approximation of optically thin medium ($\tau << 1$) the column density can be expressed as:

$$\mathrm{N_H} = 1.823 \cdot 10^{18} \int T_l \left(\frac{T_s}{T_s - T_r}\right) \frac{\mathrm{d}V}{\mathrm{km/s}} \tag{1.14}$$

Usually, $T_s >> T_r$ and the above equation is reduced to

$$\mathrm{N_H} = 1.823 \cdot 10^{18} \int T_l \frac{\mathrm{d}V}{\mathrm{km/s}} \tag{1.15}$$

With eq. 1.15 we can easily link the column density to observed brightness of the HI line. In Appendix A, we shows that in the case of a very low density, $T_s$ can drop to very small values. For instance in outskirts of a galaxy $T_s$ can be as small as $T_{\mathrm{CMB}}$, therefore eq. 1.15 is no longer a good approximation for the HI column density. However, Watson & Deguchi (1984) showed that the scatter of the Lyman $\alpha$ photons can increase $T_s$ over the background radiation $T_r$ assuring the validity of eq. 1.15. The brightness of the HI data is usually expressed in term of Jy/beam (1 Jy= $10^{-23}$ erg), thus to use eq. 1.15 a factor of conversion $f$ is needed. Considering a gaussian instrumental beam with FWHM=$\mathrm{B}_\theta$x$\mathrm{B}_\phi$ we can write:

$$f(\nu_0, F_\theta, F_\phi) = 6.065 \cdot 10^5 \cdot \left(\frac{\nu_0}{1420\ \mathrm{Mhz}}\right)^{-2} \cdot \left(\frac{\mathrm{B}_\theta}{\mathrm{arcsec}}\right)^{-1} \cdot \left(\frac{\mathrm{B}_\phi}{\mathrm{arcsec}}\right)^{-1} \quad \left[\frac{\mathrm{K}}{\mathrm{Jy/Beam}}\right] \tag{1.16}$$

where $\nu_0$ is the central frequency of the observation. Thus, eq. 1.15 becomes:

$$\mathrm{N_H} = \frac{1.106 \cdot 10^{24}}{\left(\frac{\nu_0}{1420\ \mathrm{Mhz}}\right)^2 \cdot \left(\frac{\mathrm{B}_\theta}{\mathrm{arcsec}}\right) \cdot \left(\frac{\mathrm{B}_\phi}{\mathrm{arcsec}}\right)} \cdot \int \left(\frac{S_v}{\mathrm{Jy/beam}}\right) \frac{\mathrm{d}V}{\mathrm{km/s}} \quad \left[\frac{\mathrm{p}}{\mathrm{cm}^2}\right] \tag{1.17}$$

or in more astrophysical units:

$$\Sigma = \frac{8.794 \cdot 10^3}{\left(\frac{\nu_0}{1420\ \mathrm{Mhz}}\right)^2 \cdot \left(\frac{\mathrm{B}_\theta}{\mathrm{arcsec}}\right) \cdot \left(\frac{\mathrm{B}_\phi}{\mathrm{arcsec}}\right)} \cdot \int \left(\frac{S_v}{\mathrm{Jy/beam}}\right) \frac{\mathrm{d}V}{\mathrm{km/s}} \quad \left[\frac{\mathrm{M}_\odot}{\mathrm{pc}^2}\right] \tag{1.18}$$

### 1.2.2 Total HI mass

Integrating eq. 1.15 over the surface of the emitting source we can obtain the total HI mass of the object:

$$\mathrm{M_H} = \int \mathrm{N_H} \mathrm{d}\Sigma = 1.823 \cdot 10^{18} \int \left( \int T_B d\Sigma \right) \frac{\mathrm{d}V}{\mathrm{km/s}} \tag{1.19}$$

If the source is at distance $D$ and it is seen over a solid angle $\Omega_s$, the surface will be:

$$\Sigma_s = D^2 \Omega_s \tag{1.20}$$

Using the eq. 1.20 in eq. 1.19 we obtain:

$$\mathrm{M_H} = 0.014 \cdot \left(\frac{D}{\mathrm{pc}}\right)^2 \cdot \int \left( \int T_B d\Omega \right) \frac{\mathrm{d}V}{\mathrm{km/s}} [\mathrm{M}_\odot] \tag{1.21}$$

We can use the Brightness $I$ instead of $T_B$ (eq. 1.11), to obtain:

$$\mathrm{M_H} = 2.356 \cdot 10^{16} \cdot \left(\frac{D}{\mathrm{pc}}\right)^2 \cdot \int \left( \int I \mathrm{d}\Omega \right) \frac{\mathrm{d}V}{\mathrm{km/s}} [\mathrm{M}_\odot] \tag{1.22}$$

The inner integral in the r.h.s is the definition of flux $F$[cgs] or in Jy, $F[\mathrm{Jy}] = 10^{-23} F[\mathrm{cgs}]$. The scale of distance for the galaxies are of order of Mpc, so it is useful to rewrite the above equation to obtain:

$$\mathrm{M_H} = 2.356 \cdot 10^5 \cdot \left(\frac{D}{\mathrm{Mpc}}\right)^2 \cdot \int \left(\frac{F}{\mathrm{Jy}}\right) \frac{\mathrm{d}V}{\mathrm{km/s}} [\mathrm{M}_\odot] \tag{1.23}$$

In real data we have discrete evaluations of $F$ on every velocity channel. Therefore, we calculate the total mass through summations instead of integrals:

$$\mathrm{M_H} = 2.356 \cdot 10^5 \cdot \left(\frac{D}{\mathrm{Mpc}}\right)^2 \cdot \left(\frac{\Delta V}{\mathrm{km/s}}\right) \cdot \sum_i \left(\frac{F_i}{\mathrm{Jy}}\right) [\mathrm{M}_\odot] \tag{1.24}$$

Where $F_i$ is the evaluation of flux in every channel and $\Delta V$ is the channel width in terms of velocity.

## 1.3 HI vertical profile

From the assumption of hydrostatic vertical equilibrium, we can link the gas vertical profile with the gravitational potential of the galaxies (ch. 2):

$$\rho_{\rm gas}(R,Z) = \rho_{\rm gas}(R,0)\ {\rm Exp}\left[-\frac{\Phi(R,Z)-\Phi(R,0)}{\sigma_z^2(R)}\right] \tag{1.25}$$

where $\sigma_z$ is the vertical velocity dispersion of the gas. Once calculated the vertical profile, we can define a scale height representing the thickness of the gas at radius R (see app. B). At inner radii the stellar disk produces a strong vertical potential gradient such that the HI layer thickness is usually lower than the thickness of the stellar disk. At large radii, the stellar density falls and the DM halo dominates the galactic potential. The matter distribution of the halo is less concentrate on the plane with respect to the stellar disk, thus the difference $\Phi(R,Z)-\Phi(R,0)$ decreases and accordingly the gas vertical profile becomes wider. In this case the HI layer "flares increasing its thickness as function of the radius. In addition to the importance of estimate the 3D distribution of the ISM, the gas flaring could also be useful to study the dynamics. Indeed, it depends both on the galaxy potential $\Phi$ and on the gas velocity dispersion $\sigma_z$. If one estimate the vertical profile of the gas, it could be possible to constrain the intrinsic gas velocity dispersion and the galactic matter distribution (Sicking, 1997). In particular, the gas thickness is a unique tool to study the vertical potential of the DM halo, since the analysis of the rotation curve is capable only to give information about the radial term of the potential (see app. C). Therefore, it is important to evaluate if the observed HI layer in disk galaxies exhibits flaring and their magnitude. For instance, the lack of a prominent gas flaring can means both that at large radii the gas velocity dispersions drops and that the DM halo is not spherical but is more like a thick disk. Reversing this argument, it is also possible to use the HI thickness to exclude some galactic models; for example, Cuddeford & Binney (1993) proved that the presence of a relevant galactic magnetic field can in principle causes the vanish of the disk beyond 20 kpc in contrast with the observations. In conclusion, the evaluation of the gas vertical profile in disk galaxies allows us to complete the study of the dynamic and kinematic and it also gives important answers about the DM distributions and the related cosmological implication. In the following section we will briefly summarize previous study and the related results.

### 1.3.1 Studies and results about the gas vertical profile in disk galaxies

One of the first study on the gas vertical profile was performed by van der Kruit (1981) and van der Kruit & Searle (1981) on the edge-on galaxy NGC891. They used the estimated gas thickness to confirm that the dark matter can not lie entirely on the disk, but more likely in a spheroidal distribution. In the 90s, Olling widely use the HI flaring to constrain the shape-flattening parameter $q$ of the DM halos ($q = 1$ round halo, $q < 1$ oblate ellipsoid, $q > 1$ prolate

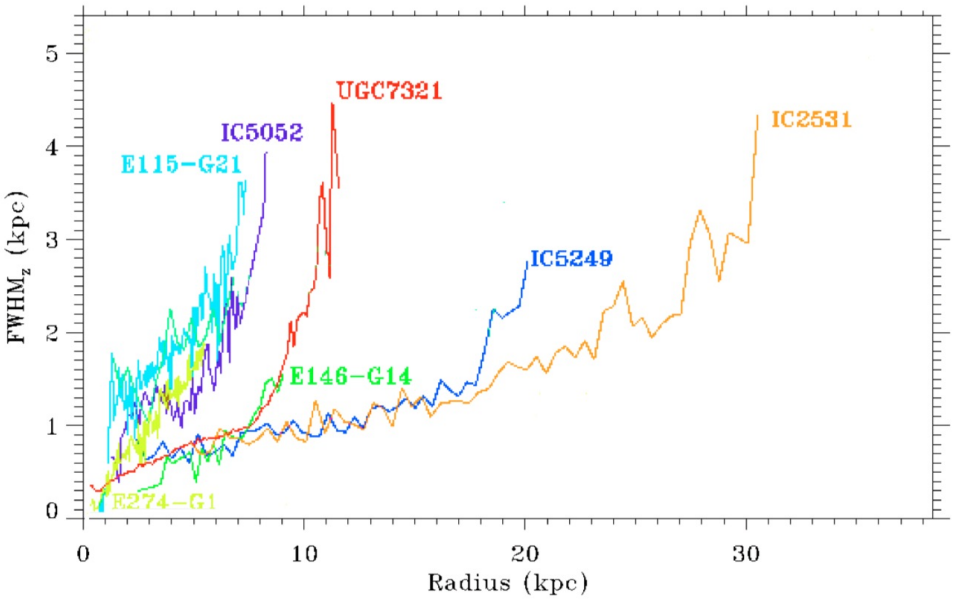


Figura 1.1: The FWHM of HI layer for seven edge-on galaxies. (O'Brian et al., 2010a)

.

ellipsoid) (Olling, 1995). Applying his model to NGC4244 (Olling, 1996), he found an heavy flattened halo with $q = 0.2 \pm 0.1$, but more recent work on the same galaxy (Zschaechner et al., 2011) showed that the study of flaring is compromised by the presence of a warp along the line of sight. A recent study of O'Brian et al. (2010a) reported the gas flaring of eight edge-on galaxies (see fig.1.1). They claim that each of them shows a prominent gas flaring that rises nearly linear at low radii and becomes exponential after the end of the stellar disk. The authors studied in dept the galaxy UGC7321 (O'Brian et al., 2010b), for this they estimated a DM halo nearly rounded ($q = 1 \pm 0.1$). However, we show in sec. 3.5 that these results seems to be in contradiction with our theoretical model. Not all observations reported a HI layer flaring for disk galaxies, for example Kamphuis (2007) found that the best models for six edge-on galaxies data cube are without significant flaring. However, these results can be afflicted by the degeneracy between the inclination angle of the galaxies and the HI thickness. In this thesis, we extensively highlight as this degeneracy can strongly afflict the evaluation of the gas vertical profile.

The Milky way deserves a separate discussion: the estimated vertical distribution of HI depends strongly on the choice of the rotation curve and Oort's constants. Olling & Merrifield (2000) used the estimates of vertical scale height up to $\approx 17$ kpc (see fig.1.2) to constrain the shape of DM halo: they found an oblate halo with $q = 0.8 \pm 0.1$. Both Kalberla et al. (2007) and Narayan et al. (2005) extended the estimate of the vertical distribution of HI to large radii. They found that a singular isothermal DM halo is not sufficient to explain the observed gas flaring: Narayan et al. (2005) used a spherical halo that fall faster than the isothermal one finding a better fit than (Olling & Merrifield, 2000) out to 24 kpc; Kalberla et al. (2007) used a

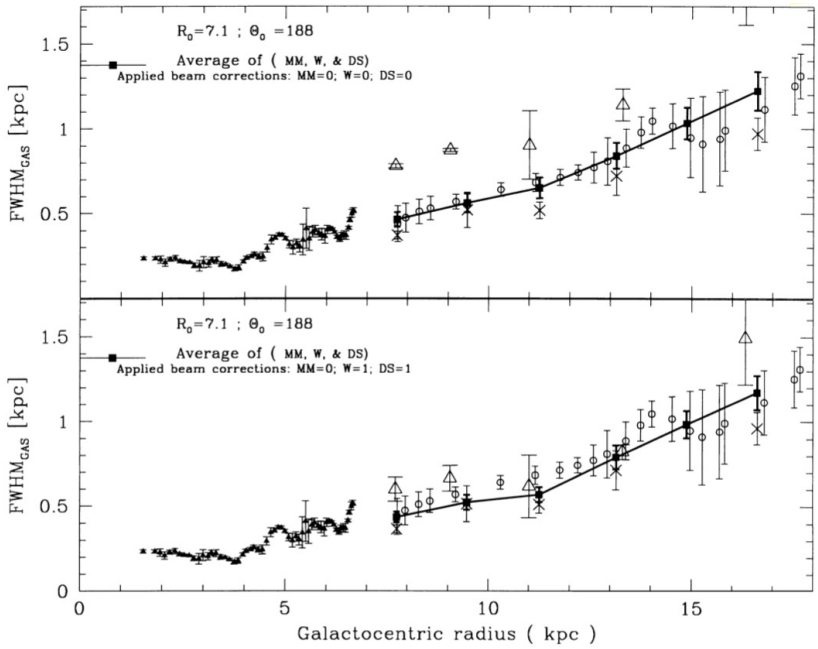


Figura 1.2: Milky way flaring from Olling & Merrifield (2000)

more complicated model with a DM halo and a DM ring to fit the data out to 40 kpc. Finally, Sanchez-Salcedo et al. (2008) used the flaring of our Galaxy to investigate the Modified Newton Dynamics.

Leaving aside the Milky way for which large uncertain remain, it is possible to detect directly the HI scale height only in galaxies with very low inclination and enough close to us to sample the vertical profile with more than one resolution element. However there are other limitations: edge-on galaxies can have warps along the line of sight or lagging halos (produced by stellar feedback) that can hide the signal from the flare (see e.g. Swaters et al. 1997). Finally, in edge on galaxies is impossible to estimate the intrinsic gas velocity dispersion as function of radius.

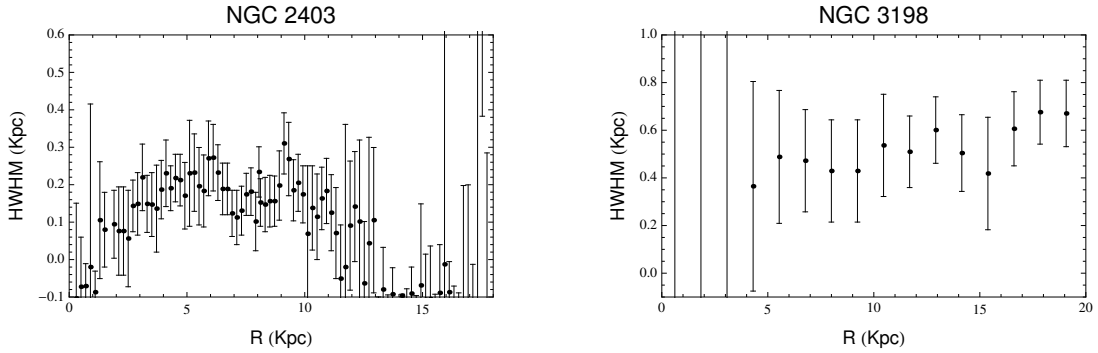


Figura 1.3: HI scale height for NGC2403 and NGC3198, from Sicking (1997)

For all the above reasons would be useful to find ways to estimate of the HI scale eight in

galaxies seen an intermediate inclination angles. Olling (1995) stated that it should be possible to infer the gas vertical profile from the analysis of the emission contours in the individual channel maps of the data cubes, nevertheless he never designed this kind of method. Sicking (1997) obtained an estimate of the HI scale height for two non edge-on galaxies (NGC2403 and NGC3198), but the results were poorly constrained, especially in the outer parts, and the gas flaring was not clearly evident (fig. 1.3).

## 1.4 This thesis

The main purpose of this thesis is to model the effect of the thickness on the observed HI emission of a gaseous layer and to study the feasibility to use it to evaluate the vertical distribution of the gas in disk galaxies seen at intermediate inclinations ($\sim 60^\circ$). Accordingly, we also investigate the theoretical HI thickness using dynamical models of galaxies.

This work is structured as follows: In chapters 2 and 3 we use the assumption of vertical hydrostatic equilibrium to estimate the theoretical vertical profile of HI gas for a given set of mass components. We derive the vertical profile both through an analytic approximation and using a numerical estimate of the galaxy potentials. Chapter 4 explains our technique. We investigate how in the presence of a thick gaseous layer the projection effects produce azimuthal asymmetries in the total HI map. The observed azimuthal profiles are directly related to the vertical and radial distributions of the gas. In chapter 5 we test our technique on simulated galaxies. We describe the method to compare our model with the simulated data and the possible bias introduced in the analysis. In addition we enquire about the effect of the flaring in the recovering of the galaxy parameters. Finally, in chapter 6 we summarize our main results. In this thesis, the analysis of the HI emission from both simulated and real galaxy has been carried out with the tasks of the package GIPSY (van der Hulst et al., 1992) and the software KARMA (Gooch, 1996). The numerical calculation of the galactic potential has been performed with the code *Galforces* by Fraternali & Binney (2006). For the others numerical calculations we used the software Mathematica[1]. Otherwise reported, the figures are originals and made either with Mathematica[1] or with GeoGebra (Markus Hohenwarter, 2002).

[1]Wolfram Research, Inc., Mathematica, Version, 9.0, Champaign, IL (2012)

# Capitolo 2

# HI Vertical distribution

In this chapter we derive the theoretical HI distribution, and its radial trend, relying on the assumption of (vertical) hydrostatic equilibrium. In section 2.1 we set the theoretical problem starting from the Euler equation and defining the vertical gas profile as a solution of a differential equation. In section 2.2 and 2.3 we find approximate and numerical solutions for this equation.

## 2.1 Hydrostatic equilibrium

The vertical distribution of the gas layer in spiral galaxy depends on both the vertical force $F_Z$ and the pressure terms. We start our analysis from the Z component of the momentum (Euler) equation written in cylindrical coordinates $(R, \phi, Z)$:

$$\frac{\partial V_Z}{\partial t} + \left( V_R \frac{\partial V_Z}{\partial R} + \frac{V_\phi}{R} \frac{\partial V_Z}{\partial \phi} + V_Z \frac{\partial V_Z}{\partial Z} \right) = -\frac{\partial \Phi}{\partial Z} - \frac{1}{\rho_{\text{gas}}} \frac{\partial P}{\partial Z} + \frac{(B \cdot \nabla) B_Z}{4\pi \rho_{\text{gas}}} \tag{2.1}$$

where the pressure term $P$ is the sum of the chaotic motion pressure (thermal and turbolent) $P_{\text{ch}}$, the magnetic pressure $P_m$ and the last term is the magnetic tension. We assume equilibrium in the vertical direction by setting $V_Z = 0$, the equation 2.1 becomes:

$$\frac{1}{\rho_{\text{gas}}} \frac{\partial P_{\text{ch}}}{\partial Z} = -\frac{\partial \Phi}{\partial Z} - \frac{1}{8\pi \rho_{\text{gas}}} \frac{\partial B^2}{\partial Z} + \frac{(B \cdot \nabla) B_Z}{4\pi \rho_{\text{gas}}} \tag{2.2}$$

To obtain the final differential equation for $\rho_{gas}$ we make the further assumptions:

- Axisymmetric system:

  The terms in equation 2.2 are independent of the azimuthal angle: $P = P(R, Z)$, $\sigma = \sigma(R, Z)$, $\rho_{\text{gas}} = \rho_{\text{gas}}(R, Z)$, $\Phi = \Phi(R, Z)$

- Plane of symmetry:

  We assume that the equatorial plane, where Z=0, is the plane of symmetry for the vertical distribution, so that $\rho(R, Z) = \rho(R, |Z|)$. In this plane the vertical force $F_Z = -\frac{\partial \Phi}{\partial Z}$ is null.

- Vertical isothermal system:

  The gaseous disk is isothermal in the vertical direction, thus $P_{\rm ch}(R,Z) = \sigma_Z^2(R)\rho(R,Z)$, whit $\sigma_Z(R)$ constant in the Z direction. Here $\sigma_Z$ is the vertical velocity dispersion of the gas, defined as the square of the quadratic sum of the thermal ($\sigma_{\rm th} = \sqrt{\frac{kT}{\mu m_H}}$) and the turbulent $\sigma_{\rm turb}$ dispersion.

- Isotropic system:

  The gaseous disk is a collisional system, therefore we can consider that the velocity dispersion of the gas is isotropic, i.e., it has the same value in every direction: $\sigma = \sigma_R = \sigma_Z = \sigma_\phi$, with $\sigma = \sigma(R)$ following the previous assumption.

- Negligible magnetic and cosmic pressures:

  The importance of non-thermal pressure in the dynamics of disk galaxies is still poorly understood. Some authors, (e.g. Battaner & Florido (2000), Ruiz-Granados et al. (2010)) have argued that the magnetic field can have an important role for the shape of the rotation curve and the gas distribution. We can roughly estimate the importance of the magnetic terms in eq. 2.1 comparing (isotropic) magnetic and thermal/turbulent pressures as follows:

$$\epsilon = \frac{P_{\rm ch}}{P_m} \approx 2 \cdot 10 \frac{\left(\frac{n}{\rm cm^{-3}}\right)\left(\frac{\sigma}{\rm 10\ km\ s^{-1}}\right)^2}{\left(\frac{B}{\mu G}\right)^2}$$

  In the inner regions of spiral galaxies $\epsilon >> 1$ and $P_m$ can be neglected, but at larger radii the magnetic pressure can become increasingly relevant also with a modest field of the order of few $\mu G$ (Battaner & Florido, 2000). This magnetic field could in principle dramatically increase the thickness of HI layer. Indeed, Cuddeford & Binney (1993) used this prediction of excessive flaring as an argument against the major role of magnetic fields in the outermost disks. Their analysis show that a dominant magnetic pressure would make the disk vanish at $R \approx 20$ kpc in disappointment with the typical sizes of the galaxy disk in HI. Hence, for the scope of this thesis, we neglect the magnetic terms of eq 2.2. Note however, that the magnetic pressure can simply have the effect of increasing the gas turbulence and this effect would implicitly included in our model.

From eq. 2.2, applying the former assumptions we can finally write:

$$\frac{\partial \ln(\rho_{\rm gas}(R,Z))}{\partial Z} = -\frac{1}{\sigma^2}\frac{\partial \Phi(R,Z)}{\partial Z} \tag{2.3}$$

Solving eq. 2.3, we found the vertical distribution of the gas layer as a function of the galactic radius R:

$$\rho_{\rm gas}(R,Z) = \rho_{\rm gas}(R,0)e^{-\frac{\Phi(R,Z)-\Phi(R,0)}{\sigma^2}} \tag{2.4}$$

Thus, if one knows the analytic potential $\Phi$, it is possible to directly derive a functional form for the gas distribution, and hence the thickness of the disk. Often this is not the case, the potential of disk galaxies is nontrivial and is made up by several mass components. In the simplest case one can consider a stellar disk and a spheroidal dark-matter (DM) halo; both contributing with their potential $\phi_i$ which there may not be an analytic form. In addition, in some regions of the disk, the self-gravity of the gas may become important.

In the next sections, we derive solutions for $\rho_{gas}$ and the related vertical scale height using both an approximate analytic approach and the numerical integration of the galaxy potential.

## 2.2 Analytic solutions

In order to find an analytic solution of eq. 2.4, we focus on the galaxy regions near the equatorial plane, where $z << R_{\rm max}$, with $R_{\rm max}$ representing the radial extension of the gaseous disk. Under this assumption we can expand the potential $\Phi$ in the Z direction as a Taylor series:

$$\Phi(R,Z) = \Phi(R,0) + Z\frac{\partial\Phi}{\partial Z}(R,0) + \frac{Z^2}{2}\frac{\partial^2\Phi}{\partial Z^2}(R,0) + O(Z^3) \tag{2.5}$$

Using this series up to the second order in eq. 2.4, and remembering that in the equatorial plane $\frac{\partial\Phi}{\partial Z} = 0$, we obtain:

$$\rho_{\rm gas}(R,Z) \approx \rho_{\rm gas}(R,0)e^{-\frac{Z^2}{2H^2}} \tag{2.6}$$

Thus, at small Z the gas has a gaussian distribution, with the following scale height:

$$H(R) = \sigma\left(\frac{\partial^2\Phi}{\partial Z^2}(R,0)\right)^{-\frac{1}{2}} \tag{2.7}$$

The vertical scale height H depends on the potential and hence on the matter distribution in the disk. We can link the potential to the total matter density $\rho_{\rm mat}$ through the Poisson equation:

$$\nabla^2\Phi(R,Z) = 4\pi G\rho_{\rm mat}(R,Z)$$

Isolating the Z partial derivative we can write:

$$\frac{\partial^2\Phi(R,Z)}{\partial Z^2} = 4\pi G\rho_{\rm mat}(R,Z) - \frac{1}{R}\frac{\partial}{\partial R}\left(R\frac{\partial\Phi(R,Z)}{\partial R}\right) \tag{2.8}$$

The second term on the r.h.s. in eq. 2.8 is related to the radial force $F_R = -\frac{\partial\Phi}{\partial R}$. The ordered circular motion dominates the kinematics of disk galaxies, thus we can estimate the radial acceleration in the galaxy plane using the observed rotation curve:

$$F_R(R) = -\frac{\partial\Phi}{\partial R} = -\frac{V_c^2}{R}$$

with $V_c$, the criculat velocity given by the HI rotation curve.

Following Olling (1995), we can define $\rho_{\rm rot}$ as:

$$\rho_{\rm rot}(R) = -\frac{1}{4\pi G}\frac{1}{R}\frac{\partial}{\partial R}\left(R\frac{\partial\Phi(R,0)}{\partial R}\right) = -\frac{1}{2\pi G}\frac{V_c}{R}\frac{\partial V_c}{\partial R} \tag{2.9}$$

which implies:

$$\frac{\partial^2\Phi(R,0)}{\partial Z^2} = 4\pi G(\rho_{\rm mat}(R,0) + \rho_{\rm rot}(R)) = 4\pi G\rho_{\rm eff}(R) \tag{2.10}$$

with $\rho_{\rm eff}$, efficient density.

Finally using eq. 2.10 in the definition 2.7, we obtain:

$$H(R) = \frac{\sigma(R)}{\sqrt{4\pi G(\rho_{\rm mat}(R,0) + \rho_{\rm rot}(R))}} \tag{2.11}$$

The gas flaring function (thickness as function of $R$) depends on both the radial matter distribution and the shape of the rotation curve. The matter density $\rho_{\rm mat}$ is the sum of every component:

$$\rho_{\rm mat} = \rho_{\rm bulge} + \rho_{\rm disk} + \rho_{H_2} + \rho_{HII} + \rho_{HI} + \rho_{\rm DM}$$

Because the molecular ($H_2$) and ionized media (HII) are expected to roughly follow the stellar distribution and the bulge is relevant only in the very inner parts of late type spirals, we can simplify the problem by taking only three mass components: the stellar disk ($\rho_*$), the neutral medium ($\rho_{HI}$) and the DM halo.

$$\rho_{\rm mat} = \rho_* + \rho_{HI} + \rho_{\rm DM}$$

Each of these has its own density profile, therefore in general $H(R)$ is not a simple function of R. However, galaxy disks can be divided in regions where a single mass component is dominant with respect to the others and small zones of transition. This implies that the scale height can be approximately written as :

$$H(R) \approx C \cdot \frac{\sigma(R)}{\sqrt{\rho_{\rm dom}(R,0)}} \tag{2.12}$$

The dominant component defines the radial trend of the flaring, while the other components principally act in reducing the value of the normalization factor C. The stellar disk usually dominates in the inner region of galaxies with minor contributions of the neutral gas and the rotational term; at intermediate radii the DM halo starts to play a major role with the stellar and gaseous disks giving nearly the same minor contribution. Finally, in the outer disk, the matter density is almost entirely due to the DM halo with a small contribution of the self-gravity of the gaseous layer. As a consequence, the study of the HI flaring in the outer parts of galaxy disks is a way to estimate the DM density distribution, in particular the halo flattening (as mentioned in ch.1 and described in ch.4).

### 2.2.1 Rotational density

Eq. 2.11 shows that the thickness of a gaseous disk is determined both by $\rho_{\rm mat}$ and $\rho_{\rm rot}$. Here we estimate the error we would make by analyzing non rotating gaseous layers ($\rho_{rot} = 0$). In contrast to the matter density, the rotational density can either be negative or positive depending on the sign of the radial gradient of the circular velocity ($V_c^{'}(R)$). We can consider three cases:

- $\mathbf{V_c^{'}(R) = 0}$ flat rotation curve:

  $\rho_{\rm rot} = 0$ and the vertical gas profile depends only on the matter density on the equatorial plane.

- $\mathbf{V_c^{'}(R) > 0}$ rising rotation curve:

  In this situation $\rho_{\rm rot} < 0$ which implies $\rho_{\rm eff} < \rho_{\rm mat}$ in eq. 2.10. The consequence of a rising rotation curve is to lower the denominator of eq. 2.4. Hence, the HI layer becomes thicker with respect to a flat rotation curve.
  We also note that when $|\rho_{\rm rot}| > \rho_{\rm mat}$, the term under the square root becomes negative and eq. 2.6 is no more an acceptable solution for the hydrostatic equilibrium; this can happen in the very inner part of galaxies, where thus either some of our assumptions or the hypothesis of vertical equilibrium must break down.

- $\mathbf{V_c^{'}(R) < 0}$ decreasing rotation curve:

  $\rho_{\rm rot} > 0$, in this case the rotational density acts to increase the effect of the matter density reducing the HI layer thickness.

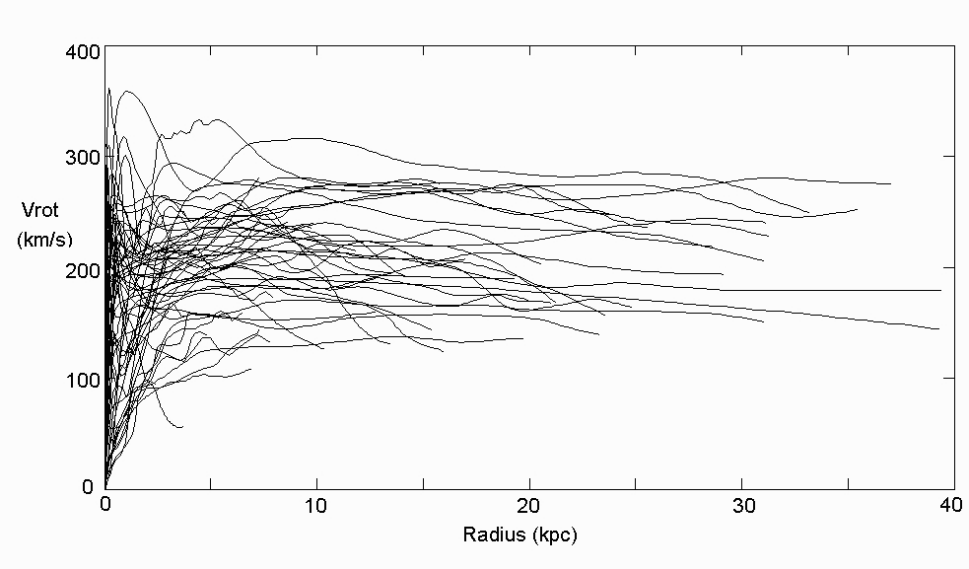


Figura 2.1: A compilation of rotation curves (CO,optical and HI data) from Sofue (1997),

Fig. 2.1 shows several rotation curves of spiral galaxies. Clearly we can divide them in two regions: an inner nearly linear rising part and an almost constant velocity for the rest of the galaxy. Therefore, $\rho_{\rm rot} \approx 0$ from few kpc to the edge of the galaxy disk, and equation 2.11 should depend only on the matter density.
In the region where the rotation curve rises linearly $V_c \propto R$:

$$\rho_{\rm rot} \approx -\frac{V}{R}\frac{\partial V}{\partial R} \approx -A$$

Where $A$ is a constant. At first glance, the steeper is the rise of the curve the more influent will be the rotational term and accordingly thicker will be the HI layer.

We define the parameter $\eta$, as follows:

$$\eta = \frac{\rho_{\rm rot}}{\rho_{\rm mat}} \tag{2.13}$$

Using eq. 2.13 we can write the eq. 2.11 as follows:

$$H(R) = \frac{\sigma(R)}{\sqrt{4\pi G \rho_{\rm mat}(R,0)}} \left(1+\eta(R)\right)^{-\frac{1}{2}} \tag{2.14}$$

In the regions where $\eta \approx 0$ we can treat the HI layer as a non rotating gaseous disk, where the vertical distribution is determined by the dominant matter component (eq. 2.12), we call this approximation "one component model.

## 2.3 Numerical solutions

We have performed a more accurate estimation of the HI thickness through a numerical calculation of the global potential of the of a typical disk galaxy. Once we know the potential at each radius $R$ and height $Z$, we use it in eq. 2.4 to get the vertical gas distribution.
In order to obtain the potential $\Phi(R,Z)$ we have used the code *Galforces* written by F. Fraternali (Fraternali & Binney, 2006). This code calculates the potential, the radial and vertical forces and the related circular velocity for a given set of mass components by numerically solving the eqs. 2.125b and 2.127 from Binney & Tremaine (2008) for the spheroidal components and the eq. 16 in Cuddeford (1993) for the disk components (stellar and gaseous matter).
We have added in the code the possibility to use a Hubble-law isothermal density distribution for the spheroidal components:

$$\rho(m) = \rho_0 \left(1+\left(\frac{m}{s}\right)^2\right)^{-1} \tag{2.15}$$

where $m = \sqrt{R^2 + \left(\frac{Z}{q}\right)^2}$ and $q$ is the flattening parameter (ratio of the axis lengths). Once we obtained the numerical potential we can calculate the the normalized density from eq. 2.4:

$$\tilde{\rho}_{\rm gas}(R,Z) = \frac{\rho_{\rm gas}(R,Z)}{\rho_{\rm gas}(R,0)} = {\rm Exp}\left(-\frac{\Phi(R,Z)-\Phi(R,0)}{\sigma^2_{gas}(R)}\right) \tag{2.16}$$

Here, in addition to the potential, we need to know the value of the gas velocity dispersion at every radius. Thus we added the velocity dispersion as an input in *Galforces*, and we modified the code to give in output the normalized density $\tilde{\rho}_{gas}$ in a grid in R and Z. Finally, we used these values to estimate the gas scale height at each radius R.

### 2.3.1 Functional forms for the vertical profile of the gas

In order to go from the normalized density ($\tilde{\rho}_{\rm gas}$) to an estimate of the scale height $H(R)$ we need to assume a functional form for the HI vertical distribution. Thus, we fitted $\tilde{\rho}_{gas}$ for each sampled radius $R$ using different functional forms. The functions we tested are the three functional forms typically used to describe the vertical distribution of baryonic matter in spiral galaxies (see Appendix B):

- **Exponential:** $\rho(R,Z) = \rho(R,0)e^{-\frac{|Z|}{H_{\rm exp}(R)}}$
- **Gaussian:** $\rho(R,Z) = \rho(R,0)e^{-\frac{Z^2}{2H^2_{\rm gau}(R)}}$
- **Hyperbolic Secant Squared:** $\rho(R,Z) = \rho(R,0){\rm sech}^2(Z/H_{\rm sec}(R))$

We defined the HI scale height as the scale eight $H(R)$ of the respective fitted function. From $H$ we can obtain other scale-height definitions as the half width half maximum HWHM (see Appendix B for more details). We tested these functions for three different matter distributions, with realistic structural parameters:

- **Stellar disk only:** Exponential density law with scale length $R_d = 2$ kpc and an hyperbolic square secant vertical profile with scale height $h_d = 0.4$ kpc (see sec. 3.1.1 for details).
- **Isothermal halo only:** Spherical isothermal halo with an Hubble density law (eq. 2.15) and a core radius of $R_c = 4.5$kpc
- **Disk + isothermal halo:** Combination of the above matter distributions.

For every mass distribution we used *galforces* to evaluate the normalized density $\tilde{\rho}_{\rm gas}$ in every sampled R and Z. Then, for every radius R we fitted these data along the Z direction with the above three functions. Figure 2.2, 2.3 and 2.4 show the best fitting functions superimposed on the numerical values (points) the data at three different radii for the mass model with disk and

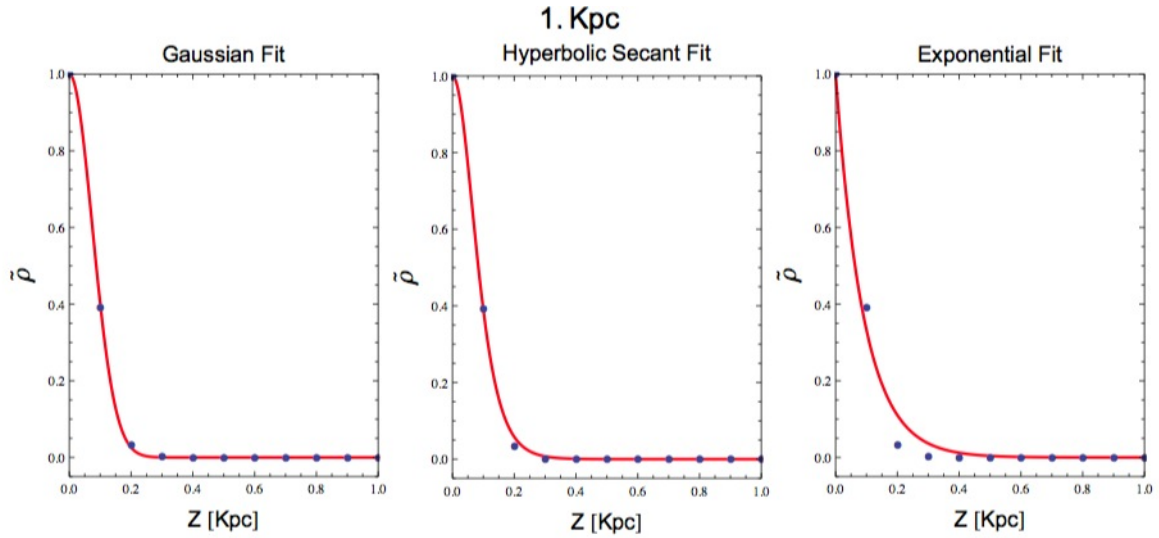


Figura 2.2: Vertical gas distribution for an inner radius ($R = 1$ kpc) for a mass model with an exponential disk and a spheroidal isothermal halo. The blue points are the numerical solutions of the eq. 2.3, the red lines show the best fits for the three different fitting functions.

halo. The exponential vertical profile always gives a poor fit of the theoretical points, so we can rule out this functional form. Both the gaussian and the hyperbolic secant squared offer a good description of the profile for every matter distribution and at every radius.

Fig. 2.5 shows the residuals of the fit for the mass models with disk and halo only: the hyperbolic secant better follows the theoretical expectation in the presence of a flattened matter distribution (upper panel), while the gaussian distribution is the optimal choice for spheroidal components (lower panel). We can understand this difference looking at eq. 2.6: if the potential varies slowly in the Z direction, its derivatives will be lower with respect to a potential with a strong vertical gradient, thus the second order truncation, namely a gaussian distribution, will be a optimal approximation. A spheroidal halo has a more uniform matter distribution in Z direction with respect to a disk, hence the variation of its potential will be lower. We can see in the lower panel of 2.5 that the vertical distribution of the gas in such potential follow perfectly a gaussian distribution at each radius.

From the upper panel of fig. 2.6 we note that, also if the secant is globally the best fitting function, there is an inner region from 0 to almost $2R_d$ where the gaussian has smaller residuals. Again we explain this by looking at the analytic approximation made in eq. 2.5. In the inner regions the matter density on the equatorial plane ($Z = 0$) is so high that the vertical region where $\tilde{\rho}_{gas}$ is significantly different from 0 are very thin (fig. 2.2). Thus, the fit depends mainly on points with small values of $Z$ ($Z < 1$). For example in fig. 2.2 we note that $\tilde{\rho}_{gas} \neq 0$ only between 0 and 0.2 kpc. For these low values of $Z$, $Z^n$ will decrease for increasing n and the approximation error of eq. 2.5 will be almost negligible.

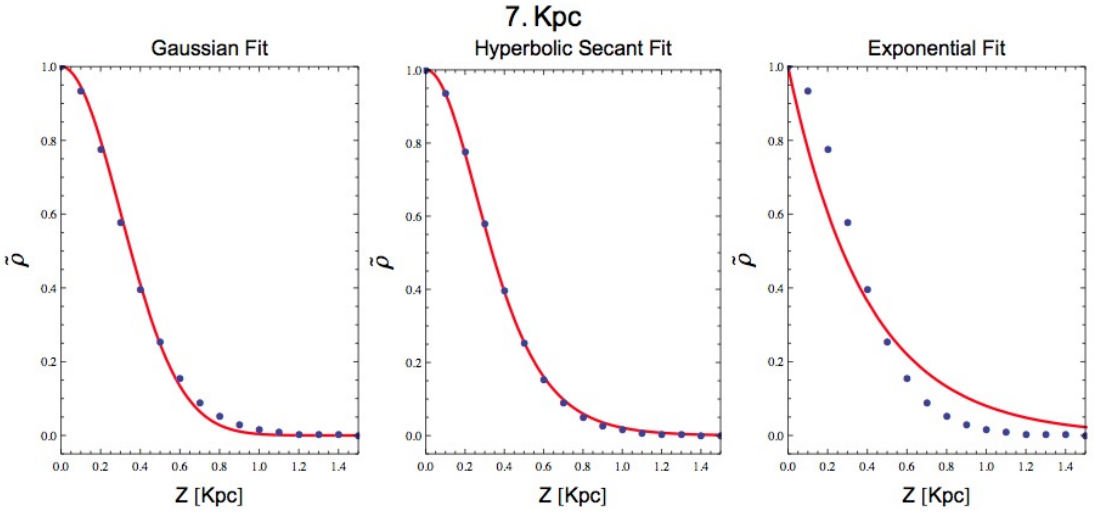


Figura 2.3: Same as in fig. 2.2 for an intermediate radius ($R = 7$ kpc)

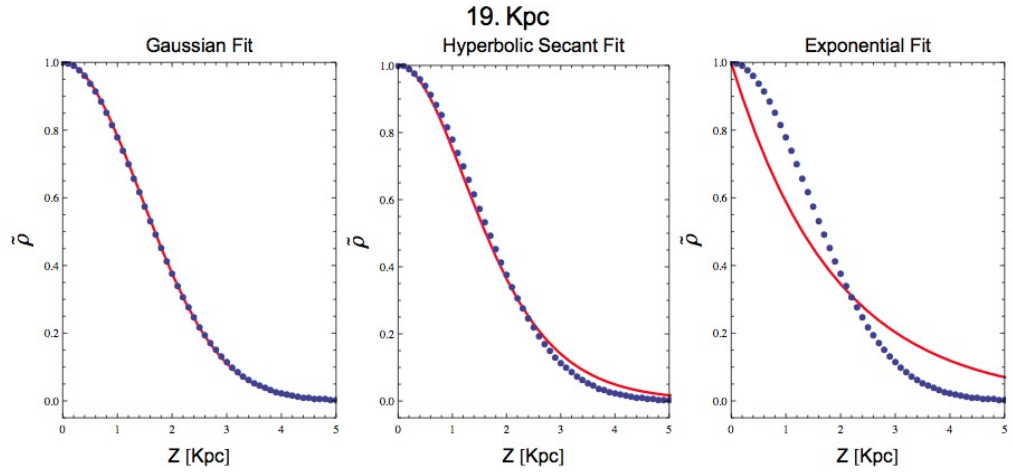


Figura 2.4: Same as in fig. 2.2 for an outer radius ($R = 19$ kpc)

Figure 2.6 shows the residuals for a realistic mass model with both disk and halo: in the very inner and outer regions the gaussians are the best functions to describe the vertical gas distribution for the reasons previously described, at intermediate radii the disk distribution is still quite important to cause a departure from a gaussian (see fig. 2.3), although the differences are small. The residuals are always comparable and the final estimations of the scale heights are almost equal, therefore we can choose either the gaussian or the hyperbolic secant as approximate functional forms for HI vertical distribution. We decided to use the gaussian function because it works better in the outer regions where our study is focused and because we can directly compare it with the analytic solution (eq. 2.7). We have tested the gaussian vertical profile again with further realistic mass models: ellipsoidal isothermal or NFW DM halos (Navarro et al., 1996) plus stellar and gaseous disk. In all cases a gaussian function is found to be a good approximation for the vertical profile of the gas layer.

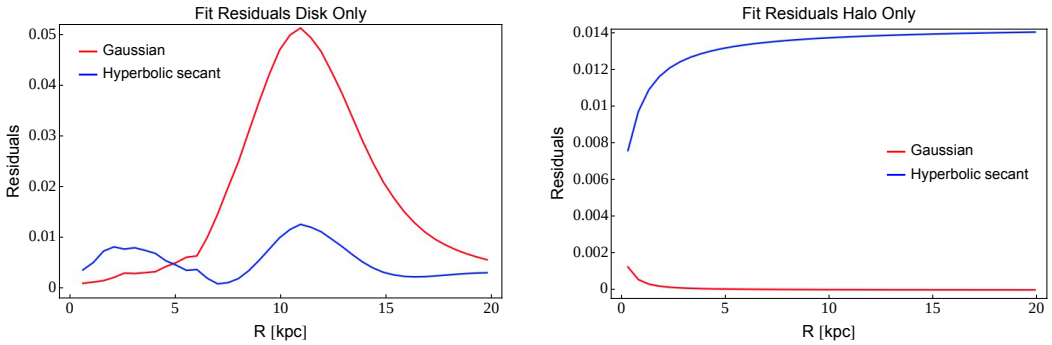


Figura 2.5: Residuals between the expected (numerically calculated) vertical profiles and the fitting with a gaussian and a hyperbolic secant squared. The residuals are calculated $\sum_i (\frac{\text{Numeric}-\text{Analytical}}{\text{Numeric}})^2$ where i represents our spatial sampling along the z axis. The left and the right panels respectively show a disk and a round DM halo mass model.

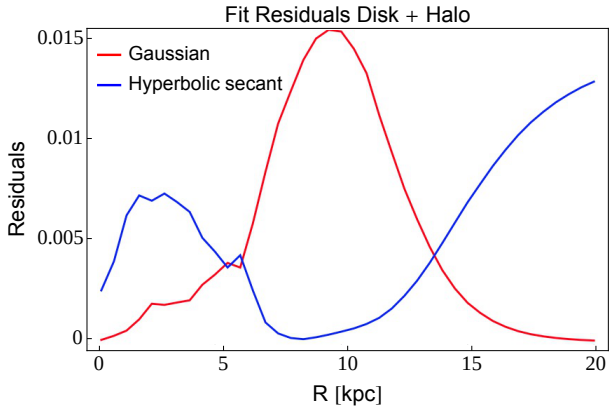


Figura 2.6: Same as fig. 2.5 but for a disk + round DM halo mass model.

### 2.3.2 The self-gravity of the gas

Equation 2.16 gives the right solution for $\tilde{\rho}_{\rm gas}$ only if $\Phi_{\rm tot}$ does not depend on the gas density distribution. However, this is only an approximation. The total potential consists of three terms: the stellar potential, the DM potential and the potential of the gaseous disk (eq. 2.17).

$$\Phi_{tot}(R,Z) = \Phi_*(R,Z) + \Phi_{\rm DM}(R,Z) + \Phi_{\rm gas}(R,Z) \tag{2.17}$$

Using the definition 2.17 in the eq. 2.3 we obtain:

$$\frac{\partial \ln(\rho_{\rm gas}(R,Z))}{\partial Z} = -\frac{1}{\sigma^2}\left(\frac{\partial \Phi_*(R,Z)}{\partial Z} + \frac{\partial \Phi_{\rm DM}(R,Z)}{\partial Z} + \frac{\partial \Phi_{\rm gas}(R,Z)}{\partial Z}\right) \tag{2.18}$$

The potential of the gas $\Phi_{gas}$ depends on the gas distribution through the poisson equation, thus $\rho_{gas}$ should be obtained from a second order PDE without analytic solutions.

In order to simplify our study we avoid solving numerically eq. 2.18 and we instead estimate the vertical profile and the scale height of the gas through a series of successive approximations. We start with a gaseous disk with given surface density and an initial guess for the scale height ($H^0$). From this density distribution we can calculate $\Phi_{\rm gas}$ with *Galforces* and we can solve eq. 2.18 as follows:

$$\tilde{\rho}_{gas}(R,Z) = \frac{\rho_{\rm gas}(R,Z)}{\rho_{\rm gas}(R,0)} = {\rm Exp}\left(-\frac{\Phi_*(R,Z) + \Phi_{\rm DM}(R,Z) + \Phi_{\rm gas}(R,Z) - \Phi_{\rm tot}(R,0)}{\sigma^2_{\rm gas}(R)}\right) \tag{2.19}$$

Then *galforces* we calculate the potential $\Phi'_{gas}(R,Z)$ produced by the this first input model ($\Phi_*$ and $\Phi_{\rm DM}$ are fixed). Inserting this new potential in eq. 2.19, we get a new estimate of the scale height of the gas ($H'$) as explained in sec. 2.3.1.. At this point, we update the model of the gaseous disk setting the scale height to $H'$, Then, we evaluating a new potential $\phi''_{gas}(R,Z)$, and then a new scale height $H''$. This procedure is repeated until two successive scale heights differ by less then a factor $\epsilon$. If not otherwise specified, in this work we have always set $H^0 = \epsilon$ and $\epsilon = 1$ pc. The scale height obtained in this way is still an approximation of the solution of eq. 2.18. However, comparing our approach to the numerical solution found by Sicking (1997) we found a good agreement: the differences are at most of the order of tens of parsec, that is a good accuracy for the aim of this work. Moreover, we note that one can conveniently constrain the value of the scale height between an upper and lower limit. The upper limit is obtained by neglecting the potential of gas in eq. 2.19, i.e., considering the gas as made of massless particles in the gravitational field produced by the stellar disk and the DM halo. The lower limit is obtained when all the gas lies in the equatorial plane (infinitely thin disk). When needed, one can use the region between these limits as a conservative estimate of the thickness of the gaseous disk, as shown for example in fig. 3.18.

## 2.4 Results and discussions

In this chapter we have studied the vertical distribution of the gas in spiral galaxies. We made the initial assumptions of vertical hydrostatic equilibrium, isothermal and isotropic gas and cylindrical symmetries. Using them in the Euler equation, we found that the vertical profile depends both on the potential of the galaxy and on the velocity dispersion of the gas (eq. 2.4). We also showed (sec. 2.2.1) that the vertical component of the potential depends both on the matter distribution and on the circular rotation of the gas. Therefore, the circular rotation of the gas layer can influence the thickness of the disk. In particular, a rising rotation curve thins the disk, while a decreasing rotation produces thicker layers. In the case of a flat rotation curve the vertical scale height will depend only on the matter distribution and on the velocity dispersion of the gas, as in the case of a static layer. We introduced a factor $\eta$ defined as follows: $\eta = \rho_{\rm mat}/\rho_{\rm rot}$ where $\rho_{\rm rot} = -\frac{1}{2\pi G}\frac{V_c}{R}\frac{\partial V_c}{\partial R}$ (Olling, 1995) and $\rho_{\rm mat}$ is the matter density. It is, basically, a measure of the influence of the rotation of the gas on the HI scale height: if $\eta << 1$ the contribution of the rotation is negligible, otherwise it must be take in account in the study of the HI thickness. We found that close to the equatorial plane the vertical distribution of the gas can be approximated by a gaussian with the vertical scale height that depends on the matter distribution on the equatorial plane the galaxy, on the circular velocity and on the velocity dispersion of the gas (eq. 2.11). In particular it is inversely proportional to the matter density, hence at large radii the gaseous disks will increase their thickness (flaring). We found that the values of the vertical scale height strongly depends on the matter components that dominates in the analyzed region (eq. 2.12). Therefore, at large radii the thickness can be an useful tool to constrain some proprieties of the DM halo, in particular its flattening (Olling, 1995; Sicking, 1997). Further, we studied the vertical profile of the gas numerically solving the galactic potential through the code *Galforces* (Fraternali & Binney, 2006). Using classical mass components (stellar disk + DM halo) for the galaxy, we found that the gaussian functions can effectively explains the whole vertical profile of the gas. We noted that also the hyperbolic secant squared can give good fit to it. Both the functional forms gives good fit of the numerical results (figs. 2.2, 2.4 and 2.3) but there are small differences:

- The gaussian seems to better follow the gas profile in presence of spheroidal component. The potential of such systems has a very slow variation on the vertical direction, in this case the truncation error of the analytical solution (i.e. a gaussian vertical profile) is negligible and for this reason the gas distribution is nearly coincident with a gaussian.

- The hyperbolic secants give the best fit in presence on a matter distribution highly concentrated on the equatorial plane, as it happens in case of a disk or a very flatten ellipsoidal halo. It is not a coincidence that the analytical solution for the vertical distribution of a self-gravity isothermal disk is the hyperbolic secant squared.

An exponential functional form gives poor fits in all the case analyzed. We stress that in our analysis we assume the gas isothermal in the vertical direction, it can be possible that deviation from this assumption can produce vertical profile showing also a nearly exponential fall off. In conclusion, we decided to use the gaussian function because it works better in the outer regions where our study is focused and because in this case, we can directly compare the numerical and the analytical evaluation of the scale height.

The numerical results take into account also the self gravity of the disk. We developed a method to avoid to solve the PDE of eq. 2.3. In practice, we used successive approximations of the scale height using the software *Galforces* to update step by step the galactic potential and accordingly the vertical scale height. Our results are comparable within ten pc with the ones of Sicking (1997). Moreover, we found that a conservative evaluation of the vertical scale height can be made considering an upper and a lower limit. The upper limit is obtained considering the gas composed by massless particles, while the lower limit is obtained considering all the gas lying in a extremely thin disk.

# Capitolo 3

# The theoretical thickness of a gaseous disk

In this chapter we use the results of Chapter 2 to determine the scale height of the gaseous disk produced by the typical mass components of spiral galaxies. In sec. 3.1 we analyze one by one the single components: an exponential stellar disk (3.1.1), an isothermal (3.1.3) and NFW (3.1.4) DM halo. For each of them we compare the numerically and analytically calculated HI thickness paying attention to the effect of the rotation ($\rho_{\rm rot}$). In sec. 3.2 we study the HI thickness produced by realistic mass models putting together the above components and considering also the self-gravity of the gaseous disk. In sec. 3.3 we investigate the role of the velocity dispersion of the gas on the thickness of the HI disk. Finally, in sec. 3.4 we use all the information of the previous sections to find a general functional form that can describe the HI flarings. We test it with galactic models coming from real observations.

## 3.1 One component models

### 3.1.1 Stellar Disk

The surface density of the stellar disks is well-approximated by an exponential law (van der Kruit & Freeman, 2011):

$$\Sigma(R) = \Sigma_0 e^{-\frac{R}{R_d}} \tag{3.1}$$

where $\Sigma_0$ is the central surface brightness and $R_d$ is the scale length. This surface density is the integral along the vertical direction ($Z$) of the stellar density $\rho_*$:

$$\Sigma(R) = \int_{-\infty}^{\infty} \rho_*(R, Z) dZ \tag{3.2}$$

Hence, we can write the stellar density as:

$$\rho_m(R,z) = \rho_0 e^{-\frac{R}{R_d}} g\left(\frac{Z}{Z_0}\right) \tag{3.3}$$

where $g$ represents the vertical profile of the stellar disk and $Z_0$ is the related scale height. It is **constancy** to parametrize $g$ with a square hyperbolic secant, which is the functional form that one expects for an isothermal distribution (van der Kruit & Searle 1982; Mosenkov et al. 2010). However, there is evidence that the vertical distribution in our Galaxy is more complex with a two component structure (thin  thick disk) both well described by exponential functions (Gilmore & Reid, 1983). For our purpose we note that, comparing the definition 3.3 and 3.1 through eq. 3.2, both a square hyperbolic secant and an exponential profile fulfill the follow identity:

$$\rho_0 = \frac{\Sigma_0}{2Z_0} \tag{3.4}$$

**Rotational velocity and rotational density**

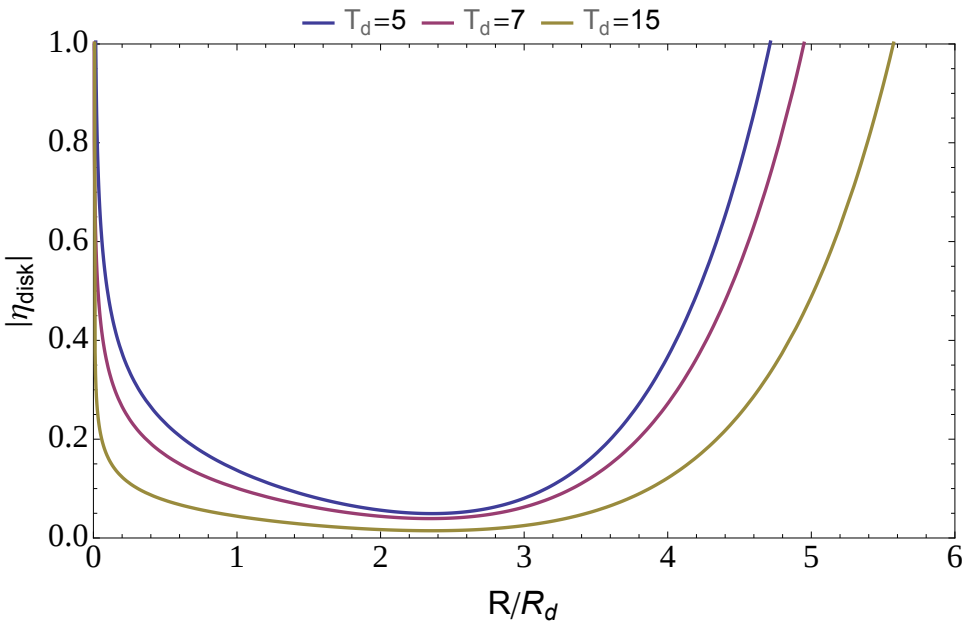


Figura 3.1: Ratio between $\rho_{\rm rot}$ and $\rho_{\rm mat}$ for exponential disks with different thickness factors $T_d$ (ratio between the radial scale length and vertical scale height of the disk).

For a exponential disk we can write the circular velocity as (Freeman, 1970):

$$V_c(R) = x\sqrt{\pi G\Sigma_0 R_d\left[I_0\left(\frac{x}{2}\right)K_0\left(\frac{x}{2}\right) - I_1\left(\frac{x}{2}\right)K_1\left(\frac{x}{2}\right)\right]} \tag{3.5}$$

where $I$ and $K$ are the modified Bessel functions of the first and second kind and $x = \frac{R}{R_d}$.

We can use the definition 3.5 in eq. 2.9 to calculate the contribution of the rotational velocity to the vertical gradient of the galactic potential (see sec. 2.2). This yields to:

$$\rho_{\rm rot}(x) = -\frac{\Sigma_0}{2R_d}\sqrt{I_0\left(\frac{x}{2}\right)K_0\left(\frac{x}{2}\right) - I_1\left(\frac{x}{2}\right)K_1\left(\frac{x}{2}\right)}\frac{\partial\left(x\sqrt{I_0\left(\frac{x}{2}\right)K_0\left(\frac{x}{2}\right) - I_1\left(\frac{x}{2}\right)K_1\left(\frac{x}{2}\right)}\right)}{\partial x}$$

We can solve the derivative on the r.h.s. using the following rules from Gradshteyn & Ryzhik (1980):

$$\begin{aligned}
\frac{\partial I_0(x)}{\partial x} &= I_1(x)\\
\frac{\partial K_0(x)}{\partial x} &= -K_1(x)\\
\frac{\partial I_1(x)}{\partial x} &= \frac{1}{2}(I_0(x) + I_2(x))\\
\frac{\partial K_1(x)}{\partial x} &= -\frac{1}{2}(K_0(x) + K_2(x))
\end{aligned}$$

Finally, we evaluate $|\eta| = \left|\frac{\rho_{\rm rot}}{\rho_{\rm m}}\right|$ (eq. 2.13) and obtain:

$$|\eta| = \frac{e^x}{8T_d}\left(xA\left(\frac{x}{2}\right) + 8B\left(\frac{x}{2}\right)\right) \tag{3.6}$$

where $A\left(\frac{x}{2}\right) = 3K_0I_1 + K_2I_1 - 3K_1I_0 - I_2K_1$ and $B\left(\frac{x}{2}\right) = I_0K_0 - I_1K_1$.

$T_d$ is the thickness factor defined as the ratio between the scale lenght and the scale height of the stellar disk. It ranges from 5 to 15, with a mean value of approximately 7 (Kregel et al., 2002). We plot $|\eta|$ from eq. 3.6 in fig. 3.1: there is a wide range of $x$ (approximately from two to four scale length) where $\eta$ is very low with a minimum coincident with the peak of the rotation curve of the exponential disk at $\approx 2.2R_d$. Beyond $x \approx 4-6$, $\eta$ starts to diverge due to the nearly Keplerian fall-off of $V_c$.

We conclude that, in the inner region where the luminous matter dominates, we can neglect the contribution of the rotational density in the study of the HI vertical distribution.

### Analytical scale height

Using eq. 3.3 and 3.4 in the definition 2.11 we can write the flaring function as:

$$H(R) = \frac{\sigma(R)\sqrt{Z_0}}{\sqrt{2\pi G\Sigma_0}}\ {\rm Exp}\left(\frac{R}{2R_d}\right) \tag{3.7}$$

de Grijs & Peletier (1997) found that $Z_0$ is almost constant over the whole dominion of the stellar disks of spiral galaxies, though in early-type spirals $Z_0$ may increase by a factor of about 1.5 at larger radii. For our purpose we consider always $Z_0$ independent of radius. Kregel

et al. (2002) obtained from a sample of edge-on galaxies that $Z_0$ correlates with the mass of the galaxies and hence with the rotational velocity:

$$Z_0 = (0.45 \pm 0.05) \left( \frac{V_{\rm flat}}{100 \text{ Km/s}} - (0.14 \pm 0.07) \right) \text{ [kpc]} \tag{3.8}$$

Where $V_{\rm flat}$ is the asymptotic value of the rotational circular velocity.

In conclusion for late-type spirals (100 km/s $< V_{\rm flat} <$ 200 km/s) we can approximate the vertical scale height as a constant $Z_0 \approx 0.4 - 0.8$ kpc

The eq. 3.7 can therefore be rewritten as:

$$H(R) = 0.122 \left( \frac{\sigma(R)}{10 \text{ km/s}} \right) \sqrt{\frac{\left( \frac{Z_0}{0.4 \text{ kpc}} \right)}{\left( \frac{\Sigma_0}{10^8 M_\odot/\text{kpc}^2} \right)}} \text{ Exp} \left( \frac{R}{2R_d} \right) \quad \text{kpc} \tag{3.9}$$

In the inner regions of galaxies we expect that the vertical scale height increases with $R$ as an exponential with a scale length twice the scale length of the disk. At very small radii ($R << R_d$) the rotational density $\rho_{\rm rot}$ thickens the HI layer (as showed in fig. 3.1), thus for $R \to 0$ eq. 3.9 becomes a lower limit. At larger radii, $\rho_{rot}$ is much greater than the stellar density (fig. 3.1), therefore the flaring function becomes:

$$H(R) = \frac{\sigma(R)}{\sqrt{4\pi G \rho_{\rm rot(R)}}} \tag{3.10}$$

For $R >> R_d$ we can approximate the rotational curve as a keplerian fall off $V_{\rm rot}(R) \approx GM_{\rm tot}R^{-0.5}$, where $M_{\rm tot}$ is the total mass of the stellar disk, and the rotational density (eq. 2.9) becomes:

$$\rho_{\rm rot} = \frac{GM_{\rm tot}^2}{4\pi R^3} \tag{3.11}$$

Using eq. 3.11 in the 3.10 we found the analytic scale height produced by an exponential disk in the keplerian fall-off dominated region:

$$H(R) = \frac{1.524 \left( \frac{\sigma(R)}{10 \text{ km/s}} \right) \left( \frac{R}{10 \text{ kpc}} \right)^{\frac{3}{2}}}{\sqrt{\frac{M_{tot}}{10^{10} \text{ M}_\odot}}} \quad \text{[kpc]} \tag{3.12}$$

We calculated that for radii greater than $\approx 4 - 5$ $\rm R_d$ an exponential stellar disk should produce an almost linear flaring.

### Numerical analysis

Using the approach described in sec. 2.3 we obtained the theoretical scale height for matter distributed as an exponential disk. As predicted by the analytic solution (eq. 3.9 and eq. 3.12),

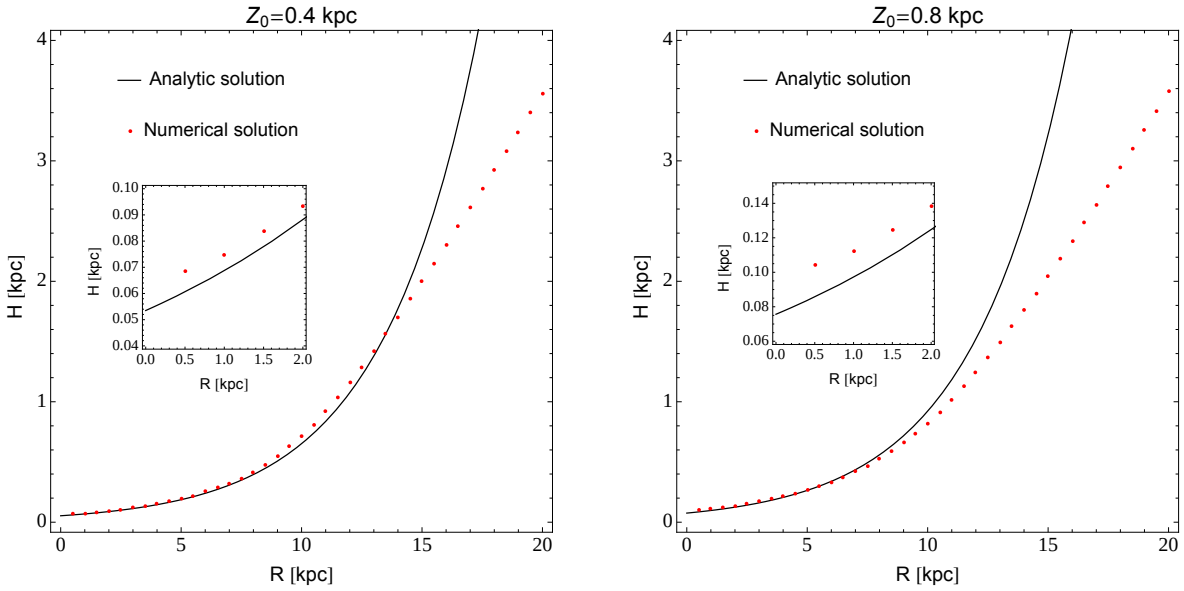


Figura 3.2: Comparison between the scale heights obtained with the analytic and the numerical approach for an exponential disk potential with central surface density $\Sigma_0 = 5e8\ M_\odot$, scale-length $R_d = 2$ kpc and a Sech$^2$ vertical distribution with a scale-eight $Z_0 = 0.4$ kpc (left panel) and $Z_0 = 0.8$ kpc (right panel). The small panels are the magnifications of the plots between 0 and 2 kpc.

in the inner regions the flaring exhibits an exponential growth, followed by an almost linear trend when the contribution of the rotational density dominates. In Fig. 3.2 we compare the analytic and the numerical thickness for a disk with a radial scale length of 2 kpc. We stress that the analytic solutions shown in fig. 3.2 take in account only the contribution of $\rho_{\rm mat}$ through eq. 3.9. Despite the approximation, the two approaches give nearly the same solution out to approximately 3 $R_{\rm d}$. However, in the inner regions (see zooms in fig. 3.2) the numerical thickness is systematically larger than the analytic one, as expected for a rising rotation curve (fig. 3.1). The two solutions diverge for $R \geq 9$ kpc, that is the radius where $\rho_{\rm rot}$ becomes larger than $\rho_{\rm disk}$ as showed in fig. 3.1. As expected, at large radii the HI scale height grows almost linearly.

In fig. 3.3 we study the changes on the gas flaring induced by varyng the disk parameters. As above, the density law used is:

$$\rho_*(R,Z) = \Sigma_0\ {\rm Exp}\left(-\frac{R}{R_d}\right)\frac{{\rm Sech}^2\left(\frac{Z}{Z_0}\right)}{2Z_0} \tag{3.13}$$

In panel a, we fixed the central surface brightness $\Sigma_0$ and the scale height $Z_0$, and we vary the scale length $R_d$. As expected, $R_d$ sets the transition between "exponential and the "linear flare, which occurs at $R \approx 5\ R_d$. In panel b, we vary only the central surface density $\Sigma_0$: a decrease of $\Sigma_0$ produces a scale height with higher normalization in the exponential region (inner radi) and a steeper linear trend at outer radii. In the last panel, we modified the vertical distribution

of matter through the scale height $Z_0$. Unlike models A and B the resulting scale heights are very similar, therefore the vertical distribution of the stellar disk does not have a relevant role in the related vertical profile of the gaseous components, especially in the outermost disk where our study is focused.

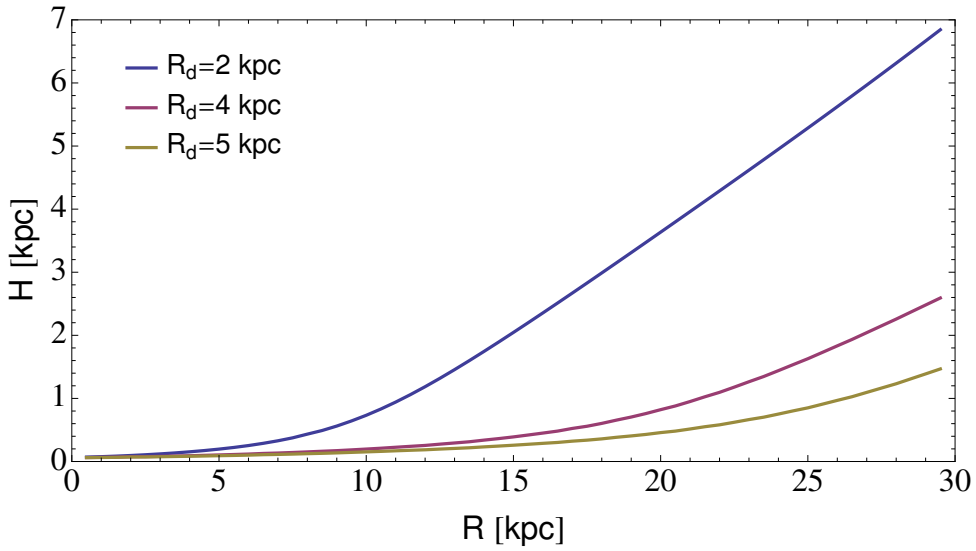


(a) Model A: $\Sigma_0 = 5 \cdot 10^8\ M_\odot/\mathrm{kpc}^2$, $Z_0 = 0.4$ kpc

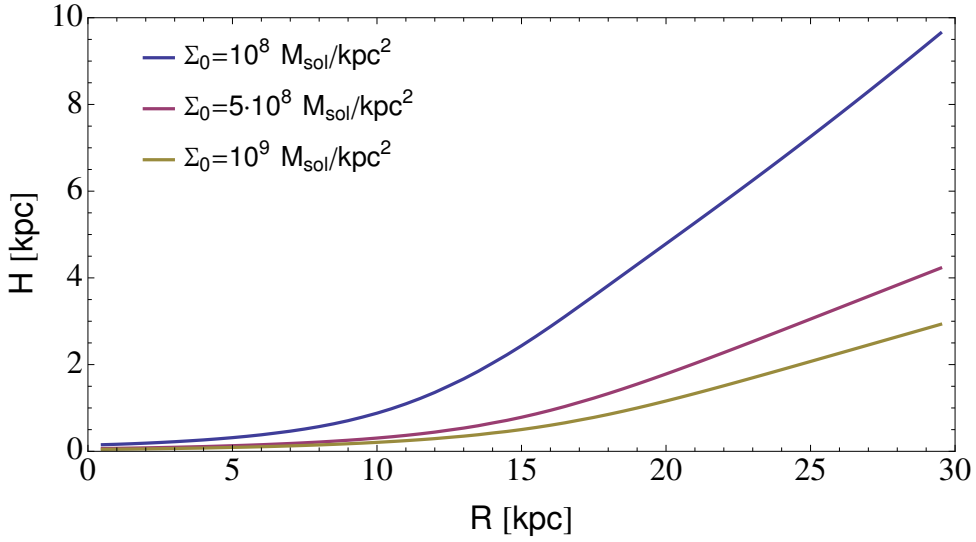


(b) Model B: $R_d = 3$ kpc, $Z_0 = 0.4$ kpc

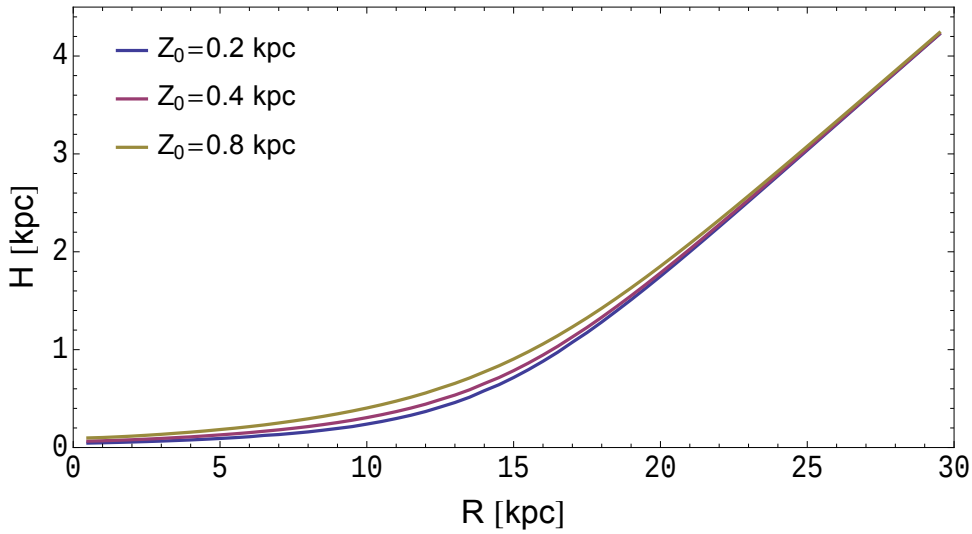


(c) Model C: $\Sigma_0 = 5 \cdot 10^8\ M_\odot/\mathrm{kpc}^2$, $R_d = 3$ kpc

Figura 3.3: HI flarings produced by exponential disks with densities given by eq. 3.13. In each panel we fixed two parameter between $\Sigma_0$, $R_d$, $Z_0$, and the third one. The scale height of the HI gas has been computed with the numerical estimation of the potential (sec. 2.3), keeping the gas velocity dispersion $\sigma$ fixed at 10 km/s.

### 3.1.2 Dark Matter Halo

The first HI observations of external galaxies showed that beyond the optical disk the circular velocity remains constant in contrast with the expected keplerian decline (Roberts & Rots 1973; Bosma 1978). This is a clear evidence that the luminous matter can not explain alone the rotational curve of the disk galaxies, and an additional mass component (Dark Matter, DM) is needed. Today we know that every galaxy is embedded in a DM halo and these halos are required in a cosmological contest to explain the formation of structures.

#### Shape of the DM halo

It is usually assumed that the Dark Matter halo has a spherical shape, but both cosmological simulation (Dubinski, 1994; Schneider et al., 2012) and observational results (Olling, 1996) indicate that it could have an ellipsoidal or even a triaxial shape. In this work we have chosen to model the DM halo assuming an ellipsoidal oblate shape with major axis $a$ and minor axis $b$. It is useful to define some parameters related to the geometrical shape of the halo:

- **The flattening $q$:** $q = b/a$
- **The ellipticity $e$:** $e = \sqrt{1 - (b/a)^2}$

- **The flattening ratio *g*:** $g = e/q$

$q$ and $e$ range from 0 to 1, while $g$ from 0 to infinity. These parameters can be interpreted geometrically by defining a right triangle with an hypotenuse $a$, a cathetus $b$ and the angle $\alpha$ between them. We can **then** redefine the shape parameters as follows:

$$q = \cos(\alpha),\ e = \sin(\alpha) \text{ and } g = \tan(\alpha)$$

.

and obtain the following identity:

$$\arcsin(e) = \arccos(q) = \arctan(g) \tag{3.14}$$

There are several density laws proposed to describe the DM halos, in this thesis we use the *Isothermal Model* (Hubble law) (Sackett & Sparke, 1990) and the *Navarro-Frenk-White Model* (NFW) (Navarro et al., 1996).

### 3.1.3 Isothermal Halo

#### Rotational velocity

The DM halo can be seen as a self-graviting ellipsoid in hydrostatical equilibrium. Assuming that the DM is isothermal, one can show that the density distribution is (Gunn & Gott, 1972):

$$\rho(m) = \frac{\rho_0}{1 + \frac{m^2}{R_c^2}} \tag{3.15}$$

where $m^2 = R^2 + (Z/q)^2$ and $q$ is the flattening parameter (see section 3.1.2).

Differentiating the potential of eq. 3b in Sackett & Sparke (1990) it is possible to derive the circular velocity on the equatorial plane (Olling, 1995; Sicking, 1997):

$$V_c^2(x) = V_\infty^2 \left( 1 - \frac{g}{\arcsin(e)} \frac{\arctan(g\sqrt{1 + (x/e)^2})}{g\sqrt{1 + (x/e)^2}} \right) \tag{3.16}$$

where $x$ is the radius in unity of the core length $R_c$, $e$ and $g$ are the halo geometrical parameters (see section 3.1.2). For $R = 0$, equation 3.16 becomes: $V_c^2(0) = V_\infty^2 \left(1 - \frac{\arctan(g)}{\arcsin(e)}\right)$, therefore from eq. 3.14 we derived that $V_c(0) = 0$ for every geometrical shape of the halo. For R going to infinity, the velocity approaches its asymptote:

$$V_\infty = \left( 4\pi G \rho_0 R_c^2 f(q) \right)^{\frac{1}{2}} \tag{3.17}$$

where:

$$f(q) = q \frac{\arccos(q)}{\sqrt{1 - q^2}} \tag{3.18}$$

the function $f(q)$ (eq. 3.18) describes the dependences of $V_\infty$ on the flattening parameter $q$. It ranges from 0 at $q = 0$ to 1 at $q = 1$ (fig. 3.4). If $q = 1$, eq. 3.17 gives the rotational velocity for a spheroidal isothermal halo.

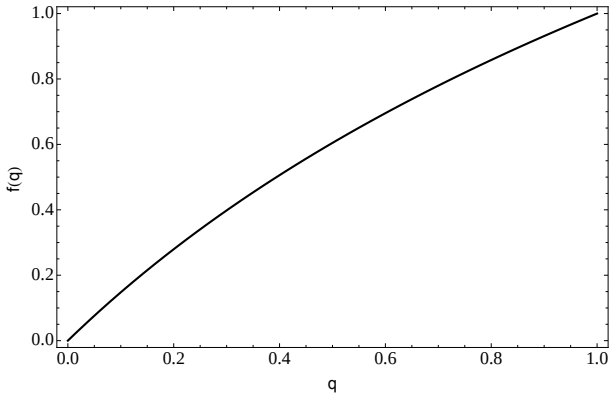


Figura 3.4: Plot of the function f(q) (eq. 3.18).

A simple analysis of eq. 3.17 shows that $V^{'}(x) > 0$ for every x, therefore the isothermal halo produces a rotation curve that grows monotonically from 0 to $V_\infty$ and becomes nearly flat for $R \geq 4\ R_c$ , as shown in fig. 3.5.

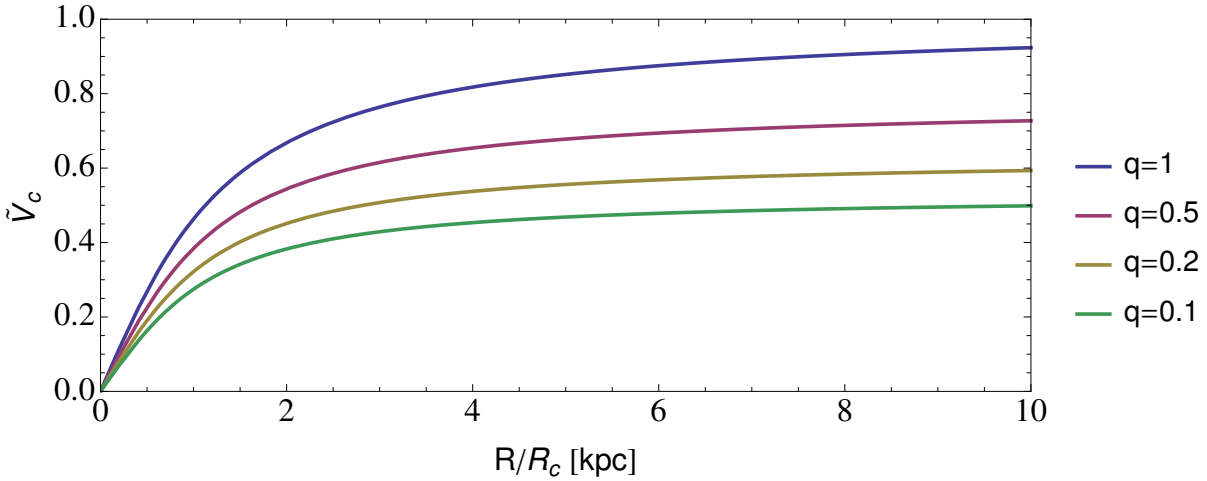


Figura 3.5: Rotation velocity produced by isothermal halos with different flattening $q$ (eq. 3.16). The velocity on the Y axis is normalized for the asymptotic velocity without the geometrical factor f(q) (eq.3.17): $\widetilde{V}_c = V_c/\sqrt{4\pi G R_c^2}$

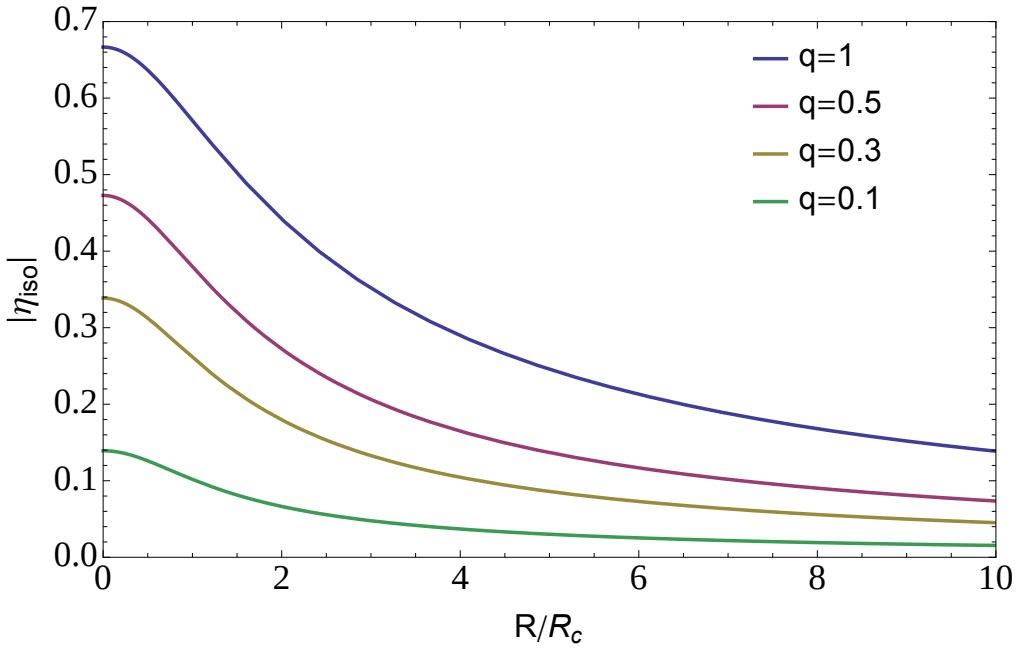


Figura 3.6: Ratio between $\rho_{\rm rot}$ and $\rho_{\rm mat}$ for isothermal halos with different flattening parameters.

### Rotational density

In order to obtain the rotational density $\rho_{\rm rot}$ (eq. 2.9), we introduce the variable y defined as follows:

$$y = g\sqrt{1+(x/e)^2} \tag{3.19}$$

Accordingly the radial velocity gradient can be written as:

$$\frac{dV_{rot}(R)}{dR} = -\frac{x}{yR_c\ q^2}\frac{dV_{rot}(y)}{dy} \tag{3.20}$$

Substituting eq. 3.20 in eq. 2.9 we obtained the rotational density:

$$\rho_{\rm rot} = -\rho_0 \left(\frac{\arctan(y)(1+y^2)-y}{(1+y^2)y^3}\right) q^{-2} \tag{3.21}$$

The derivation of $\eta_{\rm iso} = \rho_{\rm rot}/\rho_{\rm mat}$ from eq. 2.13 is straightforward :

$$\eta_{\rm iso}(x) = -\left(\frac{\arctan(y)(1+y^2)-y}{(1+y^2)y^3}\right)\frac{1+x^2}{q^2} \tag{3.22}$$

The trend of $\eta_{\rm iso}$ is shown in fig 3.6 for various values of the flattening parameter $q$. $|\eta|_{iso}$ is always lower than 0.7 and the rotational contribution to the scale height decreases as a function of radius and flattening.

It is possible to derive some considerations from the eq. 3.22:

- Sign of $\eta_{\rm iso}$:

  $x$, $q$ and $g$ are always positive, accordingly from the definition 3.19 $y(x) > 0$ for every $x$. Hence, the sign of $\eta_{iso}$ (or $\rho_{rot}$) depends on the sign of the function $\arctan(y)(1+y^2) - y$, which is always positive for every value of y[1]. The rotational density will always give a negative contribution in eq. 2.11 (the rotation curve is rising everywhere), hence the HI scale-height will be always thicker with respect to a non rotating gaseous layer.

- Value of $\eta$ at R=0:

  At $R = 0$ the variable y is equal to $g$, therefore we can write:

$$|\eta_{\rm iso}(0)| = \left( \frac{\arctan(g)(1+g^2) - g}{q^2(1+g^2)g^3} \right) \tag{3.23}$$

  For a round halo $q = 1$ and $g = 0$, hence from de L'Hopital's rule we obtain $\lim_{g\to 0}|\eta_{\rm iso}| = 2/3$. In the case of maximum flattening $q \to 0$, $g \to \infty$ and accordingly $|\eta_{\rm iso}| \to 0$

- Asymptotic behavior of $\eta_{\rm iso}$:

  When $R$ goes to infinity the variable $y$ approaches $x$, and the absolute value of equation 3.22 decreases as $R^{-1}$.

- Dependence of $\eta_{\rm iso}$ on the halo parameters:

  Eq. 3.22 only depends on the geometrical parameter $q$, hence whatever halo model we use, $\eta$ always will be the same. Comparing eq. 3.15 with eq. 3.21 it is clear that they have the same linear dependence on the central density $\rho_0$. Hence, their ratio will be independent from it.

  This feature can be generalized for every axisymetric density distribution. We can write the density as $\rho(R,Z) = \rho_0 f(R,Z)$, the related potential is obtained integrating the density over R and Z, and the constant $\rho_0$ can be taken out from the integral. Hence, one can $\Phi(R,Z) = \rho_0 g(R,Z)$. The rotational density defined in eq. 2.9 depends on radial

[1] Let f(x) be a differentiable function in the range [0:y], the mean value theorem states that exists a value c between 0 and y such that

$$\frac{df(x)}{dx}(x=c) = \frac{f(y) - f(0)}{y}$$

If $f(x) = \arctan(x)$, we can write:

$$\frac{d\arctan(x)}{dx}(x=c) = \frac{1}{1+c^2} = \frac{\arctan(y)}{y}$$

From the initial definition $c < y$, hence:

$$\frac{y}{1+y^2} < \frac{y}{1+c^2} = \arctan(y)$$

therefore: $\arctan(y)(1+y^2) > y$ for every $y$.

derivatives of $\Phi$, hence we can write $\rho_{\rm rot}(R,Z) = \rho_0 h(R,Z)$. In conclusion, for any function $f$, $h$ and $g$, the ratio between the rotational density and the matter density, will be always independent of $\rho_0$ and hence of the total mass of the halo. However, $\eta_{\rm iso}$ depends on the radial scale length of the halo $R_c$. Its variations are appreciable only if we plot it as function of $R$, instead of $R/R_c$ as shown in fig. 3.6. As an example, we consider three halo models with different flattening (q=1, 0.5 and 0.1 respectively) but the same rotation curve, as described in app. C.1.1. They have different core radii, indeed $R_c$ is a decreasing function of the flattening (eq. C.3a): if we set $R_c = 3$ kpc for the spherical model, the core radius for other two halos will be 3.36 and 3.81 kpc respectively. The resulting $\eta_{\rm iso}$ are plotted as a function of the radius in fig. 3.7. The dashed lines show $\eta_{\rm iso}$ for halo models with the same $R_c$ (and thus different rotation curve) in analogy to fig. 3.6. Is is clear that, at a fixed radius $R$, models with higher $R_c$ will have larger values of $\eta_{\rm iso}$. However the differences are very small, thus we conclude that for a given rotation curve the contribution of the rotation ($\rho_{\rm rot}$) on the HI scale height depends only on the halo flattening.

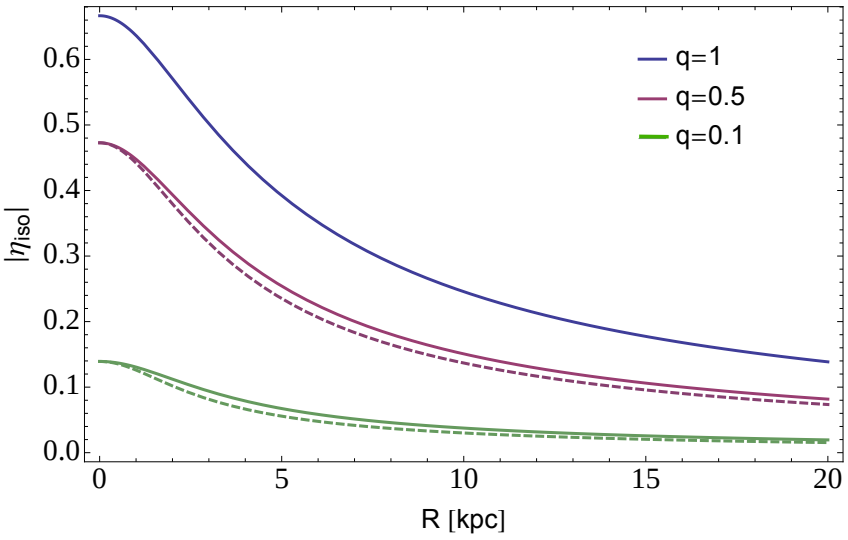


Figura 3.7: $\eta_{\rm iso}$ for three halo models (full curves) with different flattening that produce the same rotation curve (app. C.1.1). The core radii ($R_c$) are set to 3, 3.36 and 3.81 kpc following the eq. C.3a, the dashed curves have a fixed $R_c = 3$ kpc and they represent a yardstick for the models with varying core radius.

### Analytical scale height

Using the density law of an isothermal halo (eq. 3.15) in the definition of the flaring function in eq. 2.11, we can write:

$$H(R) = \frac{\sigma_z \sqrt{R_c^2 + R^2}}{\sqrt{4\pi G \rho_0 R_c^2}} \tag{3.24}$$

or

$$H(R) = 0.136 \sqrt{\frac{R_c^2 + R^2}{R_c^2}} \left( \frac{\sigma(R)}{10 \text{ km/s}} \right) \left( \frac{\rho_0}{10^8 \text{ M}_\odot/\text{kpc}^3} \right)^{-1/2} \text{kpc} \tag{3.25}$$

In order to make the dependance of the scale height on the halo flattening explicit, we note that the denominator of eq. 3.24 is equal to the asymptotic velocity $V_\infty$ (eq. 3.17), except for the factor $f(q)$. Thus, we can write:

$$H(R,q) = 0.1 \frac{\left( \frac{\sigma(R)}{10 \text{ km/s}} \right)}{\left( \frac{V_\infty}{100 \text{ km/s}} \right)} \sqrt{f(q)} \sqrt{{R_c}^2 + R^2} \text{ kpc} \tag{3.26}$$

In the central region where the radius is much lower than the core radius, we can approximate eq. 3.25 as:

$$H \approx 0.4 \frac{\left( \frac{\sigma(R)}{10 \text{ km/s}} \right)}{\left( \frac{V_\infty}{100 \text{ km/s}} \right)} \sqrt{f(q)} \left( \frac{R_c}{4 \text{ kpc}} \right) \text{ kpc} \tag{3.27}$$

In these regions the gas scale height stays approximately constant, while at larger radii it exhibits a linear growth: $H \propto R$. Eqs. 3.25 and 3.26 always represent a lower limit for the scale height of the gas layer, because we are neglecting the contribution of the rotational density.

### Numerical analysis

Figure 3.8 shows a comparison between the analytic results and the theoretical scale height obtained as described in section 2.3. At first glance one can note that the analytic solutions are always below the numerically calculated values, as expected for a rising rotation curve ($\rho_{\text{rot}}(R) > 0$), and that the two curves are parallel as expected from the nearly constant value of $\eta_{\text{iso}}$ for $R > 4\ R_c$ (fig. 3.6). The two solutions tend to overlap for large flattening of the halo. The differences between the numerical and the analytic flaring are totally explained by the the contribution of the rotational density (eq. 3.21) totally explains the differences between the numerical and the analytic flaring. This implicitly implies that the Taylor series expansion made in eq 2.5 is a good approximation of the halo galaxy potential.

In appendix C we show that there is a degeneracy in the DM isothermal models: the same rotational curve of a spiral galaxy can be explained by halos with different flattenings. Eqs. C.2 tell us that for lower $q$ the halo will have a greater central density and a larger core radius,

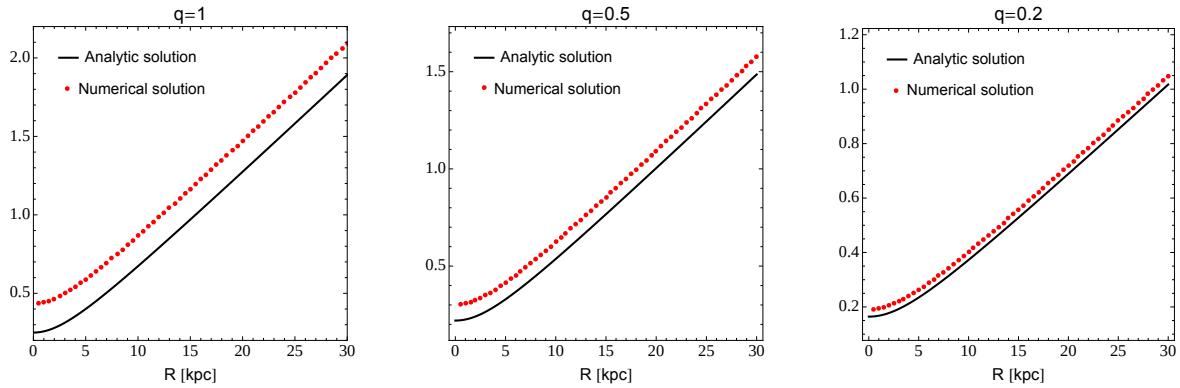


Figura 3.8: Comparison between the gas thickeness obtained with the analytic (eq. 3.26) and numerical method for an isothermal halo potential with core radius $R_c(q) = 4\kappa(q)$ kpc (eq. C.3a), asymptotic velocity $V_\infty = 160$ km/s and three different halo flattenings.

hence we expect that flatter halos will produce lower HI scale heights. To study the magnitude of these differences, we created a set of halo models with flattening parameters ranging from 1 to 0.1 with step 0.1. The central density and core radius are tuned with equations C.2 in order to obtain the same rotation curve with asymptotic velocity equal to 160 km/s. As expected the scale height of the HI disk decreases as a function of the flattening parameter q.

Figure 3.9 shows the flaring for halo models with q equal to 1, 0.5 and 0.2. The three curves are well separated especially at larger radii, hence the outer disks of spiral galaxies are the ideal regions to investigate the flattening of the DM halos.

In order to evaluate the overall variation of the layer thickness produced by the analyzed DM models, we have calculated the relative differences in scale-height for different flattening pairs ($q_1$,$q_2$). We noticed that these differences are almost constant with radius with variations of about 10 %. Therefore, we took the average over all the sampled radii obtaining a single reference value for each pair. The results are shown in fig. 3.10: in some cases the differences are so large ($> 40\%$) that also with a rough estimate of the disk thickness one could be able to rule out a significant range of halo flattenings.

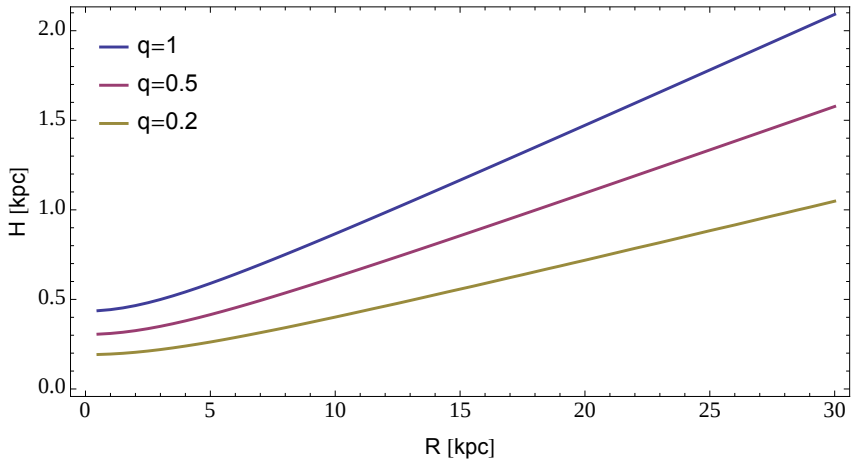


Figura 3.9: Theoretical HI flaring for three isothermal DM models with different halo flattening q. They produce the same rotation curve ($V_\infty = 160$ km/s) but different layer thickness.

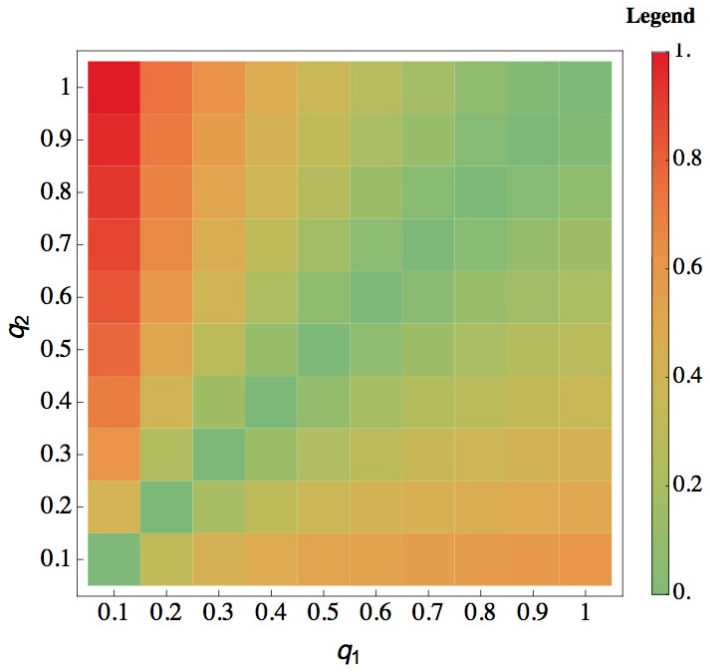


Figura 3.10: Mean relative difference between layer thickness produced by isothermal halos with different flattening parameters ($q_1$,$q_2$). The values shown in the plot are the radial averages of the relative differences calculated as $\frac{|H(q_2)-H(q_1)|}{H(q_1)}$. The central densities and the core radii of the halos have been set to produce the same rotational curve ($V_\infty = 160$ km/s) (see Appendix C ). The grid appears not symmetric because while the numerator ($|H(q_2) - H(q_1)|$) is the same inverting $q_1$ with $q_2$, the denominator $H(q_1)$ depends only on $q_1$.

### 3.1.4 NFW halo

**Rotational velocity**

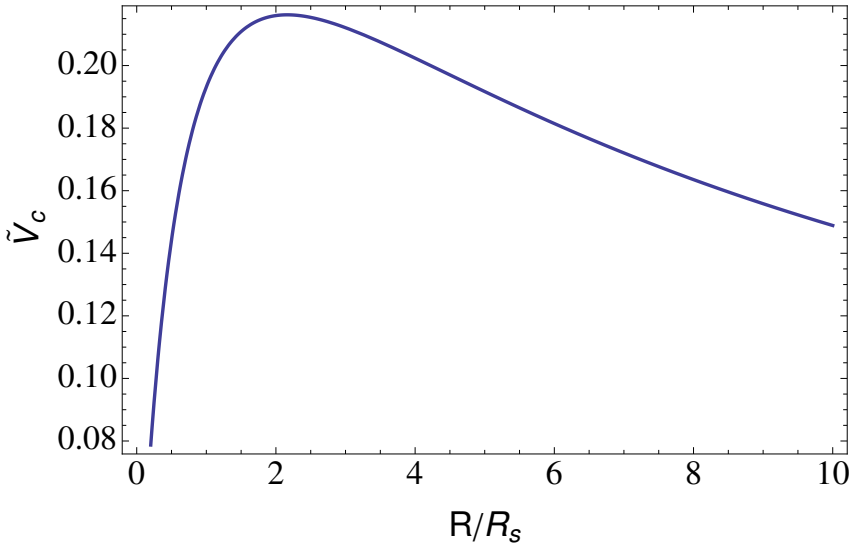


Figura 3.11: Rotation velocity produced by a NFW spheroidal halo. The velocity on the Y axis is $\tilde{V}_c = V_c/\sqrt{4\pi G R_s^2}$

Between 1995 and 1997 Navarro, Frenk & White (e.g. Navarro et al. 1996) performed a series of N-body collisionless simulations to study the density distribution of DM in the contest of the CDM (Cold Dark Matter) cosmology. They showed that from the small halos hosting dwarf galaxies up to giant structures like galaxy clusters, the DM density profile is well approximated by the following law:

$$\rho(R) = \frac{\rho_{\rm crit}\ \delta_c}{\frac{R}{R_s}\left(1+\frac{R}{R_s}\right)^2} \tag{3.28}$$

where $\rho_{\rm crit} = \frac{3H^2}{8\pi G}$ is the critical density of the Universe, $R_s$ is a scale parameter, $\delta_c$ is a concentration factor:

$$\delta_c = \frac{200}{3}\frac{c^3}{\left[\ln(1+c) - c/(1+c)\right]} \tag{3.29}$$

where $c = \frac{R_{200}}{R_s}$ is the concentration parameter. $R_{200}$ is the radius where the density of the halo is 200 times greater than the critical density $\rho_{\rm crit}$. Neto et al. (2007) showed that for the typical range of masses of spiral galaxies ($M_{\rm tot} \approx 10^{11}$- $10^{12}$ $M_\odot$) the mean value of the concentration parameter is approximately 10.

The equatorial rotational velocity produced by the NFW density profile is:

$$V_c^2(R) = V_{200}^2 \frac{c}{x}\left[\frac{\mathrm{Log}(1+x) - (x)/(1+x)}{\mathrm{Log}(1+c) - c/(1+c)}\right] \tag{3.30}$$

with $x = R/R_s$. We can calculate the mass of the halo at $R_{200} = cR_s$ assuming virial equilibrium:

$$M_{200} = \frac{V_{200}^2 c R_s}{G}$$

However, the mass can be calculated also integrating the density:

$$M_{200} = \int_0^{cR_s} 4\pi R^2 \rho(R) dR = 4\pi \rho_{\rm crit} \delta_c R_s^3 [{\rm Log}(1+c) - c/(1+c)]$$

Using the definition of critical density and eq. 3.29, we can write the solution of the above integral as:

$$M_{200} = 100 R_s^3 H^2 c^3 G^{-1}$$

Equating the two definitions of $M_{200}$ we can link $R_s$ and $V_{200}$:

$$R_s = \frac{V_{200}}{10Hc} = 14.93 \left(\frac{V_{200}}{100 \text{ km/s}}\right) \left(\frac{c}{10}\right)^{-1} \left(\frac{H}{67 \text{ km/s/Mpc}}\right)^{-1} \text{ [kpc]} \tag{3.31}$$

Therefore the $V_c(R)$ in eq. 3.30 depends only on two parameters (e.g. $c$ and $R_s$) in analogy to the isothermal case.

Alternatively we can use the general density law proposed by Dehnen & Binney (1998):

$$\rho(R) = \frac{\rho_0}{\frac{R}{R_s}\left(1 + \frac{R}{R_s}\right)^2} \tag{3.32}$$

with:

$$\rho_0 = \rho_{\rm crit}\ \delta_c = 8.34 \left(\frac{H}{67 \text{ km/s/Mpc}}\right)^2 \left(\frac{c^3}{{\rm Log}(1+c) - c/(1+c)}\right)\ 10^3\ [{\rm M}_\odot/{\rm kpc}^3] \tag{3.33}$$

From equation 2.91 in Binney & Tremaine (2008) we obtain the equatorial circular velocity for the density distribution of eq. 3.32

$$V_c^2(x) = \frac{4\pi G \rho_0 R_s^2}{x} \left({\rm Log}(1+x) - (x)/(1+x)\right) \tag{3.34}$$

A NFW halo produces a rotational curve (shown in fig. 3.11) quite different from the one generated by an isothermal halo (compare fig. 3.11 and fig. 3.5). It does not have an asymptotic velocity, and it has a steeper rise until it reaches the peak of the velocity around $2R_s$. Beyond this radius the rotational velocity decreases reaching 0 at $R = \infty$. At large radii ($R >> R_s$) it falls as $V_c \propto {\rm Log}(1+x)/x$, the logarithm can be considered practically constant with respect to the denominator, hence $V_c \propto R^{-\frac{1}{2}}$ like a keplerian rotation curve. A NFW halo produces a rotational curve similar to the one generated by an exponential disk distribution of matter (eq. 3.5), however the scales involved are very different ($R_s >> R_d$).

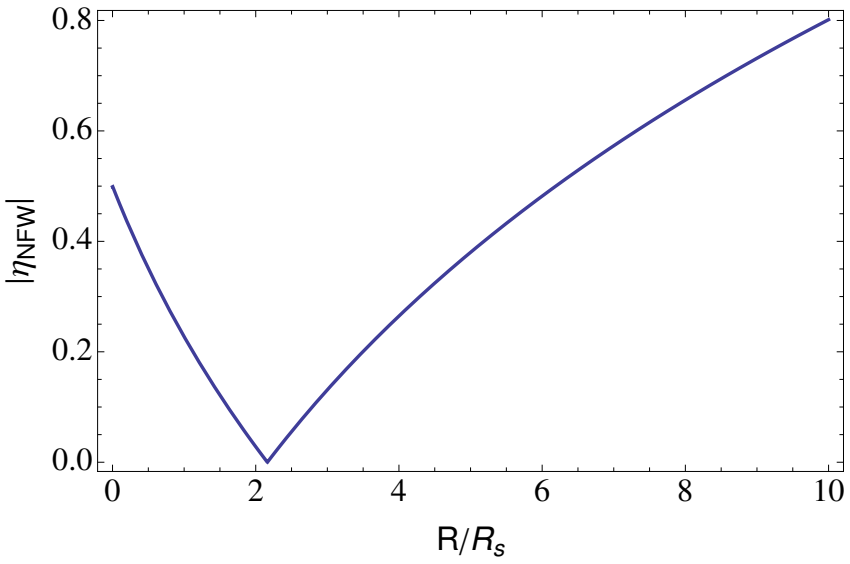


Figura 3.12: Ratio between $\rho_{\rm rot}$ and $\rho_{\rm mat}$ for NFW halos with different flattening parameters $q$.

### Rotational density

Unlike the isothermal halos, an analytic solutions for the rotation curve produced by a NFW halo exsists only for the spherical case (eq. 3.30 or eq. 3.34). Therefore, the analysis of the rotational density has been performed only for spherical system ($q$=1). Differentiating eq. 3.34 we obtain:

$$\frac{dV_c}{dR} = \frac{dV_c}{R_s dx} = \frac{4\pi G R_s}{2V_c}\left(\frac{x(2x+1)-(1+x)^2\mathrm{Log}(x+1))}{x^3(1+x)^2}\right) \tag{3.35}$$

Using the latter relation in eq. 2.9 we can write:

$$\rho_{\rm rot} = -\rho_0\left(\frac{x(2x+1)-(1+x)^2\mathrm{Log}(x+1))}{x^3(1+x)^2}\right) \tag{3.36}$$

Hence the ratio between $\rho_{\rm rot}$ and $\rho_{\rm mat}$ (eq. 2.13) becomes:

$$\left|\eta_{NFW}(x)\right| = \left|\frac{x(2x+1)-(1+x)^2\mathrm{Log}(x+1))}{x^2}\right| \tag{3.37}$$

The factor $\eta_{NFW}$ is plotted in fig. 3.12. The contribution of the rotational density is half of the matter density at R=0: $\lim_{x\to 0}\eta_{NFW}(x) = 0.5$. It rapidly decreases to 0 at $R \sim 2R_s$ where the rotation curve reaches its peak. In the range from 0 to 2R$_s$ the rotational velocity increase (3.11), thus the sign of the rotational density (eq. 3.36) is negative and the HI scale height is higher with respect to non rotating model. Beyond $2R_s$, $|\eta|$ slowly increases to infinity and becomes the dominant contribution to the scale height for $R > 10R_s$. The sign of the rotational density becomes positive in this range of radii, therefore we expect that the gas would be thinner

than in the case of a flat rotation curve. The typical value of $R_s$ found in spiral galaxies are of the order of tens kiloparsec (de Blok et al., 2008a), hence the HI disk is generally contained within a few $R_s$.

### Analytical flaring

Using the NFW density law (eq. 3.32) in the definition of the scale height (eq. 2.11), we can write:

$$H(R) = 0.430 \left(\frac{\sigma(R)}{10 \text{ km/s}}\right) \left(\frac{\rho_0}{10^7 \text{M}_\odot/\text{kpc}^3}\right)^{-\frac{1}{2}} \sqrt{\left(\frac{R}{R_s}\right)\left(1+\frac{R}{R_s}\right)^2} \text{ [kpc]} \tag{3.38}$$

It is possible to link the flaring function and the concentration parameter $c$ through eq. 3.33:

$$H(R) = 0.609 \left(\frac{\sigma(R)}{10 \text{ km/s}}\right) \left(\frac{H_{\text{hubble}}}{67 \text{ km/s/Mpc}}\right)^{-1} \left(\frac{g(c)}{600}\right)^{-\frac{1}{2}} \sqrt{\left(\frac{R}{R_s}\right)\left(1+\frac{R}{R_s}\right)^2} \text{ [kpc]} \tag{3.39}$$

where $g(c) = c^3/(\text{Log}(1+c) - c/(1+c))$. The value of the function g for $c \approx 10$ is about 600. We note that for $R >> R_s$ the thickness increase as $R^{\frac{3}{2}}$, the same trend given by a keplerian rotational velocity (eq. 3.12).

### Numerical Analysis

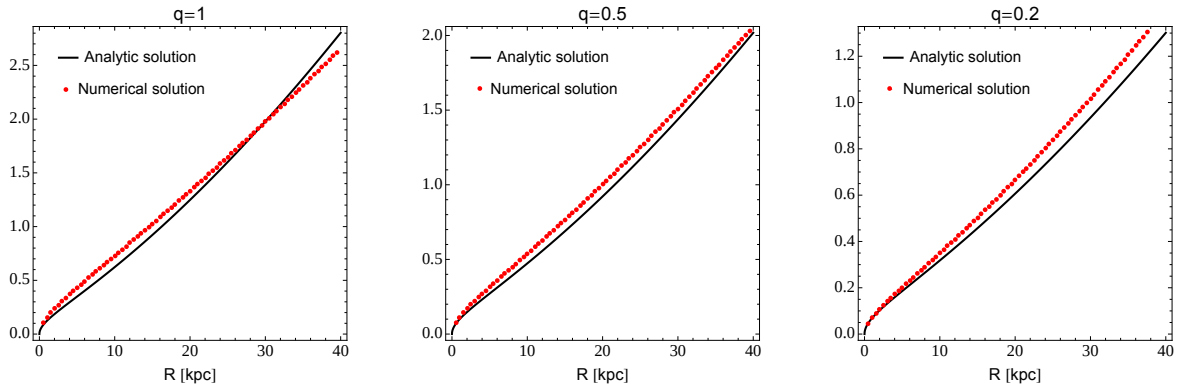


Figura 3.13: See fig. 3.8. The spherical halo ($q = 1$) has a $R_s = 14$ kpc and a central density $\rho_0 = 10^7$ $\text{M}_\odot$ $\text{kpc}^3$. The parameters of the other halos are set with eq. C.6 to reproduce the same rotation curve of the spherical halo (appendix C.1.2)

.

Figure 3.13 shows a comparison between the the analytic flaring (eq. 3.5) and the numerical calculations for NFW halos with $R_s = 14$ kpc and different flattenings (see sec. 2.3). The left panel shows a good agreement between the numerical and analytical solution. The numerical

scale height is systemitically higher from 0 to $R \approx 28$ kpc $= 2R_s$, as we expect for a rising velocity curve. It becomes lower at large radii where the decline of the velocity curve makes the gaseous layer thinner. For ellipsoidal halos ($q < 1$) we lack an analytic forms for the velocity curve and the rotational density, therefore it is impossible to estimate if the differences between analytic and numerical flaring (middle and right panels in fig. 3.13) is due only to the rotational density. It seems that the analytic equations 3.5 and 3.39 underestimate the HI scale height in the analyzed range. However, the differences are similar and the approximations made to obtain the analytic solution (sec. 2.2) seem adeguate to estimate the HI scale height out to $2 - 3\ R_s$. In contrast with what seen for the isothermal halo, the analytic and numerical scale-heights are not parallel, indeed $\eta_{\rm NFW}$ is not approximately constant as it happens at large radii for $\eta_{\rm iso}$, hence the influence of the rotational density depends on radius.

Figure 3.14 shows the numerical flaring for three halos with the same rotational curve but different flattenings $q$: the flatter is the halo, the lower will be the HI scale height. Finally, Figure 3.16 shows the mean relative differences between flaring curves produced by NFW halos with the same rotational velocity, but different flattenings parameters. As already seen for the isothermal halo the relative differences can be very high: for a variation of the flattening parameter of 0.3-0.4 the relative differences between the flaring curves are of the order 30-40 %.

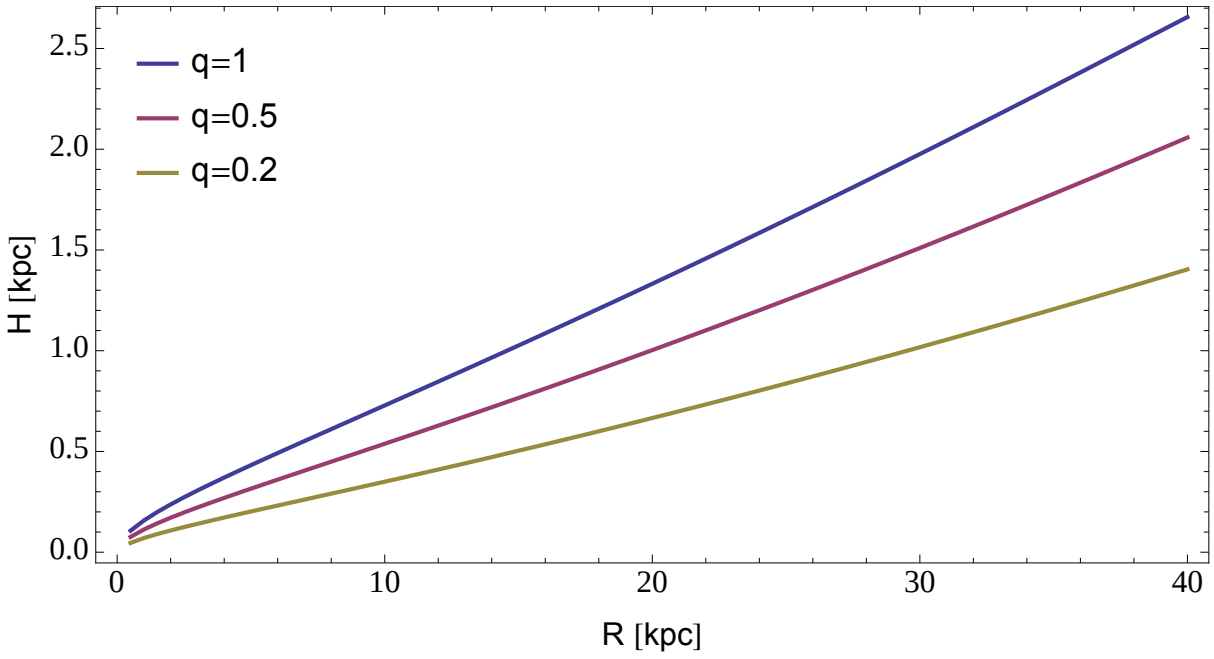


Figura 3.14: Comparison between the theoretical HI thickness for the three NFW DM models of fig. 3.13. They produce the same rotation curve but different flarings.

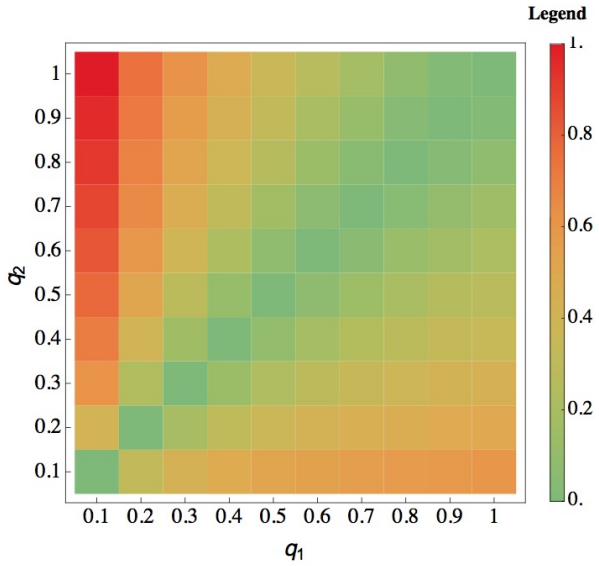


Figura 3.16: See fig. 3.10.

### 3.1.5 Isothermal vs NFW halos

In the previous sections we pointed out that the study of the gas flaring can break the degeneracy between various halo flattenings that arises from the fit of the observational rotational curve (appendix C). Another known degeneracy is related to the choice of the density law. Indeed, rotation curves of the spiral galaxies are typically well described both by an isothermal and a NFW halo (e.g. de Blok et al. (2008b)). If halos with different density laws produced HI layers

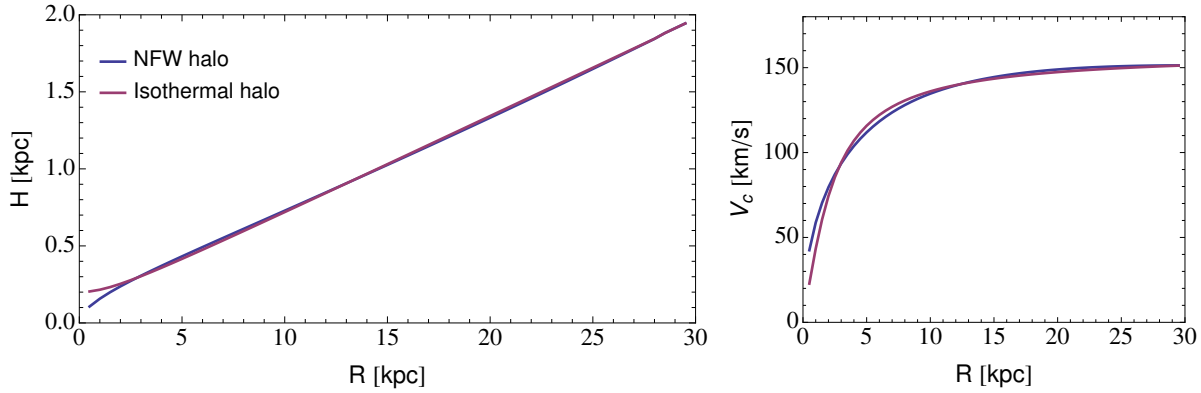


Figura 3.15: Comparison between the theoretical HI scale height produced by NFW and a Isothermal DM models (left panel). The halo parameters have been fixed to produce nearly the same rotation curve (shown in the right panel) (Appendix C.2).

with significant different thicknesses, one could use the vertical gas distribution to break this degeneracy. To study the feasibility of this approach, we numerically evaluated the flaring for two spherical halo models:

- **Halo Iso:** A matter distribution with an isothermal density law (eq. 3.15) and with parameters $R_c = 1.98$ kpc and $\rho_0 = 1.20\ 10^8\ \mathrm{M}_\odot/\mathrm{kpc}^3$.

- **Halo NFW:** A matter distribution with the NFW density law (eq. 3.32) and with parameters $R_s = 14$ kpc and $\rho_0 = 10^7\ \mathrm{M}_\odot/\mathrm{kpc}^3$.

The parameters have been set to reproduce nearly the same rotation curve (right panel of 3.15), as described in app. C.2. The resultant scale heights are shown in the left panel of figure 3.15, they clearly overlap: the relative differences are of the order of few per cent.

We have performed the analysis again for several value of the flattening parameter q, but the flaring curves always show the same behavior as the spherical case. We conclude that study of the flaring cannot break the degeneracy between different halo density laws.

**Consideration about the HI thickness produced by a DM halo**

The analytic flaring forms of eqs. 3.25 and 3.5 look different at a first glance, thus it can seem strange that an isothermal and a NFW halo produce exactly the same HI scale height over a wide range of radii. The effect of the rotational density (sec. 2.2) can not be invoked, because the main assumption made above, is that the two halos yield the same rotation curve. However, the radial scale lengths of the two DM halo models have different orders of magnitude, indeed to obtain the same rotation curve the scale length of a NFW profile must be approximately ten time greater than the one of an isothermal halo (eq. C.8 in Appendix C.2). Hence, while the extension of a gaseous disk is generally several time greater than the scale length ($R_c$) of an isothermal halo, for the NFW halo it is of the order of $R_s$. As a results, for most radii the condition $R >> R_c$ is fulfilled and the eq. 3.5 becomes proportional to R. On the other hand, the flaring produced by a NFW halo follows a power law $R^a$ with $a$ that assumes intermediate values between 0.5 for $R << R_s$ and 1.5 for $R >> R_s$. We performed a numerical analysis that shows that the exponent $a$ is approximately equal to one for most radii, as in the case of the isothermal halo. In the case of an oblate DM halo we know form Appendix C that to reproduce the same rotation curve, the scale length must increase as the halo becomes flatter. As a result, the condition $R >> R_c$ is less strong for an isothermal halo, while for a most of the disk becomes closer to the condition $R << R_s$. In both cases the HI scale height will grow more gently with respect to the spherical case.

Overall, we can state that a DM halo produces a growth of the HI scale height proportional to $R^\alpha$, where $\alpha$ in nearly equal to 1 for spherical halos and tends to toward lower values for flatter halos. We stress that this analysis is based on the assumption of flat rotation curves, as it is the case for the most spirals. In galaxies that exhibit a rising rotation curve at all radii (see e.g. Swaters 1999), the core radius of the isothermal halo can assume very high values and the condition $R >> R_c$ is no longer fulfilled.

## 3.2 Multicomponent models

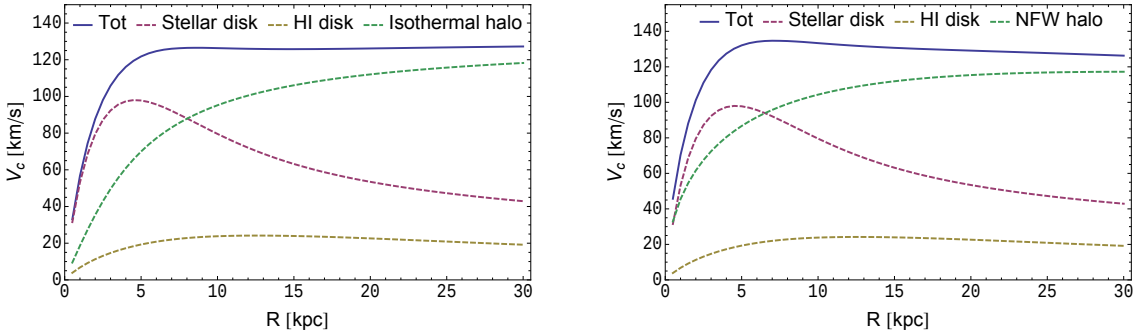


Figura 3.17: **Rotation curves produced by the mass models described in the text. The difference between the two panels is the use of an isothermal (left panel) and a NFW (right panel) halo.**

In the previous sections we showed the theoretical flaring produced by individual mass components: stellar disks or DM halos. However, in real spiral galaxies these are embedded together with the addition of the self-gravity of the gaseous disk. In this section we used the numerical approach, outlined in sec. 2.3, to obtain the theoretical scale height of an HI disk produced by a realistic distribution of matter. The self gravity of the gas has been treated as explained in sec. 2.3.2.

The Variuos mass components have been set as follows:

- Exponential stellar disk: central surface density $\Sigma_{0s} = 5 \cdot 10^8 \mathrm{M}_\odot/\mathrm{kpc}^2$ and radial scale length $R_{ds} = 2$ kpc; the vertical distribution is a hyperbolic square secant with a scale height $Z_0 = 0.4$ kpc.
- Exponential gaseous disk: central surface density $\Sigma_{0g} = 10^7 \mathrm{M}_\odot/\mathrm{kpc}^2$ and radial scale length $R_{dg} = 6$ kpc.
- Isothermal halo: central density $\rho_0 = 2\ 10^7 \mathrm{M}_\odot/\mathrm{kpc}^3$, core radius $R_c = 4$ kpc and spherical shape ($q = 1$).
- NFW halo: central density $\rho_0 = 2\ 10^6 \mathrm{M}_\odot/\mathrm{kpc}^3$, scale radius $R_s = 25$ kpc and spherical shape ($q = 1$).

We combined the mass components above in two realistic galaxy models: the first was composed by the stellar and gaseous disks in addition to the isothermal halo, in the other the isothermal halo has been replaced by the NFW halo.

The parameters of the mass components have been chosen to reproduce both a realistic flat rotation curve (fig. 3.17) and a significative HI scale height in the outer part (fig. 3.18), while

the velocity dispersion of the gas has been fixed to the characteristic value of 10 km/s (Tamburro et al., 2009).

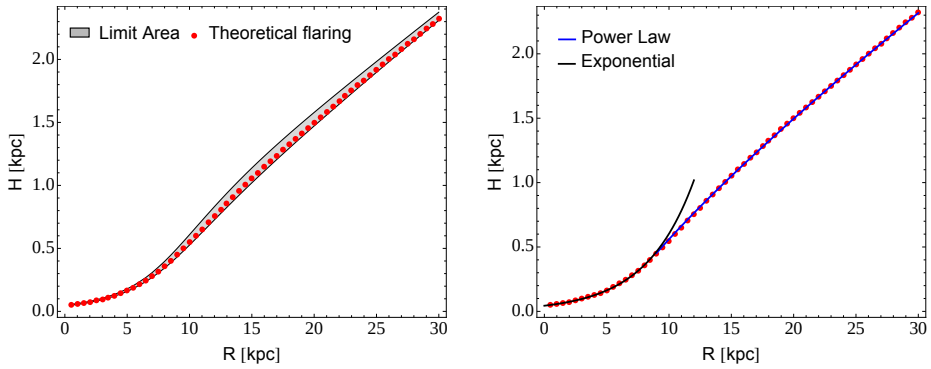


(a) Model A: Isothermal halo

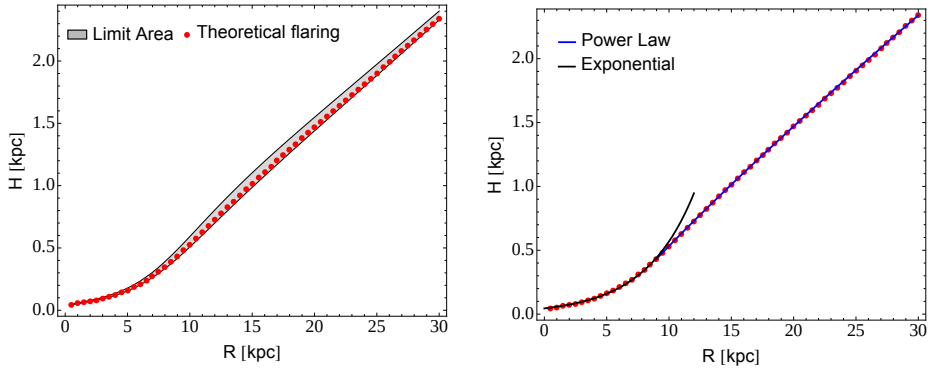


(b) Model B: NFW halo

Figura 3.18: Theoretical flaring (numerically calculated) produced by the galaxy models described in the text. The black shaded regions in the left panels represent the area between the upper and lower limit of the HI scale height (see sec. 2.3.2). In the right panels we show the best functions that describe the inner and outer forms of the flaring.

Figures 3.18 a and b show the flaring produced by the two models: in the left panels we plotted the numerical scale heights and their upper and lower limits (see sec. 2.3.2), while in the right panels we show the best fitting functions in the inner and outer regions for the radial trend of the scale heights. The results are very similar, independently of the DM halo used. At first glance, it is evident that the flaring curves can be parted in two regions: at small radii, up to $R \approx 4 - 6R_{ds}$, the scale height follows an exponential law, while in the outer part the disk thickness increases as a power law ($H(R) \propto R^{\alpha}$). The scale length of the exponential best-fit function is approximately 4 kpc, that is the value expected for a stellar disk in the one-component model (eq. 3.9). The parameter $\alpha$ that give the best-fit function for the outer radii ranges between 0.8 and 0.9 depending on the radii used in the fit. These values are slightly

lower than what expected for the halo in the one-component model (sec. 3.1.5 ). These results confirm that the HI scale height, at certain radius, depends on the locally dominant matter component: the stellar disk at small radii and the DM halo in the outermost disk. The gaseous disk seems to have a very low influence on its scale height, indeed as we can see in the left panels of fig. 3.18, the numerical flaring curves are nearly coincident with its lower limit, that is the flaring expected when all the gas lies in a razor-thin disk ($H = 0$).

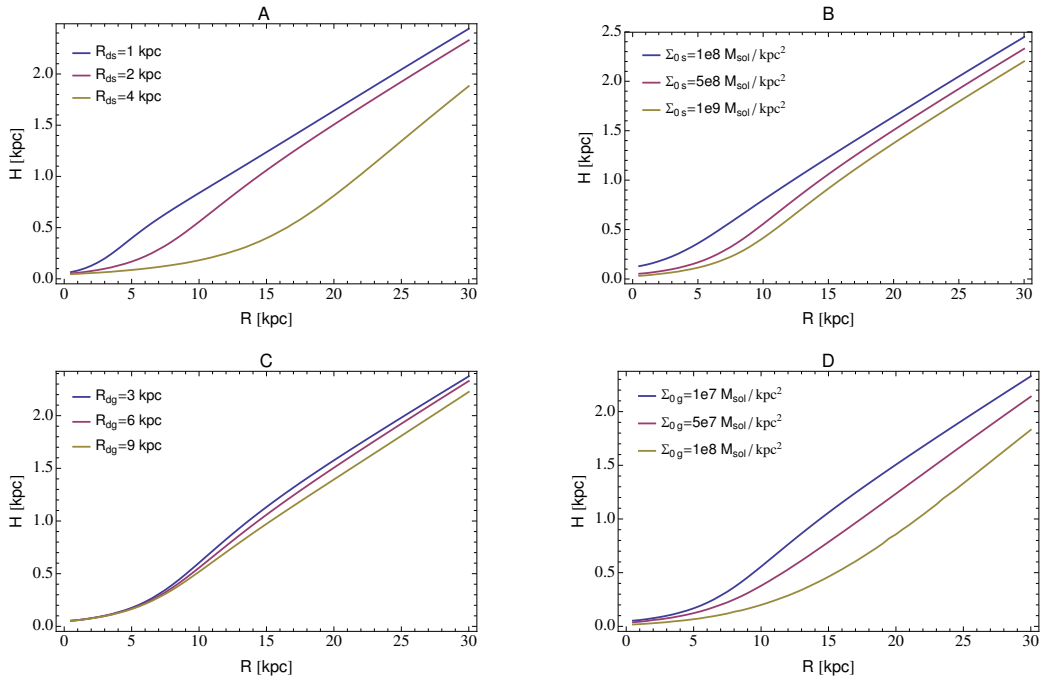


Figura 3.19: Influences of parameters of the stellar disk (A-B) and of gaseous disk (C-D) on the flaring curves. The mass components have been set as in fig. 3.18a except for the parameters showed in the panels. Note that these mass models do not produce the same rotation curve.

In figures 3.19 and 3.20 we investigate the effect of the parameters of the matter compontents on the HI scale height. Since the models with isothermal or NFW DM halos produce nearly the same flaring, in this analysis we use only the isothermal halo. Panel A shows that the disk scale length heavily influences the flaring. Indeed, as previous seen in fig. 3.18, the stellar disk dominates up to $R \approx 5\mathrm{R_d}$ where the transitions between the "exponential and the "linear flaring takes place. An increase in the central density of the stellar disk influences mostly the central radii (panel B). In panels C and D we show the flaring curves obtained varying the parameters of the gaseous disks: the increase of the scale length or of the central density causes a decrease of the gaseous scale height. Moreover, when the central density of the gaseous disk becomes comparable with the one of the stellar disk, the scale length of the "exponential flaring becomes larger assuming an intermediate value between $2R_{ds}$ and $2R_{dg}$ (panel D). Observations of HI emission in spiral galaxies have shown that the surface density exhibits a depression in the inner disk (out to a few kpc varying from galaxy to galaxy), but in our analysis we assumed that the

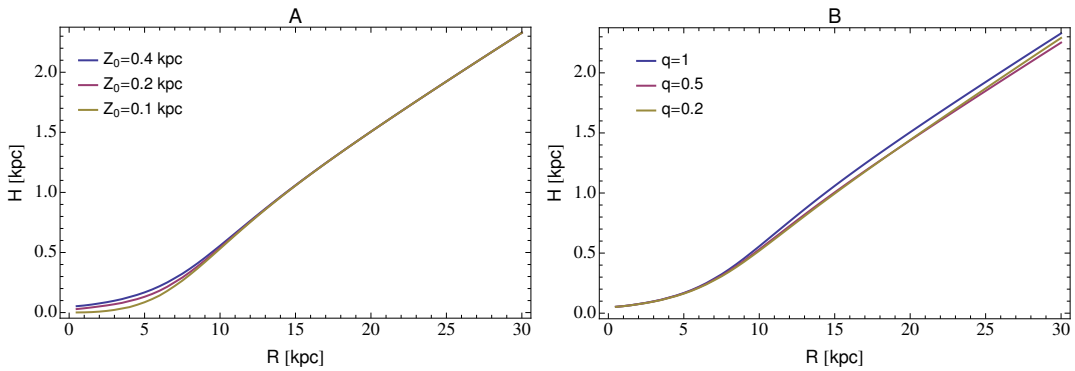


Figura 3.20: Influences of stellar scale height (A) and of halo flattening (B) on the flaring curves. The mass components have been set as in fig. 3.18a excepts for two parameters mentioned before.

surface density follows an exponential law at every radius. The results showed in fig. 3.19C and 3.19D prove that it is a reasonable approximation, indeed, the scale height at inner radii is completely defined by the stellar disk, unless the gaseous disk has a dynamical relevance similar to the stellar disk, but this is not the case in the type of galaxies studied in this thesis.

Figure 3.20 shows that neither the scale height of the stellar disk nor the halo flattening can significantly modify the flaring curve. In the first case (panel A) we can see only small variation for very inner radii, while in the outer disk the three curves are indistinguishable. The change in the halo flattening (panel B) causes a very small variation of the HI scale height at large radius. The analytic flaring (eq. 3.25) depends only on the central density and on the core radius, hence once they are kept fixed, we would expect to obtain the same flaring curve for every halo flattening. The small differences seen in figure 3.20B can be due both to differences in the contribution of the rotational density (fig. 3.6) and to the fact that for a very flatten component of matter ($q \leq 0.2$) the choice of a gaussian vertical profile (sec. 2.3.1) could underestimate the HI scale height. What just said could seem in contradiction with the results of sec. 3.1.3 and 3.1.4, where we stated that DM halos with different flattenings produce substantially different HI scale heights. However, in those cases the parameters of the halo have been tuned to produce the same rotation curve, while the scale heights shown in fig. 3.20B are referred to halo models with same $R_c$ and $\rho_0$ and hence different rotation curves.

Note that, regardless of the values of the parameters of the stellar and gaseous disks, the scale height curves are parallel from middle to large radii (fig. 3.19 and 3.20). This is a further evidence that, for most radii, the flaring is dominated by the DM halo that determines its linear trend while, the other mass components act only to globally increase or decrease the scale height. Hence, all the features highlighted for the halo one-component model (sec. 3.1.4 and 3.1.3) are

still fulfilled in the outer regions of the gaseous disk of spiral galaxies.

## 3.3 The role of the gas velocity dispersion

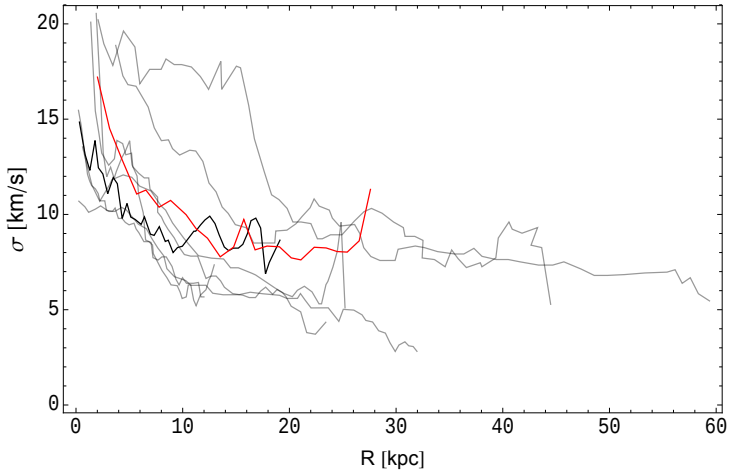


Figura 3.21: Velocity dispersion profile of the gas for a sample of spiral galaxies. The grey curves show the velocity dispersion of the galaxies in the sample of Tamburro et al. (2009); the red and black curves are for NGC 3198 (Sicking, 1997) and NGC 2403 (Fraternali et al., 2002).

The velocity dispersion of the gas ($\sigma$) plays a fundamental role in the determination of the scale height of the gaseous disk in spiral galaxies (eq. 2.3). It is possible to evaluate the velocity dispersion of the gas from the width of HI line profile. The dispersion, is both due to the thermal broadening (Field et al., 1969; Wolfire et al., 1995) and to the turbulence driven by stellar feedback (e.g. Joung & Mac Low 2006; Tamburro et al. 2009) or hydrodinamical instabilities (e.g. Piontek & Ostriker 2005; Sellwood & Balbus 1999). The typical HI line widths observed in spiral galaxies range between 5 to 20 km/s, with a typical valued of about 10 km/s across the disk. In some galaxies, as one can see in fig. 3.21, the velocity dispersion shows an outward decrease down to $\sigma \approx$ 6-8 km/s (Boulanger & Viallefond, 1992; Petric & Rupen, 2007; Sicking, 1997; Tamburro et al., 2009). The radial trend of the velocity dispersion is a crucial issue for the study of the HI flaring as we see below.

Figure 3.21 reports the velocity dispersion profiles for a sample of galaxies showing a coherent decrease of $\sigma$ as a function of the galactic radius. The overall trend of $\sigma$ exhibits a cusp at small radii and a smooth decrease at large radii, nearly as an hyperbole ($\sigma \approx \frac{A}{B+R}$). Alotugh, the central cusp observed in the some galaxies could be partially due to beam smearing. There is no doubt that $\sigma$ tends to be higher in the inner part of the disks. Furthermore the layer thickness can increase the observed velocity dispersion due to projection effects (Sicking, 1997). Accordingly, the values of $\sigma$ at intermediate radii should suffer the lowest bias, both because the rotation curve is in general already flat, lowering the effect of the beam smearing, and because

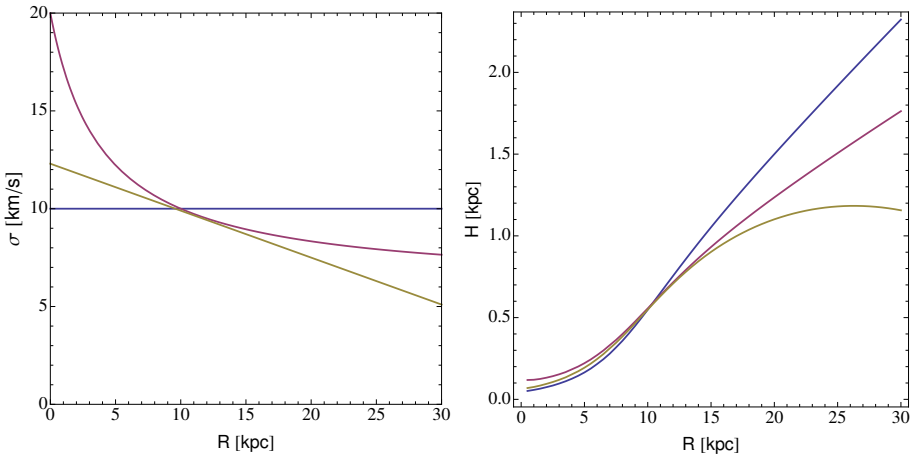


Figura 3.22: flaring curves obtained for three different velocity dispersion profiles (left panel). The parameters of the galaxy model are the same of fig. 3.18a.

the scale height of the gas could be small enough. Generally, the velocity dispersion at these radii is well fitted by a linear function ranging from $\sigma \approx 15-11$ km/s in the centre to $\sigma \approx 7-5$ km/s at the edge of the HI disk.

Figure 3.22 shows the theoretical flaring produced by three galaxy models with different velocity dispersion. As showed in the left panel, one of the models has $\sigma$ fixed to 10 km/s, in the other two the velocity dispersion decreases either linearly with $R$ or as $R^{-1}$. The mass components parameters have been set as in sec. 3.2. The radial decrease of the velocity dispersions significantly influences the HI scale height, especially at large radii, where the matter density is low. Indeed, in the most extreme case, the decrease of $\sigma$(R) can keep nearly constant the vertical scale height of the gas preventing the layer to flare.

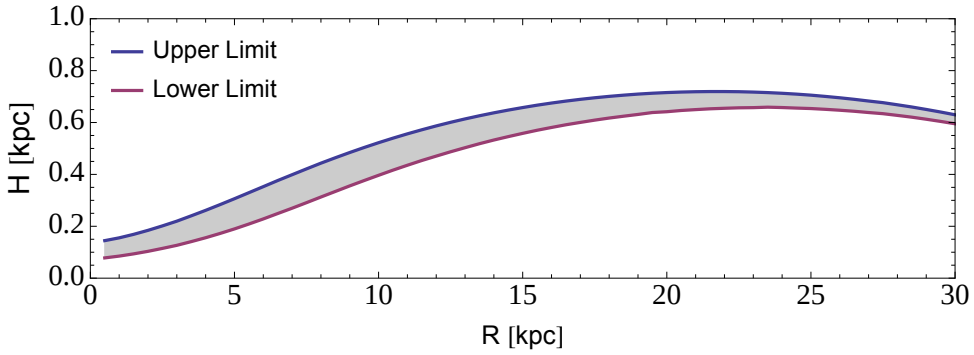


Figura 3.23: HI scale height as function of radius R, for a galaxy with an highly flatten isothermal halo (q=0.2) and a velocity dispersion of the gas that linear decreases linearly from 15 km/s at R=0 kpc to 5 km/s at R=30 kpc. The other parameters of the galaxy model are the same of fig. 3.18a.

We have seen in sections 3.1.3 and 3.1.4 that a flatten DM halo can dramatically decrease the HI scale height, hence the combination of a steep decreasing of the velocity dispersion and

an heavy flatten DM halo can produce a relatively thin gaseous layer ($H(R) < 1$ kpc) with an almost constant scale height as showed in fig. 3.23.

Observation of edge-on galaxies have shown that the HI scale heigth always increases at large radii (Kalberla et al., 2007; Merrifield, 1992; O'Brian et al., 2010a; Olling, 1996). This would imply that in the outer disk, either the velocity dispersion decreases with a very low gradient, or it flattens to the typical value of the WNM (Wolfire et al., 1995). Unfortunately in edge-on galaxies is is very difficult to derive $\sigma$ as function of the radius. The problem can be overcome by studying galaxies see at intermediate inclinations wehere one ca in principle derive both the flaring and the dispersion profile simultaneously. The following chapters describe this approach and the possibility of this application to real galaxies.

## 3.4 Functional form for the HI flaring

In order to estimate the flaring in real galaxies, it would be useful to have an a-priori convenient functional that describes the theoretically expected HI scale height as a function of radius. For simplicity we require this function to be continuos and the simplest possible (small number of free parameters). This is not a trivial task, indeed, the theoretical flaring is a combination of several functional forms depending on several parameters. Examples of the radial trend of the HI scale heights are shown in fig. 3.18 and 3.19. The scale height shows one or more points of inflection, moreover the decrease of the velocity dispersion of gas can produce an asymptote of the flaring at large radii, as shown in fig. 3.21. Trigonometric functions as the hyperbolic tangent, are able to fit both a nearly linear rising curve and an outer asymptote. To follow the change of slope we use a radial power law as the argument of the trigonometric functions. The most versatile and convenient functions turned out to be:

- **Hyperbolic Tangent:**

$$H_t(R) = \mathbf{H_0} + \mathbf{C} \cdot \tanh\left(\frac{R^2}{\mathbf{R_f^2}}\right) \tag{3.40}$$

- **Hyperbolic Arcsine:**

$$H_s(R) = \mathbf{H_0} + \mathbf{C} \cdot \operatorname{arcsinh}\left(\left(\frac{R^2}{\mathbf{R_f^2}}\right)\right) \tag{3.41}$$

Where $H_0$, C and $R_f$ are the free parameters of the functional forms. In principle the exponent outside the round bracket (now set to 2) could also be a free parameter, but the improvement in the fit does not justify the introduction of a fourth parameter. In the next pages we will test this two functional forms for various theoretical flarings produced by realistic galaxy models. The galaxies we used are: NGC 2403 (Fraternali et al., 2002), NGC 3198

(Sicking, 1997) and the Milky Way (Marasco & Fraternali, 2011). The theoretical flaring for each mass model is computed using the software *galforces* (Fraternali & Binney, 2006), as we explained in sec. 2.3. In order to take into account the self-gravity of the disk we used the approach described in sec. 2.3.2.

### Milky Way

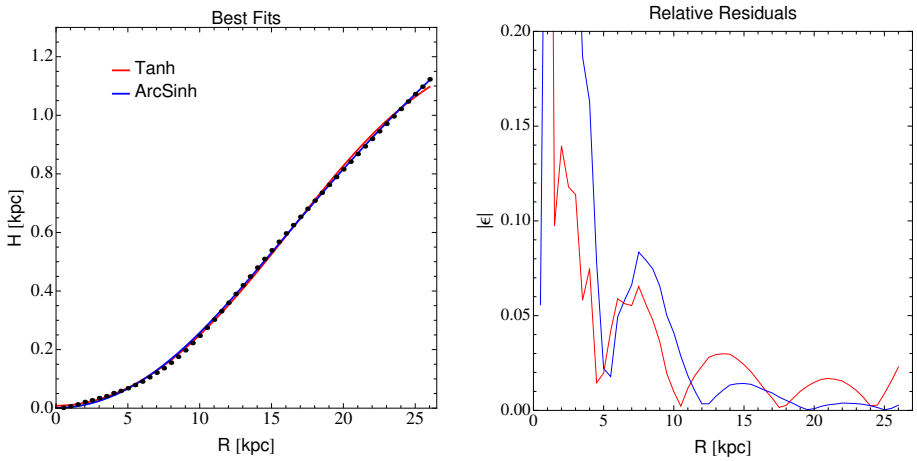


Figura 3.24: Comparison between the theoretical flaring of the MW disk (points) and the best fits with the functions in eq. 3.40 and 3.41. The right plot shows represents the relative residuals of the fits.

The dynamical model of our Galaxy has been taken from Marasco & Fraternali (2011). The velocity dispersion of the gas has been fixed to 10 km/s constant with radius, as suggested by Malhotra (1995).

The figure 3.24 shows the comparison between the theoretical flaring (black dot) and the best fit functional forms found for the equations 3.40 and 3.41. They matches clearly the data, especially at larger radii where the relative errors are of the order of one-five percent. At the edge of the galaxy the Hyperbolic Tangent tends to underestimate the scale height, but this afflicts only few data points.

### NGC 2403

The disk galaxy NGC 2403 is a well-studied late type spiral (Scd) located at about 3 Mpc from us (de Blok et al., 2008b; Fraternali et al., 2002; Sicking, 1997). The kinematic and dynamical parameters that we used here come from Fraternali et al. (2002). The observational velocity dispersion of the gas is shown in figure 3.25. We use two functional forms to describe the radial trend of $\sigma$: an hyperbolic (Model A) and a linear (Model B) function. Model A has been fitted over the whole radial dominion, while model B only in the range between 5 and 10 kpc, where the observational data are likely less influenced by spurious effects, as explained in sec. 3.3. For

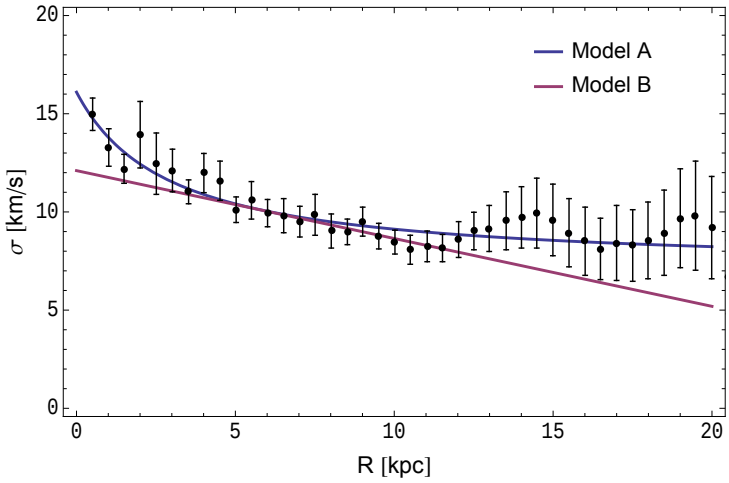


Figura 3.25: Velocity dispersion of the gas for the galaxy NGC 2403. The data (black dot) are from Fraternali et al. (2002). The two curves represent two functional fits to the data.

the distribution of matter we used two sets of mass components: one with a maximum disk and a spherical isothermal halo, the other with a minimum disk and a spherical NFW halo. Hence, combining the two functional forms for $\sigma$ and the two sets of mass components we end up with four different galaxy models:

- **M1**: hyperbolic velocity dispersion, maxim disk and isothermal halo.
- **M2**: hyperbolic velocity dispersion, minim disk and NFW halo.
- **M3**: linear velocity dispersion, maxim disk and isothermal halo.
- **M4**: linear velocity dispersion, minim disk and NFW halo.

The comparison between the flaring curve and the best-fit functions of eq. 3.40 and 3.41 are shown in figure 3.26. The differences between the maximal (M1-M3) and the minimal (M2-M4) disk models are very modest, especially at large radii. Instead, the models with different velocity dispersions produce distinct flaring curves: in the first case (model A) the HI scale height increase as a linear function of radius and both the functional forms are able to give a good fit of the flaring (M1-M2); while, the model B of the velocity dispersion flattens the HI scale height in the outermost disk. For this flattened thickeness the hyperbolic tangent give a significative better fit with respect to the hyperbolic arcsin (panels M3 and M4).

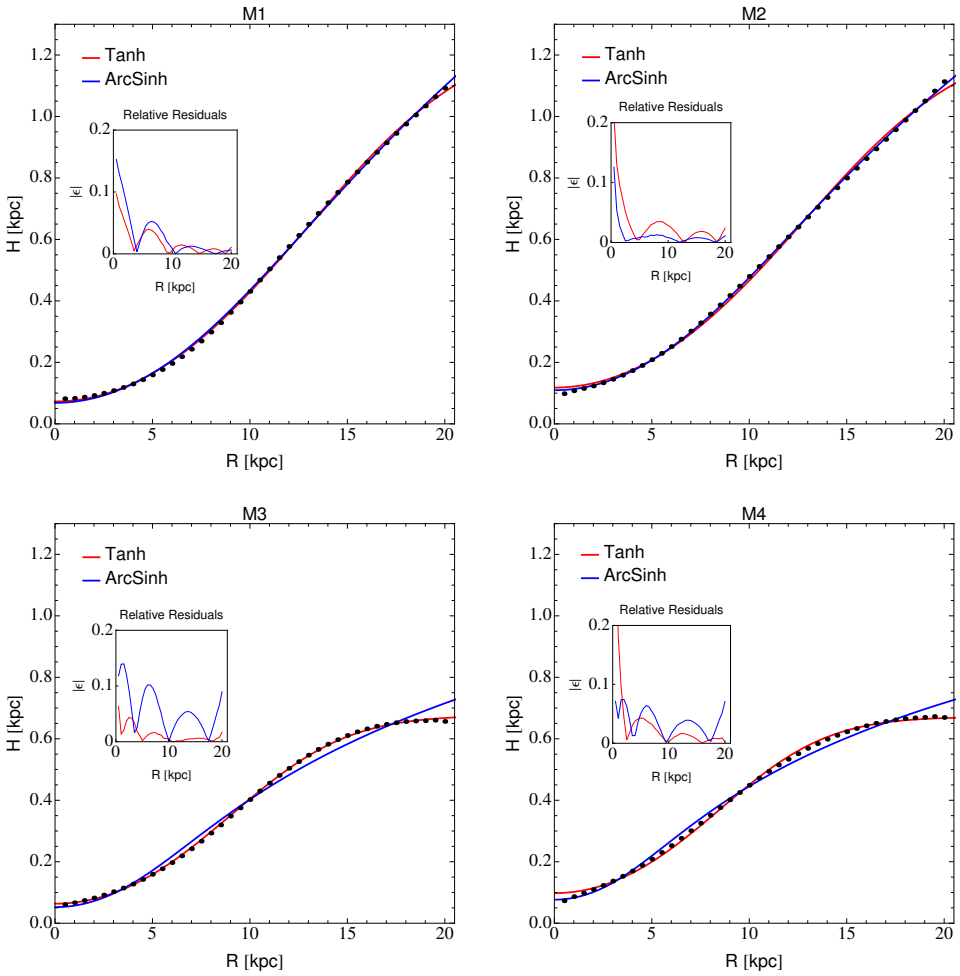


Figura 3.26: Comparison between the theoretical flaring and the best fits with the functional forms in eq. 3.40 and 3.41 for the galactic models of NGC 2403 described in the text. The small plots show the relative residuals of the fits.

### NGC 3198

NGC 3198 is a nearby Sc galaxy and the prototype of galaxies with a flat rotation curve (Begeman, 1987). Both the dynamical and the kinematic parameters are taken from Sicking (1997). The velocity dispersion of the gas is plotted in fig. 3.27 as function of radius. As for NGC 2403 we have fitted $\sigma$(R) with two functional forms: hyperbolic (model A) and linear (model B). Model A has been fitted over the whole radial dominion, while model B only in the range between 6 and 20 kpc.

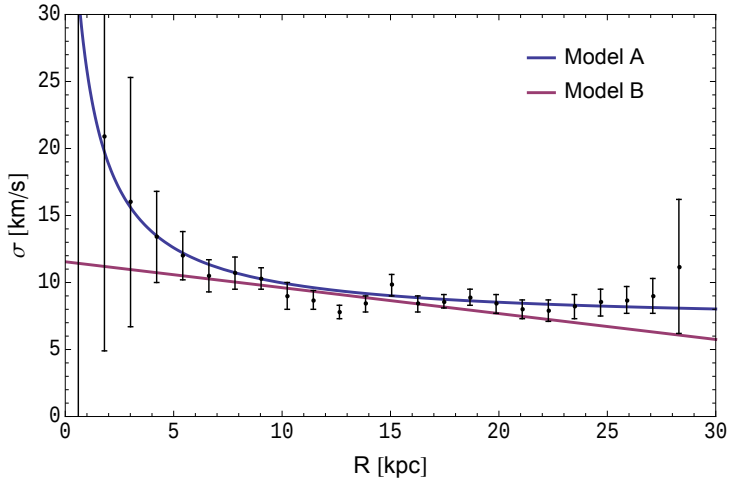


Figura 3.27: Velocity dispersion of the gas for the galaxy NGC 3198. The data (black dot) are from Sicking (1997). The two curves represent two functional fit to the data.

We use the mass components of the maxim and minim disk models reported in Sicking (1997), both models include an isothermal spherical halo. Combining the two mass settings with the two velocity dispersion forms, we defined four galaxy models, as follow:

- **N1**: hyperbolic velocity dispersion, maxim disk mass components.
- **N2**: hyperbolic velocity dispersion, minim disk mass components.
- **N3**: linear velocity dispersion, maxim disk mass components.
- **N4**: linear velocity dispersion, minim disk mass components.

The flaring curves and the best fit functions found for models N1, N2, N3 and N4 are shown in figure 3.28. The general results are similar to what already seen for the galaxy NGC 2403: when we used the velocity dispersion as in model A the flaring exhibit a nearly linear increase as a function of radius (N1 and N2), while using model B the HI scale height flattens at large radii (N3 and N4), though the flattening is less evident with respect to NGC 2403 (panels M3 and M4 in fig. 3.26). We note that the large velocity dispersion at small radii of model A

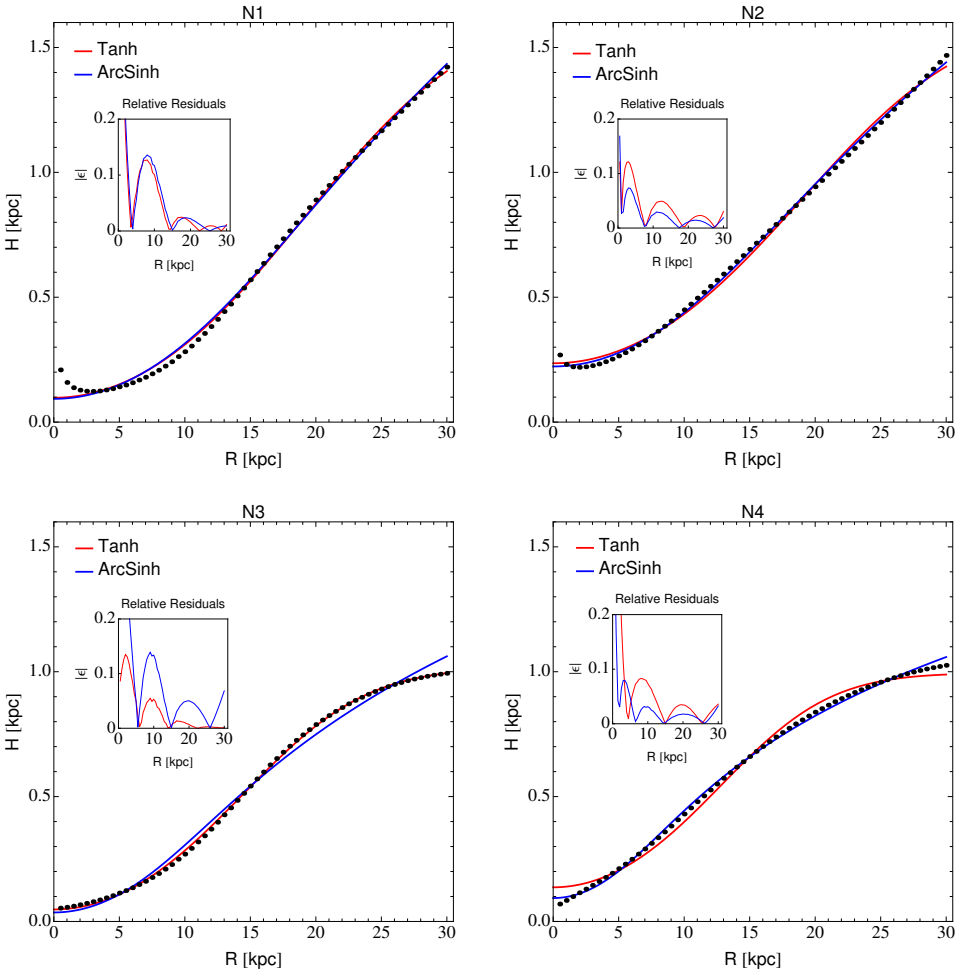


Figura 3.28: As figure 3.26 but for the galaxy models of NGC 3198.

(fig. 3.27) produces an inner cusp in the flaring curve (panels N1 and N2). However, this high central velocity dispersion, is probably only a spurious effect introduced by the instrumental beam (see sec. 3.3 for further details). If we exclude the most inner points the functional fits are in better agreement with the theoretical curves. In general, the two functions seem be both a good approximation for the flaring in models N1 and N2. If we consider model B for the velocity dispersion, the two functional forms seem to give different results. Using the maximal disk (N3), eq. 3.40 follows perfectly the radial trend of the scale height, especially at larger radii where the relative errors drop below one percent. Instead, the hyperbolic arcsin is not able to follow the rapid change of slope exhibited by the theoretical flaring, though its relative differences are below ten per cent for the most radii. In the case of a minimal disk (N4) the situation is reversed: the functional form in eq. 3.41 follows very well the gently increase of the scale height, while the best fit hyperbolic tangent exhibits an excessive flattening. The discrepancy between the maximal and the minimal disk models are more relevant than for NGC2403 (fig. 3.26), this is easily explained by the fact that while the differences between the mass of the maximum an the

minimum stellar disk of NGC 2403 is of a factor of 2, it rises up to 5-6 for NGC3198.

Fro completeness we used also the mass models containing an high flatten halo (q=0.2), as reported in Sicking (1997). We defined four more galaxy models (N1b, N2b, N3b, N4b) with the same procedure previously described. The results are shown in figure 3.29: we note a general decrease of the scale height with respect to the spherical halo (fig. 3.28) with a difference that increases up to 40-60 % at larger radii, as expected from the analysis in the section 3.1.3 (fig. 3.10). Despite this difference, the flaring trends are very similar, indeed the comparison between the best fit functional forms and the theoretical flarings gives the same results as described for the models with spherical halos.

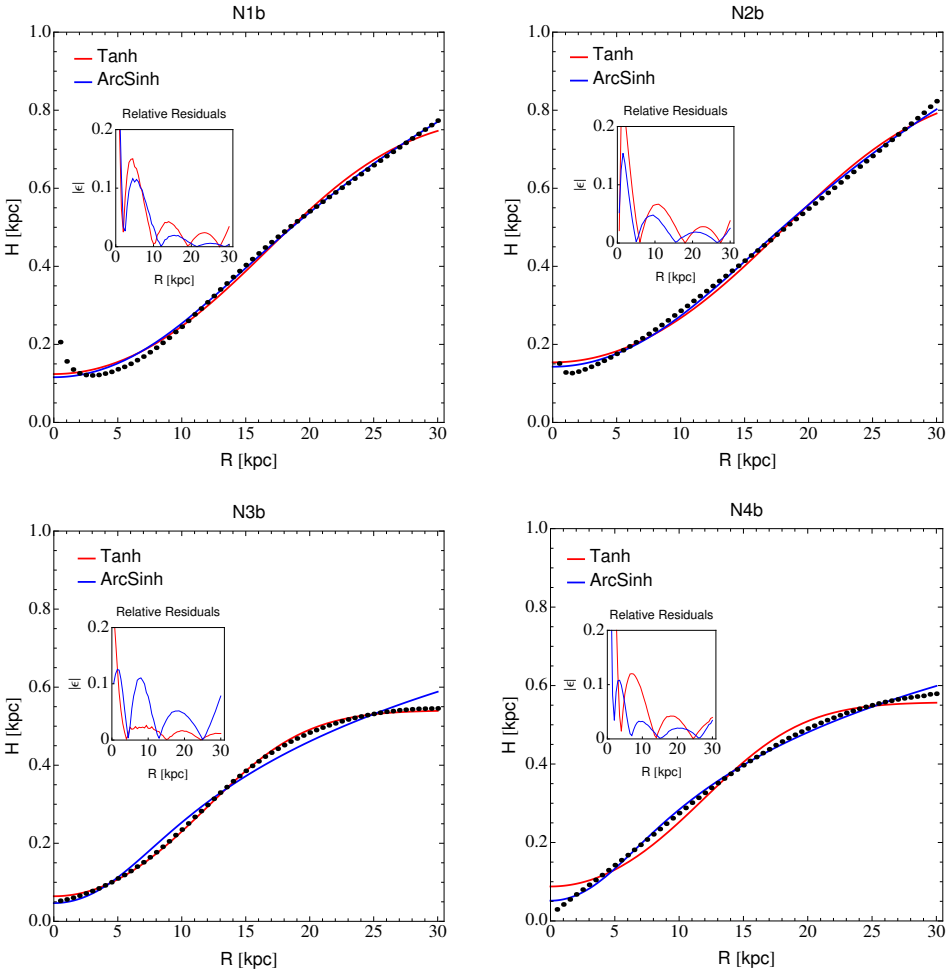


Figura 3.29: As figure 3.28, but with an highly flattened isothermal halo (q=0.2).

We note that at small radii, approximately out to a quarter of the extension of the gaseous disk, the differences between the best fit functions and the theoretical thickeness are relatively high; however, in these regions the evaluation of the HI scale height is afflicted both by uncertains on velocity dispersion (modified by the instrumental beam) and by the uncertain in the mass to

light ratio of the stellar disk. Moreover, our study is focused on the outermost disk, hence the increase of the fit-errors toward small radii is not a real issue.

In conclusion the two functional forms of eq. 3.40 and 3.41 are a good approximation for the theoretical flaring expected in spiral galaxies. These results can be considered quite robust since we tested the two functions on three galaxies with different dynamics and kinematics, and for two of them we considered various mass and velocity dispersion models. Since the goodness of the fit is similar for both the functional forms analyzed, in the following we will use hyperbolic arcsin as the general functional form for the HI flaring.

As previously mentiones, at large radii, the relative fit errors are lower than ten percent. Hence, when we estimate the flaring of the gaseous disk using the functional form of eq. 3.40, we showed always consider a conservative relative error of ten per cent the HI scale eight. This kind of error, however, easily allows us to disentangle between flarings produced by spherical or a flat halo, since they produce differences significantly greater than 10 % (3.1.3 and 3.1.4).

### 3.4.1 Comparison with other works

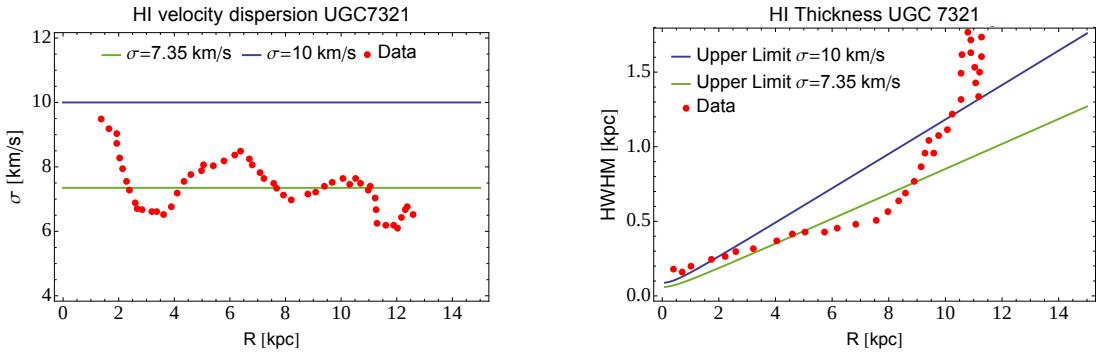


Figura 3.30: Velocity dispersion (left panel) and scale height (right panel) of the gas as function of radius for the galaxy UGC 7321. The data (red points) are from O'Brian et al. (2010b). The green line on the left shows the average value of the data, while the blue line is an upper limit. In the right panel we overplotted to the data two theoretical upper limits for the HI scale heights. They are numerically calculated (sec. 2.3) using an isothermal halo and a $\sigma$ of 10 and 7.5 km/s respectively for the blue and green curve. The parameters of the halo come from the analysis of the rotation curve of the galaxy (O'Brian et al., 2010b).

The theoretical HI flaring profiles found in this chapter are very similar to the results of Olling (1995), Sicking (1997) and Jog & Banerjee (2008). These works start from assumptions similar to the ones made in this thesis, but each of them uses different methods to evaluate the galactic potential and the self-gravity of the HI disk. Despite these differences, the final results are largely compatible. The comparison with the observational data are more complex. The observations of the edge-on galaxy NGC 4244 (Olling, 1996) shows that the vertical scale height

of the gas increases nearly linearly as expected from the theoretical prevision. Also our Galaxy (Olling & Merrifield 2000, Kalberla et al. 2007) shows similar proprieties. However, there are also observational data that are incompatible with our theoretical results. The most emblematic is in O'Brian et al. (2010a). The authors found that the HI flaring profiles of seven edge-on galaxies increase linearly where stellar disks dominate, while in the outer disks where the DM halos dominate they growth as an exponential. This kind of radial trend is clearly opposite and incompatible with our theoretical predictions. In particular, the outer exponential rising is hardly compatible with our model. It could imply a very steep rising of the gas velocity dispersion in the outer disk, but this is unlikely and incompatible with the evaluation of $\sigma$ in this same work and in many others (e.g. Tamburro et al. 2009). In the outer regions are strongly dominated by the self-graviting HI disk, we should observe a nearly keplerian decrease of the rotation curve and, the influence of the rotational density on the vertical scale height should produce again a linearly increase flaring profile (eq. 3.12). Moreover, the galaxies in this sample are all dynamically dominated by the DM halo at all radii. We used the dynamical and kinematical informations of the deeper analysis of the galaxy UGC 7321 (O'Brian et al., 2010b) to perform a simple test. The rotation curve of the galaxy is best fitted by a spheroidal isothermal halo with $\rho_0 = 0.73 \pm 0.05 \mathrm{M}_\odot/\mathrm{pc}^3$ and $R_c = 0.52 \pm 0.02$, while the measured velocity dispersion is shown in the left panel of fig. 3.30. We used these data to build a theoretical upper limit of the vertical scale height using *Galforces* with only the DM halo as mass component. We used two values for the gas velocity dispersion, one fixed at the mean value obtained from the data ($\sigma = 7.35$ km/s) and the other at a maximum realistic value of 10 km/s. In the second case we obtain a firm upper limit for the HI thickness. The comparison between these two limits and the observational evaluation are shown in the right panel of fig. 3.30. The observed exponential rise is too large with respect to the upper limit calculated using the mean velocity dispersions (green curve) but it is unlikely also for our firm upper limit (blue curve). The source of this large inconsistency is unclear, but it seems likely that the method used to extract the data has biases at large radii. For instance, Matthews & Wood (2003) found for the same galaxy that the best fit of the total map is done with a thick HI (lagging) halo of a constant thickness of 3.3 kpc and a HI disk that flare nearly linearly $H(R) \propto R^{\frac{5}{4}}$ from 130 pc at the center to 821 pc at 11.8 kpc (very similar to the trend of the green curve in fig. 3.30). While, Kamphuis (2007) found, directly fitting the data cube of UGC7321, that the best model has a constant scale height. Incidentally we note that in measuring the flare of an HI disk one should eliminate the emission from the lagging halo because this is a component produced by the stellar feedback and not in hydrostatic equilibrium in the potential (e.g. Marinacci et al. 2010).

## 3.5 Results and discussions

We have used the theoretical results of Chapter 2 to calculate the HI flaring profiles produced by typical mass models of spiral galaxies. We decomposed the galaxy into three mass components: an exponential stellar disk, a DM halo (isothermal or NFW density law) and a HI self-gravitating disk. We neglected the bulge both because it has an influence only on the very inner disk and because or study is focused on the late-type spirals where the bulge has a negligible dynamical importance. Firstly, we calculated the radial trend of the HI vertical scale height ($H(R)$) for the singular components:

- Exponential stellar disk. From eq. 2.11, neglecting the rotational density ($\rho_{\rm rot}$), we obtained:

$$H_{\rm disk}(R) = 0.122 \left(\frac{\sigma(R)}{10\ {\rm km/s}}\right) \sqrt{\frac{\left(\frac{Z_0}{0.4\ {\rm kpc}}\right)}{\left(\frac{\Sigma_0}{10^8 M_\odot/{\rm kpc}^2}\right)}}\ {\rm Exp}\left(\frac{R}{2Rd}\right) \quad {\rm kpc}$$

  where $R_d$ and $Z_0$ are respectively the radial and the vertical scale length of the disk, and $\Sigma_0$ is its central surface density. Thus, in the presence of an exponential disk the gas layer flares exponentially. However, the comparison with the numerical calculation shows that beyond $R \approx 4R_d$ the nearly keplerian fall of the rotation curve makes $\rho_{\rm rot}$ the dominant component, as shown from the radial trend of $\eta_{\rm disk}$ (fig. 3.6). At this radius we showed a transition from an exponential to a nearly linear "flare (fig. 3.2).

- Isothermal DM halo. As above we obtained the analytical trend of $H_{\rm iso}$:

$$H_{\rm iso}(R,q) = 0.1 \frac{\left(\frac{\sigma(R)}{10\ {\rm km/s}}\right)}{\left(\frac{V_\infty}{100\ {\rm km/s}}\right)} \sqrt{f(q)} \sqrt{{R_c}^2 + R^2}\ \ {\rm kpc}$$

  where the DM halo has the core radius $R_c$ and produces a rotation curve with the asymptotic value $V_\infty$. The function $f(q)$ (eq. 3.18) contains the dependence of $H_{\rm iso}$ on the halo flattening $q$ (halo axes ratio) and it is equal to 1 for round halos. The flaring of the gas is nearly linear for most of the disk. $\eta_{\rm iso}$ is always positive and lower than 0.7, thus the rotational density is always subdominant with respect of the matter density. The numerically calculated $H_{\rm iso}$ confirms that the effect of the rotational density is only ti shift the gas flaring toward larger scale heights.

- NFW DM halo:

$$H_{\rm NFW}(R) = 0.430 \left(\frac{\sigma(R)}{10\ {\rm km/s}}\right) \left(\frac{\rho_0}{10^7 {\rm M}_\odot/{\rm kpc}^3}\right)^{-\frac{1}{2}} \sqrt{\left(\frac{R}{R_s}\right)\left(1+\frac{R}{R_s}\right)^2}\ [{\rm kpc}]$$

  where $\rho_0$ and $R_s$ are respectively the central density and the scale length of a spherical NFW halo. In this case there are no analytical ways to obtain the $\eta_{\rm NFW}$ for flattened

halo. However the comparison between the above $H_{\rm NFW}$ and the numerical calculations (fig. 3.13) shows very small differences.

The main conclusion of this analysis is that the differences between the analytically and numerically calculated HI thickness are mainly due the contribution of the rotational density. Therefore, the Taylor series expansion made in eq. 2.5 is a good approximation of the halo galaxy potential. Subsequently, we built realistic mass models (stellar disk + DM halo + self-gravitating gaseous disk), and we found that the final $H_{\rm tot}$ strongly depends on the dominant mass component. Indeed, it rises exponentially at small radii where the stellar disk dominates, while the gas flaring becomes nearly linear at large radii, where the dynamics is dominated by the DM. The transition between the two regions depends mainly on the scale length of the disk, indeed it is located at about $R \approx 5R_d$. However, if the mass of the halo is much larger that the mass of the stellar disk the flaring of the gas will be linear at almost all radii. The gaseous disk has a small relevance on the shape of the flaring, it mainly acts to slightly lower the value of the vertical scale height at large radii. We note that the outer regions of spiral galaxies are totally dominated by the DM, hence these are the best regions to study the DM proprieties. In particular, we found in App. C that the same rotation curve can be explained with a family of DM halos with different flattening. We found that this degeneracy can be broken by studying the HI thickness. Indeed, halos with the same rotation curve, but different q, should produce very different flaring profiles in the outer disk. The relative differences can be larger than 40%, hence also with a rough estimate of the disk thickness it is possible to rule out a significant range of halo flattenings. We analyzed also the possibility to use the vertical scale height to break the degeneracy between the choice of the isothermal or NFW density profile. We found that in these two cases the resultant thickness will be essentially the same over a wide range of radii.

The first analysis made in this chapter used a constant value for the gas velocity dispersion, but there is are evidence that some galaxies show an outer decrease of $\sigma$ (e.g. Tamburro et al. 2009). We found that in this case the vertical scale hight of the gas can be substantially lowered at large radii.

To conclude the chapter we used all the previous results to find a functional form than can fit the expected radial trends of the vertical scale height. We required this function to be the simplest possible and to take into account also the variation of the velocity dispersion of the gas. We found that both $H_t(R) = H_0 + C \cdot \tanh\left(\frac{R^2}{R_f^2}\right)$ and $H_s(R) = H_0 + C \cdot \mathrm{arcsinh}\left(\frac{R^2}{R_f^2}\right)$ fulfill these requirements. We tested these functions on a set of realistic galactic models extrapolated by real observations (Sicking 1997; Fraternali et al. 2002; Marasco & Fraternali 2011). Both the functions work very well for all the analyzed cases and they can be used to describe the flaring of the gas layer using a conservative error of 10 %. We stress that these functions have no physical basis: they represent only a local approximation of the HI scale height. Therefore, they can not be used to extend the behavior of the flaring beyond the analyzed radii.

# Capitolo 4

# Measuring the HI thickness: The model

In this chapter we build a method to model the effect of a thick HI layer on the observed emission of a gaseous disk. In sec. 4.1 we set the frame of references and the basic assumptions needed to model the galaxies and their emission. In sec. 4.2 we find the fundamental relations between the galactic coordinates to link the observed emission to the 3D density distribution of the gas. We take into account also the possibility of a cut-off of the signal at the edge of the galaxies. Finally, in sec. 4.3 we used the previous results to analyze the expected emission from various density distributions of the gas. In particular, we study the separate influence of the surface density, of the gas flaring and of the galactic inclination angle.

## 4.1 Frame of reference and assumptions

To derive the dependence of the HI emission as a function of the sky coordinates, we set two frames of reference:

- **The "observational frame of reference on the sky plane ($x$,$y$,$s$):**

  We fix the $x$-$y$ plane on the plane of the sky, with the $s$ axis perpendicular to this plane, representing the line of sight. The $x$ axis lies on the line of nodes which is the intersection between the plane of the sky and the plane of the galaxy. In practice, it is the apparent major axis. With this construction the apparent minor axis lies on $y$. The direction of s is fixed, thus according to the "right-hand rule the $x$ and $y$ can have two different directions. To fix them in a objective way we use the kinematic information: we select as positive $x$-direction the one that points toward the receding-half of the galaxy, hence the $y$ direction is determined by the right-handed convention for a orthonormal frame of reference.

- **The "natural frame of reference ($X$,$Y$,$Z$):**

We set the $X$-$Y$ plane on the equatorial plane of gas layer, the $X$ axis lies on the line of nodes, as the $x$ axis, therefore it is fully determined by kinematics and projection geometry (see above). The $Z$ axis is perpendicular to the galaxy plane, we set its positive direction as the one that forms an angle $i$ ranging from 0 to $\frac{\pi}{2}$ with the positive s axis. We call **i the inclination angle**. As for the $y$ axis the $Y$ direction is fixed by the assumptions on the other two axes. We define the **position angle PA** as the angle taken anti-clockwise between the positive major axis and the north direction onto sky-plane.

Moreover, in order to develop our model we made the following assumptions:

- **No Warp**: we model our galaxy as a disks made of a series of rings with fixed position and inclination angles.
- **Axisymmetry**: we suppose that the disk distribution is axisymmetric, thus every physical variable depends only on the radius ($R$) and the height ($Z$). For the rest of this thesis we will use a cylindrical coordinate system.
- **Symmetry with respect to the galaxy plane**: At a fixed radius the physical variables depend only on the module of the height $|Z|$.

  The last two conditions are generally fulfilled in galaxies, while the first assumption is more uncertain (e.g. Garcia-Ruiz et al. 2002). We caution the reader that the methods and results of this thesis may not be valid in presence of strong warping of the outer disk.

### 4.1.1 Geometrical Analysis

A galaxy disk is supposed to be intrinsically circular, thus we can think of it as a series of rings (Begeman, 1987) described by the equation:

$$X^2 + Y^2 = R^2; \quad Z = Z \tag{4.1}$$

We define a cylindrical frame or reference $(\mathbf{R}, \boldsymbol{\phi}, \mathbf{Z})$ to parameterize each ring as:

$$\begin{cases} X = R\cos(\phi) \\ Y = R\sin(\phi) \\ Z = Z \end{cases} \tag{4.2}$$

where the **azimuthal angle $\boldsymbol{\phi}$** is defined as the angle between the radius of the ring and the relative positive X axis. We can obtain the observational frame of reference rotating the natural one of an angle i and vice versa. In a more rigorous form we can use a rotation matrix:

$$\mathbf{x} = R_X \mathbf{X}$$

where **X** and **x** represent vectors respectively in the original and in rotated frame of reference. $R_X$ is the rotation matrix, it is orthogonal, i.e., the inverse matrix $R_X^{-1}$ is equal to $R_X^T$. Therefore, we can write:

$$\mathbf{X} = \mathbf{x}R_X^{-1} = \mathbf{x}R_X^T$$

in extended notation:

$$\begin{pmatrix} X \\ Y \\ Z \end{pmatrix} = \begin{pmatrix} x & y & s \end{pmatrix} \cdot \begin{vmatrix} 1 & 0 & 0 \\ 0 & \cos(i) & \sin(i) \\ 0 & -\sin(i) & \cos(i) \end{vmatrix}$$

Thus the conversions between the two frames of reference are as follows:

$$\begin{cases} X = x \\ Y = y \cdot \cos(i) + s \cdot \sin(i) \\ Z = -y \cdot \sin(i) + s \cdot \cos(i) \end{cases} \tag{4.3}$$

and

$$\begin{cases} x = X \\ y = Y \cdot \cos(i) - Z \cdot \sin(i) \\ s = Y \cdot \sin(i) + Z \cdot \cos(i) \end{cases} \tag{4.4}$$

In the middle plane of the galaxy, $Z = 0$ and the transformations in eq.4.4 become:

$$\begin{cases} x = X = R \cdot \cos(\phi) \\ y = Y \cos(i) = R \cdot \cos(i) \cdot \sin(\phi) \end{cases} \tag{4.5}$$

The galaxy in the equatorial plane can be seen as a series of rings of equation 4.1. Using the transformation of 4.5, the rings can be described on the observational frame of reference as follows:

$$\frac{x^2}{R^2} + \frac{y^2}{R^2 \cos^2(i)} = 1 \tag{4.6}$$

Eq. 4.6 represents an ellipse, hence the circular galaxy disk is projected onto sky as an ellipse with the major axis equal to galaxy radius and minor axis equal to $R\cos(i)$.

### 4.1.2 Elliptical angle

The azimuthal angle, as defined before, is useful to parametrize the rings on the plane of the galaxy. When the rings are projected onto the sky-plane, $\phi$ has a less direct interpretation (fig. 4.1), indeed it has the same role as the eccentric anomaly in celestial mechanics. For an

elliptical ring with position angle PA, inclination $i$, centre $(x_0, y_0)$, and major axis $R$, we have that (Begeman, 1987):

$$\begin{cases} \cos(\phi) = \dfrac{-(x-x_0)\sin(PA) + (y-y_0)\cos(PA)}{R} \\ \sin(\phi) = \dfrac{-(x-x_0)\cos(PA) - (y-y_0)\sin(PA)}{R\cos(i)} \end{cases} \tag{4.7}$$

For the purpose of our analysis it is fundamental to evaluate the flux along the projected elliptical rings, so it can be helpful to introduce the concept of **elliptical angle $\boldsymbol{\theta}$**. In figure 4.1 we define a point A on the galaxy plane of coordinates $X_P$ and $Y_P$, that is projected onto the sky-plane in the point B with coordinate $x_P$ and $y_P$. The elliptical angle $\theta$ is defined as the angle between the point B and the positive major axis of the galaxy.

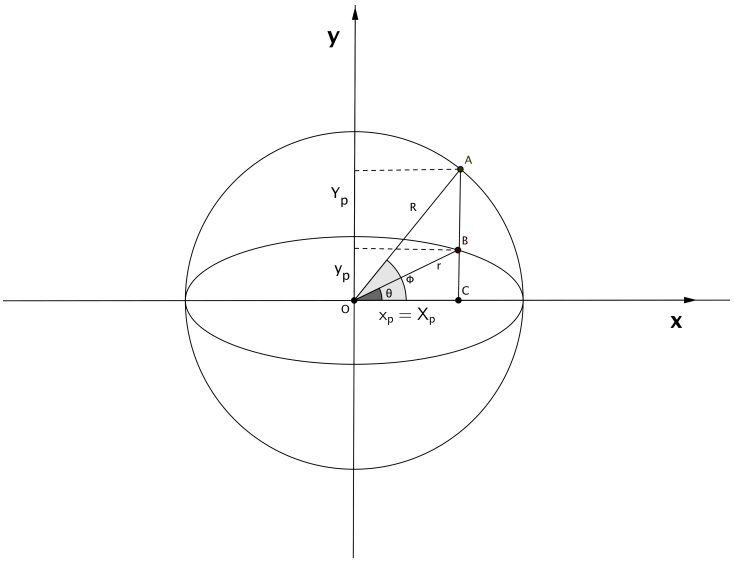


Figura 4.1: Ring of radius $R$ and its sky-projection into ellipses of major axis $R$ and minor axis $R\cos(i)$. $\phi$ is the azimuthal angle, $\theta$ the elliptical angle.

From fig. 4.1, we can write:

$$\tan(\theta) = \frac{BC}{OC}$$

with $BC = y_p$ and $OC = x_p$. Then using the parametrization 4.5 we obtain

$$\tan(\theta) = \frac{y_p}{x_p} = \frac{\cos(i)R\sin(\phi)}{R\cos(\phi)}$$

and finally,

$$\phi = \arctan\left(\frac{\tan(\theta)}{\cos(i)}\right) \tag{4.8}$$

Equation 4.8 is plotted in fig. 4.2 for various values of the inclination angle. The azimuthal angle is always larger than the elliptical angle, the two angles start to be significantly different

for inclination greater than 30°. We note that the two angles have the same value on the major and the minor axis of the projected rings.

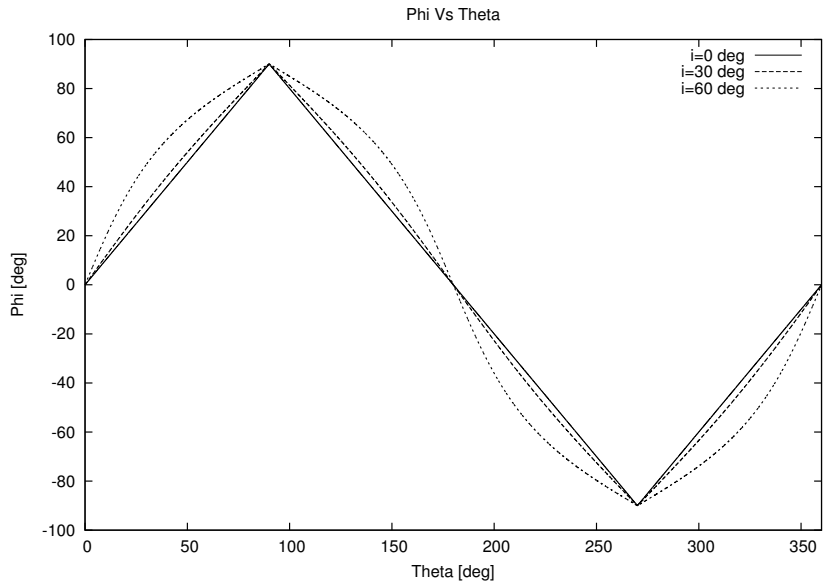


Figura 4.2: Relation between azimuthal ($\phi$) and elliptical angles ($\theta$), see fig. 4.1 for a geometrical description.

## 4.2 The model

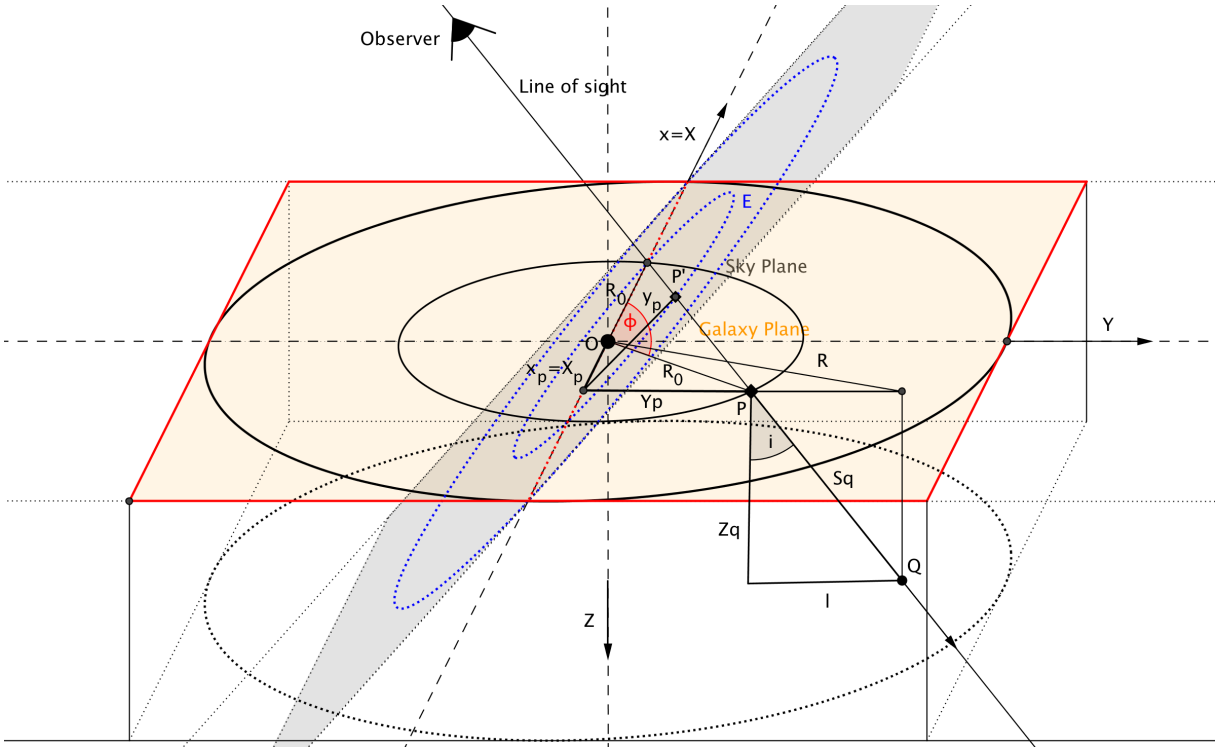


Figura 4.3: The orange plane with the red border represents the galaxy equatorial plane, where $Z = 0$; The grey plane is the plane of the sky, perpendicular to the observer line of sight; the dotted blue ellipses are the projections of the galaxy onto sky-plane, in particular the ellipse E is the projection of the ring of radius $R_0$. The two frames of reference ($x$,$y$,$s$) and ($X$,$Y$,$Z$) have been designed as explained in sec. 4.1; The point $P$ in the galaxy plane is projected on a point $P^{'}$ on the sky-plane: $i$ and $\phi$ are respectively the inclination angle and the azimuthal angle of points $P$ and $P^{'}$. This figure shows only half of the galaxy height ($Z > 0$), for the layer with $Z < 0$ the description made above is mirrored.

The total emission of a source a certain point on the sky is due to all the emitting units along the observer line of sight (los) passing for the point. In the case of 21 cm the signal comes from the HI clouds plus a radio continuum. Once the continuum has been subtracted, one can directly link the observed brightness to the HI column density along the los (sec. 1.2). Following the definition in fig. 4.3, we focused on a point $P^{'}$ in the observational ellipse of major axis $R_0$. The los passing through $P^{'}$ intercepts the galaxy equatorial plane at a point $P$ on the ring of radius $R_0$. If the HI layer of galaxy was infinitely thin, P would be the only point contributing to the emission, and the emission at $P^{'}$ would be $\propto \Sigma(R)$, where $\Sigma(R)$ is the surface density of the galaxy. Hence, the observed signal would preserve the cylindrical symmetry. The aim of this chapter is to go beyond the approximation of a HI thin layer and to explore the effect of thickness on the velocity integrated (so called total) map.

In the case of a thick gas layer, the observed emission will depend on the points intercepted

by the los, not only in the equatorial plane, but also above or below it. Looking at fig. 4.3, we can define the "reference ring as the one where the los intercepts the galaxy equatorial plane ($Z = 0$) at point $P$. This ring has a "reference radius $R_0$ and its sky projection is the ellipse E, which intercepts the los in the point $P^{'}$. $P$ and $P^{'}$ have coordinate $(X_p, Y_p, 0)$ and $(x_p, y_p, 0)$ respectively. From the eq. 4.5 and 4.2 we know that:

$$\begin{cases} X_p = x_p = R_0 \cos(\phi) \\ Y_p = R_0 \sin(\phi) \\ y_p = R_0 \sin(\phi) \cos(i) \end{cases} \tag{4.9}$$

Now, we consider a generic point $Q$ along the los with coordinates $(X_q, Y_q, Z_q)$: from a geometrical analysis of fig. 4.3, the following identities are obtained:

$$\begin{cases} X_q = X_p \\ Y_q = Y_p + l \\ Z_q = Z_q \end{cases} \tag{4.10}$$

with

$$l = Z_q \tan(i) \tag{4.11}$$

The generic point $Q$ belongs to the galaxy ring of equation:

$$X_q^2 + Y_q^2 = R_q^2; \quad Z = Z_q \tag{4.12}$$

Using eqs. 4.9, 4.10 and 4.11 in eq. 4.12 we can write:

$$(R_0 \cos(\phi_q))^2 + (R_0 \sin(\phi_q) + Z_q \tan(i))^2 = R_q^2$$

Therefore, returning to the generic coordinates R, Z and $\phi$, we obtain:

$$R(Z, \phi, i) = \sqrt{|R_0^2 + Z^2 \tan^2(i) + 2 Z R_0 \sin(\phi) \tan(i)|} \tag{4.13}$$

using elliptical angles (sec. 4.1.2):

$$R(Z, \theta, i) = \sqrt{\left| R_0^2 + Z^2 \tan^2(i) + 2 Z R_0 \sin\left(\arctan\left(\frac{\tan(\theta)}{\cos(i)}\right)\right) \tan(i) \right|} \tag{4.14}$$

Eq. 4.14 allows us to know the $R$ and $Z$ coordinates of all the points intercepted by the los passing for a generic observational point with coordinates $R_0$ and $\theta$. Thus, we can evaluate the integrating column density over the s axis, as follows:

$$\Sigma(R_0, \theta, i) = \int_{-\infty}^{\infty} \rho(R(Z, \theta, i), Z(s)) ds \tag{4.15}$$

and finally, the emission (as flux or brightness):

$$S_\nu(R_0, \theta, i) = A \cdot \Sigma(R_0, \theta, i)$$

where A is a conversion factor between column density and flux or brightness (see section 1.2)

Recalling eq. 4.4, we can relate the Z and s coordinates as follows:

$$Z = s \cdot \cos(i) - y \cdot \sin(i) \tag{4.16}$$

From figure 4.3 one can see that all the points intercepted by the los passing for a observational point $P^{'}$ have the same $y$ coordinate. Therefore, differentiating eq. 4.16 we can treat $y$ as a constant obtaining: $ds = \frac{dZ}{\cos(i)}$. Then, we can rewrite the integral in eq. 4.15 in terms of the natural coordinates:

$$\Sigma(R_0, \theta, i) = \int_{-\infty}^{\infty} \frac{\rho(R(R_0, Z, \theta, i), Z)}{\cos(i)} dZ \tag{4.17}$$

With $i$ ranging from 0 to $\frac{\pi}{2}$.

Now, we focus on the integrand function $\rho$: assuming cylindrical symmetry the density distribution of the gas can be parted in a radial and a vertical contribution, respectively defined as $\rho_0(R)$ and $f(Z)$:

$$\rho(R, Z) = \rho_0(R) f(Z)$$

It is usually assumed that $f(Z)$ is one of the functional forms described in Appendix B, i.e., a gaussian, an exponential or an hyperbolic secant squared. We note that in the case of a non constant thickness (e.g. flaring layers), the function $f$ will depend also on the galactic radius $f = f(R, Z)$, but we will introduce this complication later in this chapter. The radial contribution $\rho_0$ can be related to the intrinsic surface density $\Sigma_{\text{int}}$, indeed for a face-on galaxy the inclination angle is equal to 0, and from eq. 4.14 we obtain $R(Z, \theta, i) = R_0$, hence eq. 4.17 becomes:

$$\Sigma_{\text{int}}(R_0) = \rho_0(R_0) \int_{-\infty}^{\infty} f(Z) dZ \tag{4.18}$$

Therefore, for a generic inclination angle $i$, the observed surface density will be:

$$\Sigma_{\text{obs}}(R_0, \theta, i) = \int_{-\infty}^{\infty} \left( \frac{\Sigma_{\text{int}}(Z, R(R_0, \theta, i, Z))}{\int_{-\infty}^{\infty} f(Z) dZ} \right) f(Z) \frac{dZ}{\cos(i)} \tag{4.19}$$

In the case of a razor-thin disk the vertical distribution f(Z) is a Dirac delta $\delta(Z)$. Using it in eq. 4.19 we obtain:

$$\Sigma_{\text{obs}} = \Sigma_{\text{int}} \cos(i) \tag{4.20}$$

This is the relation commonly used in the literature to obtain the intrinsic surface density from the observed one. This is only true for extremely thin disks. In the case of a thick gas

layer the observed surface density depends also on the azimuthal angle. However, for each ring of major axis $R_0$, we can define the azimuthal mean of thsurface density as $\overline{\Sigma}_{\rm obs}(R_0)$, and we can write:

$$\Sigma_{\rm int} \approx \overline{\Sigma}_{\rm obs} \cos(i) \tag{4.21}$$

This relation is only an approximation that becomes progressively worse with increasing thickness of the gas, as we see in the next section (4.3). The effect of the thickness of the gaseous layer is not only to create azimuthal oscillation around the value of the intrinsic surface density, but also to modify the radial distribution of the observed surface density (with respect to the razor-thin case). This introduces a non trivial complication in the analysis of the vertical profile of gas: the observed radial distribution is not trivially linked to the thickness and we do not have an independent observational way to obtain the intrinsic surface density $\Sigma_{\rm int}$(R).

As a consequence, to obtain information about the vertical profile of the HI layer we need to fit eq. 4.19 to the observed surface density using as parameters both the ones of the vertical profile and of the surface density. In this case, the azimuthal mean of the observational surface density $\overline{\Sigma}_{\rm obs}$ can be a reasonable initial guest for $\Sigma_{\rm int}$, as we will show in sec. 5.3.

### 4.2.1 The border effect

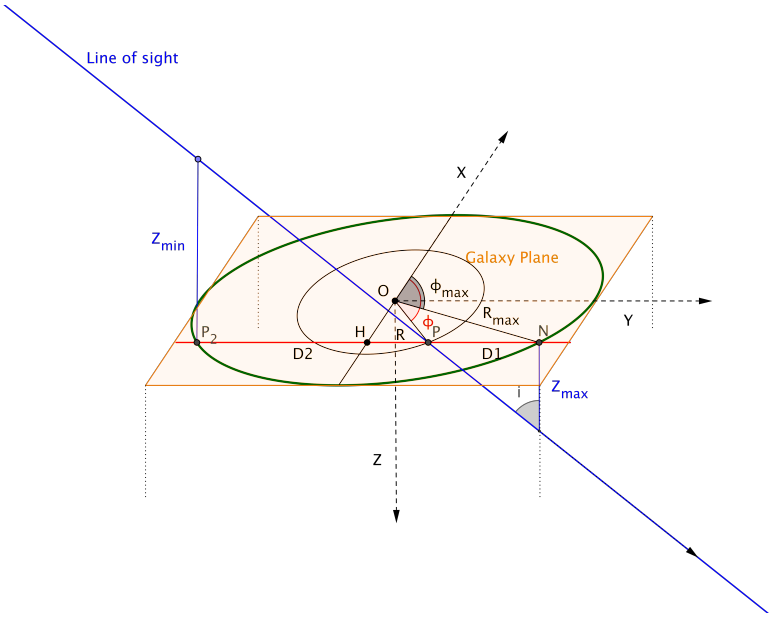


Figura 4.4: Border effect: the coordinate set and the meaning of the colors are the same in fig. 4.3, but in this case we have highlighted the last ring of the border (thick green line) with radius $R_{\rm max}$. $Z_{\rm max}$ and $Z_{\rm min}$ are the heights of the first and last points intercepted by the los passing through the point $P$. The definition of the segments $D1$, $D2$ (along the red line) and of the angle $\phi_{\rm max}$ are expressed in the text.

Eq. 4.17 is integrated over all the real dominion. However, the disks of neutral gas in real galaxies do not have infinite distribution. Indeed, below a certain column density threshold the

UV background is able to ionize the neutral hydrogen creating a finite border on the gaseous disk (Dove & Shull, 1994). Moreover, the simulated galaxies that we used as tests for our model (Ch. 5), have a very sharp truncation at the maximum radius $R_{\max}$. This feature can create a bias on the final analysis, so it is important to understand and model the "border effect. We can approach the problem in a geometrical way with the help of fig. 4.4. $X$,$Y$ and $Z$ are the coordinates on the plane of galaxy and the vertical axis Z makes an angle ($i$) with the los. The galaxy has a maximum radius $R_{\max}$, thus the los intercepts the HI layer only between $Z_{\min}$ and $Z_{\max}$: they coincide with the heights of the points that belong to the last galaxy ring of radius $R_{\max}$ shown as the green circle in fig. 4.4.

Both $Z_{\min}$ and $Z_{\max}$ depend on the position of the point intercepted by the los on the equatorial plane of the galaxy (the orange shaded region in fig. 4.4). This point ($P$) can be represented by the generic coordinate $X$,$Y$ ($Z = 0$ in the equatorial plane) or in the cylindrical frame of reference with $R$, $\phi$. The los passing through $P$ reaches the vertical limits at a point with the same X coordinate, but different Y that we called respectively $Y_{\min}$ and $Y_{\max}$, for the symmetry of the problem $Y_{\min}$=-$Y_{\max}$. We define the lengths $D1$ and $D2$ as the absolute values of $Y$-$Y_{\max}$ and $Y$-$Y_{\min}$. From fig. 4.4 we can write:

$$\begin{cases} Z_{\max} = \dfrac{D1}{\tan(i)} \\ Z_{\min} = -\dfrac{D2}{\tan(i)} \end{cases} \tag{4.22}$$

In cylindrical coordinate $|Y_{\max}| = |Y_{\min}| = \left|R_{\max}\sin(\phi_{\max})\right|$ and $Y = R\sin(\phi)$, thus we defined $D1$ and $D2$ as follows:

$$\begin{cases} D1 = |Y_{\max}(R_{\max}, \phi_{\max})| - Y(R, \phi) \\ D2 = |Y_{\max}(R_{\max}, \phi_{\max})| + Y(R, \phi) \end{cases} \tag{4.23}$$

In order to find a final form for $Z_{\max}$ and $Z_{\min}$ for every $\phi$ and $R$, we need a relation between the angles $\phi$ and $\phi_{max}$. We exploited the fact that every point along a certain los have the same X coordinate, thus defining the segment OH in fig. 4.4 as:

$$OH = R_{\max}\cos(\phi_{\max}) = R\cos(\phi)$$

and $r = \frac{R}{R_{max}}$, we obtained the following identity:

$$\begin{cases} \cos(\phi_{\max}) = r\cos(\phi) \\ \sin(\phi_{\max}) = \pm\sqrt{1 - (r\cos(\phi))^2} \end{cases} \tag{4.24}$$

Finally using 4.23 and 4.24 in 4.22, we obtained the final dependence of the integral limits on the coordinate of the point intercepted by the los in the equatorial plane:

$$\begin{cases} Z_{\min} = \dfrac{-R_{\max}(\sqrt{1-(r\cos(\phi))^2} + r\sin(\phi))}{\tan(i)} \\ Z_{\max} = \dfrac{R_{\max}(\sqrt{1-(r\cos(\phi))^2} - r\sin(\phi))}{\tan(i)} \end{cases} \tag{4.25}$$

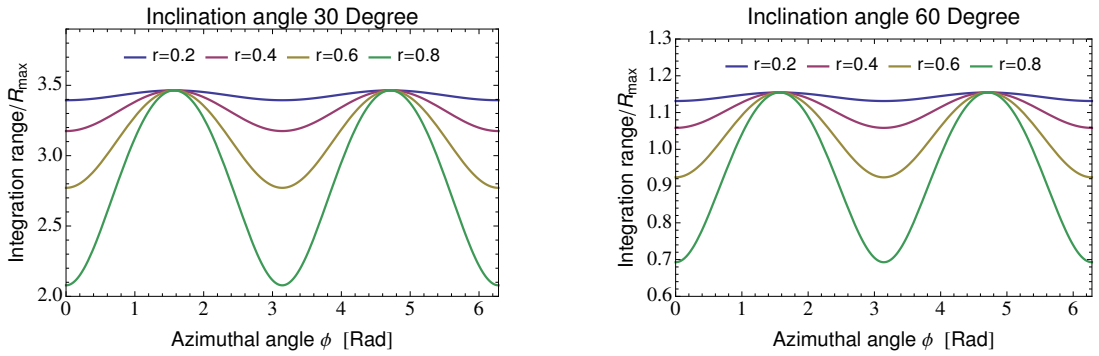


Figura 4.5: Dependence of the integration range ($Z_{\max} - Z_{\min}$ from eq. 4.25) on the position (radius and azimuthal angle) for two different inclination angles. The four curves show the azimuthal trend for four different reference radii. Both the integration range and the radii are normalized to the maximum radius $R_{\max}$.

Once we assume a value for the maximum extension of the HI disk ($R_{\max}$), the definitions in 4.25 give us the extremes of integration to use in eq. 4.17, that depend on azimuthal angle, radius and inclination angle. The dependence of the integration range ($Z_{\max} - Z_{\min}$) on these parameters is shown in fig. 4.5: for two different values of the inclination angle (30 and 60 degree), we plotted the azimuthal trend of the integration range for four different normalized radii. The inclination angle acts merely as a factor of normalization, indeed the patterns exhibited by the curves are the same for both panels in fig. 4.5. The overall azimuthal behavior is similar at every radius: the integration range rises from the (projected) major axis to the (projected) minor axis and the difference between the maximum and the minimum value increases as function of radius, creating sharper peaks at larger radii. The values at 90 and 270 degrees are independent of the radius, and they are always equal to $\frac{2R_{\max}}{\tan(i)}$, indeed it is clear from fig. 4.4 that the los passing through a point laying on the apparent minor axis intercepts all the rings of the galaxy.

## 4.3 Theoretical predictions

In this section we used the equations 4.19 and 4.25 to show the radial and the azimuthal patterns caused by the thickness of the gaseous layer on the observed HI emission.

The integral 4.19 has been computed numerically with the software *Mathematica*[1]. The build-in function *NIntegrate* uses different methods and strategies to numerically evaluate the integral. We choose to use an adaptive strategy, which means that the intervals used in the numerical integration are not fixed but adaptively refined depending on the behavior of the integrand function. Finally, we choose to use a Romberg method to perform the integration.

As input for the density distribution we used an intrinsic surface density of this form:

$$\Sigma(R) = \Sigma_0 \left(1 + \frac{R}{R_d}\right)^{\alpha} \mathrm{Exp}\left(-\frac{R}{R_d}\right) \tag{4.26}$$

This is a versatile functional form that gives a good description of the observed surface density in disk galaxies (e.g. Oosterloo et al. 2007). It exhibits a central "hole and a nearly exponential fall-off at larger radii. The parameter $\alpha$ controls the importance of the "central hole, in the extreme situation $\alpha$ can be set to 0 to obtain an exponential surface. In the following sections the unit of the parameter $\Sigma_0$ will be aU (arbitrary units), the surface density can be expressed in a variety of units (particle per $cm^2$, solar masses per $pc^2$), and the HI emission flux of brightness can be also a measure of the HI surface density through the equations 1.15 or 1.17. All these measures differ only for some conversion factors. The vertical distribution of the gas was considered gaussian given the theoretical analysis in sec. 2.3.1, its dispersion has been defined as $H(R)$.

### 4.3.1 Azimuthal density profiles of flaring HI disks

In this section we analyzed the observed surface density produced by three different models for the density distribution of the gas: they have the same intrinsic surface density (left panel in fig. 4.6), but different flarings (right panel in fig. 4.6).

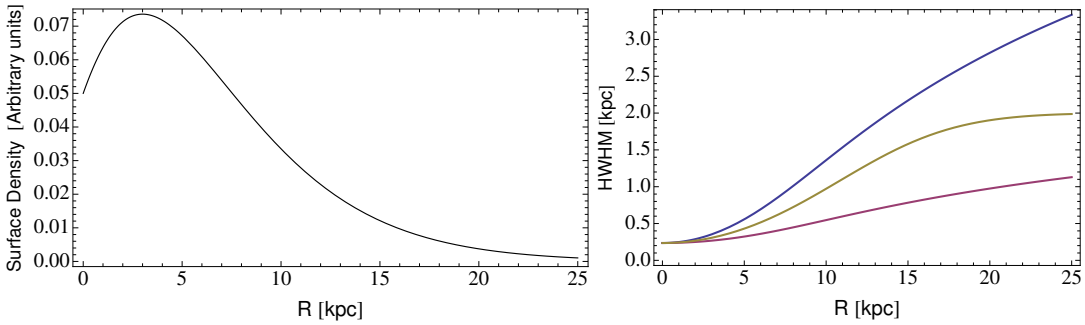


Figura 4.6: Input models for the density distribution of the gas in eq. 4.17: in the left panel is shown the function used for the intrinsic surface density; in the right panel are plotted three different models for the radial trend of the scale height of the gaussian vertical profile.

The intrinsic surface density has the functional form of eq. 4.26, its parameters have been set as: $\alpha = 2$, $R_d = 3$ kpc and $\Sigma_0 = 0.05$ aU. The disk scale height (H) flares following three different curves as showed in fig.4.6:

[1] Wolfram Research, Inc., Mathematica, Version 9.0, Champaign, IL (2012).

- **extreme flare** (blue curve): The vertical scale height rises from 0.2 to 3.3 kpc following the functional form of eq. 3.41.
- **flattened flare** (yellow curve): We use the functional form of eq. 3.40 to represent the case in which at large radii the thickness tends to be constant due to a decreasing velocity dispersion of the gas (sec. 3.3). H flares from 0.2 to about 1.6 at $R = 16$ kpc, beyond this radius it remains nearly constant.
- **realistic flare** (purple curve) We use the same functional form of the extreme flare, but we set its parameters to obtain a realistic flaring profile, similar to the ones shown in sec. 3.4. H starts from 200 pc at the center and it reaches about 900 pc at the edge of the disk.

| | func | $H_0$ (kpc) | $C$ kpc | $R_f$ (kpc) |
|---|---|---|---|---|
| Extreme flare (blue) | asinh | 0.2 | 1 | 9.5 |
| Flattened flare (yellow) | tanh | 0.2 | 1.5 | 15 |
| Realistic flare (purple) | asinh | 0.2 | 0.3 | 10 |

Tabella 4.1: Parameters of the flaring profiles shown in fig. 4.6. The functional forms used are from eqs. 3.40 (tanh) and 3.41 (asinh).

The parameters used for the flaring profiles are summarized in the tab. 4.1. The flaring of the blue curve and the flattening of the yellow curve are magnified in order to amplify the effects, the flaring curve expressed by the purple line represents a more realistic case. The border of the galaxy has been set to 26 kpc for all the three models.

We performed a ring-by-ring analysis, fixing the reference radius $R_0$ and using eq. 4.19 to obtain the azimuthal profile of the observed surface density. Figures 4.7 and 4.8 show the angular pattern at various representative radii (displayed above the panels). We can divide the galaxy in three regions where the azimuthal profile assumes different configurations:

- Inner radii (0-3 kpc): This is the region where the surface density exhibits the "hole, i.e., the only radii where $\Sigma_{\rm int}$ is an increasing function of the radius. Moreover, in this region the scale height is relatively small for all the three models of disk thickness, thus the rings contributing to the signal are only those very close to the reference ring[2]. The combination of a thin layer with a radially increasing surface density produces azimuthal density peaks on the major axis of the galaxy (fig. 4.7, top panels). Around the radial peak density, located at 3 kpc, the intrinsic surface density is approximately flat and this causes a decrease of the signal around the major axis and an increase around the minor

[2]Recalling the geometrical analysis done in sec. 4.2, the reference radius is the radius of the ring intercepted by the LOS on the equatorial plane of the galaxy where Z=0.

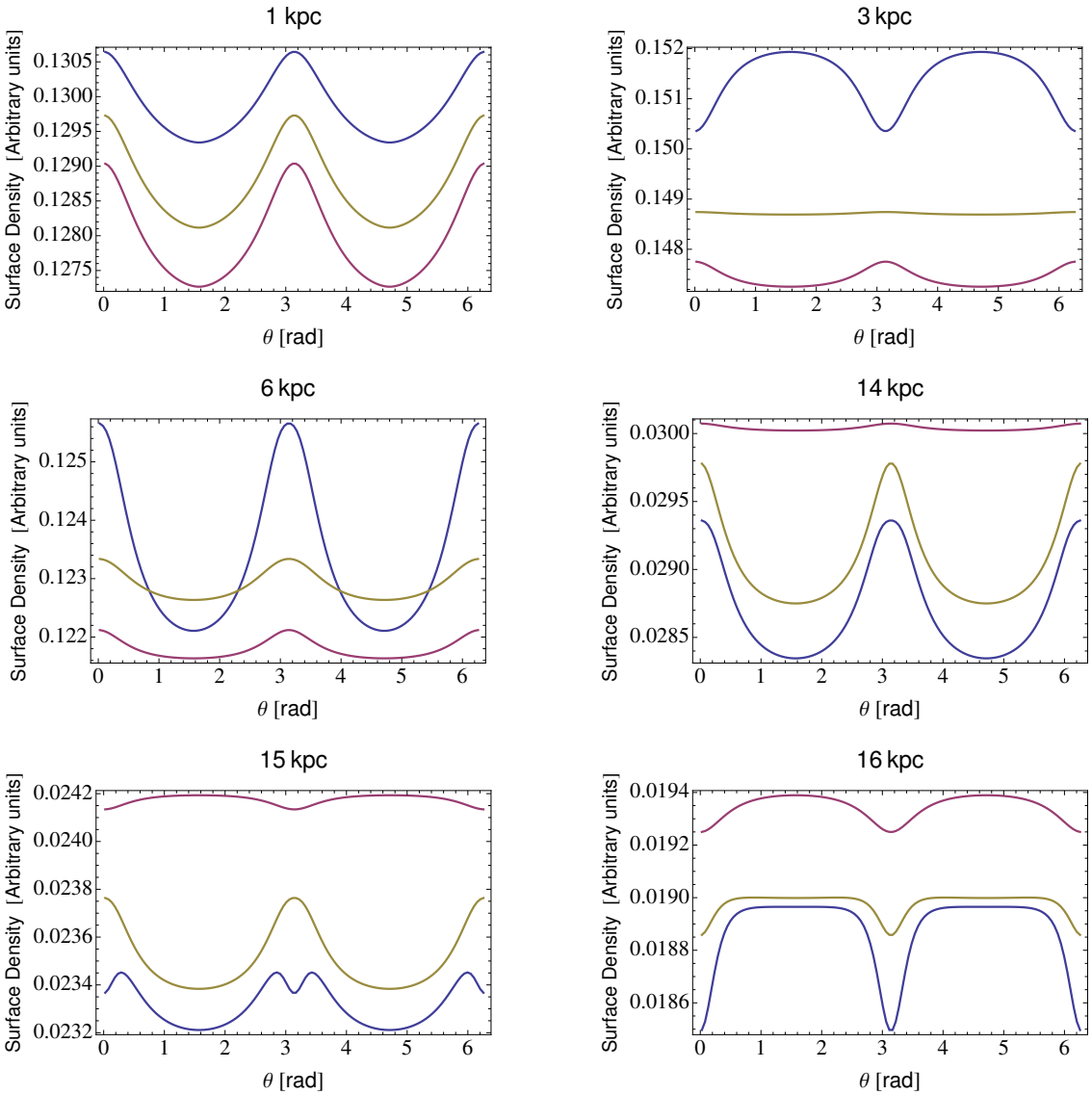


Figura 4.7: Angular density profiles caused by the thickness of the disk on the observed surface density. The colors of the three curves are the same as the three models of thickness shown in fig. 4.6. The angles represented in the X axis is the elliptical angle (sec. 4.1.2). The radii shown on the top of the panels are the lengths of the major axis of the "observed elliptical ring. In the plots the major axis is at $\theta = 0$ and $\theta = \pi$.

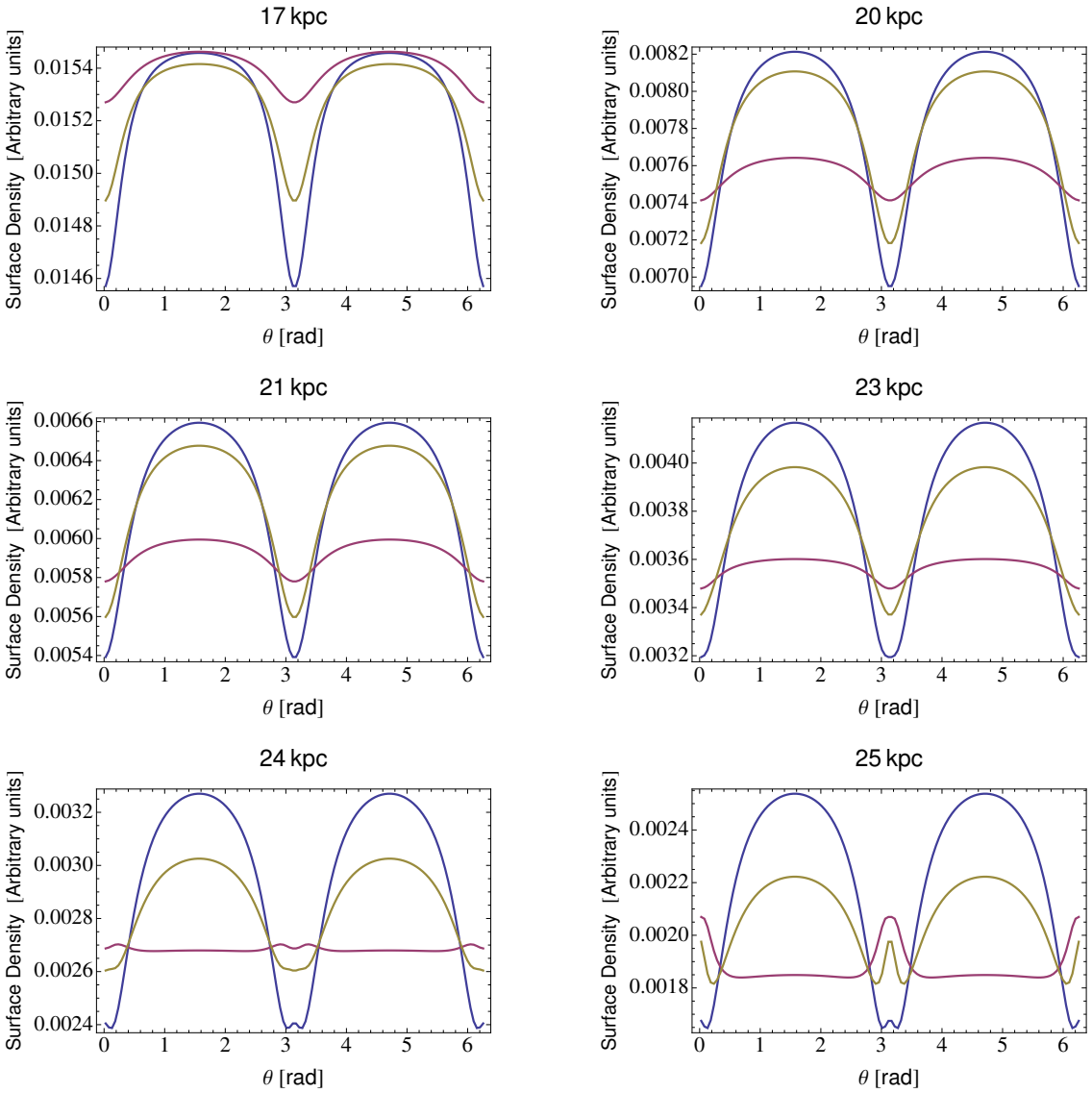


Figura 4.8: Same as 4.7.

axis. The three models this transition at different radii. At 3 kpc the "extreme flaring model has completely modified its pattern, the flattened flaring model (yellow) exhibits a flat profile, while the model with the low scale height maintains the peak on the major axis albeit reducing the difference between the maximum and the minimum.

- Intermediate radii (4-16 kpc): Beyond a region of transition near the peak of the surface density, the azimuthal profiles exhibit a similar pattern for all the three models: a peak on the major axis and a depression around the minor axis. Approaching the radius of $R \sim 5R_d$, the differences between maxima and minima decrease until there is a second switch of the position of the peak from the major to the minor axis. The variation of the azimuthal profile is very fast for the model with a "realistic flaring (purple curve) while slower for the other two models are slower, especially for the model with the flat thickness at large radii (yellow curve).

- Outer radii (17-25 kpc): In this region the thickness of the gaseous layer produces the most considerable effect on the azimuthal profiles of the observed surface density. The profiles exhibit broad peaks on the minor axis, more substantial for the models with higher thickness. Near 23 kpc the shape of the azimuthal profiles start to be heavily influenced by the "border effect (sec. 4.2.1): the profiles are lowered around the minor axis and they are increased around the major axis. This effect is most significant in the model with realistic flaring, indeed it causes, around 24 kpc, a further switch of the peak from the minor to the major axes. The azimuthal profiles of the other two models are less afflicted by the "border effect, especially in the case of the "extreme flaring.

**The gamma parameter**

The previous analysis of the azimuthal profile of the observed surface density can be summarized in a single plot through the definition of the gamma parameter. We defined it for every ring of radius R as follow:

$$\gamma(R) = 100 \cdot \frac{\text{Max}(R) \text{ - } \text{Min}(R)}{\text{Mean}(R)} \quad [\%] \tag{4.27}$$

where Max, Min and Mean are respectively the maximum the minimum and the mean value of the surface density along an observed ring of major axis R. This parameter is essentially a percentage measure of the importance of the azimuthal oscillations caused by the layer thickness with respect to the mean value of the observed surface density at certain radius $R$.

The behavior of $\gamma(R)$ for the three models of the disk thickness of fig.4.6 is shown in fig. 4.9: the radial trend of $\gamma$ can be parted in three regions using its minima approximately located at 3-5 and 15 kpc, this division roughly follows the one made previously on the basis of the panels in figs. 4.7 and 4.8. The minima correspond to the transition regions caused by the switch of azimuthal peaks of the observed surface density from major to minor axis or vice versa. In these

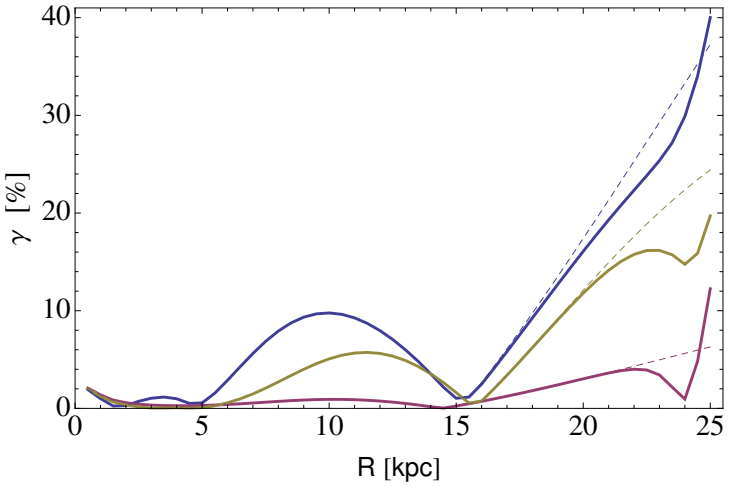


Figura 4.9: The gamma parameter (eq. 4.27) for the three model of the thickness shown in fig. 4.6. The dashed and the full curve represent the same galaxy models with the difference that the first do not have a finite border, i.e., the eq. 4.19 has been integrated over all the real dominion[3]. The border of the full curves has been set to 26 kpc.

regions the azimuthal profiles are nearly flat, as we can see for example from the yellow curve in the panel at 3 kpc of fig. 4.7, hence the related gamma parameter is very small. The overall radial trends of $\gamma$ are very similar for the three models and the minima are located approximately at the same radii, this means that the observed azimuthal pattern is mainly governed by the radial profile of the intrinsic surface density. The role of the thickness is to amplify the azimuthal oscillations.

### 4.3.2 The influence of the galaxy border

At large radii the $\gamma$ parameter rapidly increases for all three models, but it also starts to be influenced by the finite border of the galaxy. The influence of the border is highlighted by the differences between the full and the dashed curves in fig. 4.9: the first represents galactic models with the border located at 26 kpc, while the latter with not borders, that means that eq. 4.19 has been integrated over the whole real dominion[3]. Hereafter, we call the radius where the gammas of the models with and without border start to diverge ridge influence ($R_{\rm ri}$)

Without the presence of a border the gamma parameter rises linearly as a function of the radius, while models with a finite borders exhibit a more complex behavior depending on the disk thickness. The gamma of the "extreme flaring reaches its ridge radius very early ($R \sim 17$ kpc), beyond the gamma initially rises slower than the dashed curve and then at approximately 24 kpc, exhibits a very steep rise. The radius of influence of the other two models are located at larger radii: 20 kpc for the "flat model (yellow curve) and 22 kpc for the 'realistic flaring (purple

[3]In pratice, we do not perform an integration over the whole real dominion, but we fix an arbitrarily large integral limit $Z_{\rm lim}$ ten times $R_{\rm max}$.

curve). Beyond the ridge radius, $\gamma$ changes its slope until it reaches a local minimum around 24 kpc. Beyond the minimum, gamma begins to rise very steeply again for both the models.

We can interpret the location of the ridge radius as follows: in our model the vertical profile of the gas is gaussian with a dispersion $H(R)$, hence the signal contributing to the observed emission roughly comes from the points intercepted by the los with $|Z| \leq 2H(R)$. The ridge radius is roughly located at the radius of the reference ring where the los intercepts for the first time a point on the border with $|Z| = |Z_\mathrm{l}| = 2H(R_\mathrm{max})$, where $Z_\mathrm{l}$ is equal to $Z_\mathrm{max}$ if $Z_\mathrm{max} < |Z_\mathrm{min}|$, otherwise it is equal to $Z_\mathrm{min}$ (see fig. 4.4 for the definition of $Z_\mathrm{max}$ and $Z_\mathrm{min}$).

Using the definition of $R_\mathrm{max}$ and $Z_\mathrm{l}$ in eq. 4.14, we obtained the following equation:

$$R_0^2 + 2Z_\mathrm{l}R_0 \tan(i) \sin(\phi) + Z_\mathrm{l}^2 \tan^2(i) - R_\mathrm{max} = 0 \tag{4.28}$$

which is a second-order polynomial in $R_0$. Eq. 4.28 by construction is symmetric with respect to the apparent major axis (X axis in fig. 4.4), and we can focus our study between azimuthal angles from 0 to 180 degree. We subsisted $\sin(\phi)$ with a new variable $a$, in the analyzed range of $\phi$, $a$ ranges from 0 to 1. The minimum root of eq. 4.28 is the following:

$$R_0(a) = -Z_\mathrm{l} \tan(i) a + \sqrt{Z_\mathrm{l}^2 \tan^2(i)(a^2 - 1) + R_\mathrm{max}^2} \tag{4.29}$$

Since $Z_\mathrm{l}$ and the inclination angle are fixed by the galactic model, the solution assumes different values depending on $a$, hence to estimate the ridge radius we have to find the minimum value of $R_0$. The derivative of eq. 4.29 with respect to $a$ is always negative, hence $R_0$ is a monotonically decreasing function of $a$ and hence the minimum of $R_0$ is located at the upper limit of the interval where a=1, i.e., $\phi = 90°$, on the apparent minor axis.

In conclusion, a rough estimate of the radius of influence can be obtained from the eq. 4.29 setting $a = 1$:

$$R_\mathrm{in} \approx R_0(a = 1) = R_\mathrm{max} - 2H(R_\mathrm{max}) \tan(i) \tag{4.30}$$

For the three models of fig. 4.9 the eq. 4.30 gives the values of 16, 20 and 22 kpc, very close to the true values of the radius of influence shown in fig. 4.9.

Eq. 4.29 is a monotonically decreasing function of $\sin(\phi)$, hence, going from $R_\mathrm{ri}$ to $R_\mathrm{max}$ the influence of the border is propagated from the minor axis to the major axis. The major axis is the last to be affected by the HI emission cut-off at the border, therefore from the ridge radius, the peak on the minor axis starts to decrease while the minimum around the major axis remains virtually unchanged. The decrease of the difference between the maximum and the minimum produces the observed decrement of gamma in fig. 4.9. The "border effect can heavily influence the shape of the azimuthal profile, especially in the model with lower thickness, indeed the galaxy model with realistic flaring (purple curve) exhibits the most prominent variation of the

gamma parameter with respect to no-border model. It is due to the switch of the peaks located around 24 kpc as we can see in the bottom panels of fig. 4.8. In conclusion the influence of a finite border on the observed surface density depends on the thickness of the gaseous layer at the edge of the galaxy: the greater the thickness, the further in will be the first ring influenced by the border. However, a relatively thin gaseous layer will exhibit a stronger effect in the observed surface density: in this case the azimuthal pattern and its peaks can be heavily modified.

As final note, we focus our attention on the purple curve, because its thickness (shown on the left panel of fig. 4.6) has the same order of magnitude of the theoretical thickness obtained from the dynamical modelling of realistic spiral galaxies (sec. 3.4). Its gamma parameter is quite small: excluding the extreme border of the disk it is always below 4 %, and inside 20 kpc it is lower than 2 %. Therefore, we can expect that the typical thickness of a spiral galaxies would produce observed effects that are of order a few percent of the mean signal. Unfortunately, the local fluctuations of the observed signal in real galaxy are often of the order or greater of the expected values of $\gamma$, hence we can anticipate that to find and to extrapolate the expected theoretical signature in real data is an arduous task (see chapters 5 and 6). We show in App. D that the combination of an exponential surface density and a constant scale height can produce large values of $\gamma$ also for relative low disk thickness.

### 4.3.3 The observed radial surface density

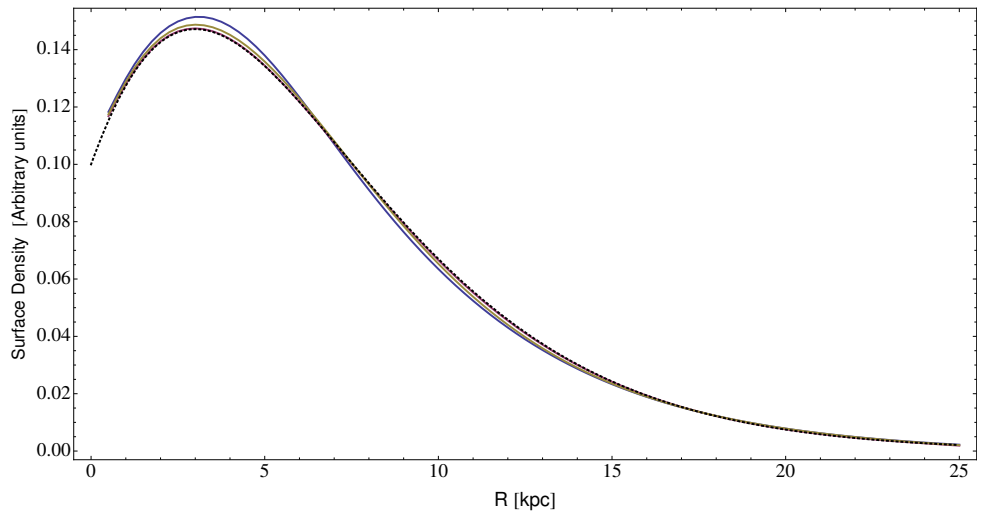


Figura 4.10: Radial trend of the surface density: the black curve is the intrinsic surface density of fig. 4.6 multiplied for the factor $\cos^{-1}(i)$; the colored curves display the azimuthal mean of the observed surface density (eq. 4.19) for the three models of thickness shown in fig. 4.6

The knowledge of the intrinsic surface density is fundamental to model the observed patterns produced by the thickness of the gaseous layer. As mentioned in the presence of a thick disk, this does not coincide with the observed surface density ($\Sigma_{\rm obs}(R)$) because of the projection

effects. In this section we analyzed the differences between the intrinsic and the observational radial trend of the surface density.

We considered the three above models and calculate the radial profiles of the observed surface density by averaging the azimuthal signal along every projected ring of major axis R, simulating what one should see in an hypothetical observation of a galaxy with the density distribution of gas in fig. 4.6. In fig. 4.10 we compared the three radial profiles obtained. As previously anticipated (sec. 4.2), the thicker gaseous disks.

We note some general trends followed by the three models: the thickness of the gaseous layer increases the relevance of the peak, and it tends to be shifted to larger radii, as it is clearly shown by the blue curve. At intermediate radii the observed curves stay systematically below the intrinsic surface density. One time again we stress that this effect is higher for model with higher vertical thickness. the purple model (realistic flare) show differences $\leq 1\%$. In genera, it would seem that the observed surface density, once corrected for the factor $\cos(i)$ (eq. 4.21), can be an acceptable approximation of the intrinsic surface density. However, we will show (sec. 5.3) that this approximation is to rough to be directly used in eq. 4.19 to fit the azimuthal pattern of the observed surface density but one can use it as first guess of an iterative procedure to compare data and models.

### 4.3.4 The role of the intrinsic surface density

In the previous section, we analyzed the observed surface density produced by galaxy models with a given radial distribution of the gas, but with different vertical profiles (fig. 4.6). In the following we keep fixed the vertical distribution of the gaseous disk and vary the radial distribution of the intrinsic surface density. In order to magnify the effect of the thickness on the observed surface density, we chose to set the scale height of the vertical profile as the blue curve shown in the right panel of fig. 4.6.

The intrinsic surface density has been modeled with the functional form in eq. 4.26: we varied the parameter $\alpha$ and the scale length $R_d$ maintaining the central surface density $\Sigma_0$ fixed to 0.1 aU, given that this is only a normalization factor. The inclination angle has been set to 60 Degree and the galaxy border is located at 26 kpc.

The use of galactic models with different intrinsic surface densities (as shown in fig. 4.11 and 4.12) makes it difficult to compare their azimuthal profiles in single plots for each galactic ring of radius R, as done in fig. 4.7 and 4.8. Therefore, in the following, we will make extensive use of the gamma parameter (4.27). When a comparison between angular pattern at singular radii is needed, the surface density will be normalized to the maximum value along the projected ring.

For the first comparison, we kept $R_d$ fixed to 3 kpc and three models of the intrinsic surface densities have been built with $\alpha$ respectively equal to 0, 1 and 2. The three models are shown in fig. 4.11 respectively by the red, green and cyan curves: the increase of the exponent causes

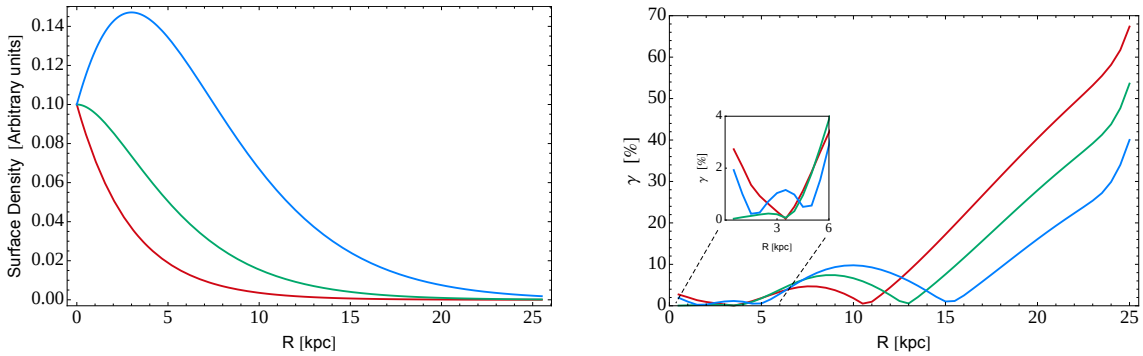


Figura 4.11: Models of the intrinsic surface density (left panel) and the related $\gamma$ parameter of the observed surface density. The vertical profile of the gas is gaussian with the scale height of the blue model of fig. 4.6. The inclination angle and the galaxy border has been set to 60 degree and 26 kpc respectively.

the shift of peak toward larger radii (it is absent in the pure exponential model shown by the red curve) and a general increase of the surface density. The gamma parameters (eq. 4.27) are shown as a function of the galactic radius in the right panel of fig. 4.11. The overall trend is very similar for all the three curves: it exhibits four distinct regions separated by three local minima. At large radii the magnitude of the oscillations shown by the exponential model is systematically larger. The effect of increasing $\alpha$ is mainly to shift the pattern of gamma towards larger radii, the other properties are similar to those already highlighted for fig. 4.9. Once the azimuthal profiles of the observed density are normalized, their shape is very similar for all the three models, as we can see in fig. 4.12: lower values of $\alpha$ produce azimuthal patterns with slightly shaper peaks at large radii, the situation is reversed at small radii.

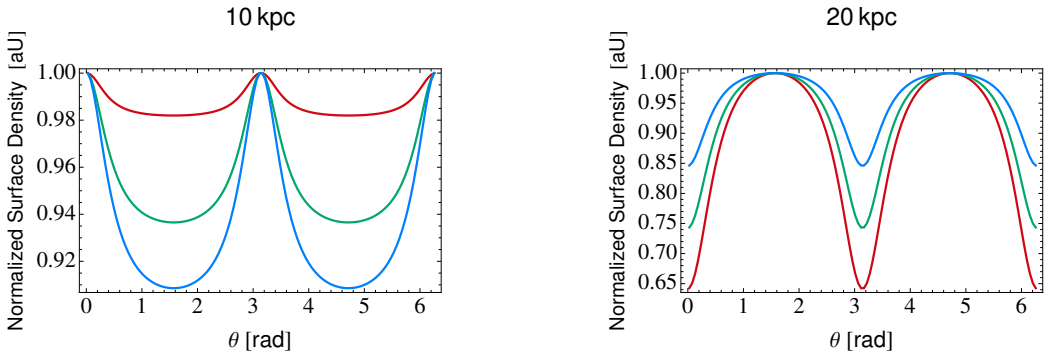


Figura 4.12: Azimuthal patterns of the observed surface density along projected rings of major axis 10 and 20 kpc. The colors are referred to the models of fig. 4.11. The profiles have been normalized to the maximum azimuthal value.

We performed a second comparison by keeping fixed $\alpha$ to 2, while the radial scale length has been set to 1, 2 and 3 kpc, respectively for the red, light green and the cyan curves of fig. 4.13.

The increase of the radial scale length causes both a shift of the peak and a slower decrease of the radial profile at larger radii. This seems to have a strong effect on the observed surface density, as it is shown by the gamma parameter (right panel in fig. 4.13).

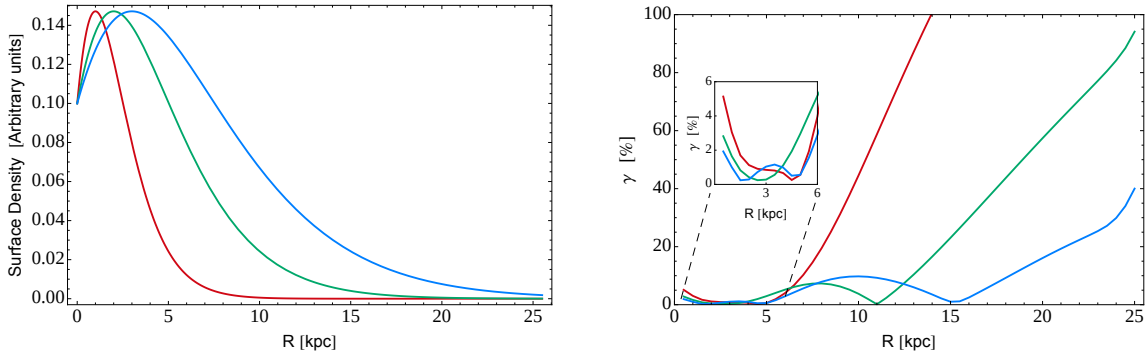


Figura 4.13: Same as fig. 4.11, except that $\alpha$ has been fixed to 2 and the radial scale length has been set to 1, 2 and 3 kpc respectively for red, light green and cyan curves.

After an initial transition phase (magnified in the insert, right panel of 4.13), the azimuthal profiles exhibit a peak around the major axis until the radius becomes approximately five times the radial scale length of the intrinsic surface density. The shape of the azimuthal profiles in these regions are shown in the first panel of fig. 4.14 for the blue model and in the second panels for the yellow and magenta models. Around $R \approx 5\ R_d$, $\gamma(R)$ drops to a minimum due to the switch of the peak from the major to the minor axis. Beyond the minimum, the magnitude of the azimuthal oscillations becomes very prominent as confirmed by the rapid increase of gamma as a function of radius. In substance the switch of the peak happens at a radius $R_s$ in a range 4

Comparing the behavior of gamma between models with fixed $R_d$ (4.11) and models with a fixed exponent $\alpha$ (4.13), it is evident that the radial scale length has a stronger influence than $\alpha$ on the azimuthal oscillations. Indeed, in the first case the various gammas rise in an almost parallel way, while in the second case the $\gamma$ clearly diverge. Hence, at large radii ($R > R_d$), the magnitude of the observed angular patterns is heavily linked with the radial scale length of the intrinsic surface density, more specifically $\gamma(R) \propto R/R_d$. Note that these results refer to exponential fall-offs of the radial profiles. In case of different functional forms the pattern may differ.

As expected from the study of $\gamma(R)$, the shape of the azimuthal pattern along the projected galactic rings, shown for some radii in fig. 4.14, exhibits strong differences between the three models. The first and the last panels of fig. 4.14 show that decreasing the radial scale length the azimuthal profile produces a sharper peaks. The middle show more complex shapes: for example at 5 kpc the red curve already show a peaks on the minor axis, while at 15 kpc the minimum in $\gamma(R)$ for the cyan model corresponds to a nearly flat azimuthal caused the switch of the peak position.

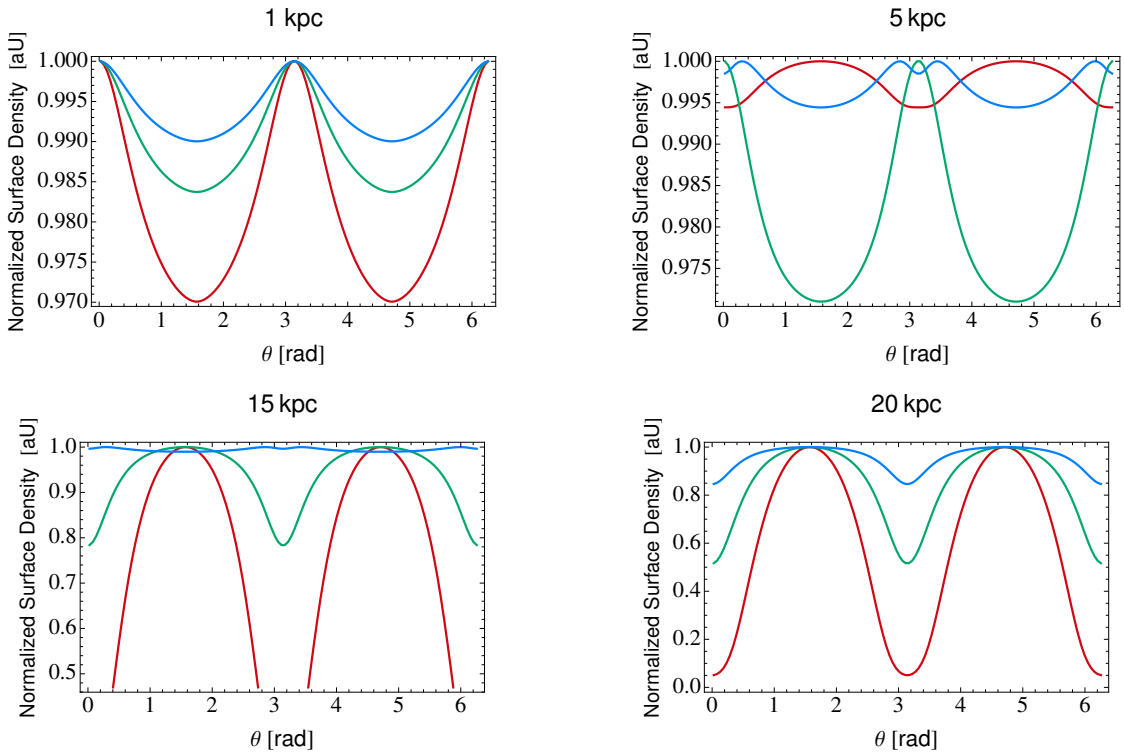


Figura 4.14: see fig. 4.12

### 4.3.5 The influence of the inclination angle

The inclination angle has a fundamental role in the angular pattern of the observed surface density. From figure 4.3, it is evident that in more inclined systems the los crosses more points close enough to the equatorial plane to give important contributions to projected emission. Thus, we expect that an increase of the inclination angle will cause an amplification of the observed azimuthal oscillations. In order to study this effect, we set the input density distribution of the gas layer using to the intrinsic surface density of the right panel of fig. 4.6 and a gaussian vertical profile with an extreme flare (the blue curve in left panel of fig. 4.6). Then, we used the eq. 4.19 to calculate the observed density and the related gamma parameter for four different inclination angles: 20, 40, 60 and 80 degrees.

The gamma parameters are shown in the four panels of fig. 4.15. We can use the model with i=60° as yardstick for the other models, because it was extensively analyzed in the previous section. The first evidence is that increasing the inclination angle, $\gamma(R)$ exhibits large variations with an increase of almost two orders of magnitude.

We first focus on the models with low inclinations, because the case with $i = 80°$ requires a dedicated treatment. Despite the great differences in normalization, the overall radial trend of $\gamma$ is quite similar for the three models. As seen in the previous sections, the disk can be divided in regions between local minima of $\gamma(R)$. We recall that the minima are located at radii where

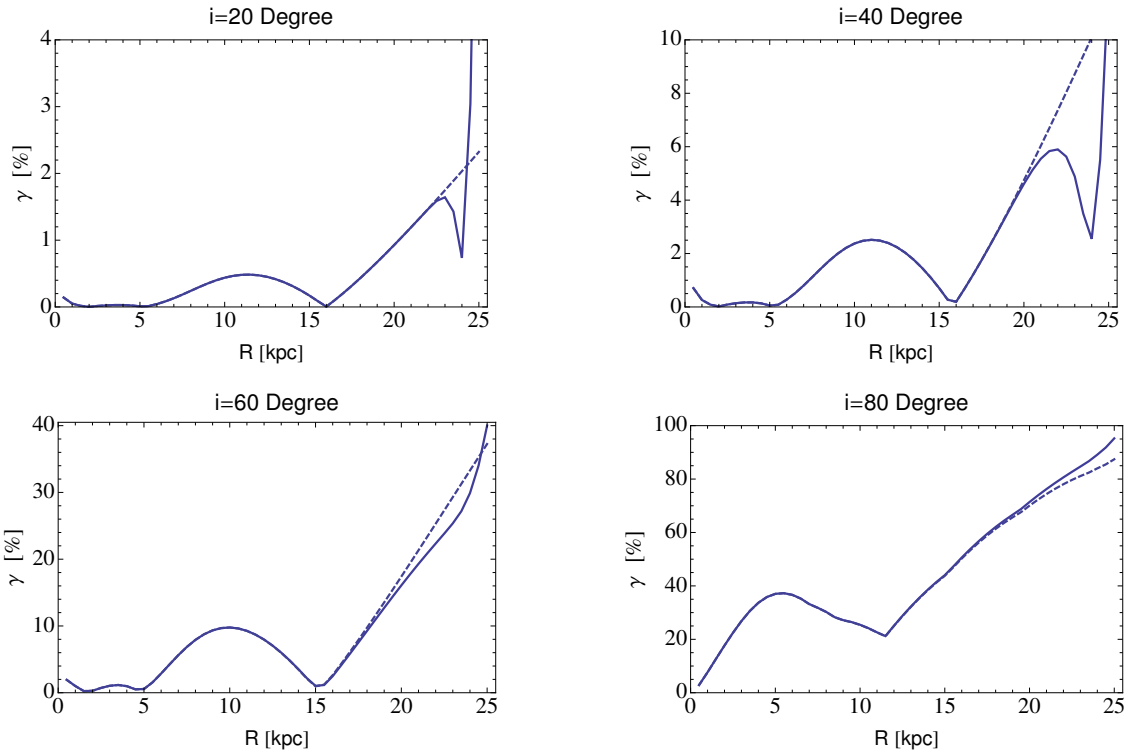


Figura 4.15: Radial trends of the gamma parameter for four galactic models seen at different inclination angles (shown above each panel): the density profile has been set to the intrinsic surface density of the right panel of fig. 4.6 and to the vertical profile shown by the blue curve in the left panel of the same figure. The full lines represent $\gamma(R)$ for galactic models with the radial density truncated (border) at 26 kpc, while the dashed lines show models without truncation.

the peaks of the observed azimuthal patterns switch between the major and the minor axis. Out to $R \sim 15$ kpc, the only effect produced by the inclination angle is a very small shift of the minima. The main differences between models with low inclination angles and the reference model ($i = 60°$) is seen at large radii. In this region the gamma profiles for low inclination models exhibit local drops around 24 kpc produced by the border effect, while this is much less evident for the $i = 60°$ model. Fig. 4.15 also shows that from 20 to 60 degree the ridge radius (the radius where the cut-off of the HI disk starts to influence the observed surface density) decreases with increasing inclination angle, roughly as predicted by the eq. 4.30. As an example we show in fig. 4.16 the observed azimuthal profiles for models with $i$ equal to 20, 40 and 60 degrees, for a galactic ring that is located very close to the border at 25 kpc. The azimuthal profiles a of galactic models without a border (dashed curves) and with the border located at 26 kpc (full curves) are compared. It is evident that the models with the lowest inclinations suffered an heavier modification of their profiles. Finally, it is interesting to note the behavior of these profiles around the major axis: the lower the inclination, the wider is the azimuthal region around the major axis unaffected by the cut-off of the disk.

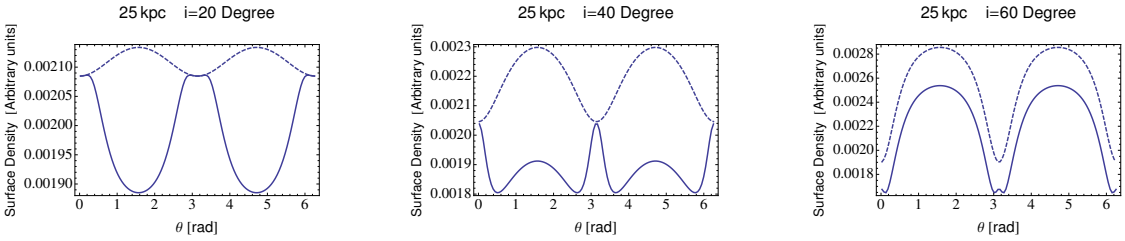


Figura 4.16: Azimuthal profiles of the observed surface density for projected rings with a major axis of 25 kpc. The galactic models and the meaning of the two curves are the same as in fig. 4.15.

Inclination angles higher than approximately 75 degrees deserve a separate discussion. As we can see comparing the variuos panels of fig. 4.15, the radial trend of $\gamma$ is very different for the highly inclined model. The initial zone of transition disappears and the outer minimum is located 3-4 kpc inward with respect to the minimum of the model with an inclination of 60°. In fig. 4.17 we compare the azimuthal patterns of the model with inclination angles of 60 and 80 degrees. The $i = 80°$ profiles display a very sharp feature around the major axis whathever it is a peak or a depression of the signal, while the surface density at the other angles are nearly constant. Another considerable difference is about the influence due to the disk border. From the trend shown is the models with lower inclination angles, we would expect that the ridge radius for the i=80 degree model will be smaller with respect to the reference model ($i = 60°$), instead it appears approximately at same radius. Moreover, differently from the other three models, beyond that radius, $\gamma(R)$ of the model with border rises more steeply than of the model with not border.

We performed a simple analysis using eq. 4.30, and found that for inclination angles greater than approximately 75 degree, the cut-off of the border should influence all the observed emission of the gaseous disk. More generally, in these high inclined galaxies every point along the los gives a significant contribution to the final emission, hence the observed azimuthal profile along every projected rings "feels the influence of the density distribution of the whole galaxy: in this case the analysis done in this chapter for low inclined system fails to explain the observed feature.

In conclusion, based of the high value of the gamma parameter, one would think that very highly inclined galaxy are the best systems where to look for signatures of the disk thickness. But this is not the case. The main reason is that for these systems the analysis of the gamma parameter has a less direct interpretation with respect to galaxies seem at lower inclination angles, indeed the very high values of the gamma parameter are produced by an almost flat profile with a very sharp structure located in a very small angular interval along the major axis (visible in fig. 4.17). Features of this kind can be very difficult to find in the real observations, because of the local spurious oscillations of the flux (e.g. spiral arms) and because of the influence of the instrumental convolution. Moreover, the observed emission of high inclined galaxies may

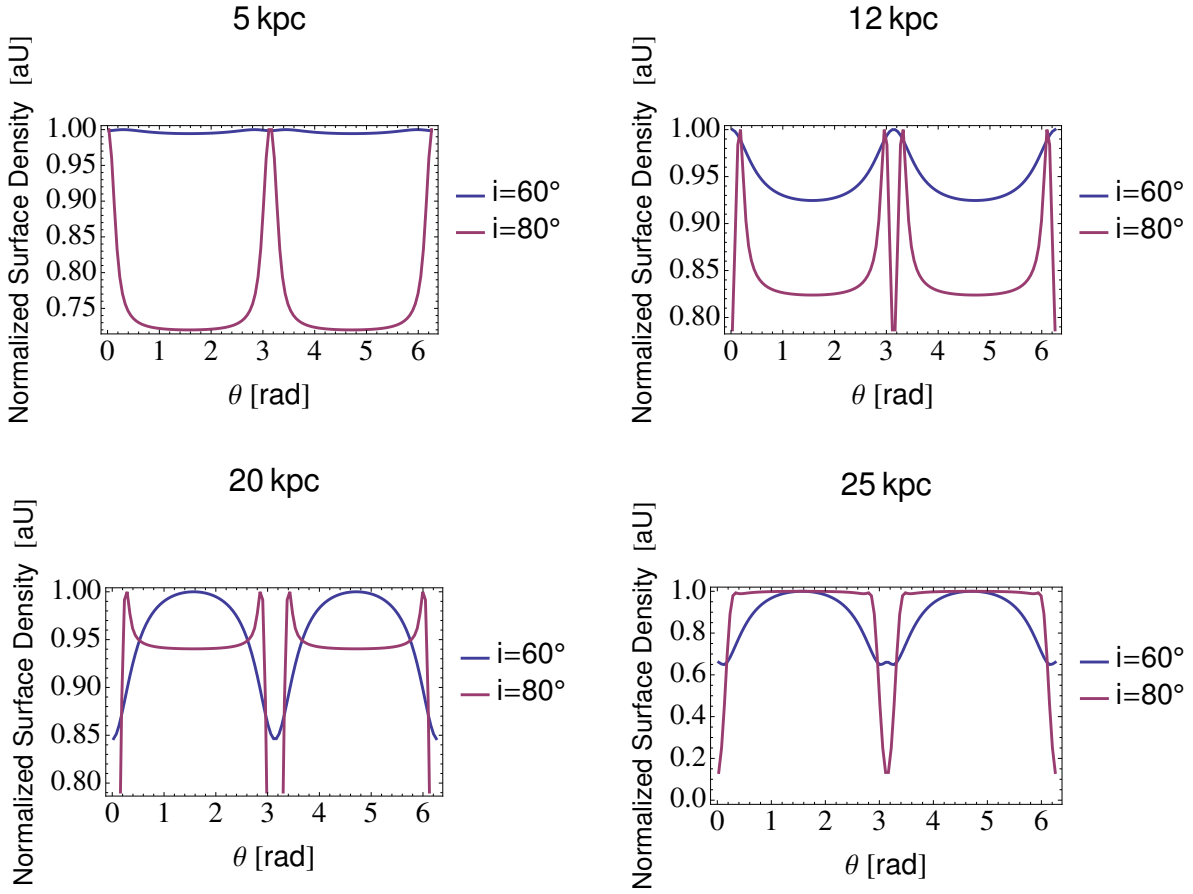


Figura 4.17: Azimuthal profiles of the observed surface density for four projected rings with major axis 5, 12, 20 and 25 kpc. The two curves represent the azimuthal profile of galactic models with the same surface density but different inclination angles: 60 degree for the blue curve and 80 for the magenta curve. The surface density has been normalized to the maximum value of each ring.

be affected by the self-absorption of the gas, and the relation used to link the flux with the surface density is no longer valid.

## 4.4 Results and discussions

In this chapter we have linked the observed HI emission of a disk galaxy with its 3D distribution of the gas.

Relying on the assumptions of cylindrical symmetry and non-warped gas layer, we found

that along every los (line of sight) the following relation is fulfilled:

$$R(R_0,\theta,i,Z)=\sqrt{\left|R_0^2+Z^2\tan^2(i)+2ZR_0\sin\left(\arctan\left(\frac{\tan(\theta)}{\cos(i)}\right)\right)\tan(i)\right|} \tag{4.31}$$

In practice, eq. 4.31 allows us to know the coordinates $(R, Z)$ of every point intercepted by the los at the observational coordinates ($R_0$, $\theta$). In this way, we can write the observed emission as:

$$S_{\rm obs}(R_0,\theta,i)=A\int_{Z_{\rm min}}^{Z_{\rm max}}\left(\frac{\Sigma_{\rm int}(Z,R(R_0,\theta,i,Z))}{\int_{-\infty}^{\infty}f(R,Z)dZ}\right)f(R,Z)\frac{dZ}{\cos(i)} \tag{4.32}$$

where A is a conversion factor between the surface density and the flux or brightness (sec. 1.2). $\Sigma_{\rm int}$ and $f$ are respectively the intrinsic surface density and the vertical profile of the gas. The extremes of integration take in account the presence of a finite galaxy border. Indeed, they are the heights of the first and the last points intercepted by the los passing through ($R_0$, $\theta$). They depend on the radius of the border ($R_{\rm max}$) and on the observational parameters $(R_0, \theta, i)$ as shown in eq. 4.25. Using eq. 4.32, we found that the presence of a thick disk ($f(R,Z)\neq\delta(Z)$) the commonly used relation $S_{\rm obs}=A\ \Sigma_{\rm int}\cos(i)$ is no longer fulfilled and the observed emission depends both on the radius and on the azimuthal angle.

The azimuthal profiles produced by a thick layer have characteristic patterns: they oscillate with a periodicity of $\pi$ and, in general, they show either a maximum/minimum on the projected galactic major/minor axis or vice-versa. However, there are also zones of transition where the azimuthal profiles show either a nearly flat profile or a more complex multi-peaked distribution. The shape and the magnitude of the oscillations depend on the gas density distribution. In general, we found that the vertical profile of the gas acts mainly to amplify the oscillation (the more important is the gas flaring, the larger will be the magnitude), while the the radial distribution of the gas has also a fundamental role in the shaping of the profiles (i.e. in the location of the maximum and the minimum).

We found that at large radii the magnitude of the azimuthal oscillations can become very important with respect to the mean values of the emission. This effect is magnified both by a significant vertical scale height and by a nearly constant profile of the surface density. In particular for a surface density falling exponentially with a scale lenght $R_d$, the azimuthal oscillations start to become progressively important beyond $4-5R_d$ where the radial fall of the density proceeds slowly. The inclination angle also plays a fundamental role increasing the magnitude of the oscillations at large $i$. However, we found that for inclination angles higher than $i\sim75^\circ$ the azimuthal profiles show an almost constant pattern with sharp peaks/depressions of the emission only in very small angle intervals (fig. 4.17). Features of this kind are difficult

to seek in real observations. Finally, the presence of a finite galactic border can influence the azimuthal profiles beyond a certain radius $R_{\rm ri}$ that depends on the last galactic radius $R_{\rm max}$ and on the layer thickness (eq. 4.30). The cut-off of the emission at the border decreases the emission primarily around the minor axis, while the major axis is influenced only at larger radii, closer to the galactic border. In conclusion, the best galaxies where to try to compare this model with the observational data should be system with the following observational properties:

- extended disk, it should be the smoothest possible without the presence of other azimuthal asymmetries (e.g. spiral arms or HI holes);
- emission with a radial relatively fast decrease, using the functional form in eq. 4.26 this means low value of $\alpha$ and $R_d$.

However, the fundamental condition to reveal these azimuthal signatures is that their magnitudes must be larger with respect to the oscillations due to other features in the data. Unfortunately, we found that the theoretical scale heights expected from dynamical models of realistic galaxies (sec. 3.4) will produce low oscillation, also in the case of high inclination angles (always of the order of few percent with respect of the mean emission). Therefore, it appears very difficult or even impossible to find this kind of signal in real observations.

As a suggestion, in app. D, we notice that the combination of a pure exponential fall of the emission and of a constant vertical scale height can produce important azimuthal features also with a relative low scale height ($H \sim 0.5$ kpc). These conditions can for istance, be fulfilled in a stellar disk (van der Kruit & Freeman, 2011). Therefore, it could be interesting in the future to perform this kind of analysis also for stellar disks of spiral galaxies, especially in the infrared band, where the disks appear "smooth. Indeed, the emission at these wavelengths is dominated by red and old stellar populations and hence, it is less influenced by local over densities due to star forming regions and/or spiral arms. Moreover, the stellar disks are less afflicted by the warp with respect to the gas layers.

# Capitolo 5

# Test on artificial data

In this chapter we compare the prediction of the model described in Ch. 4 with simulated spiral galaxies, of which we a priori know the kinematic and the structural features. After an introduction about the simulation method (sec. 5.1) , the chapter continues with the making and the study of the simulate galaxies. The first model (sec. 5.2) has been made with a constant surface density, a $\mathrm{sech}^2$ vertical profile with and fixed scale height: this simple model is a benchmark to test the procedure. Secs. 5.2.3 and 5.2.4 contain a detailed treatment of errors and biases introduced in the data analysis. They can be skipped at a first lecture going directly to the results on sec. 5.2.5. The second galactic model (sec. 5.3) has a surface density and a vertical profile similar to the one used in sec. 4.3.1, hence it is more realistic and comparable with real galaxies . We test the fit procedure to obtain information about the vertical profile from the features of the observed surface density (sec. 5.3.4) and the influence of the thickness on the estimate of the geometrical and kinematical parameters (sec. 5.3.5).

## 5.1 Preliminary concepts

### 5.1.1 Galmod

We simulate HI observations of disk galaxies we used the task *Galmod* (Sicking, 1997) included in the software package GIPSY (van der Hulst et al., 1992).

*Galmod* creates a galaxy model using the concept of tilted rings (Begeman, 1987): the galaxy disk is divided in a series of circular rings with their own geometrical and kinetic properties. The rings are filled with discrete "clouds to reproduce the density distribution of the gas given in input. The inclination and the position angles of the rings are allowed to vary with radius, but in our simulations we kept them fixed in agreement with the assumption in sec. 4.1. The gas density on each rings is assigned depending on its intrinsic surface density $\epsilon(R)$ and on the vertical profile. This latter can be implemented to follow implemented a gaussian, exponential or hyperbolic secant squared profile with a scale height (app. B) that can be defined ring by

ring. In our simulations we chose always to use a gaussian or a hyperbolic secant squared given the theoretical results of sec. 2.3.1. In order to complete the input, *Galmod* also needs the kinematic information such as the rotation and the systemic velocity and the velocity dispersion of the gas. The velocity dispersion and the rotation velocity are allowed to change with radius, while the systemic velocity is the same for every ring.

Once the input data have been set, *Galmod* starts to model the rings one by one, distributing the gas in discrete clouds. Each ring is filled randomly through a Monte Carlo method, both in the azimuthal and in the vertical direction. Each cloud has a velocity that is the sum of the systemic of the galaxy and the rotation velocity at that radius corrected for the azimuthal angle of the cloud and the inclination angle of the ring: $V_{\rm obs}(R) = V_{\rm sys}(R) + V_c(R)\cos(\phi)\sin(i)$ (Begeman, 1987). To create the profile of the HI line emission, the clouds are further divided into subclouds to which the code assigns a velocity equal to the velocity of the parent cloud plus a random contribution drawn from a gaussian distribution with $\sigma$ equal to the velocity dispersion at that radius. Once each rings has been constructed, *Galmod* produces a final cube (2 spatial and 1 velocity dimension) with HI flux as a function of position and line of sight velocity. The pixel of the final cube will contain the sum of the signal of every subcloud there located.

The distribution of the gas in discrete subclouds causes the presence of a discretization noise in the simulated model. Since each subcloud has the same amount of signal, this discretization noise will be proportional to the square root of the number of subclouds. Hence, in order to minimize this noise we needs to use a large number of clouds and subclouds. This is possible by varying the *Galmod* input parameters CDENS and NV, however their increase causes a substantial increase of the computational time. We found a good compromise between speed using NV=600 and CDENS=50. The output cube has a resolution of one pixel in each direction. Therefore, to complete the procedure we convolved the *Galmod* output cube with gaussian both the spatial and velocity directions to simulate the effect of the instrumental smoothing of the data. We follow the convolution method shown by Sicking (see Sicking 1997). The idea is to exploit a simple propriety of the convolution operator: the convolution of two gaussians is a gaussian with standard deviation equal to quadratic mean of the two original standard deviations.

The problem is that the "beams of *Galmod* output are the pixels and they cannot be considered gaussians, Sicking (1997) suggests is possible to approximate them as gaussian pass-bands with standard deviation equal to $\delta(\sqrt{12})^{-1}$, where $\delta$ is the pixel dimension. Hence the FWHM will be $\frac{2.35}{\sqrt{12}}\delta$, and accordingly, the FWHM of the convolution gaussian will be:

$$FWHM_i = \sqrt{{B_i}^2 - 0.462\delta_i^2}$$

where $i$ is the $x$ or $y$ grid coordinate, the observational beam that we aim to simulate has a FWHM equal to $B_x$x$B_y$ and the pixel sizes is $\delta_x$x$\delta_y$. Analogously, if we aim to build an

artificial galaxy model with gas velocity dispersion $\sigma(R)$, we must impose as input in *Galmod* the following:

$$\sigma_{\rm inp}(R) = \sqrt{\sigma^2(R) + \sigma^2_{\rm ins} - \delta v^2/12}$$

where $\delta v$ is the channel separation in velocity of the reference data cube and $\sigma_{\rm ins}$ is the instrumental broadening.

After the model cube has been smoothed, we rescale the total flux by a factor $f$ chosen to ensure that the simulated galaxies have the same total mass of the theoretical models used as input, i.e.:

$$\mathrm{M_{HIteo}} = f \cdot M_{\rm HImod}$$

The theoretical mass for a galaxy with an axisymmetric density distribution can be determined from the following integral in cylindrical coordinates:

$$\mathrm{M_{HIteo}} = 2\pi \int_0^{R_{\rm max}} \int_{-\infty}^{\infty} R\rho(R,Z) dR dZ \tag{5.1}$$

while for the simulations we can use the equation 1.22. Note that the integral in (eq. 5.1) direction goes from 0 to $R_{\rm max}$ to take into account that simulated galaxies have always a finite border (see 4.2.1).

### 5.1.2 Comparing theory and simulations

The theoretical model described in ch. 4 predicts that the observed emission of a thick HI disk should show distinct azimuthal signatures. The typical analysis of non-edge on galaxies is often focused only on the radial behavior of the emission. Hence, in order to compare the theoretical azimuthal profiles with data (real or simulated), we need an "original procedure to extract the azimuthal profiles from the data cube.

First of all, we build a total map of the HI emission: this is obtained through the GIPSY task *Sum* that simply adds for each pixel all signal in every velocity channel above a certain threshold specified by the user. Then, to obtain the azimuthal profiles we use the task *Ellint*, which overlaps over the total map an elliptical ring of major axis $R_e$, position angle $PA_e$, inclination angle $i_e$ and width $\Delta R$. Once the ellipse has been set, it is possible to obtain various statistical information about the overlapped data such as: the mean, the median, the total sum and so on. It is also possible to derive the original ellipse in segments subtended by elliptical angles $\Delta\theta$ (see sec. 4.1.2). For our study thus we measure the average signal in every segment assigning it to the azimuthal angle (mean elliptical angle) of that segment. Finally, we can compare these values with our theoretical model.

Before performing the comparison between theory we make sure that no systematic errors or spurious features are introduced by the above described procedure. For simplicity we keep

the ring width $\Delta R$ and the elliptical angle interval $\Delta\theta$ fixes in *Ellint*. The width $\Delta R$ used by the task refers to the width of the ring in the galaxy plane, therefore the projected ring width $\Delta r$ will depend on the azimuthal angle $\theta$ and on the inclination angle $i$. To make explicit this dependence, we note that a generic point in the galaxy with galactic coordinates ($X$,$Y$,$Z$) and sky coordinates ($x$,$y$,$s$) (see fig. 4.3) belongs to the geometrical loci of equation:

$$X^2 + Y^2 = R^2 \qquad \text{and} \qquad x^2 + y^2 = r^2$$

these equations can be combined using the definition $Y = \frac{y}{\cos(i)}$ (eq. 4.4) and the polar-cartesian relation on the sky plane $y = r\sin(\theta)$, hence we can write:

$$r^2 = \frac{R^2}{(1 + (\sin(\theta)\tan(i))^2)} \tag{5.2}$$

We note that on the major axis, $\sin(\theta) = 0$ and $r = R$, while the minor axis $\sin(\theta) = 1$ and $r = R\cos(i)$ as expected. Therefore, the width of the elliptical ring used by *Ellint* is:

$$\Delta r = \frac{\Delta R}{\sqrt{1 + (\sin(\theta)\tan(i))^2}} \tag{5.3}$$

The segment area and therefore the pixels overlapped by the elliptical segments vary with elliptical angle and radius causing a non-uniform sampling. The area of an elliptical segment with a width $\Delta r$ and subtended by an elliptical angle $\Delta\theta$ can be obtained by solving the following integral in polar coordinates:

$$A_e = \int_{r_m - \frac{\Delta r}{2}}^{r_m + \frac{\Delta r}{2}} \int_{\theta_m - \frac{\Delta\theta}{2}}^{\theta_m + \frac{\Delta\theta}{2}} r(\theta) d\theta dr \tag{5.4}$$

Where r is the radius from the centre of the ellipse to a point in the ellipse that forms an angle $\theta$ with the major axis. $r_m$ and $\theta_m$ are the polar coordinates of the centre of the segment. At this point, it is helpful to operate a change of variable from $r$ to $R$ through eq. 5.2 and 5.3: the new radial range goes from $R_l = R_m - \frac{\Delta R}{2}$ to $R_u = R_m + \frac{\Delta R}{2}$, where $R_m$ is the radius of the ring on the plane of the galaxy or the major axis. Defining:

$$a(\theta, i) = \sqrt{(1 + (\sin(\theta)\tan(i))^2)} \tag{5.5}$$

and

$$\theta_u = \theta_m + \frac{\Delta\theta}{2} \quad \& \quad \theta_l = \theta_m - \frac{\Delta\theta}{2} \tag{5.6}$$

we reach the final form for the integral in eq. 5.4:

$$A_e = \int_{R_l}^{R_u} R dR \int_{\theta_l}^{\theta_u} a(\theta, i)^{-2} d\theta \tag{5.7}$$

Integrating in $dR$, we obtain:

$$A_e = R\Delta R \int_{\theta_l}^{\theta_u} a(\theta, i)^{-2} d\theta \tag{5.8}$$

Finally, integrating in $d\theta$, we can write:

$$A_e = R\Delta R \left( \arctan\left(\frac{\tan(\theta_u)}{\cos(i)}\right) - \arctan\left(\frac{\tan(\theta_l)}{\cos(i)}\right)\right) cos(i) \tag{5.9}$$

It is interesting to note that with the angle transformation (eq. 4.8) the area becomes:

$$A_e = R\ \Delta R\ \Delta\phi\ cos(i)$$

Thus, $A_e$ is the area of a segment on the plane of the galaxy ($R\ \Delta R\ \Delta\phi$) compressed by the projection on the plane of the sky.

Dividing the total area $A_e$ for the pixel surface we get an estimate of the number of pixels sampled in an elliptical segment. It is obvious from eq. 5.7 that the bigger R and $\Delta R$, the larger will be the segment area, therefore the trend is to undersample the inner rings and oversample the outer ones (considering the beam as the sampling unity). The integral of the function $a(\theta, i)^{-2}$ in eqs. 5.8 and 5.9 describes the angular behavior of the segment area it as can be seen in fig 5.1: in this case we note an oversampling near the major axis and un undersampling near the minor axis for the same ring of radius R. Thus there are systematic features introduced by the use of fixed $\Delta R$ and $\Delta\theta$. Our analysis focuses on the average value of the flux over the elliptical segments and it should not be affect by these sampling features. They may however influence the error estimates as described more deeply in sec. 5.2.4.

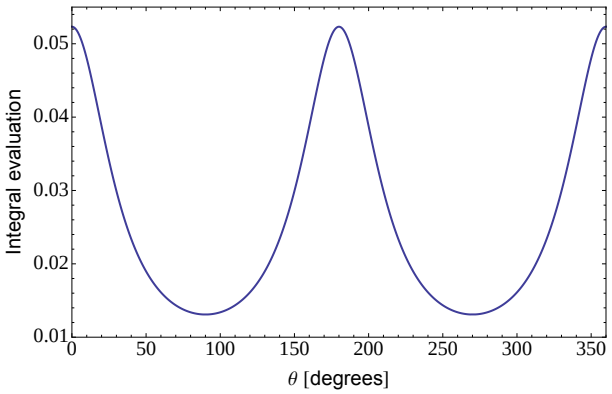


Figura 5.1: Evaluation of the integral in eq. 5.8 with $i = 60°$ and $\Delta\theta = 3°$. The major axis is at $\theta = 0°$ and $\theta = 180°$ and the minor axis at $\theta = 90°$ and $\theta = 270°$.

## 5.2 Preliminary analysis: toy model with radially independent density distribution

In this section we simulate and analyze a simple galaxy model to study the effect of a finite border and to analyze possible biases arising from the sampling and the numerical integration. The simplest radial distribution for the surface density of the gas is a constant at every radius:

$$\rho(R, Z) = Cf(Z) = \rho(Z) \tag{5.10}$$

Where $f(Z)$ represents the vertical profile of the gas, in this case we use a hyperbolic secant squared, hence using eq. 4.18 we can write:

$$\rho(Z) = \frac{\Sigma_{\rm int}}{2Z_d}\mathrm{sech}^2\left(\frac{Z}{Z_d}\right) \tag{5.11}$$

where $\Sigma_{\rm int}$ is the surface density of the gaseous disk seen face-on. We can calculate the observed surface density using eq. 4.19:

$$\Sigma_{\rm obs} = \frac{\Sigma_{\rm int}}{2Z_d\cos(i)}\int_{-\infty}^{\infty}\mathrm{sech}^2\left(\frac{Z}{Z_d}\right)dZ = \frac{\Sigma_{\rm int}}{\cos(i)} \tag{5.12}$$

Therefore $\Sigma_{\rm obs}$ is simply the intrinsic surface density corrected for inclination angle $i$. This is the same as thecase of a very thin disk (eq. 4.20). The model predicts an observed signal constant with R, but our simulated galaxy has a finite border at certain radius $R_{\rm max}$, hence the range of integration of 5.12 need to range from $Z_{\rm min}$ to $Z_{\rm max}$, rather than from $-\infty$ to $\infty$ (see fig. 4.4). Therefore, we can write:

$$\Sigma_{\rm obs} = \frac{\Sigma_{\rm int}}{2Z_d\cos(i)}\int_{Z_{\rm min}}^{Z_{\rm max}}\mathrm{sech}^2\left(\frac{Z}{Z_d}\right)dZ \tag{5.13}$$

The integral in eq. 5.13 has a simple analytic solution ($\tanh(Z)$) and this the only case in which we can compare the numerical integration with the analytic solution. Using the relation of eq. 4.25 in eq. 5.13 we obtain:

$$\Sigma_{\rm obs}(R,\theta) = \frac{\Sigma_{\rm int}}{2\cos(i)}\left(\tanh\left(\frac{Z_{\rm max}(R_{\rm max},\theta,R)}{Z_d}\right) - \tanh\left(\frac{Z_{\rm min}(R_{\rm max},\theta,R)}{Z_d}\right)\right) \tag{5.14}$$

In conclusion in the presence of a finite border, the observed surface density of a galaxy will always depend on the radius and on the elliptical (or azimuthal) angle also if the intrinsic surface density is independent from them.

### 5.2.1 Numerical integration test

As anticipated the particular density distribution used in this section allows us to compare the numerical and the analytic solution of eq. 5.13. To test our numerical method (sec. 4.3), we

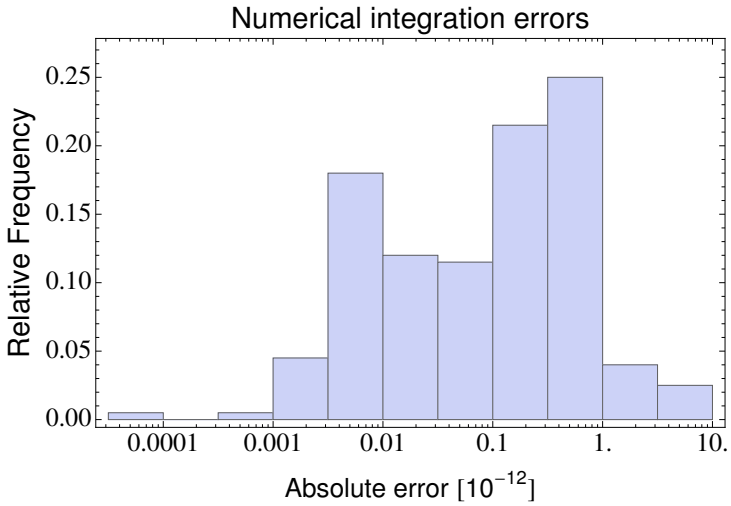


Figura 5.2: Distribution of the absolute difference between the numerical and the analytic solution of the integral in eq. 5.13. The differences have been calculated for 1000 randomly chosen sets of parameters (see text).

calculated the absolute differences between the numerical and analytic result for several set of galactic parameters. The galaxy parameters are chosen randomly within the following intervals:

- inclination angle: from 10° to 80°, we chose this range to avoid too edge-on or too face-on systems.
- Vertical scale height: from 0.1 to 8 kpc.
- Maximum radius: from 10 to 50 kpc.
- Elliptical angle: from 0° to 90°. These values are referred only to a single quadrant of the observed disk, but the theoretical signal has a periodicity of $\pi/2$, therefore using this interval we do not lose in generality.
- Galactic radius: from 0.1 to 0.9 times the value of the maximum radius.

We selected 1000 random parameters sets, and for each of them we calculated the absolute differences between the numerical and the analytical solutions of the eq. 5.13. The distribution of the errors is shown in fig. 5.2: most of the sets (approximately 80 %) have errors lower than $10^{-12}$, few of them have higher errors but always of the order of $10^{-12}$-$10^{-11}$. Errors of this magnitude are negligible for our study. Moreover, if we focus on the parameter set used for the artificial galaxy of this section (see tab. 5.1) the errors fall down to $10^{-15}$-$10^{-16}$, i.e., of the order of the machine precision. In conclusion, we can consider the numerical method of integration valid and appropiate.

In this section we will refer to both the numerical and analytic solution of eq. 5.13 indistinctly as the "theoretical model.

### 5.2.2 Making of simulate galaxy

| Galaxy parameters | | Cube parameters | |
|---|---|---|---|
| Radial density distribution | Constant | Pixel sizes (arcsec) | 4x4 |
| Vertical density distribution | $\mathrm{sech}^2$ | Channels separation (km/s) | 5.15 |
| Vertical scale height (kpc) | 4.0 | Assumed distance (Mpc) | 3.2 |
| Function scale height (arcsec) | 259.5 | Scale (pc/arcsec) | 15.4 |
| $R_{\max}$ (kpc) | 20.8 | Systemic velocity (km/s) | 130 |
| $R_{\max}$ (arcsec) | 1350.0 | | |
| Intrinsic surface density ($10^{21}$ cm$^{-2}$) | 5 | | |
| Inclination angle | 60° | | |
| Position angle | 90° | | |

Tabella 5.1: Parameters used as input in *Galmod* to build the artificial galaxy analyzed in this section.

We build an artificial galaxy with the density distribution described in eq. 5.11. The intrinsic surface density of the gas has been set to the arbitrary value of $5 \cdot 10^{21}$ particles/cm$^2$. To highlight the effect of the galaxy border on the observed signal, we chose to use a large vertical scale height of 4 kpc so that almost all the gaseous disk is influenced by the cut-off of the signal at the border. The border of the galaxy disk is located at 20.8 kpc. For the inclination and the position angle we used fixed values of 60° and 90° respectively. In this section we focus only on the observed emission of the total map of the artificial model, thus for simplicity the rotation velocity has been kept fixed at value of 130 km/s. The input value of the velocity dispersion is also constant at 10 km/s.

The lengths used in *Galmod* are in unity of arcsec, hence we need to assume a scale $S$ to convert from physical values (pc) to observed one (arsec). It can be obtained from:

$$S = \frac{d}{\alpha} = 4.848 \left( \frac{D}{1 \text{ Mpc}} \right) \quad \left[ \frac{\text{pc}}{\text{arcsec}} \right]$$

In this case we used a distance of D=3.2 Mpc, accordingly the scale S will be equal to 15.4 pc/arcsec. A summary of the input parameters used in *Galmod* is shown in tab. 5.1.

Once the galaxy has been simulated, we smoothed it to an observational beam of 15″x15″ (see sec. 5.1.1 for further details). This is a typical beam for observation through interferometers such as the Westerbork Radio Telescope or the VLA. Finally, we obtained the total map adding all the signal over the frequencies axis for every pixels through the task *Sum*. The result is shown in fig. 5.3. Using this beam of 15″x15″, we expect that the input surface density of $5 \cdot 10^{21}$ p/cm$^2$ will produce an observed brightness of about 0.395 Jy/beam (eq. 1.17). This is visible

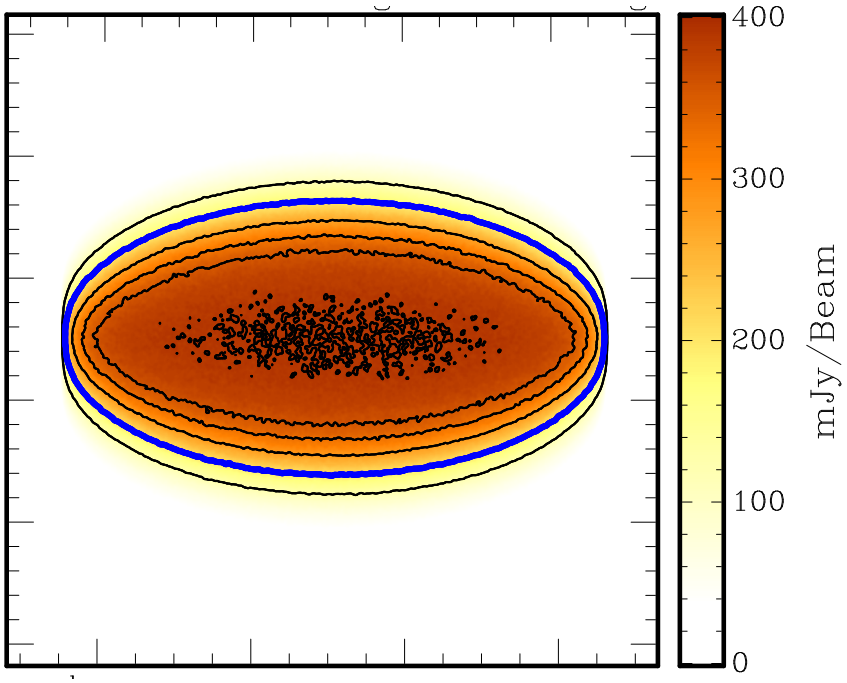


Figura 5.3: Total map of the artificial galaxy produced by *Galmod* with the parameters shown in tab. 5.1. The color scale is the brightness in units of mJy/Beam, while the isodensity contours represent the projected surface density of 1, 0.9, 0.8, 0.7, 0.55, 0.3 $10^{22}$ p/cm$^2$. The blu contour of 0.55 $10^{22}$ p/cm$^2$ represents the projection of the galactic ring with $R = R_{\max}$ onto the sky plane. The size of the bos is $50'$x$50'$ corresponding to 46.3x46.3 kpc.

only in the innermost disk, while at large radii the surface brightness decreases as function of the radius. This trend can be explained invoking the "border effect (sec. 4.2.1).

The blue contour in fig. 5.3 represents both the isodensity curve relative to the projected surface density of 0.55 $10^{22}$ p/cm$^2$ and the projection of the border of the galaxy onto the skyplane. Indeed, it has a major axis equal to $R_{\max}$ and a minor axis equal to $R_{\max}\cos(i)$. It is clear that beyond this contour there is further emission, especially around the minor axis. This extra emission is due to the thickness of the gaseous layer: its projection on the sky appears as an extension of the disk around the minor axis. Since the blue curve represents the right ellipticity, and hence the right inclination angle of the projected rings ($i = \arccos(b/a)$, where b and a are the minor and major axis), it can be used as a yardstick for the ellipticity of the other isocontours in fig. 5.3. At inner radii the ellipticity of the contours is higher than the true one, it progressively decreases as a function of radius until it assumes the right value at $R = R_{\max}$. Beyond this radius the isocontours appear more face-on, however the outermost contour in fig. 5.3 is an exact ellipse because of boxy shape close on the major axis.

We conclude that in the case of constant density if one derives the inclination of the disk from the isophotes alone neglecting the thickness, this will results in an inclination angle that decreases as function of radius. This is a simple example of the correlation between the inclination angle

and the thickness of the gaseous disk. A deeper analysis will be performed in sec. 5.3.

### 5.2.3 Data extraction

This and the following contain detailed tests of the biases introduced by our data analysis and error estimate. If the reader is mostly interest in the comparison between simulated data and theoretical model we refer him/her to sec. 5.2.5.

We analyzed the azimuthal behavior on the total HI map using the task *Ellint* , as explained in sec. 5.1.2 . We have shown above that using a fixed radial and angular width, the area of the segments sampled by *Ellint* is not constant but vary approximately as expressed in eq. 5.9. Since the final value is averaged over the elliptical segments, the difference in area should not influence our analysis. However, the azimuthal profile of the segment area (fig. 5.1) exhibits a periodic behavior very similar to the signal that we are trying to measure (figs. 4.7, 5.9 and 5.10). Hence, to be sure that the observed azimuthal profiles are not afflicted by the sampling procedure we run *Ellint* also with a non-fixed elliptical interval.

For this purpose we note that the sum of the first nine terms of the famous Fibonacci sequence incidentally is nearly 90 (exactly 88). Thus we set $\Delta\theta$ equal to the values of Fibonaccis's sequence, we start from the major axis of the disk. In this way we obtain an angular trend of the segment area opposite to that case with fixed elliptical angle (fig. 5.1).

Finally we compared the values extracted in this way with those obtained with a fixed $\Delta\theta$ for two different galactic radii, as it is shown in fig. 5.4. As expected the differences in the elliptical intervals have a large influence on the evaluation of the total flux but they have a very low repercussion on the mean flux. The Fibonacci intervals are smoother because we mediate on a larger area decreasing the local discretization noise (sec. 5.1.1). We stress that this analysis is extreme in the sense that the differences between the angular widths are very high, especially around the minor axis where they reach values of 30°.

Another bias that can be introduced by the data extraction is that the values obtained with *Ellint* are average fluxes over elliptical segments, but we compare them with models evaluated exactly at the center of the segment. In order to analyze this effect, we note that the equation used by *Ellint* is the following:

$$\overline{y} = \frac{\sum_i^N y_i}{N}$$

where $y_i$ is the flux (or the surface density) in the i pixel of the total map and N is the number of pixels inside the analyzed elliptical segment. For the theoretical model, $y_i$ represents the value of the function model at a certain elliptical angle $\theta_i$ for a ring of major axis $R_i$ and it is the discretization of the continue model function $y = f(\theta_i, R_i, p)$, where $p$ carries all the information about the rings parameters (inclination, position angle and so on). From the definition of the Riemann integral we can consider the function $f$ as a series of infinite N points over an elliptical intervals of width $\Delta\theta$ and $\Delta R$ centered in the point $(R_m, \theta_m)$, hence, we can reach a

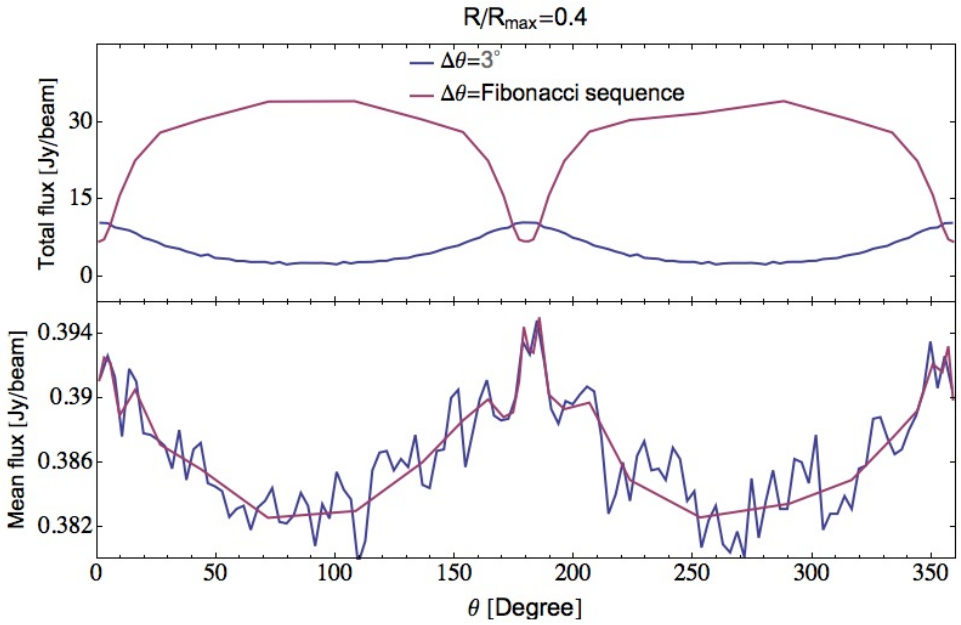


(a)

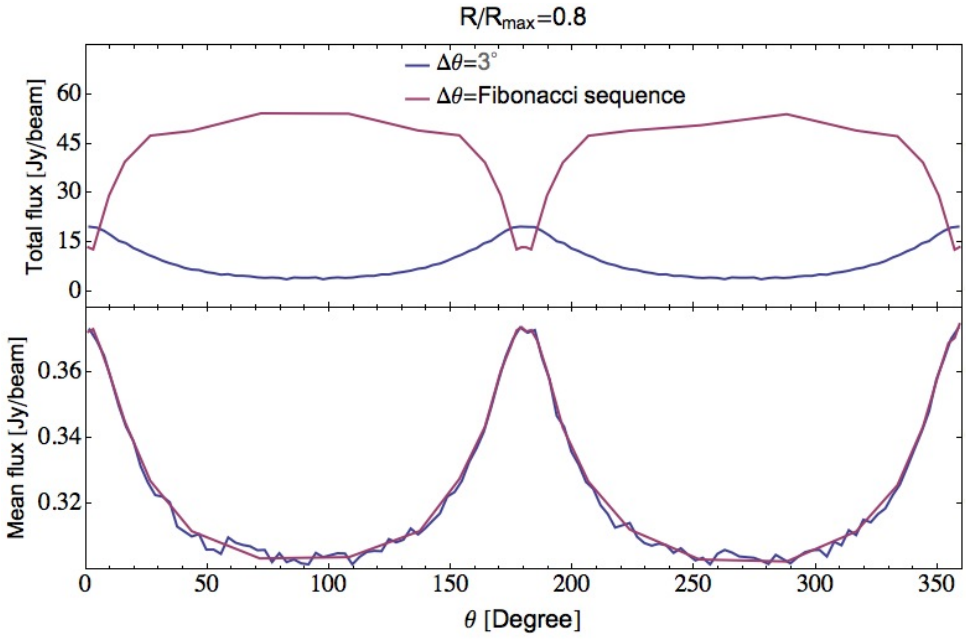


(b)

Figura 5.4: Total and mean flux of the elliptical segments subtended by an elliptical angle $\Delta\theta$. The blu curves are referred to a constant $\Delta\theta = 3°$, while the purple curves to am increasing $\Delta\theta$ that follows the Fibonacci sequence. The upper and lower panels refer to projected galaxy rings of major axes respectively 0.4 and 0.8 times $R_{\max}$, i.e, approximately 8 kpc and 16 kpc. The width of the sampling ellipses have been set to 15″ for both the panels.

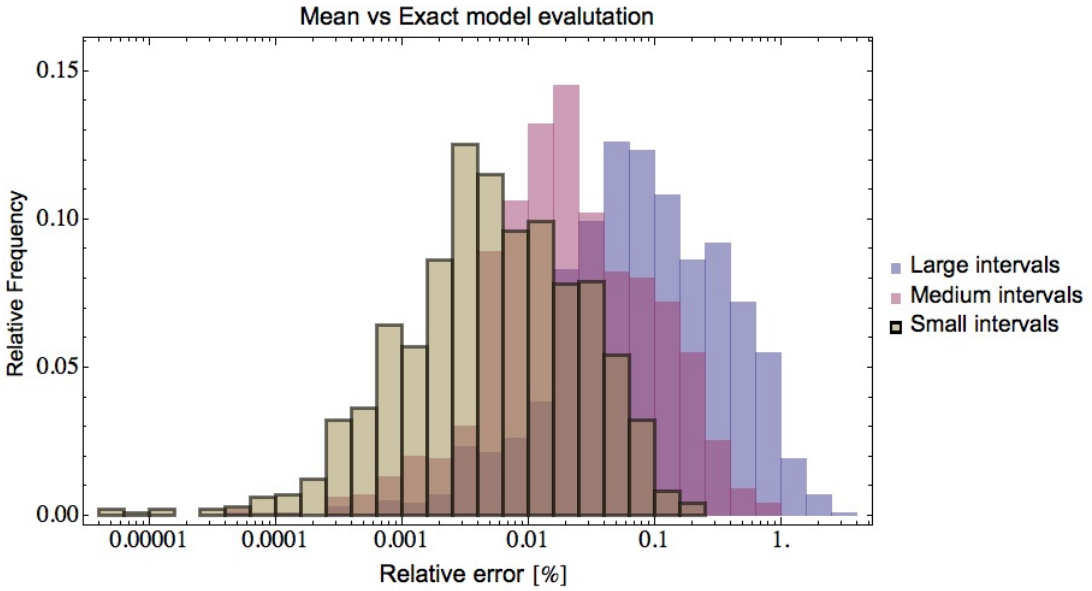


Figura 5.5: Distributions of the relative errors $\epsilon$ as defined in 5.16, i.e., the difference between the theoretical emission calculated from eq. 5.14 at $(R_m, \theta_m)$ and the mean signal calculated over an elliptical segment centered in $(R_m, \theta_m)$ through the eq. 5.15. The relative frequencies are related to 1000 value of $\epsilon$ found varying randomly the coordinates $R_m$ and $\theta_m$ and the width of the elliptical segments as explained in the text. The galactic parameters have been set as in tab. 5.1

.

continuos generalization of the mean flux over an elliptical segment using the following integral in cylindrical coordinates:

$$\overline{y}(R_m, \theta_m) = \frac{1}{A_e} \int_{R_m - \frac{\Delta R}{2}}^{R_m + \frac{\Delta R}{2}} \int_{\theta_m - \frac{\Delta \theta}{2}}^{\theta_m + \frac{\Delta \theta}{2}} \frac{R}{a(\theta, p)} f(\theta, R, p) d\theta dR \tag{5.15}$$

where the function $a(\theta, p)$ as been previously defined in eq. 5.5 and $A_e$ is the area of the elliptical segment (eq. 5.8). Substituting eq. 5.13 in $f$, we can compare the the mean value of $\Sigma_{obs}$ calculated in an interval of width $[R_m - \Delta R/2, R_m + \Delta R/2]$ subtended by an elliptical angle $[\theta_m - \Delta\theta/2, \theta_m + \Delta\theta/2]$ with the value calculated at $(R_m, \theta_m)$.

To analyze in deep this possible source of bias, we calculated the differences between the two estimates for various and randomly chosen sets of parameters as already done for the numerical integration test. First of all we define three kind of "elliptical intervals:

- Small intervals: $\Delta R$ can assume values from $15''$ (the beam size) to $65''$, $\Delta\theta$ can range from $0.5°$ to $10°$
- Medium intervals: $\Delta R$= $65''$ -$130''$ or $\Delta R$= 1 - 2 kpc, $\Delta\theta$= $10°$ - $20°$.
- Large intervals: $\Delta R$= $130''$ -$260''$ or $\Delta R$= 2 - 4 kpc, $\Delta\theta$= $20°$ - $40°$.

Using the galactic parameter of tab. 5.1, we varied randomly the $R_m$, $\theta_m$ respectively in the range 0.1-0.9 $R_{max}$ and 0°-90°, in addition $\Delta R$ and $\Delta\theta$ have been taken randomly in the range defined above. For every set of parameters we calculate the relative difference between the mean and the correct value as follows:

$$\epsilon = 100 \cdot \frac{\left|\overline{\Sigma}_{obs} - \Sigma_{obs}\right|}{\Sigma_{obs}} \tag{5.16}$$

We repeated this analysis 1000 times for each defined intervals (small, medium and large). The distributions of the resultant $\epsilon$ are shown in fig. 5.5. The yellow bars display the distribution of the small intervals: the frequencies are similar between $\epsilon \approx 0.001\%$ and $\epsilon \approx 0.05\%$ with a peak around $\epsilon \approx 0.005\%$ and they become practically 0 for $\epsilon > 0.5\%$.

Purple and blu histograms refer to the medium and large intervals respectively: their distributions of $\epsilon$ are shifted to larger values with respect to the yellow case. The peak of the medium intervals is located approximately at $\epsilon = 0.05\%$, one order of magnitude greater with respect to the case of the small intervals, while the blue distribution peaks approximately at 0.1 %.

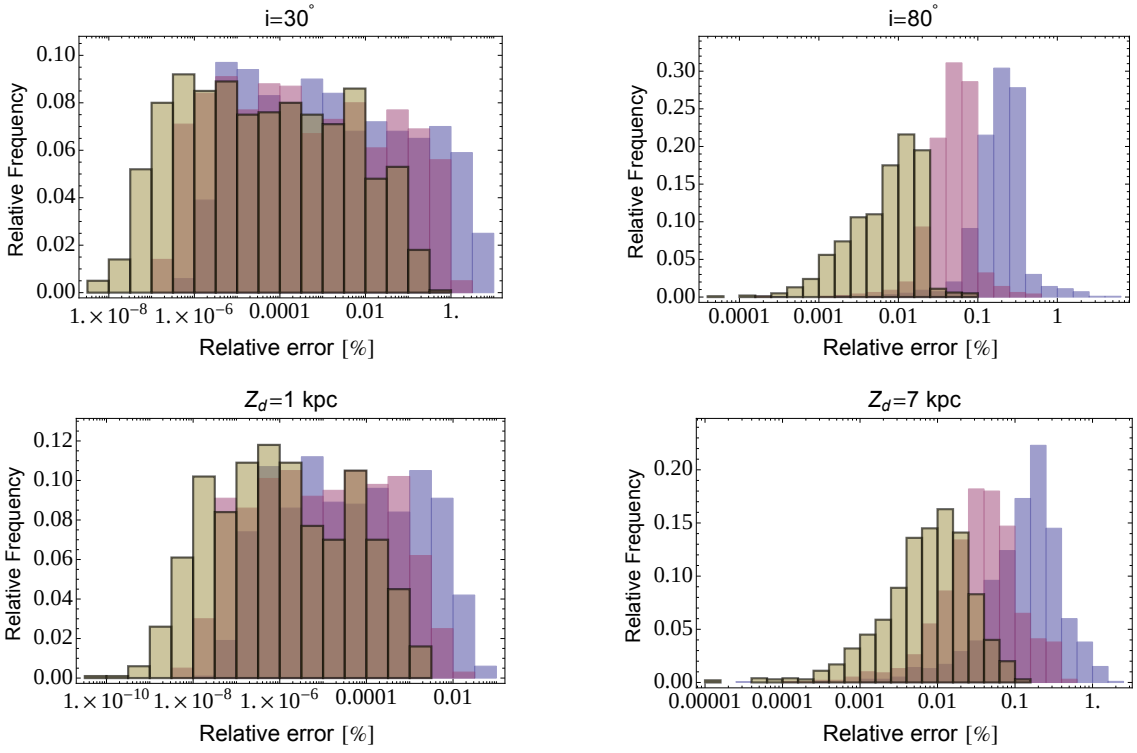


Figura 5.6: Same as fig. 5.5, but for each of the four panels we varied one galactic parameter with respect to tab. 5.1. The changed parameters and their new values are displayed on the top of the panels.

We performed again this kind of analysis varying the inclination angle (using $i = 30°$ and $i = 80°$) and the vertical scale height ($Z_d = 1$ kpc and $Z_d = 7$ kpc ) of the galactic model. The distributions of the resultant $\epsilon$ are shown in fig. 5.6, it is clear the presence of two different behaviors:

- Increasing the inclination angle and/or the vertical scale height: The distributions of $\epsilon$ are similar in shape to the one shown in fig. 5.5, but they are more peaked, especially in the case with $i = 80°$.

- Decreasing the inclination angle and/or the vertical scale height: The distributions become uniform over a wide range of values, indeed the peaks exhibited in the other cases disappear. In this cases $\epsilon$ can reach very low values such as $10^{-8}$ %.

The influence of the inclination angle and the vertical scale height can be understood considering that $\epsilon$ depends on the variation of the observed surface density over the analyzed elliptical segment. In an idealistic case where the observed surface density is constant over a certain elliptical segment the related $\epsilon$ will be equal to 0. Basically $\epsilon$ depends on the radial and the angular gradient of the observed surface density.

The most important conclusion of this analysis is that the errors produced by averaging over $\Delta\theta$ and $\Delta R$ are very small and negligible for a wide range of sampling parameters, therefore we can compare the mean estimation of *Ellint* with the theoretical value calculated in the centre of the elliptical sampling intervals.

The above is true for the artificial galaxies where the only source of noise is due do the discretization of the gas in clouds. In a real galaxy there are many local oscillations of the surface density, such as overdensities due to spiral arms or clumped star forming region or lack of the flux due to hole in the HI disk. Therefore, the use of a sampling scale lower or on the order of this local structure can heavily influence the final evaluation of the azimuthal profiles. In this case, it can be useful to increase the sampling interval or to perform a binning of the data. We stress that the conclusion of this analysis are referred to the galactic toy-model studied in this section. However, the exaggerated value of the scale height used for this simulated galaxy causes a radial and angular behavior of the observed surface density very similar to what already seen in ch. 4 for more realistic cases. Hence we are confident that we can safely extend the results of this section.

### 5.2.4 Noise on *Galmod* models

This section contain a detailed study on the error estimate. From the definition of $\chi^2$ we know that for N independent, normally distributed variables, each with mean $\mu_i$ and variance $\sigma_i$ the new variable $\chi^2 = \sum_{i=1}^{N} \frac{(X_i-\mu_i)^2}{\sigma_i^2}$ follows a chi-square distribution with $\nu = N - 1$ degree of freedom. From the shape of $\chi^2$ function we can conclude that the model is a good description of the data if the reduced chi-square $\frac{\chi^2}{\nu} \approx 1$. If in the observational data the noise is normally distributed, the $\chi^2$ value is a good way to have an estimate of the goodness of the fit, but this is not true for a simulated map. As explained in sec. 5.1.1 the artificial galaxies are filled through a Monte Carlo method. Despite trying to restore the input density distributions, the signal is

stored in discrete clouds and discretization noise will always arise in the final simulated map. Unlike the real observational noise, this one correlates with the intensity (because it depends on the number of discrete clouds) and is an artifact of the simulation procedure.

There is a further source of uncertain (in both real and simulated data) caused by the ring sampling. In the extreme situation with no noise, no beam convolution and with data distributed exactly as the theoretical model, the final *Ellint* output would still have a non zero value of rms. This because we are mediating over a non constant function in a elliptical interval of width $\Delta\theta$ and $\Delta R$. The mean flux and the rms outputed by *Ellint* are calculated as follows:

$$\overline{y} = \frac{\sum_i^N y_i}{N} \tag{5.17a}$$

$$\sigma = \sqrt{\frac{\sum_i^N (y_i - \overline{y})^2}{N}} \tag{5.17b}$$

As seen, the mean value of the signal over an elliptical segment can be estimated from the theoretical model through a continuos generalization of $\overline{y}$ (eq. 5.15). In analogy we can also generalize the discrete evaluation of the rms $\sigma$. Following the same argument that allowed us to write the eq. 5.15, we can estimate the rms of the theoretical model over an elliptical segment with the following equation:

$$\sigma_y(R_m, \theta_m) = \left( \frac{1}{A_e} \left( \int_{R_m - \frac{\Delta R}{2}}^{R_m + \frac{\Delta R}{2}} \int_{\theta_m - \frac{\Delta\theta}{2}}^{\theta_m + \frac{\Delta\theta}{2}} \frac{R}{a(\theta, p)} f(\theta, R, p)^2 d\theta - \overline{y}^2 A_e \right) \right)^{\frac{1}{2}} \tag{5.18}$$

So if we have enough pixels in an elliptical segment, we can estimate this error from our model, bearing in mind that, in the case of under sampled segments with a small number of pixels, the real rms may be very different. In conclusion the rms has its own intrinsic azimuthal radial and azimuthal profile caused by the shape of the model function $f$ and the width of the elliptical segments. Clearly this is an approximation of the real situation, but it is important to estimate the theoretical rms of the model and check whether it is comparable in intensity and azimuthal profile with the rms of the data.

We calculated the theoretical rms using the function 5.14 as integrand function of eq. 5.18 and we compared it to the rms of the galactic model calculated by *Ellint* on the simulated galaxy (eq. 5.17b). The sampling parameters are ellipse width $\Delta R$ 15″ and elliptical angle $\Delta\theta = 3°$. The angular comparison for four different radii are shown in fig. 5.7: we can see that this systematic "theoretical rms component becomes quite important for outer radii and until at the edge of the galaxy this is the dominant source of dispersion (last panel). In general the real noise is overestimated by this effect and this can significantly influence the $\chi^2$ analysis. Indeed, the discretization noise of *Galmod* should be proportional to the emission, hence we expected that the rms would decrease as a function of the radius. Instead, the rms calculated with *Ellint*

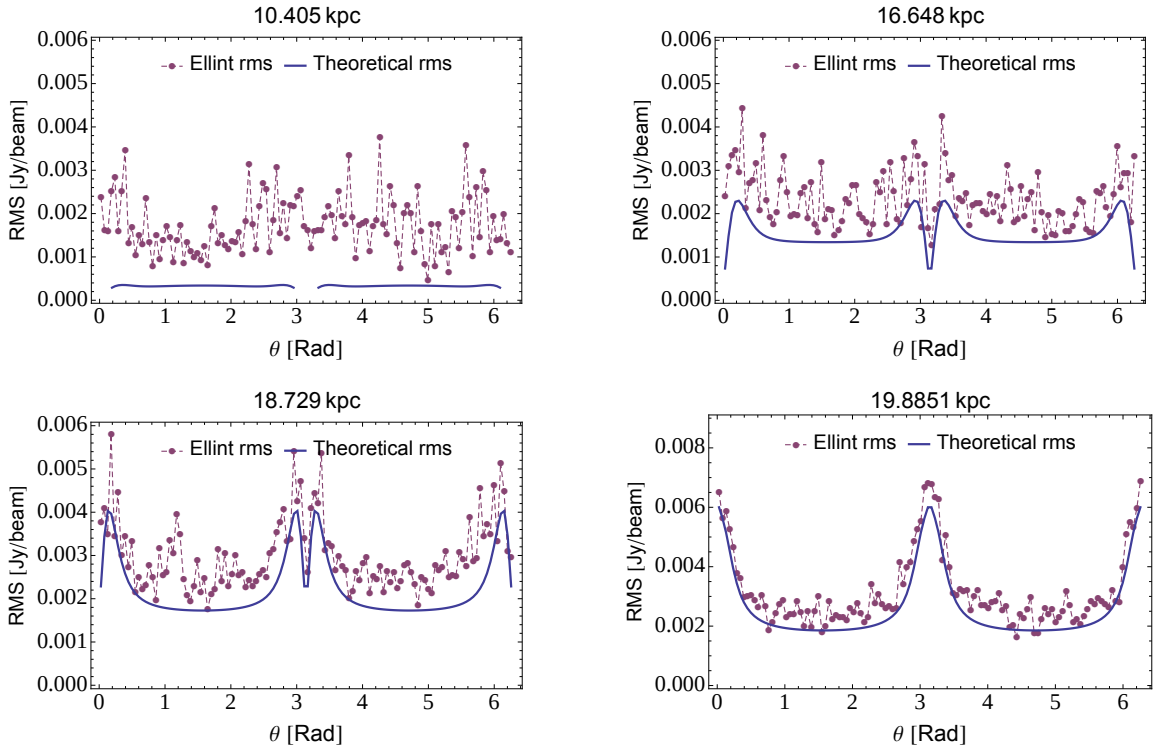


Figura 5.7: Comparison between the rms calculated by *Ellint* and that evaluated for the theoretical model (eq. 5.18) as a function of the azimuthal angle for four different radii (they are shown at the top of the panels). The sampling parameters used in *Ellint* are $\Delta R = 15''$ and $\Delta\theta = 3°$.

appears to increase at large radii as it is clear comparing the first and the third panel of fig. 5.7. This is the clear effect of the systematic rms profile expressed by eq. 5.18. Indeed, it increases as a function of the radius because of the model functions have steep radial and azimuthal gradients at large radii. We conclude that, with simulated galaxies, we must be careful to use the segment rms as the error of the measurements. In sec. 5.2.3 we have shown that the differences between the true model values and the values calculated averaging on sampling segments are negligible; therefore the theoretical rms here reported does not give a true evaluation of the uncertain of the measurements. For this reason, in the following we choose to evaluate a goodness of the theoretical models using as weight for the data simply their squared value, to take in account only the discretization noise introduced by *Galmod* .

Finally, we note that independently of the source of error, the data taken with *Ellint* are also correlated due to the instrumental beam, hence the assumption of independent and normally distributed variables is hardly fulfilled. The theoretical distribution of the variable $\chi^2$ is not known, hence its value can not be interpreted in a statistical way. Nevertheless $\chi^2$ is a measure of the differences between a model and the data and as such we can use it to compare different models and we can try to minimize it in a fitting procedure to find the best set of parameters for a given model.

### 5.2.5 Comparison with the theoretical model

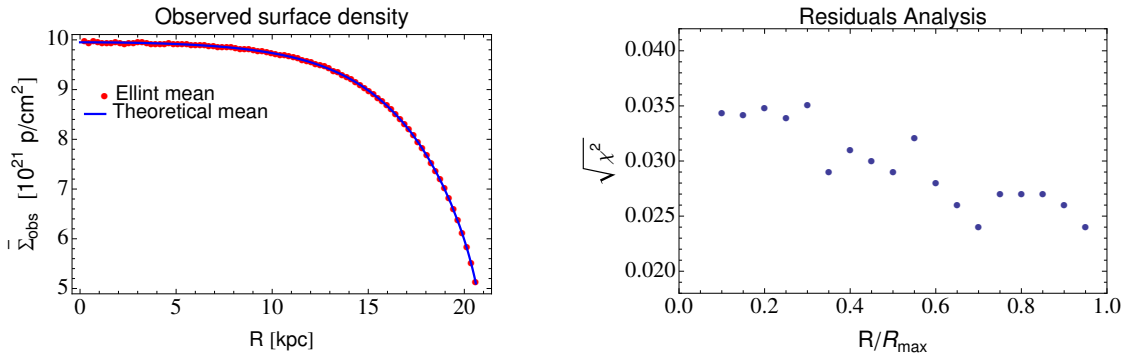


Figura 5.8: Left panel: Comparison between the mean radial surface density calculated from the total map using *Ellint* and the one calculated theoretically from eq. 5.15. Right panel: value of $\chi^2$ (eq. 5.19) calculated for the azimuthal profiles with a radial step of 0.05 $R_{\max}$.

In the following pages we will compare the observed surface density of the simulated galaxy with the expectation of the theoretical model (ch. 4). We consider the artificial galaxy built with the parameters described in tab. 5.1.

First of all, we obtained the radial distribution of the surface density by running *Ellint* with $\Delta\theta = 360°$ and $\Delta R = 15''$ for elliptical rings sampled every $15''$. Basically, we averaged the signal along every projected galactic rings of radius Nx15″, where N is an integer that goes from 1 to 90. The resultant profile is shown with red points in the left panel of fig. 5.8. As already shown by the total map in fig. 5.3, the observed surface density monotonically decreases as function of radius, while not considering the "border effect we will expect a constant surface density of $\Sigma_{\rm int}/\cos(i)$=$10^{22}$ p/cm$^2$. In oder to compare the data with the theoretical predictions, we used eq. 5.15 with $\Delta R = 15''$ and $\Delta\theta = 360°$. The resultant profile is displayed in fig. 5.8 by the blue line. It is evident that the observed the theoretical surface density match perfectly. Therefore, the radial behavior of the observed surface density is totally explained by the presence of the finite border on the galactic model.

We obtained again the mean radial profile of the observed and theoretical surface density by increasing the value of $\Delta R$ both in *Ellint* and in eq. 5.15. The differences with respect to the simulated data start to be significant only when $\Delta R$ becomes very large, i.e, greater than approximately 4 kpc. This confirms that this analysis is independent of the sampling parameter as already argued in the previous pages.

Subsequently, we extracted the azimuthal profile of the simulated emission. We sampled the galaxy through elliptical rings with major axis that increases from 0.05 to 0.95 $R_{\max}$ with step of 0.05 $R_{\max}$. The widths used for the related elliptical segments of *Ellint* have been set to $\Delta R = 15''$ and $\Delta\theta = 3°$. Finally, we compared the data extracted in this way with the

theoretical prediction of eq. 5.14 through the variable $\chi^2$, defined as follows:

$$\chi^2 = \sum_i \left( \frac{\mathrm{Data}_i - \mathrm{Theory}_i}{\sqrt{\mathrm{Data}_i}} \right)^2 \tag{5.19}$$

We stress that the data are the mean of the simulated emission calculated over elliptical segments of center ($R_m$,$\theta_m$) while the theory is referred exactly at the point of coordinates ($R_m$,$\theta_m$). However, we already saw that this do not cause appreciable effect on the comparison between theory and data (see sec. 5.2.3).

The value of $\sqrt{\chi^2}$ for each sampled ring is shown in the right panel of fig. 5.8, while a sample of azimuthal comparisons between the theoretical model and the simulated data are shown in fig. 5.9 and 5.10. We can not assign a precise statistical meaning to the value of $\chi^2$ (see sec. 5.2.4 for further details), but we note that all the values are very similar as they are constrained included between the narrow interval 0.24-0.35. There seems to be a tendency of $\sqrt{\chi^2}$ to decrease at large radii, this behavior can be understood by looking at figs. 5.9 and 5.10. At very small radii, the simulated data are dominated by the scatter while a more regular pattern emerges at large radii. This is due to the combination of two factors: first the discretization noise is larger where the signal is higher, since it is proportional to the square root of it, secondly the magnitude of the oscillation due to the "border effect becomes progressively more important for increasing radii. These two effects cause, at small radii, the local oscillations to become dominant with respect to the trend expected by the theoretical model.

We performed the same analysis varying the width of the angular intervals $\Delta\theta$ and the width of the rings $\Delta R$ in a reasonable range ($1^\circ < \Delta\theta < 10^\circ$ and pixel size $< \Delta R < 2$ Beam size). We obtained the same results as in the case with $\Delta R = 15''$ and $\Delta\theta = 3^\circ$, again confirming that our analysis is independent of the sampling used in the data extraction.

We conclude that out theoretical model, taking into account the "border effect gives a good description of the simulated galaxy.

As a final check we performed a further test on *Galmod* : we simulated a new galaxy model with the parameters shown in tab. 5.1 but we considerably decreased the number of clouds and subclouds. Indeed, the parameters CDENS and NV have been reduced respectively from 10 to 0.1 and from 400 to 10. In this way the discretization noise is expected to increase significantly.

The resultant azimuthal profiles of the simulated emission for four representative elliptical rings are shown in fig. 5.11 overplotted with the theoretical model. As expected the data noise has become very large, as we can clearly seen comparing fig. 5.11 with fig. 5.9 and 5.10. The noise is so large that even at very large radii ($R \approx 17$ - 20 kpc), it causes variations of the same order of the oscillations due to the border effect.

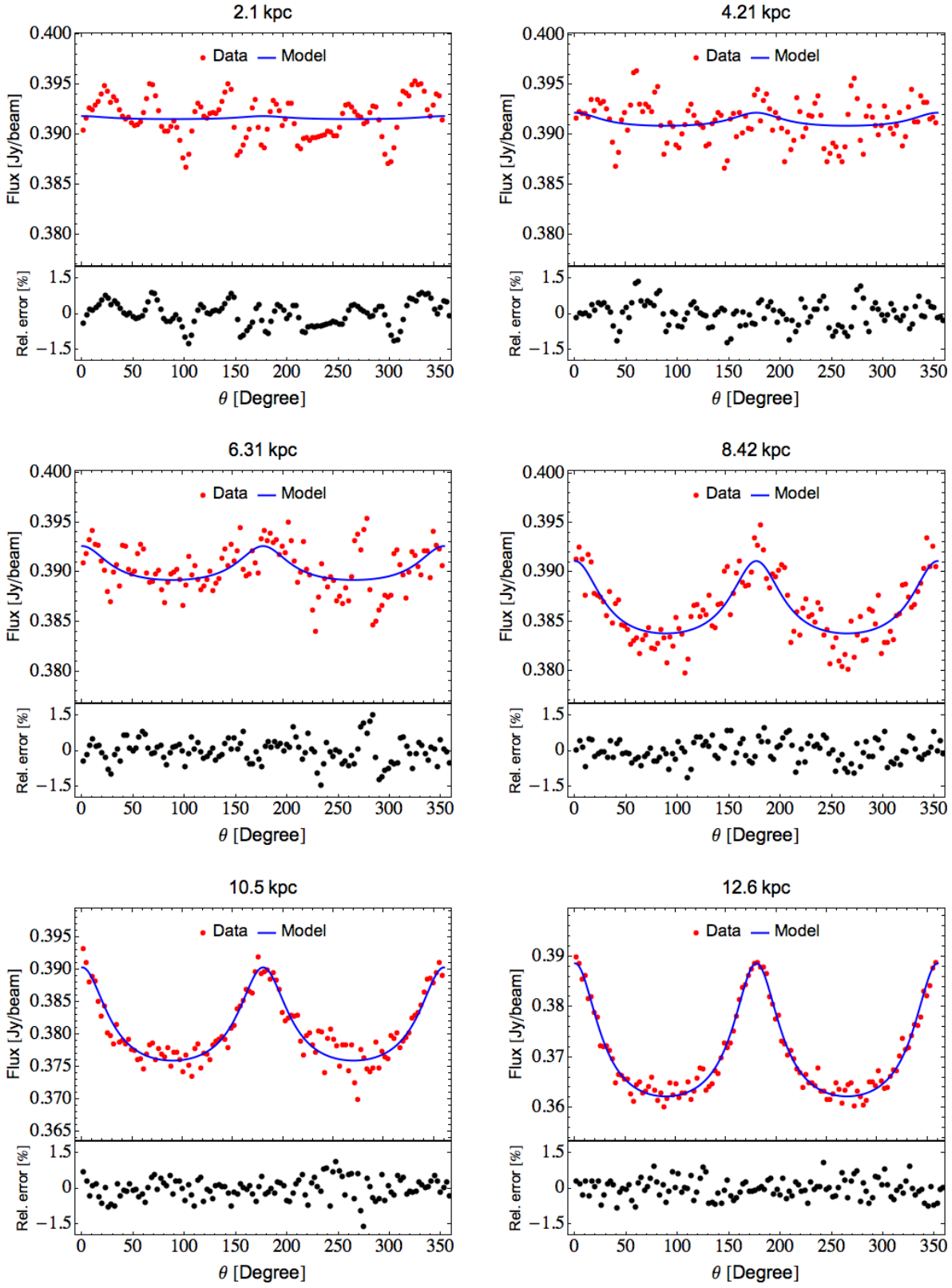


Figura 5.9: The red points represent the azimuthal profiles of emission calculated by *Ellint* (5.1.2) from the total map of fig. 5.3 every ∼2 kpc in radiu (see value above the panels). The blue curves are the theoretical predictions calculated with eq. 5.14. The black points in the small plots below the main panels show the relative difference in percentange between the red points and the blue curves.

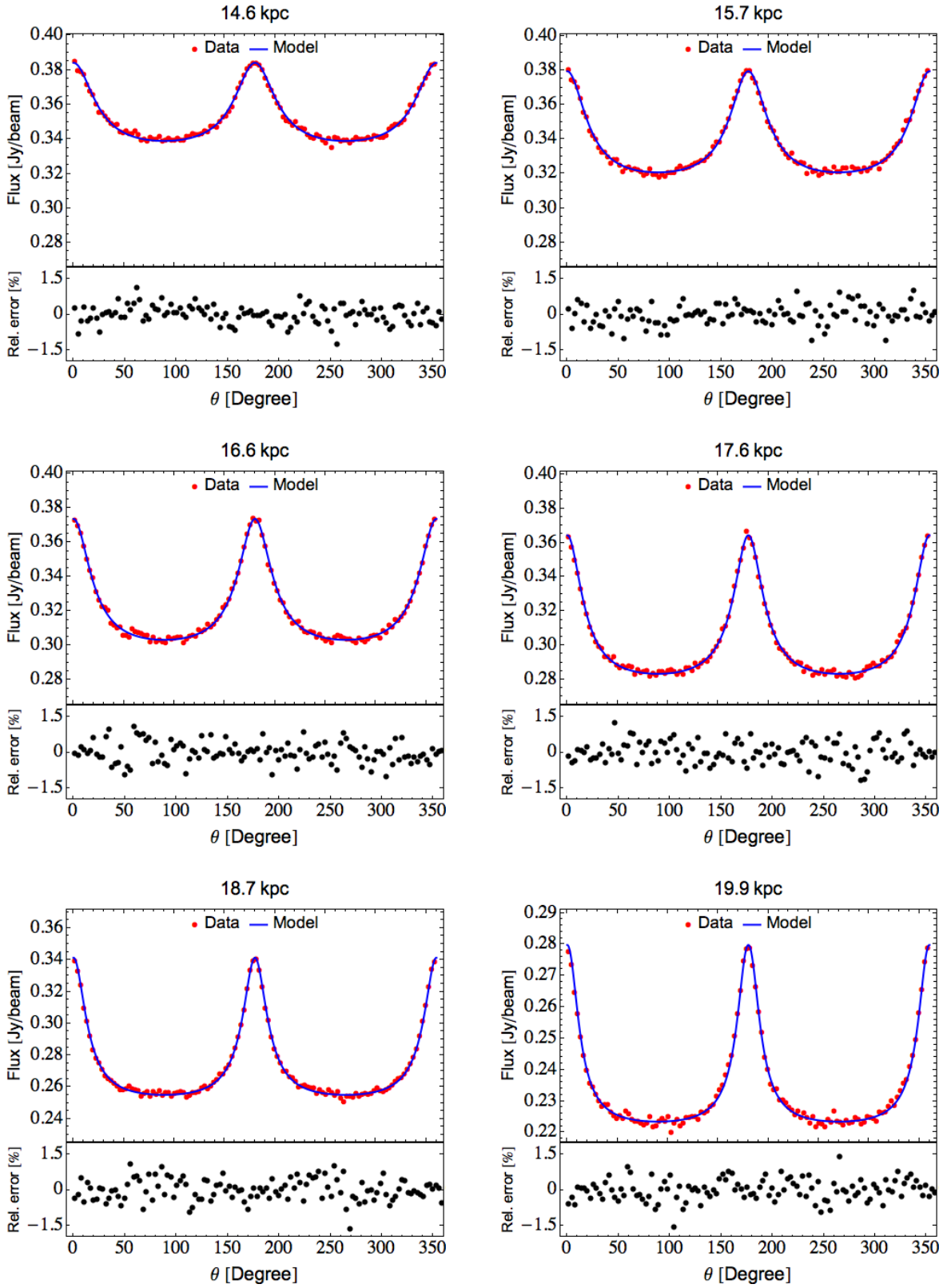


Figura 5.10: Same as fig. 5.9.

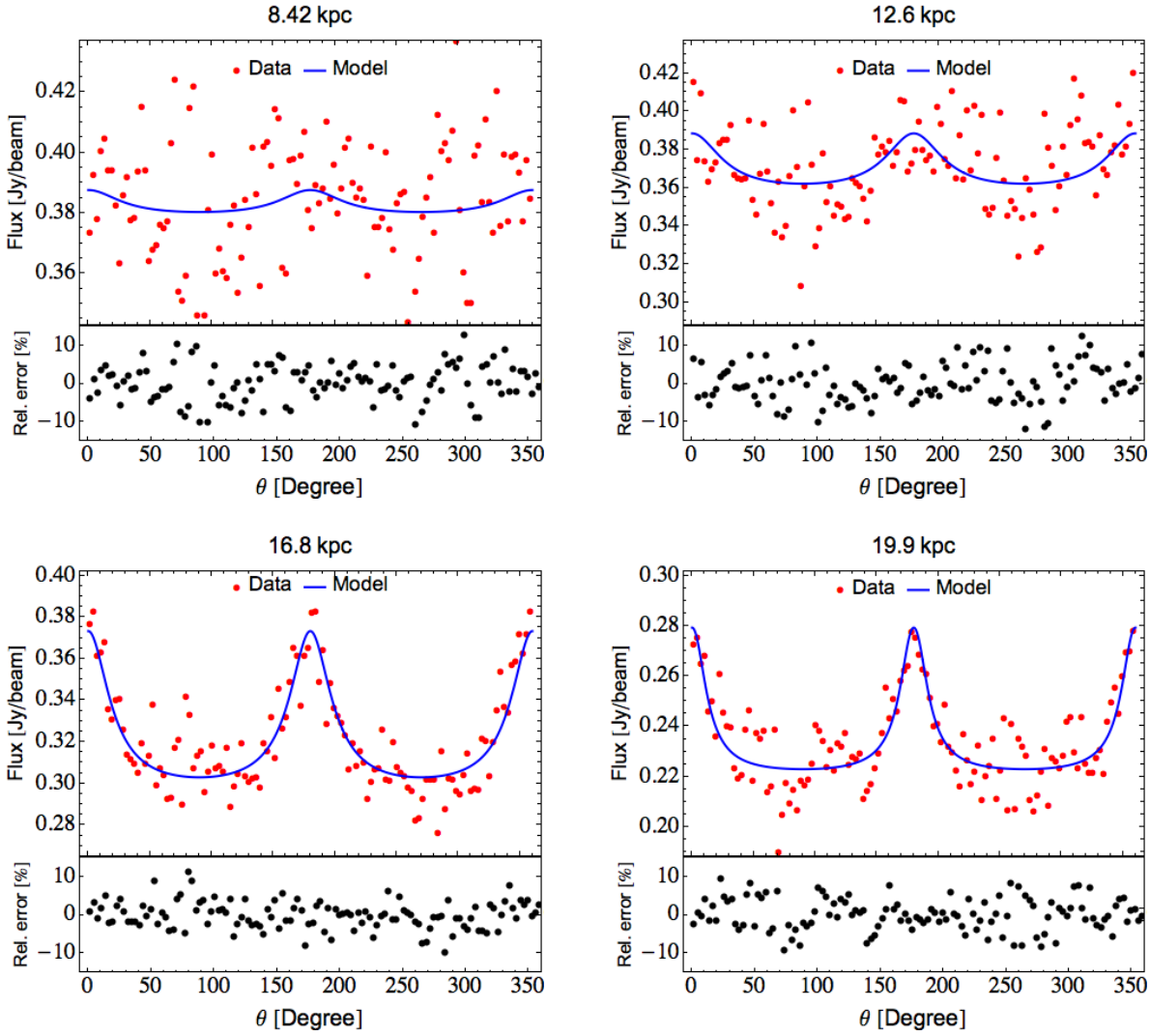


Figura 5.11: Same as fig. 5.9, but in these panels the red points come from a galaxy simulated with fewer clouds with respect of fig. 5.9 (see text for further details).

| Galaxy parameters | |
|---|---|
| Radial density distribution | see fig. 5.12 |
| Vertical density distribution | Gaussian |
| Vertical scale height (kpc) | 0 flaring to about 3.6 (fig. 5.12) |
| $R_{\max}$ (kpc) | 26.13 |
| Rotation velocity (km/s) | from 0 to about 130 |
| Systemic velocity (km/s) | 130 |
| Velocity dispersion (km/s) | from 17 to about 8 |
| Inclination angle | 60° |
| Position angle | 90° |

Tabella 5.2: Galactic parameters used as input in *Galmod* to build the artificial galaxy we analyze in this section. The parameters of the data cube are the same of tab. 5.1.

## 5.3 Realistic gas distribution

In this section we describe a galactic model with a realistic distribution of the surface density of the gas. In order to magnify the effect of the thickness on the observed surface density we used an extended disk ($R_{\max}$=26.1 kpc) and a gaussian vertical profile for the gas that exhibits a prominent flare: the vertical scale height rises from 0 kpc at the center to approximately 3.6 kpc at the edge of the disk.

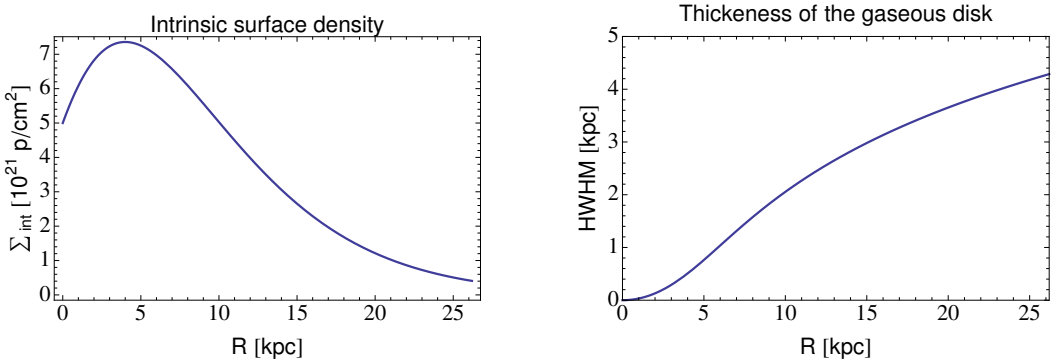


Figura 5.12: Radial trend of the intrinsic surface density (left panel) and of thickness of the gaseous disk (right panel) used as input in *Galmod* .

We modeled the intrinsic surface density with the eq. 4.26:

$$\Sigma_{\rm int}(R) = \Sigma_0 \left(1 + \frac{R}{R_d}\right)^2 \mathrm{Exp}\left(-\frac{R}{R_d}\right)$$

The parameters have been set as $\Sigma_0 = 5 \cdot 10^{21}$ p/cm$^2$, $R_d = 4$ kpc and $\alpha = 2$. The resultant radial distribution is shown in the left panel of fig. 5.12. The radial trend of the vertical scale height follows the functional form of eq. 3.41:

$$H(R) = H_0 + C \cdot \text{arcsinh}\left(\frac{R^2}{R_f^2}\right)$$

with $H_0 = 0$ kpc, $c = 1$ kpc and $R_f = 6$ kpc. The resultant radial trend of the thickness is shown, in terms of half width half maximum (see App. B), in the right panel of fig. 5.12. Unlike

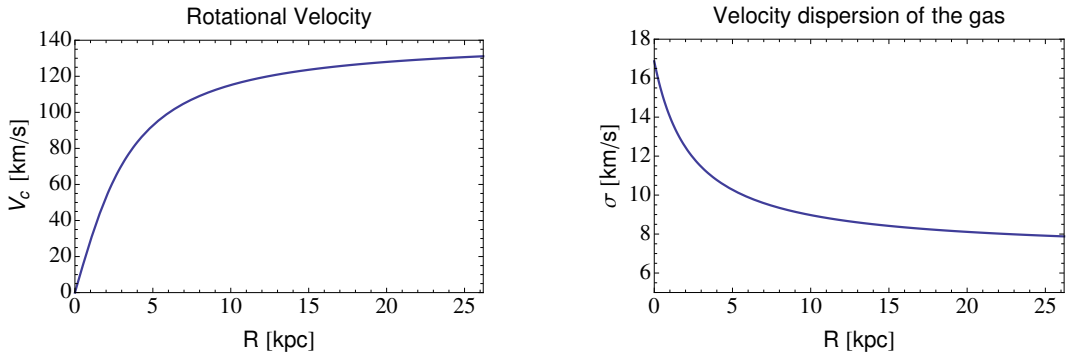


Figura 5.13: Circular rotation curve (left panel) and velocity dispersion of the gas (right panel) used as input in *Galmod* .

for the previous galactic model (sec. 5.2), this time we aim to study the influence of the thickness on observed kinematical parameters (sec. 5.3.5). For this purpose we set a plausible input in *Galmod* for the rotation curve and for the velocity dispersion of the gas. For the rotation curve we used the following functional form:

$$V_c(R) = 90 \tan\left(\frac{R}{R_c}\right) \text{[km/s]} \tag{5.20}$$

where $R_c$ has been set to 3 kpc, in this way the resultant rotation curve rises from 0 to approximately 130 km/s as shown in the left panel of fig. 5.13. We note that the rise of $V_c$ is very slow, in this way we minimize the effect of beam smearing on the analysis of the kinematics of the galaxy (sec. 5.3.5).

The velocity dispersion follows an hyperbolic radial trend as already shown in sec. 3.3, in particular we used the following functional form:

$$\sigma(R) = 7.04 + \frac{24.07}{R + 2.45}$$

As we can see in the right panel of fig. 5.13 the velocity dispersion has a inner cusp that reaches approximately 17 km/s in the centre, beyond $R = 6 - 7$ kpc the radial decline is very slow and $\sigma$ remains nearly constant at a value of 8 km/s. A summary of the properties of this galactic model are shown in tab. 5.2.

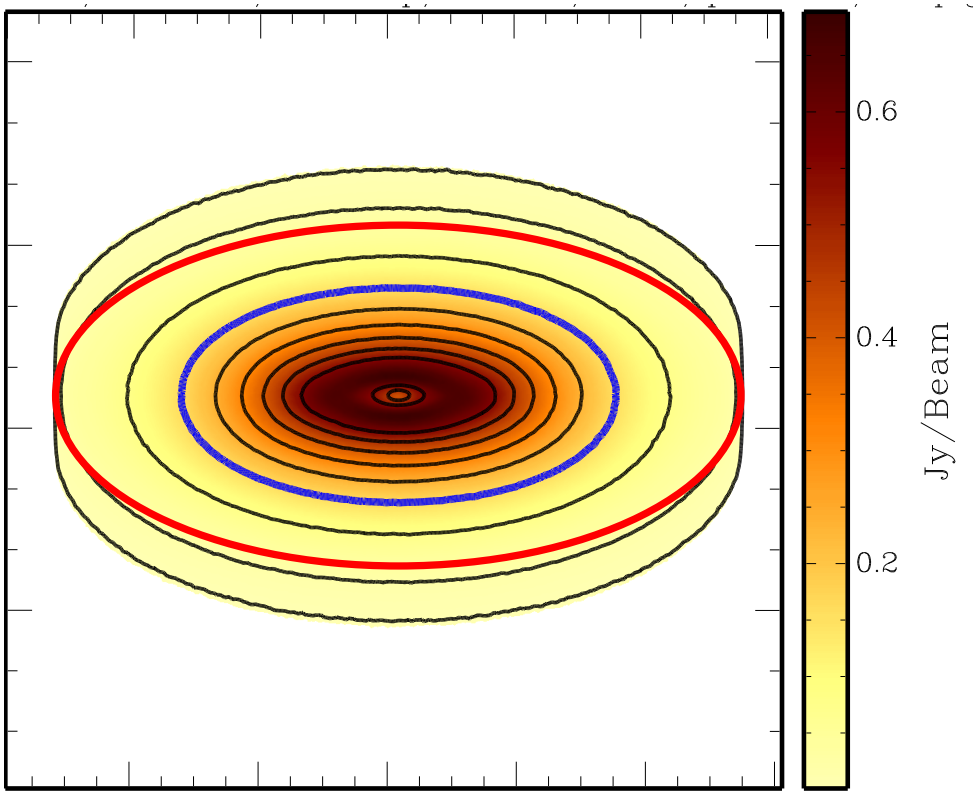


Figura 5.14: Total HI map of the artificial galaxy made with *Galmod* with the parameters shown in tab. 5.2. The color scale represents the brightness in units of Jy/Beam, the isodensity contours mark the projected surface density of 14, 12, 1, 0.8, 0.6, 0.4, 0.2, 0.05, 0.01 $10^{22}$ p/cm$^2$. The blue contour at 0.4 $10^{22}$ p/cm$^2$ represents the projection of the galactic ring with $R \approx 16$ kpc onto the sky plane. While, the red ellipse shows the border of the galaxy, i.e., the galaxy ring with $R = R_{\max}$. In order to have a cleaner plot, we blanked all the signal below the threshold of 3 mJy/Beam.

We note that the galactic model simulated in this section is not dynamically self consistent, for instance the vertical scale height does not have any link with the velocity dispersion and with the mass components that produce the assumed circular velocity. Moreover, the rotation curve (eq. 5.20) is only a useful parameterization not based on any of the classical functional forms found for the DM halo (see sec. 3.1.3 and 3.1.4). Essentially, the aim of this section is to study the influence of the thickness on the observational properties of galaxies.

Once *Galmod* built the cube with the simulated galaxy, we convolved the channel maps simulating an observational beam of 15″x15″ (see sec. 5.1.1). Finally, using the task *Sum*, we made the total map shown in fig. 5.14.

Using the relation of eq. 1.17, we note that with the used beam, $10^{21}$ p/cm$^2$ column density of the gas will produce an observed brightness of about 0.0395 Jy/Beam. Therefore, we expect that the projected central brightness of our simulate observation ($10^{22}$ p/cm$^2$) will be about 0.39 mJy/Beam. However, this is true only in the case of a thin disk where $\Sigma_{\rm obs} = \Sigma_{\rm int}/\cos(i)$, for a thick disk the central value can be estimated with the eq. 4.19 using the density distribution

described above. In this case the central density results equal to about 0.43 Jy/beam, as confirmed by the total map.

The emission on the total map exhibits a rapid variation out to $R \approx 16$ kpc (where the blue contour is located), beyond this radius the decline is more gentle. The blue ellipse represents both the isodensity contour for $\Sigma_{\rm obs} \approx 4 \cdot 10^{21}$ p/cm$^2$ and the projection onto the skyplane of the galactic ring of radius $R \approx 16.4$ kpc. Instead, the red ellipse is the projection on the skyplane of the border of the galaxy ($R = R_{\rm max}$), but not at constant emission. In the case of a thin disk the red curve would be also the border of the observed galaxy, instead it is clear that there is extra emission beyond it. In fig. 5.14 we blanked all the emission below the threshold of 3 mJy/Beam to obtain a clearer plot, therefore the extra emission is even more extended.

### 5.3.1 Estimate of the inclination angle

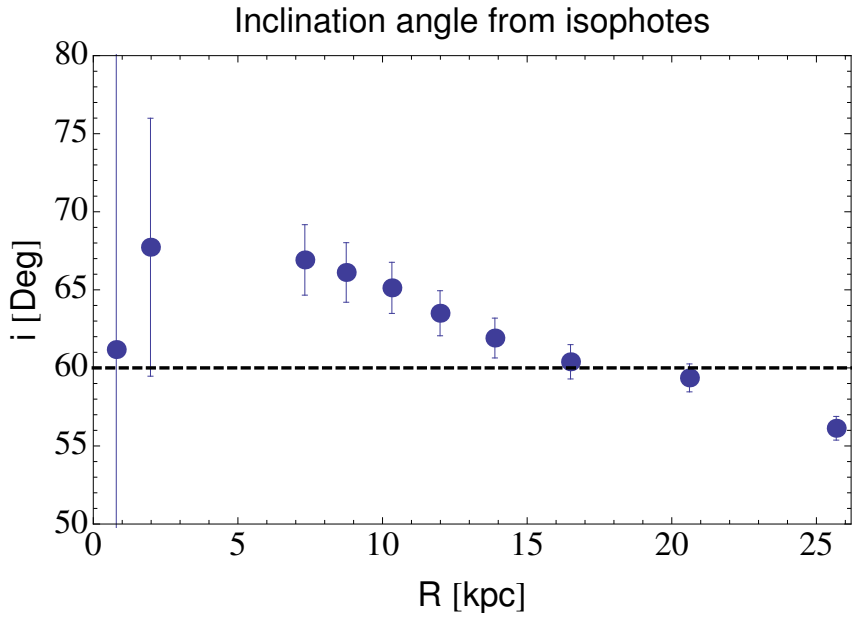


Figura 5.15: The blue dots represent the inclination angle calculated by the ratio of the axes of the isodensity contours shown in total map (fig. 5.14). The input value of the inclination is shown for comparison by the dashed line.

The colored ellipses in fig. 5.14 have the right ellipticity, i.e., the ratio of their axes is equal to $\cos(i)$, where $i = 60°$ (tab. 5.2). At small radii the isophotes are flatter with respect to the blue ellipse, while beyond $R \approx 16$ kpc they appears more face-on, i.e, with a lower ratio of their axes. To better analyze this effect, we estimate the inclination angle of the galaxy from the axes ratio of these isophotes. We used the task *Sliceview*, which is the standard data viewer of GIPSY, that also allows to overlap elliptical rings to the data. We tuned the axes of the elliptical rings trying to overlap the shape of the isophotes. Subsequent corrections are made paing attention that the emission remains nearly constant over the ellipses. Once the ellipses

have been set, we calculate the inclination angle as:

$$i = \arccos\left(\frac{b}{a}\right)$$

where a and b are respectively the value of the major and minor axis. We repeated this procedure for each isodensity contour shown in fig. 5.14, except for the last one because its shape is hardly reproducible with an ellipse. We noted that the analyzed isophotes have some deformation that disturbs their shapes, but it never exceeds 4 pixels or $16''$ from the used ellipse, i.e, roughly the value of beam. We used this value as a conservative estimate of the uncertain of the measurements. The final error on the estimation of the inclination angle comes from the error propagation errors. The results are shown in fig. 5.15.

Despite the large errors of the first two points and the lack of data between 2 and 6 kpc fig. 5.15 confirms what qualitatively asserted from the analysis of fig. 5.14: from about 7 kpc the ellipticity of the isophotes and hence the related inclination angle exhibits a monotonically decreases from about $i = 68°$ to about $i = 56°$, the right inclination angle is reached at $R \approx 16$ kpc, blue contour of fig. 5.14. Therefore from this kind of photometric analysis one would derive a highly warped disk, despite the fact that the input model had a constant intrinsic inclination angle.

### 5.3.2 Azimuthal profiles

A deeper analysis of fig. 5.15 shows us that the general behavior of the estimated $i$ is similar to the radial profile of the intrinsic surface density (left panel of fig. 5.12). Indeed, it increases at small radii and it exhibits a monotonically decrease beyond about 5 kpc. This is not a chance, as exhaustively described in chapter 4. In particular, one can note that the vertical scale height and also the surface density used for this galactic model (fig. 5.12) is very similar to the "extreme flaring model described in sec. 4.3.1 and shown in fig. 4.6. Remembering the analysis done for this theoretical model (in particular see the $\gamma$ parameter in fig. 4.9) we can divide the azimuthal profiles of the emission in three zones. In the following we will link this division with the behavior of the inclination angle estimated with the isophotes:

- Small Radii: from 0 to about the radius of the peak of the surface density ($R \approx 5$ kpc). The emission along the projected galactic rings exhibits a maximum in the minor axis and a minimum on the major axis (see fig. 5.18). We call the flux on the major axis of a general elliptical ring in this regions as $F$. Now consider the isophote at the level $F$. The elliptical ring and the isophote will have the same major axis $R$, but because of the oscillation of the flux due to the thickness they will have different minor axis, and therefore different ellipticity. For $\theta \neq 0 \pm n\pi$, the isophote needs to intercepts regions of the galaxy with respect to the elliptical ring with the corrected inclination. From the left panel of

fig. 5.16 we note that in these regions the emission is a rising function of the radius, hence the minor axis of the isophote will be lower with respect to the minor axis of the elliptical ring. Therefore, this produces an estimated inclination angle greater than the correct one.

- Intermediate radii: In this region, between the peak of the surface density and about 4 - 5 $R_d$ (16-20 kpc for this model), the elliptical rings exhibits a peak on the major axis and a minimum on the minor axis (fig. 5.19). Hence, in contrast with what happens at small radii, the isodensity contours intercept galaxy rings with higher emission with respect to the elliptical rings with the same major axis. But in these regions the surface density is a decreasing function of the radius. The combination of these two effects, both opposite to the situation at small radii, produces again isodensity contours with higher axes ratio with respect of the one of the elliptical rings, and the estimated inclination angle will be again higher than the true one. The magnitude of the angular oscillation decreases and accordingly the estimated values of the inclination angles become progressively lower. Between 15-20 kpc, the azimuthal profiles exhibit a transition phase due to a new switch of the peak, the resultant profiles will result nearly constant and the elliptical rings and isophotes will be very similar. Indeed, the two estimations taken in this region are very close to 60°.

- Large radii: Beyond about 20 kpc, the angular emission exhibits again a peak on the minor axis (see fig. 5.19), as at small radii, but in this case the radial trend of the surface density is slowly decreasing. Therefore the estimated inclination angle from the isophote will be lower that 60°. Beyond $R = R_{\max}$ the emission in only due to the projection of the vertical thickness, hence it is nearly constant around the minor axis and practically 0 around the major axis. The resultant profiles will exhibit an exaggerated boxy shape, see the last contours shown in fig. 5.14.

### 5.3.3 The fitting method

In this section we describe how to constrain the parameters of our theoretical model to find the set that gives the best agreement with the simulated data. Basically, we want to minimize the differences between model and data. The most used function for this purpose is the following:

$$\chi^2 = \sum_i (y_i(\vec{x}) - f(\vec{x}, p))^2 w_i(\vec{x}) \tag{5.21}$$

where $y_i$ and $w_i$ are respectively the value of the data and their weight (often the inverse of the data error) at the point of coordinate $\vec{x}$, while $f$ is the expected value of the theoretical model and p is a vector that contains all the parameters of this function. The value of p that minimizes eq. 5.21 is found though the condition:

$$\frac{\partial \chi^2}{\partial p} = 0$$

If our model were linear in $p$ we could solve the above condition in an analytic way, and the problem would be reduced to a classical least square minimization. However, it is clear that this not our case (see eq. 4.19), hence other procedures need to be used for the minimization of eq. 5.21. There are several methods to perform a non linear fit, one of the most used is the Levenberg-Marquardt (LM) method (Marquardt, 1963).

It minimizes the function $\chi^2$ with an iterative procedure: from an user defined initial guess the value of $p$ is progressively updated as $p+\delta$ until the change caused in the value of $\chi^2$ remains below a certain threshold. The theoretical value of $f$ at the new point $(\vec{x}, p+\delta)$ can be linearized as follows:

$$f(\vec{x}, p+\delta) \approx f(\vec{x}, p) + \frac{\partial f}{\partial p}\delta = f(x_i, p) + J_p(\vec{x})\delta$$

where $J_p$ is the Jacobian matrix. Hence the new value of the variable $\chi^2$ will be:

$$\chi^2 \approx \sum_i (y_i(\vec{x}) - f(\vec{x}, p) - J_p\delta)^2 \tag{5.22}$$

where the value weights have been set to 1 for simplicity.

We note that the eq. 5.22 is linear in $\delta$, hence its minimum can be find analytically setting to 0 its derivative $\partial\chi^2/\partial\delta$. This leads to the following result (Marquardt, 1963):

$$(J_p^T J_p)\delta = J_p^T(y(x) - f(x, p)) \tag{5.23}$$

This is a set of linear equations that can be solved to find the value of $\delta$. Up to this point, eq. 5.23 is in common with a large number of non linear methods. The peculiarity of the LM method is the introduction of a damping parameter $\lambda$ such that eq. 5.23 becomes:

$$(J_p^T J_p + \lambda \mathrm{diag}(J_p^T J_p))\delta = J_p^T(y(x) - f(x, p)) \tag{5.24}$$

In this section we will use the *NonLinearModelFit*, a bult-in function of *Mathematica* to perform a fit that implements the LM algorithm. The damped parameter is adaptively varied to derive with high accuracy the best set of parameters.

As most of the non linear fitting methods, the LM heavily depends on the initial guess of p. If only one minimum exists this is not a problem, but in the case of local multiminima the estimate of the initial set of p is crucial to found the true global minimum. However, from the observational estimated data we should be able to get a reasonable initial guess for the parameters.

### 5.3.4 The fitting procedure

First of all we extract the radial profile of the surface density for the total map in fig. 5.14. For this purpose we run *Ellint* from $R = 15''$ to $R = 1695''$ with step and width of the elliptical rings equal to the beam size of $15''$. The outcoming radial profile is displayed by the blue points in fig.

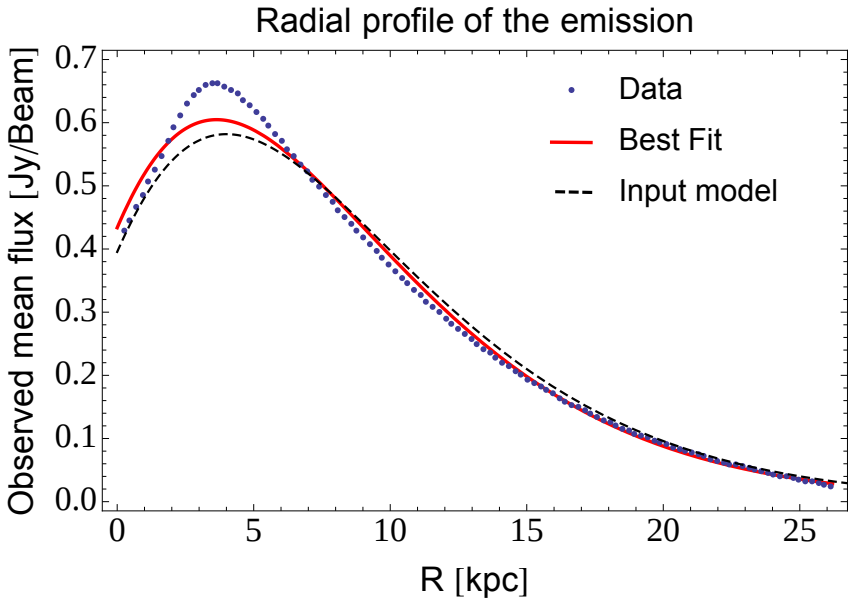


Figura 5.16: The blue points represent the radial profile of the "observed flux averaged over the elliptical angle. The Red curve is the best fit function found from the functional form of eq. 4.26. The black dashed curve shows the intrinsic radial profile used as an input in *Galmod* .

5.16. The intrinsic profile given in input is shown for comparison as a black dashed line: it this is the profile shown on the left panel of fig. 5.12 converted to Jy/beam through eq. 1.17 and multiplied with the projection factor $\cos(i)$. As already seen in ch. 4, in particular in fig. 4.10, the projected emission exhibits higher values around the peak and lower values at intermediate radii with respect of the intrinsic profile.

We fitted the data with the functional form of eq. 4.26 using as weight the inverse of the data, in this way we minimize the relative residuals. The best fit parameters are shown in tab,, 5.3 The second step is to obtain 2D data, i.e., the emission at every sampled galaxy segment

| | Best Fit | Input | $\epsilon$ |
|---|---|---|---|
| $\Sigma_0$ (Jy/Beam) | $0.433 \pm 0.008$ | 0.395 | 9.6 % |
| $\alpha$ | $1.92 \pm 0.02$ | 2 | 4 % |
| $R_d$ (kpc) | $3.95 \pm 0.03$ | 4 | 1.2 % |

Tabella 5.3: Parameter of the radial profile of the emission. $\epsilon$ represents the relative difference between the right and the best fit value of the parameters.

with center of coordinates $(R, \theta)$. We run again *Ellint* following the procedure described in sec. 5.1.2. The sampling segments have been set to a radial width of 15″ or 0.23 kpc and an angular width of 3°. We exclude the data at $R < 2$ kpc both because the discretization noise results higher than the expected oscillation of the emission and because the chosen sampling parameters produce segment that contain very few point. The resultant data have been stored in an unique

file which contains all the information needed to *Mathematica* to perform the 2D fit using the eq. 4.19, to perform the fit we further set the vertical profile to a gaussian and the vertical scale height to follow the functional form of eq. 3.41.

**The data weigth**

In this brief section we discuss what weight $w_i$ (eq. 5.21) is better to use in the fitting procedure. In presence of a true gaussian noise one can use the rms calculated by *Ellint*, but we already seen (fig. 5.7) that in artificial galaxies this can be highly contaminated by the rms due to the non constant value of the emission (eq. 5.18). On the other hand the use of a constant weight for all the data can be very dangerous. Indeed, the fitting procedure will tend to minimize the residuals mainly of data with greater emission, giving less importance to the one with lower emission. To solve this issue we can instead minimize the relative residuals using the inverse of the data as weight.

Moreover, we must pay attention to another effect due to the non uniform sampling of the data (see sec. 5.1.2). The use of a constant $\Delta\theta$ and $\Delta R$ produces sampling segments that have different areas and hence different numbers of pixels. In particular, the larger is the central radius of the segment the greater will be the area, while its azimuthal behavior is shown in fig. 5.1. Thus at large radii and near the major axis the areas of the elliptical segments are several times larger than those of segments with smaller radii and elliptical angle far from the major axis. Therefore the weight of the data should also take into account this effect: the larger is the area subtended by the segment the greater should be its statistical weight. This weight can be calculated in several ways, for example theoretically through equation 5.9, or more simply using the number of points contained in the analyzed segment, that is one of the outputs of the task *Ellint* .

We tested the fit procedure used in this section with various choices for the fitting weights and found that the best results are obtained using

$$w_i = \frac{N_i}{y_i}$$

where $N_i$ is the number of pixels contained in the analyzed segment and $y_i$ is the average value obtained for the flux in the same segment. In the rest of the section we will use this weight.

**The fit**

In the first fitting procedure, we kept the parameters of the $\Sigma_{\rm int}$ of the model fixed to what found from the radial profile of the projected emission (red curve in fig. 5.16). The value of the parameters are shown in tab. 5.3. Therefore, we only have three free parameters, i.e., $H_0$, $C$, $R_f$ of the functional form of the thickness (eq. 3.41). In order to further simplify the fit we set $H_0$ to 0, in general this is always a reasonable assumption, given that the galactic potential at

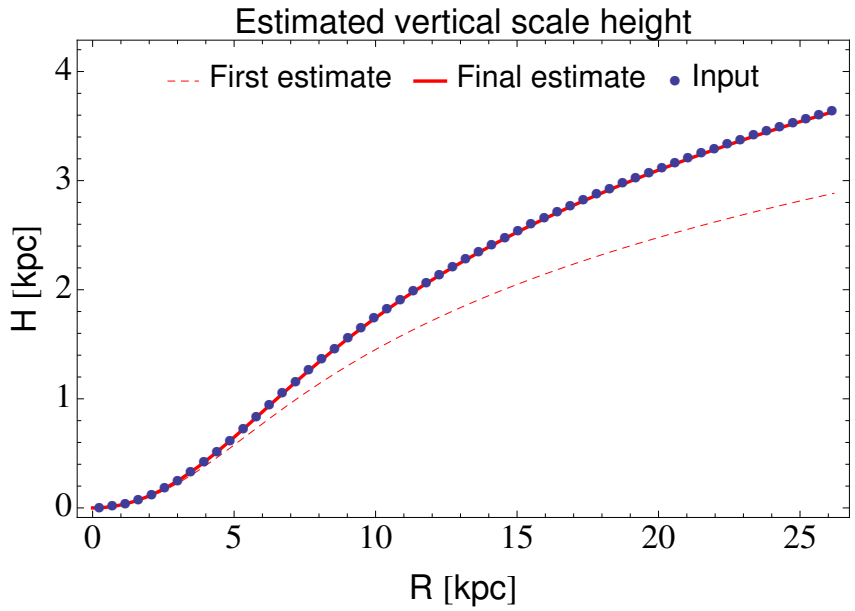


Figura 5.17: Radial trend of the scale height found by the fitting procedure compared with the true values(blue dots). The dashed curve is found keping fixed the parameters of the intrinsic surface density at the value shown in tab. 5.3. The full lines come from the fit procedure where all the parameters of eq. 4.19 have been left free.

the center is very high and it produce very low vertical scale height of the gas (see examples in sec. 3.4). Finally, we fitted the data to constrain the last two remaining parameters $c$ and $R_f$. The results are shown under the column "First Run in the table 5.4, while the resultant radial profile of the vertical scale height is shown as a dashed curve in fig. 5.17. Obviously this is not a good result. We note that the initial guesses for the fitted parameters have been set arbitrarily as $C = 1$ kpc and $R_f = 10$ kpc We tried to change these values, and accordingly the resultant best fit slightly varies, but in a coherent manner so that the radial behavior of $H$ always remains nearly equal to the one shown in fig. 5.17. At this point, we used the previously

| | Input | Best Fit- First Run | $\epsilon$ | Best Fit - Second Run | $\epsilon$ |
|---|---|---|---|---|---|
| $c$ (kpc) | 1.00 | 0.75 $\pm$ 0.01 | 24.9 % | 0.99 $\pm$ 0.01 | 1.0 % |
| $R_f$ (kpc) | 6.00 | 5.44 $\pm$ 0.03 | 9.3 % | 5.99 $\pm$ 0.01 | 0.2 % |

Tabella 5.4: Best fit parameters of the vertical scale height. $\epsilon$ is the same of tab. 5.3.

estimated values of the vertical scale height parameters to perform a new fit. This time we left all the parameters related to the distribution of the gas free to vary. These are:

- the three parameters of the intrinsic surface density or intrinsic emission: $\Sigma_0$, $\alpha$, $R_d$. As initial guesses for them we used the observational values shown in tab. 5.3.

- the two parameters of the radial profile of the scale height: $c$ and $R_f$, their initial values are the ones obtained in the previous fit. $H_0$ is kept fixed to 0 again.

- one parameter for the galaxy border: $R_{\max}$. The initial guess used for it is the radius of the last elliptical rings analyzed.

The best fit parameters found for the vertical scale height are shown in the "Second Run column of tab. 5.4, while the others are shown in tab. 5.5. The new radial profile of the vertical scale height is plotted as a solid red line in fig. 5.17. The new results are essentially perfect, all the parameters of the input model have been recoverd. The agreement is further highlighted by the comparison between the best fit model and the azimithal profiles over the elliptical segments shown in fig. 5.18 and 5.19. The red points and the blue curves (theory) are clearly coincident at every radius, and also the residuals plotted below the main panels do not exhibit any systematic substructure. Moreover, between the two runs the value of the $\chi^2$ drops from the initial value of $\chi^2 \approx 0.29$ to $\chi^2 \approx 0.003$.

| | Input | Best Fit | $\epsilon$ |
|---|---|---|---|
| $\Sigma_0$ (Jy/Beam) | 0.395 | $0.394 \pm 0.001$ | 0.3 % |
| $\alpha$ | 2.00 | $2.00 \pm 0.01$ | $\approx 0$ % |
| $R_d$ (kpc) | 4.00 | $4.00 \pm 0.01$ | $\approx 0$ % |
| $R_{\max}$ (kpc) | 26.13 | $26.12 \pm 0.02$ | $\approx 0$ % |

Tabella 5.5: Best fit parameters. $\epsilon$ is the same of 5.3.

We tested our technique also in a simulated galaxy with a more realistic gas vertical profile. We were able to find the correct values for the HI thickness (fig. 5.20). However, in the fitting procedure we excluded the data from the center to 5 kpc because the azimuthal profiles are totally dominated by the discretization noise.

In conclusion, from the observed proprieties of the total map of a non edge-on galaxy we have been able to restore both the intrinsic profile of the surface density and the information about the vertical structure of the disk as a function of the radius.

### 5.3.5 Kinematical parameters

The simulated data used in the fitting procedure discussed before, are taken by sampling the observed galaxy with elliptical rings (sec. 5.1.2). The geometrical properties of these rings, i.e., their centre, inclination angle and position angle have been set to the know input values (tab. 5.2). However, we have already discussed that inclination angle and the thickness of the disk are highly correlated, indeed the estimate of $i$ from the isodensity contours on the total map gives wrong results (fig. 5.15).

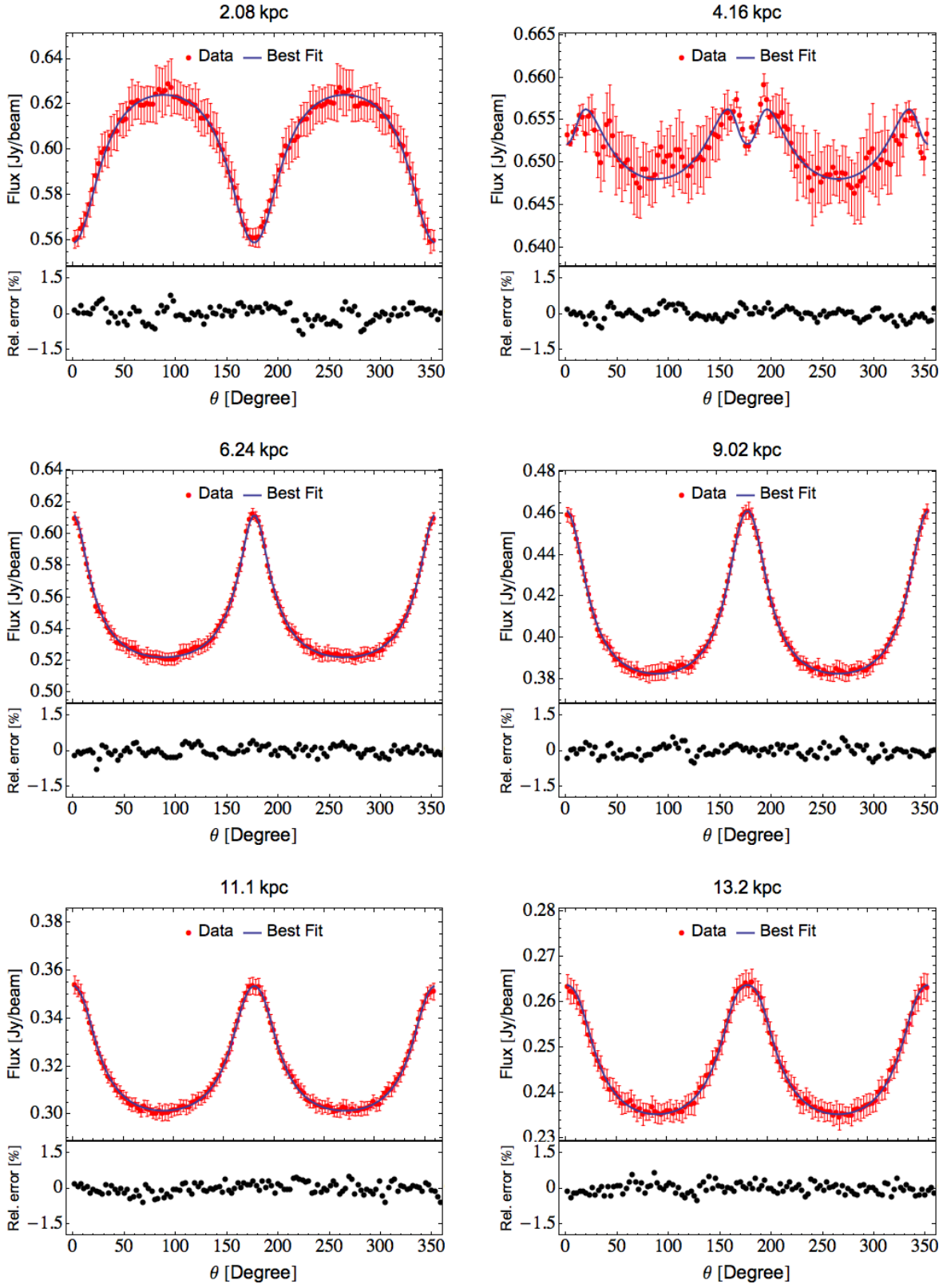


Figura 5.18: The red points represent the azimuthal profiles of emission calculated by *Ellint* from the total map of fig. 5.14. The error bars represent the rms calculated by *Ellint* in the sampling elliptical segments. The blue curves represent the theoretical profile with the parameters found by the fitting procedure.

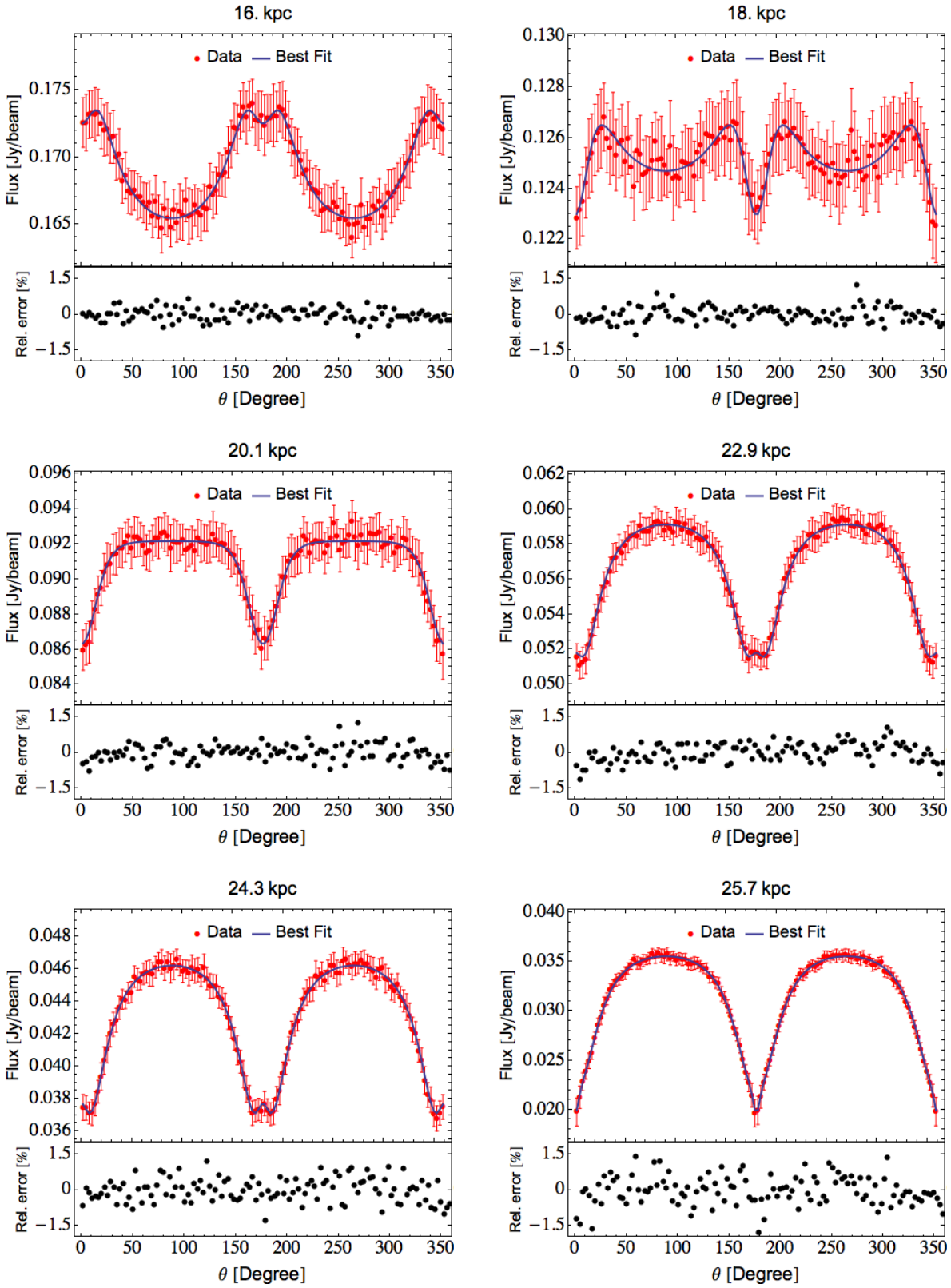


Figura 5.19: As in fig. 5.18

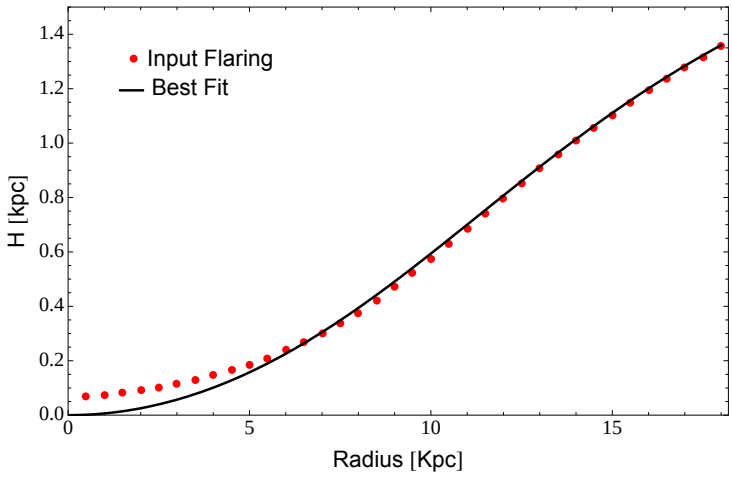


Figura 5.20: Radial trend of the scale height found by the fitting procedure compared with the true values (red dots) for a simulated galaxy with a realistic HI thickness.

In the analysis of spiral galaxies the geometrical parameters of the disk are usually obtained through the fitting of the observed velocity field with the following equation (Begeman, 1987):

$$V_{\rm obs} = V_{\rm sys} + V_c \cos(\theta) \sin(i) \tag{5.25}$$

where $V_{\rm sys}$ is the systemic velocity and $V_c$ the intrinsic circular velocity. The equation is derived considering a thin gaseous disk. In this section we study the effect of a thick disk in the derivation of the kinematical parameters (circular velocity and velocity dispersion of the gas).

In order to have a yardstick for our artificial galaxy we used *Galmod* to simulate a new galaxy with the parameters of tab. 5.2, except for the vertical scale height that has been set to 0. To obtain the velocity field, we used the GIPSY task *Gaufit* that, for every pixel in the data cube, fits a gaussian function over the frequency axis. Using the best fit parameters we created two maps: one with the values of the central velocity of the gaussian, i.e., the velocity field, and the other with the dispersion of the fitted gaussian, i.e., the velocity dispersion of the gas. These maps are shown in fig. 5.21 and 5.22.

We focus on the differences between the galaxy with the thick disk (TK), and the one with the thin disk (TN). It is evident from fig. 5.21 that beyond a certain radius the TK velocity contours bend toward the minor axis of the image in the sky. Even greater differences are evident in the dispersion map of fig. 5.22. The TN model exhibits a very ordinate behavior: the velocity dispersion is constant on every elliptical rings and it decreases as function of the radius, in analogy with the input values (right panel of fig. 5.13). In contrast, the dispersion map of the TK model is dominated by an X-shape feature that is a clear sign of the presence of a thick gaseous disk. Indeed, Sicking (1997) found that in the presence of a thick disk the maximum of the observed velocity dispersion lies on the plane of the sky along the lines where $y = \pm x \cos(i)$. We can use *Ellint* on the velocity dispersion map to obtain the mean value of $\sigma$

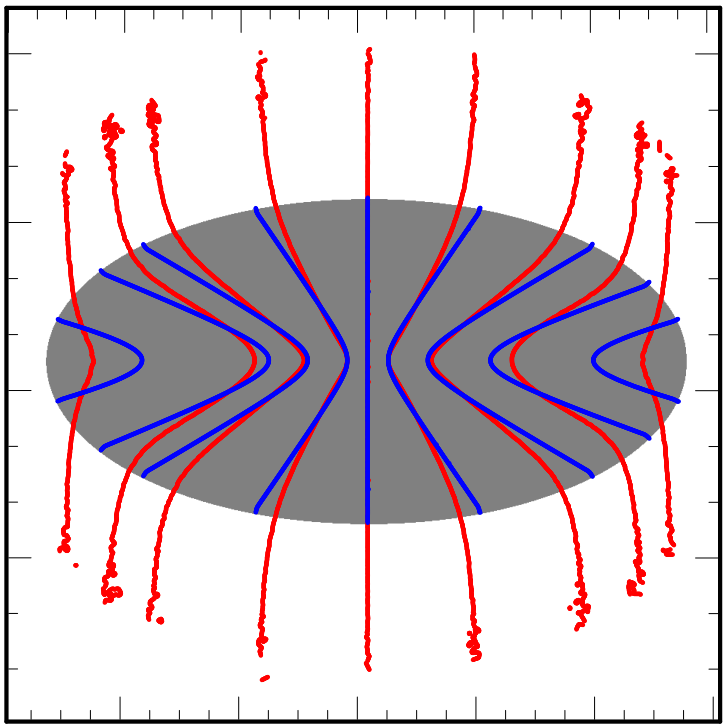

Figura 5.21: Velocity contours for the TK (red) and TN (blue) simulated galaxies. From the left to the right of the image they have the following values (in km/s): 240, 225, 210, 170, 130, 90, 50 35, 20. The grey disk represent the projection of the TN disk onto skyplane.

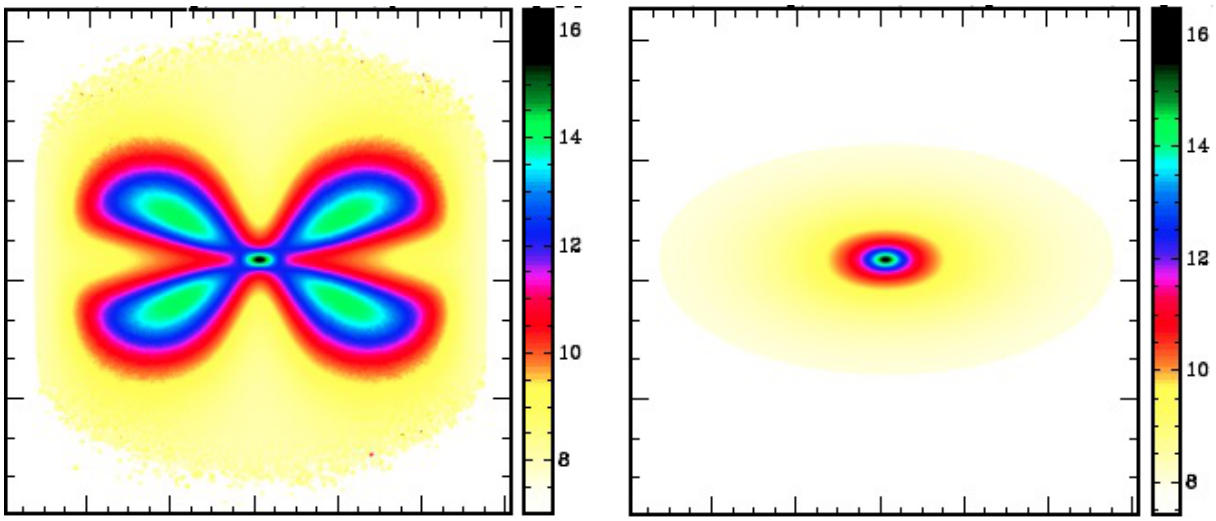


Figura 5.22: Map of the velocity dispersion of the gas for the TK galaxy (left panel) and for the TN galaxy (right panel). The color scale is in unit of km/s.

at each radius R. The resultant profiles are shown in fig. 5.23 overplotted with the input values used in *Galmod* . It is evident that the TN data (red points) are in perfect agreement with the input profile. Instead, the velocity dispersion in the TK model is systematically 3-4 km/s larger. We note that usually the instrumental beam causes a spurious increase on the observed values

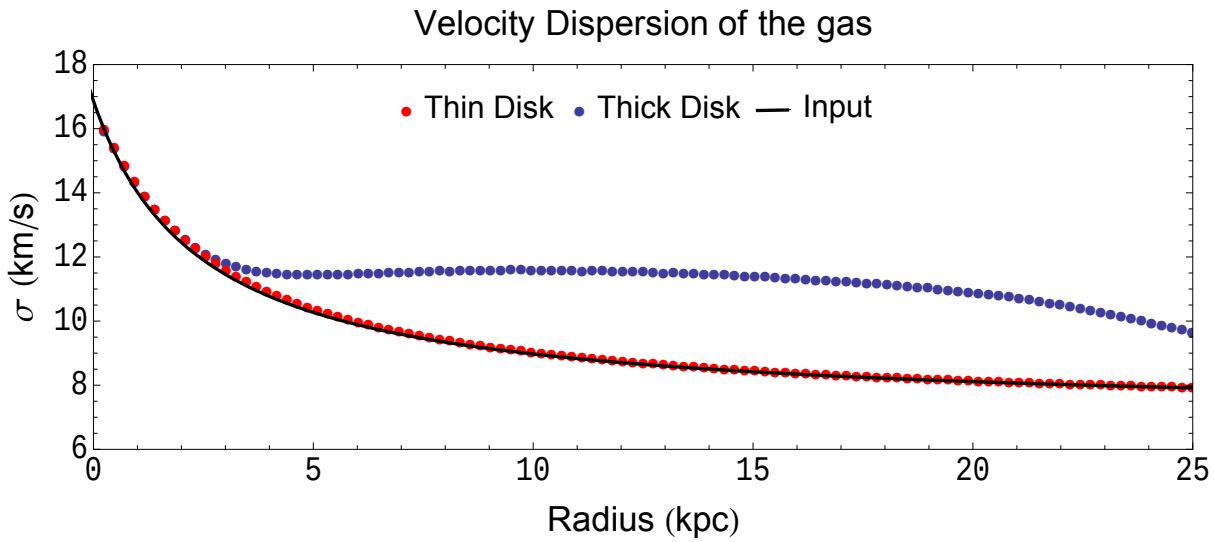


Figura 5.23: Values of the observed velocity dispersion averaged along elliptical rings compared with the profile used as input in *Galmod* (black line).

of the velocity dispersion at the centre of a galaxy. This because in these regions the rotation curves are often rising steeply. However, this does not happen in our case because of the slow rising curve used as input in *Galmod* (fig. 5.13)

In conclusion, in the presence of a thick gaseous disk the observed $\sigma$ represents always an overstimate for the velocity dispersion of the gas.

We now turn to rotation and inclination. We used the velocity field of the galaxy to obtain an estimate of the geometrical and kinematical parameters of the disk through the task *Rotcur.* This task fits a 2D velocity field with the theoretical eq. 5.25. In the fitting procedure the galaxy is modeled as a series of independent circular rings and the task finds the best set of parameters in each of them. The fitting procedure involves many free parameters, hence it is common to run the task more than once, fixing at each execution some parameters found in the previous runs. In our case, we ran *Rotcur* four times. Initially, we left all the parameters free to vary. These are: galaxy center (POS), systemic velocity ($V_{\rm sys}$), position angle (PA), inclination ($i$) and finally the rotation velocity ($V_c$). We focus on the estimated value of the POS fixing it to the mean value along the rings. We run again *Rotcur* to find the average value of the systemic velocity. Then we left only PA, $i$ and $V_c$ free. Since the PA results practically constant over the whole disk, we fixed it and subsequently run *Rotcur* for the last time.

Except for $i$ and $V_c$ of the TK galaxy, the parameter estimates were in perfect agreement

with the related intrinsic input values (tab. 5.2) both for the TK and the TN model. Instead, the fitting of the inclination angle is highly influenced by the deviation of the velocity field shown by the TK galaxy with respect to the TN model. Once again, the thickness of the gas layer causes an artificial deviation of the inclination angle from the true value, as it can bee seen in the upper panel of fig. 5.24. After a slight increase of $i$ at small radii, it monotonically decreases down to 40°-50° around 20 kpc. The abrupt fall-off beyond $R \approx 21$ kpc is probably due to the cut-off of the signal at the border of the galaxy. On the other hand, the estimate of the inclination angle for the TN disk is clearly in agreement whit the input value of 60°.

In the theoretical model used by *Rotcur* (eq. 5.25) it is evident that the inclination angle and the intrinsic value of the circular velocity are strongly linked. Indeed, the wrong estimate of the inclination angle in the TK galaxy causes also a bad evalutation of the rotation curve as one can see in the low panel of fig. 5.24. For radii where $i > 60°$ the rotational velocity found for the TK model (blue dots) is systematically below the input value (represented by the black line), when $i < 60°$ the effect is reversed. As expected, the fit of the TN model gives exactly the right value of the intrinsic rotation velocity.

We stress that the vertical scale height used for the TK galactic model is extreme. One can show that for more reasonable vertical profiles of the gas, the influence of the thickness on the velocity field is very small. However, the analysis performed in this section highlights that also the observed kinematics of the galaxies can suffer from the degeneracy between the layer thickness and the inclination angle. Therefore, theoretically it is ardous to design a method to obtain the inclination angle without the "disturbance of the vertical thickness of the disk.

It is interesting to note that the thickness of the disk produces always an inclination angle that decreases as function of radius. Instead, if a disk has a warp in the outer part the inclination would increase or decrease depending on the orientation and there is not reason for warped disks to become systematically more face-on. Hence, one could investigate whether there is any significative tendency of spiral galaxies to have lower inclination s in the outer disks. This could be the signature of the thickness of the gaseous layers.

From a very preliminary analysis of some galaxies in our possession this kind of statical tendency does not appear to exist. This could mean that the flaring of the gaseous disks is modest in line with found in ch. 4 for realistic galaxy potentials.

As a final not, we point out that one of the initial assumptions of our model is that the geometrical parameters (inclination and position angles) of the disk remain constant with radius. Future studies should be performed on the observational effects of a disk that is both warped and has a significative thickness.

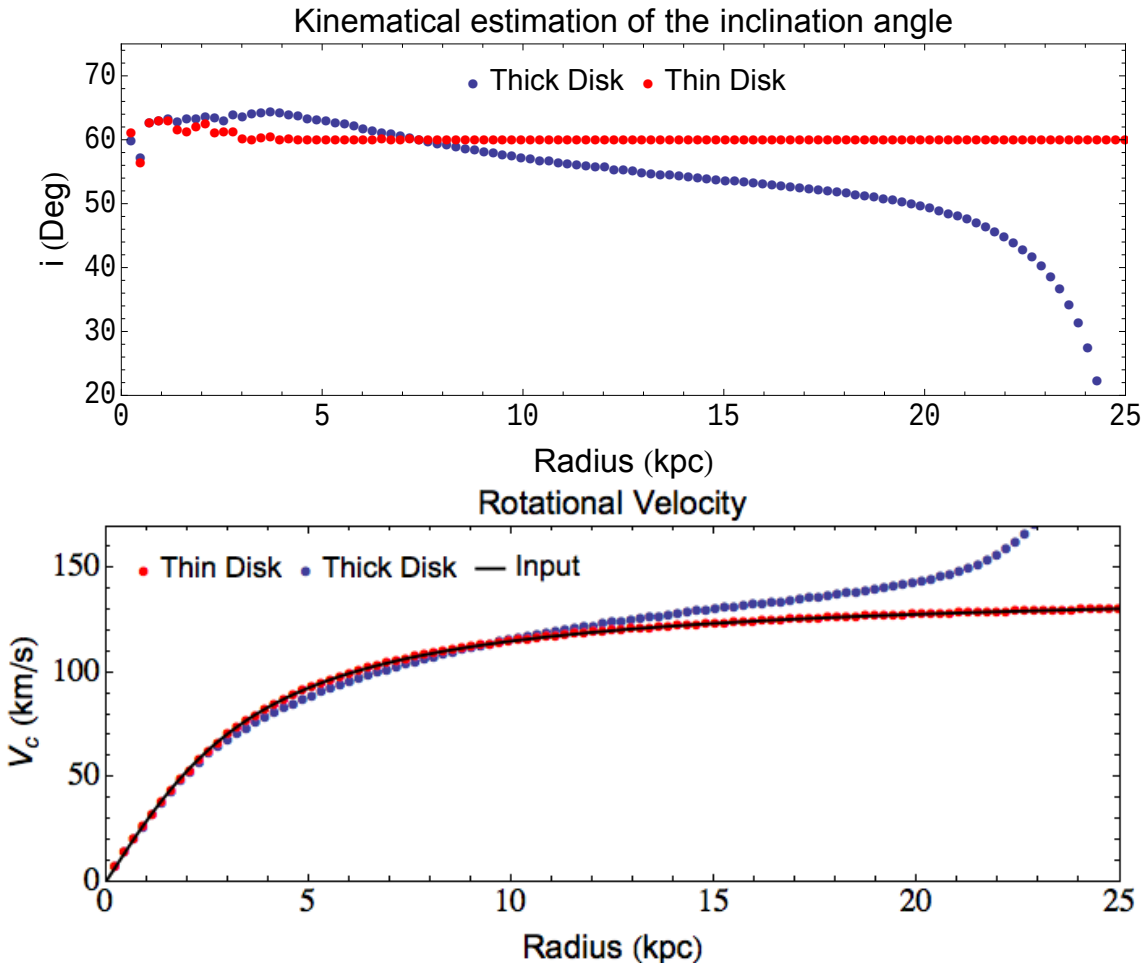


Figura 5.24: Estimate of the inclination angle and rotation curve from the velocity fields of TN and TK.

### 5.3.6 The effect of a wrong estimate of the geometrical parameters

In the previous sections we showed that a significantly thick gaseous disk can strongly influence the estimate of the inclination angle of the galaxy. Moreover, in real observations all the geometrical parameters are influenced by the data disomogeneties. Therefore, also for spirals that do not have a prominent warp the values of the galaxy center, position angle and inclination angle can have relatively large uncertainties (de Blok et al., 2008a). The right estimate of these parameters is fundamental to set the elliptical rings needed to extract the azimuthal data through *Ellint* . Therefore, in this section we will study the effect of the choice of a wrong set of parameters.

We varied the position and the inclination angle in a range of 2° around the correct values of $PA_{true}$=90° and $i_{true}$ = 60°. We shifted the coordinates of the centre of the ellipses along the major and minor axis of a distance of 4 pixels (the value of the beam) with respect of the correct

center. With these settings we run *Ellint* to obtain the azimuthal profiles of the emission every 15″. Once the data have been extracted, we tried again to perform the fit and estimate the vertical profile of the gas. Unfortunately, we were unable to do so. This is due to the differences in the azimuthal profiles caused by even a small mistake ($\pm$ 1°) in the inclination or in position angle. The comparison between the right azimuthal profiles and the one sampled with wrong elliptical rings are shown in fig. 5.25, 5.26 and 5.27. In the following we discus these profiles in some detail.

- Inclination angle: the panels of fig. 5.25 shows the effect of the wrong estimate of the inclination angle. If we use values of $i$ greater than $i_{\rm true}$, the elliptical rings made by *Ellint* will have higher ellipticity, hence they will intercept emission that comes from galactic rings with radius smaller than the true ellipse. Therefore, considering that for most of the disk the emission decreases with radius (fig. 5.16), we expect that around the minor axis there will be an excess of emission. At intermediate radii ($R < 15$ kpc), the thickness produces a minimum of the emission along the minor axis. The choice of a wrong $i$ compensates this effect decreasing the magnitude of the observed azimuthal oscillations as clearly shown in the first two panels of fig. 5.25. Focusing in these regions, we should estimate a vertical scale heigth lower with respect to the true one. Around 15 kpc the combined effects of the wrong value of $i$ and the decreasing of the magnitude of the azimuthal oscillation can produce a flat profile or even it can switch the position of the peak from the major to the minor axis as happens for $i = 62°$. At large radii the thickness produces azimuthal profiles that exhibit a peak of the emission on the major axis. The use of a $i > i_{\rm true}$ magnifies this effect creating very prominent oscillations. Therefore using the data of these regions we would erroneously infer the presence of a very thick gaseous layer also in the case of a disk with a thin gaseous layer. The opposite influence of a wrong $i$ on the azimuthal profiles between intermediate and large radii causes the fit method to fail when used to estimate the best set of parameters to explain the overall profile of the emission. For inclination angles lower than $i_{\rm true}$ all the effects just highlighted are reversed as shown in fig. 5.25. The plot of the gamma parameters on top of fig. 5.25 summarizes what just said.

- Position angle: The effects of using elliptical rings with wrong PA are shown in fig. 5.26. Firstly we focus our analysis on the gamma parameter (top panel). The magnitude of the azimuthal oscillations is very similar to the expected one (dashed line) up to about ten kpc, beyond this radius the gamma parameter becomes progressively larger with the increase or the decrease of PA with respect to the true value . It is evident that the behavior of gamma depends only on the absolute difference between the chosen PA and $\rm PA_{true}$. We can better understand what happens by analyzing the profiles in the other panels of fig. 5.26. It is clear that at small radii the influence of PA is very weak, it acts mainly to shift the profiles to the left for PA>$\rm PA_{true}$ and to the right for PA<$\rm PA_{true}$. In the panel at about

10 kpc, an increment of the difference between the maximum and the minimum of the emission starts to be evident. Beyond this radius the profiles suffer a strong modification of their shape, the classical smooth oscillations are deformed in a sow-tooth profile that becomes increasingly evident with increasing radius. It is clear that in these cases the fitting method is unable to fit the observed profiles at large radii. However, the signatures of the choice of a wrong PA are so evident that we think they could be easily recognized and hence corrected.

- Coordinates of the center: The main effect of the use of a wrong position for the centre of the elliptical rings is to obtain asymmetric profiles of the emission. Another clear proprerty that is shown in fig. 5.27 is that the influence on the azimuthal profile strongly depends on which coordinates were wrong. We call X the coordinate that lays along the major axis of the galaxy and Y the one that lays on the minor axis. If we vary the X position the profile remains symmetric over the elliptical angle and most of the differences are confined around the major axis. Instead, the shift along the minor axis (Y) produces strong asymmetries between the region of the ring above and below the major axis. In general the profiles still exhibits features similar to the expected oscillation, but they have very different magnitudes on the two sides . Of course, the combination of variations on both the coordinates creates more complex modifications of the profiles as shown in fig. 5.27 by the green curves. However, also in this case it is plausible that an effect of this kind could be recognized and corrected in the observed profiles.

In conclusion, we found that the use of a wrong set of geometrical parameters in *Ellint* can have a dramatic influence on the emission profiles theoretically expected for a thick gaseous disk. The effect of the PA and the center coordinate can be recognized and corrected. Once again the most problematic parameter is the inclination angle, if wrongly estimated it can cause signatures on the profiles very similar to the one produced by a thick layer also in presence of a disk with a moderate vertical scale height. Finally, if more than one parameter is wrongly estimated the various effects just described can combine and the resultant azimuthal profiles can show even more complex patterns.

## 5.4 Results and discussions

In this chapter we have compared the observed emission of artificial galaxies made with *Galmod* (sec. 5.1.1) with the theoretical predictions of the model described in ch. 4.

The main conclusions are the following:

- We developed a technique to extract and analyze the azimuthal pattern of the galactic emission. It uses the task *Ellint* (sec. 5.1.2) to sample the total map with user defined

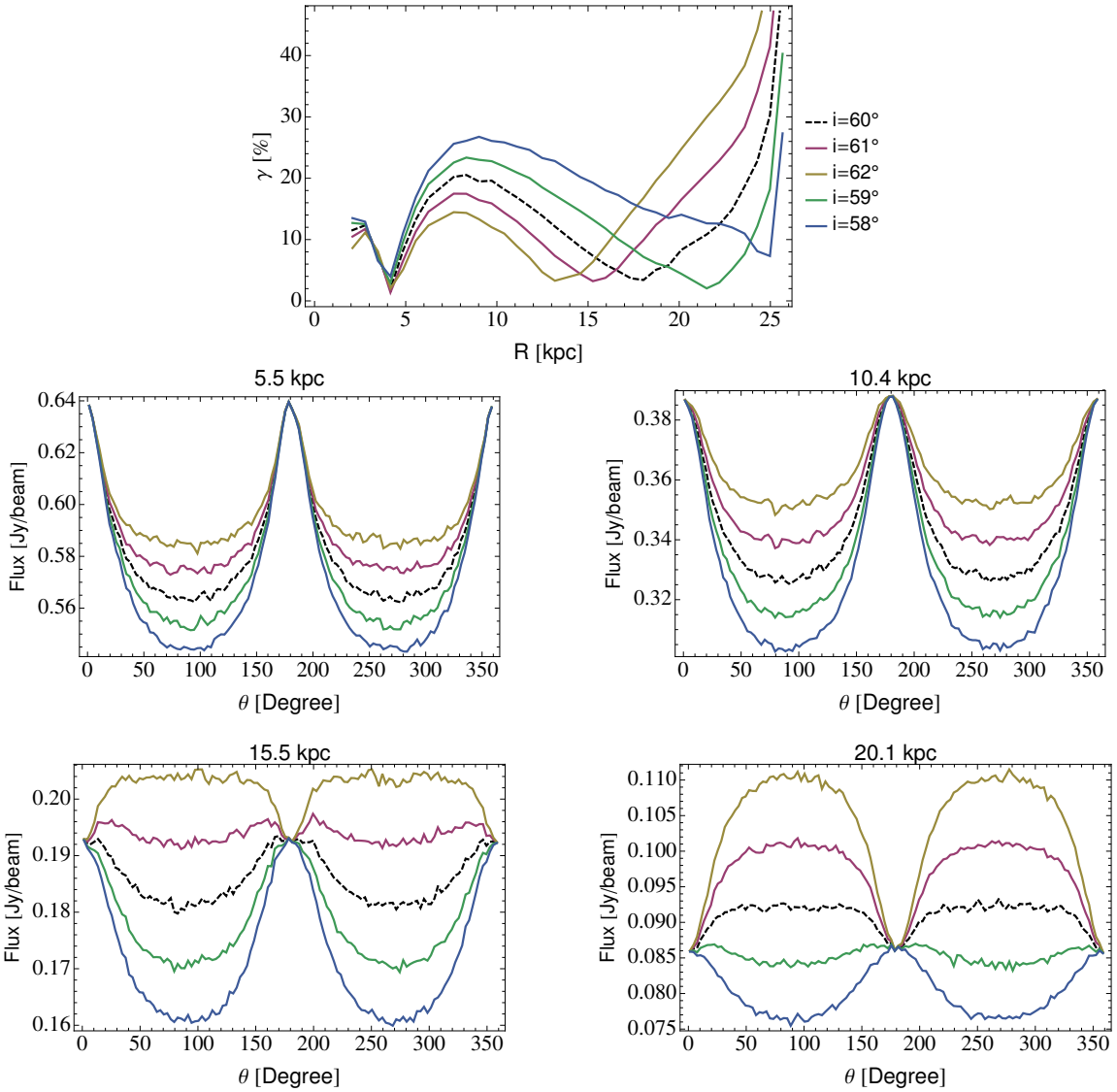


Figura 5.25: Up panel: value of the gamma parameter (eq. 4.27). Low panels: Azimuthal profiles of the emission calculated approximately every 5 kpc from the total map of fig. 5.14. The dashed curves are referred to data taken by *Ellint* with the right values of the geometrical parameters (tab. 5.2). The data of the colored curves are taken with elliptical rings that have a wrong value of $i$ as shown in the legends.

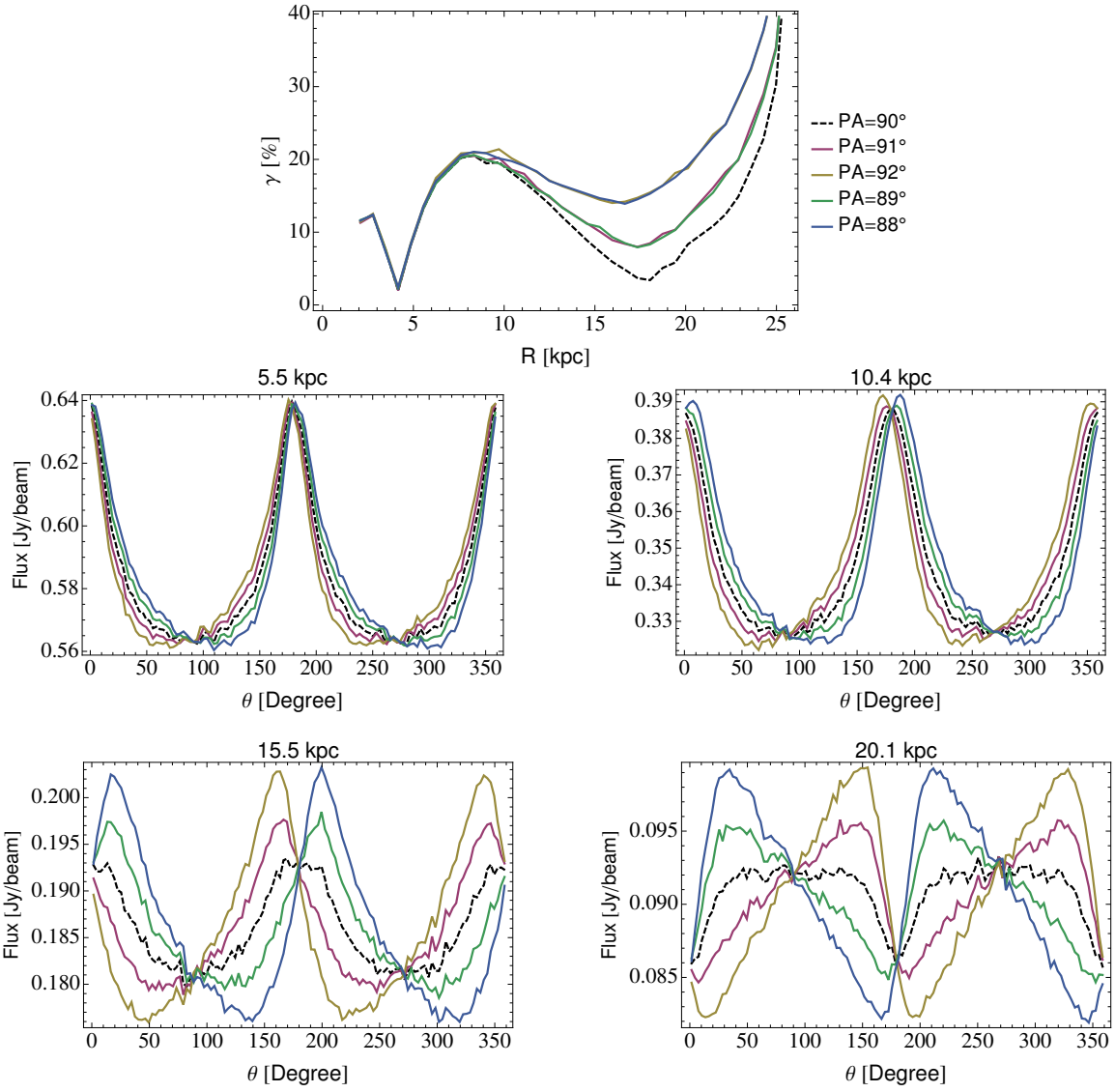


Figura 5.26: As in fig. 5.25, but the colored curves are referred to data taken with the wrong value of PA.

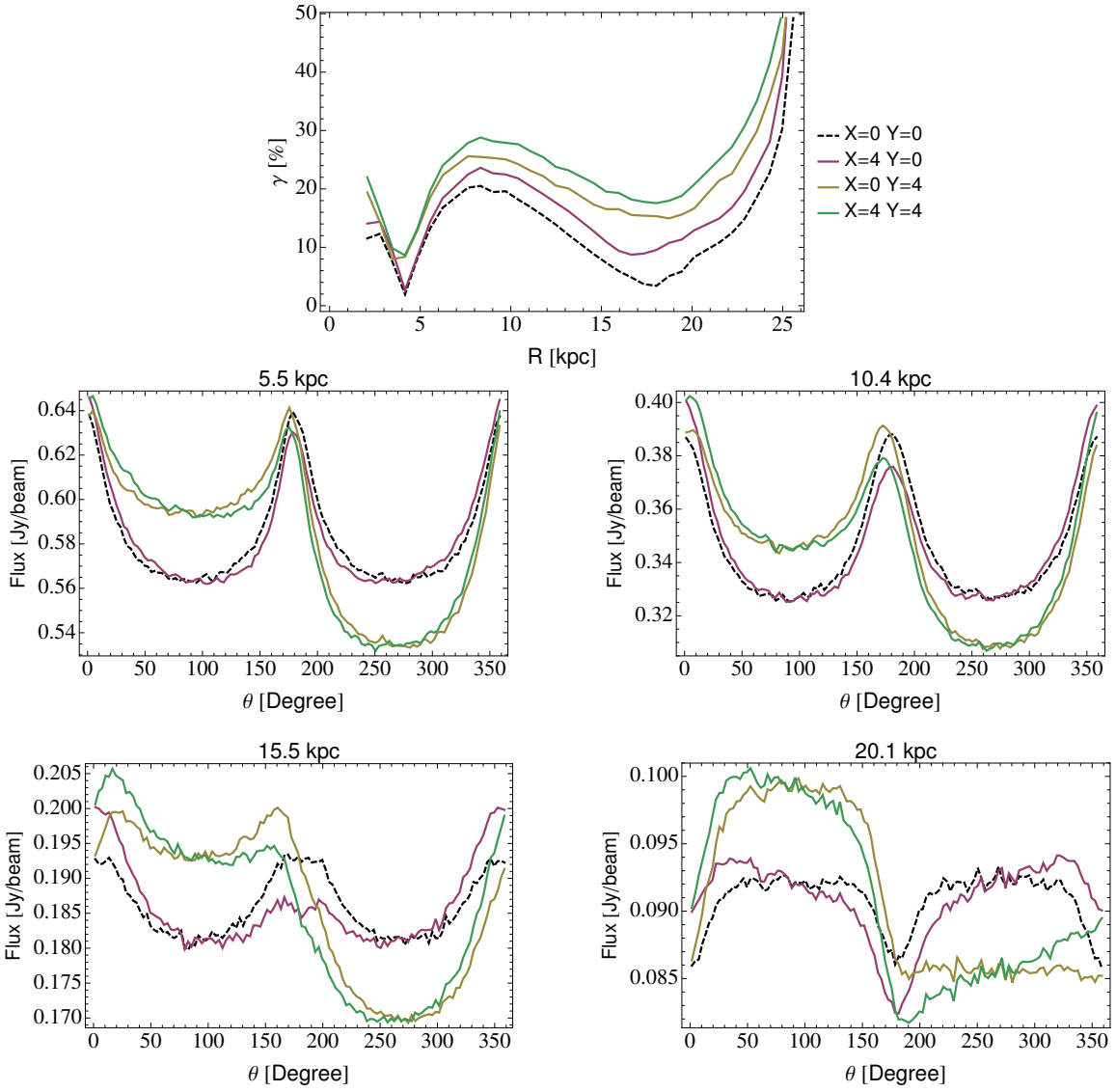


Figura 5.27: As in fig. 5.25, but the colored curves are referred to data taken with the wrong coordinate of the center of the ellipses.

elliptical segments. The data taken in such way can be compared with the theoretical model expressed by eq. 4.19. Both the sampling procedure and the numerical integration of the model can introduce biases on the data analysis, but we found that their influence is negligible as it can be seen from the distribution of the related errors shown in fig. 5.2 and 5.5.

- From the study of two artificial galaxies (sec. 5.2 and 5.3), we conclude that our model successfully describes the effect of the layer thickness on the observed emission. Moreover, we showed that, theoretically, we can use it to obtain information on the intrinsic 3D profile of the gas also for galaxies with moderate inclination angles (see fig. 5.17).

- We found that the presence of a thick gaseous disk can heavily influence the estimate of geometrical and kinematics proprieties of the galaxy. The deviation of the velocity field from the one expected for a thin disk is shown in fig. 5.21. In practice, in the presence of a thick disk the velocity contours are bent toward the minor axis. We found that this effect does not influence the estimate of the position angle and of the galaxy center, but it causes a wrong estimate of the inclination angle and of the circular velocity (fig. 5.24). The inclination angle is the geometrical parameter that is most influenced by the presence of a thick disk. Indeed, its estimate either from the ellipticity of the isophotes (fig. 5.15) or from the just mentioned analysis of the the velocity field may lead to significantly wrong values. However the deviation from the true value shows a systematic trend. Indeed, the estimated $i$ exhibits always a relevant decrease with the radius. We suggested that it can interesting in the future to study if this kind of behavior has a statistical incidence on observed spiral galaxies.

- The wrong estimation of the geometrical parameters can heavily influence the data sampling and the subsequent analysis as shown in fig. 5.25, 5.26 and 5.27. We found that also a relative small difference from the correct value causes the failure of the fitting method described in this chapter. In some cases, it can be applied but only in small portion of the galaxies.

# Capitolo 6

# Conclusions

## 6.1 Summary of the results

In the following, we briefly summarize the conclusions of our work. More detailed discussion of results and conclusions can be found at the end of each chapter.

- Assuming cylindrical symmetry, hydrostatic vertical equilibrium and and isothermal and isotropic gas, we found that the gas vertical profile of disk galaxies depends both on the potential of the galaxy and on the gas velocity dispersion (eq. 2.4). We evaluated the galactic potential both with analytical approximations and with the numerical code *Galforces* (Fraternali & Binney, 2006). In both cases we found that the gas vertical profile is well fitted both by a gaussian and by hyperbolic secant squared.

- The scale-height of these functions depends on the vertical gradient of the potential, i.e, on the galactic matter distribution and on the gas velocity dispersion. At large radii, where the matter density drops, the gas layer "flares increasing its thickness with radius. The kinematics of the gas influences its thickness, however for almost flat rotation curves this contribution is negligible. Using realistic mass models, we found that the HI thickness (H) strongly depends on the dominant matter component. In particular, at inner radii H rises exponentially with a scale length nearly twice the scale length of the stellar disk. At larger radii, where the DM dominates, the HI thickness grows as a power-law $\mathrm{H}(R) \propto R^{\alpha}$, whit $\alpha \sim 1$. The gas velocity dispersion ($\sigma$) also plays an important role for the value of the gas scale-height: we showed that a rapid decrease of $\sigma$ can even prevent the HI layer to flare. Finally, we defined two functional forms (eqs. 3.40 and 3.41) that well describe the radial trend of H for real galaxies.

- As mentioned, at large radii the thickness of the HI layer is strongly related to the density distribution of the DM halo. Therefore, in principle, it can be used to break the degeneracy on the shape of the halo models. Indeed, in app. C we show that every rotation curve can

be explained by a family of DM halos (both isothermal or NFW) with different flattenings. However, they produce different gas flaring in the outer disk. These differences can be as larger as 40 %, hence also with a rough estimate of H it could be possible to rule out at least some of the halo models.

- Performing a geometrical analysis of galaxy disks projected on the sky, we modeled the effect of a thick HI layer on the observed emission. We found that it produces azimuthal asymmetries on the projected galaxy rings: the emission oscillates with a periodicity of $\pi$ and the shape and the magnitude of these oscillations depend on the radial and vertical distribution of the gas. Therefore, in principle they can be used to obtain information about the intrinsic gas density profile, especially in the vertical direction.

- We test the feasibility of this approach on simulated galaxies. We showed that in the case of large HI thickness, it is possible to recover the intrinsic gas density profile from the emission of galaxies with moderate inclinations ($i \sim 50^\circ - 70^\circ$). As H decreases the expected azimuthal profiles become smaller than the local oscillation due to data noise. and, the oscillations become visible only in the outskirt of the galaxies making it difficult to compare them with the theoretical model. In simulate galaxies the noise is maintained quite low (under few percent of the data value) with respect to the typical observational noise. Therefore, we guess that the typical gas flaring expected for disk galaxies is probably too low to produce an appreciable effect in real observations.

- We investigated how, the HI layer thickness can bias the observed kinematics and influence the derivation of galactic parameters. In particular, we found that the inclination angle estimated using the velocity field fitting would be systematical lower than the true one. Finally, we found that also a relative low error on the estimate of the galactic geometrical parameters (inclination angle, position angle and galactic center) can cause large modifications of the azimuthal profiles and can make very hard the comparison between the data and the model, also in the presence of an HI layer with a considerable scale height.

To conclude this thesis we briefly report a preliminary analysis performed on the galaxy NGC 2403. We chose this galaxy because it has an extended HI disk without prominent spiral arms or a warp and it is not disturbed by interaction with nearby objects. The aim of the following analysis is to give a simple example of practical applications of the theoretical topics described in the previous chapters. Therefore, we will focus on the results rather than on the deep description of the method used. An exhaustive description of the analysis of a HI data cube, of the use of the tilted ring model and of the mass decomposition through the rotation curve can be found in Begeman (1987). The extraction method of the emission azimuthal profiles and the calculation of the theoretical thickness of the HI layer have been already explained in this thesis.

## 6.2 Test on NGC 2403

NGC 2403 is a well studied nearby spiral galaxy located at the outskirt of M81 group. The RC3 catalogue (Corwin et al., 1994) defines it as a SAB(s)cd isolated galaxy. The HI emission analyzed in this section has been taken with the VLA interferometer, the reader can find detailed information about observations and data reduction in Fraternali et al. (2002). For this galaxy we assumed a distance of 3.18 Mpc (Davidge, 2003). In the following, all the words in italic are referred to tasks of the GIPSY package (van der Hulst et al., 1992).

| NGC2403 parameters | | |
|---|---|---|
| Type | SAB(s) | Corwin et al. (1994) |
| D (Mpc) | 3.18 | Davidge (2003) |
| $i$ (degrees) | 61.48±1.84 | This work |
| PA (degrees) | 124.74±0.33 | 〃 〃 |
| Center RA | 7h36m52.84s±0.93s | 〃 〃 |
| Center DEC | $65°36'3.5''\pm1.97''$ | 〃 〃 |
| $V_{sys}$ (km/s) | 132.77±3.22 | 〃 〃 |
| $M_{HI}$ ($M_\odot$) | $3.23 \cdot 10^9$ | 〃 〃 |

Tabella 6.1: Galaxy parameters: the values estimated in this work come from the fitting of the velocity field (*Rotcur*), except for the HI mass that has been calculated from the total flux (*Flux*) using eq. 1.24.

The data cube is composed by 800x800 spatial pixels with a dimension of $4''$x$4''$, while the velocity domain is divided in 60 channels of width $\Delta V$=5.15 km/s. The spatial resolution of the data is given by the FWHM of the instrumental beam $15.2''$x$13.2''$ or 0.238x205 pc at the assumed distance. The cube has been hanning smoothed so that the velocity resolution is FWHM$_v$=2 $\Delta V$ and the related instrumental broadening is:

$$\sigma_s = \frac{\mathrm{FWHM}_v}{2\sqrt{2\ln(2)}} = 4.37 \text{ km/s} \tag{6.1}$$

### Clean noise

The data cube shows some noise, moreover in the channels between 6.36 km/s and -14.24 km/s the signal is critically influenced by the emission of our Galaxy. To highlight the source emission we smoothed (*Smooth*) the data to the lower resolution of $60''$. Subsequently we evaluated the noise rms ($\sigma_n$) in the first and last channels that are free by the galactic emission. By eye inspection we choose to consider real signal all the emission above the threshold of 3.5 $\sigma_n$. In the channels contaminated by the Milky way we manually highlighted the emission regions. All the noise pixels have been blanked and the resultant pixels have been normalized creating a mask.

Finally, the original data cube and the mask have been multiplied (*Combine*). The resultant noise free data cube has been corrected for the primary beam (*PBcorr*) and we constructed the HI total map (right panel of fig. 6.1(a)) adding the emission of every channel (*Sum*).

### Velocity Field and Galaxy parameters

There are different ways to extract the radial velocity of the gas in a certain pixel. The two most common methods are the first moment of the HI emission or the central value of a fitting function (usually a gaussian). From Fraternali et al. (2002) we know that NGC 2403 has a considerable amount of extra planar gas in the central parts that can influence the evaluation of the gas kinematic. From ab inspection of velocity profiles (*Gauproof*) we noted that in most of them there is a main gaussian component with the addition of noise and/or minor tails of emission. This tail may shift the value of the velocity found with the first moment. Therefore we choose to evaluate the galaxy velocity field fitting a gaussian pixel by pixel. The resultant velocity field is shown in the right panel of fig. 6.1(b), while the fitted velocity dispersion is shown in the right panel of fig. 6.1(c). Both the maps do not show the typical features we expect in presence of a thick HI layer (figs. 5.21 and 5.22). Indeed, the "perturbations of velocity contours and the "hot spots on the dispersion map seem linked to the spiral arm features visible in the total map.

As already explained in sec. 5.3.5 we fitted the velocity field of the galaxy with the theoretical tilted ring model Begeman (1987) to estimate the galaxy parameters as the inclination angle, the systemic velocity and so on. The velocity field fitting has been performed through the task *Rotcur*: the results are shown in tab. 6.1 while the rotation curve is plotted in the left panel of fig. 6.1(b). The inclination and position angles do not show systematic variations with radius, hence we fixed them averaging their radial values. Our results are in good agreement with the values found by Fraternali et al. (2002).

The estimated galactic parameters have been used in *Ellint* (see sec. 5.1.2) to evaluate the radial trend of the emission and of the gas velocity dispersion (left panels of figs. 6.1(a) and 6.1(c)).

### Mass decomposition and vertical scale height

The rotation curve of a disk galaxy is due to the sum of the contributions of the single galactic mass components. Neglecting the stellar bulge, we can write:

$$V_c^2(R) = V_{\rm DM}^2(R) + \Upsilon_*^2 V_*^2(R) + V_{\rm gas}^2(R) \tag{6.2}$$

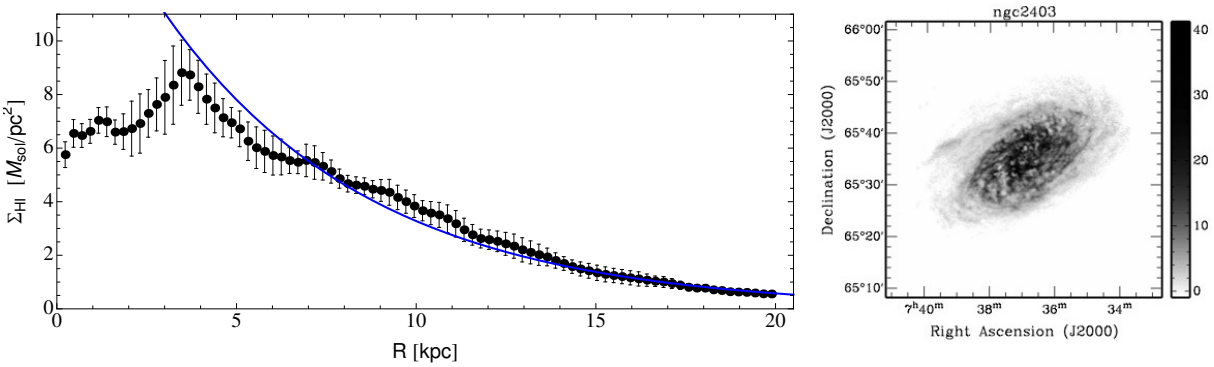


(a) Right: total HI map obtained by summing of the emission on the various velocity channels. The grey scale are in units of $M_\odot/pc^2$ (eq. 1.18). Left: Radial trend of the surface density obtained using the galactic parameters in tab. 6.1, the error bars come from the difference between the evaluation on the approaching and receding side of the galaxy. The blue curve shows the best fitting exponential function for the data beyond 5 kpc.

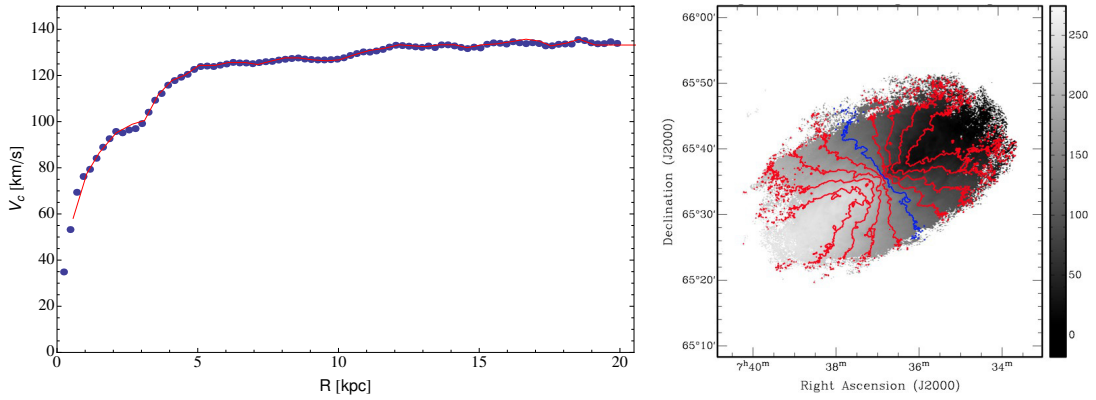


(b) Right: velocity field of the galaxy obtained by fitting gaussian functions to the velocity profiles. The grey scale is in km/s, while the velocity contours range from 32.8 km/s to 232.8 with step of 25 km/s and the blue curve represents the systemic velocity of 132.8 km/s. Left: Rotation curve obtained by the fitting of the velocity field with the tilted ring model (Begeman, 1987), the red curve shows the rotation curve found by Fraternali et al. (2002).

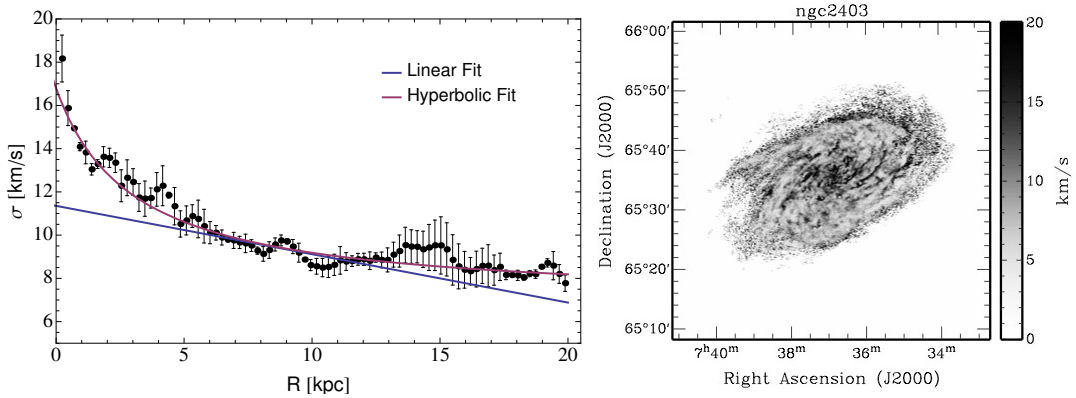


(c) Right: gas velocity dispersion ($\sigma$) map obtained by fitting gaussian functions to the velocity profiles. The grey scale is km/s. The values have been corrected for the instrumental broadening (eq. 6.1). Left: Radial trend of $\sigma$ obtained using the galactic parameters in tab. 6.1, the error bars come from the difference between the evaluation on the approaching and the receding side of the galaxy. The purple and the blue curves show respectively an hyperbolic and a linear fit of the data. The first is fitted to the whole disk, while the second only between 6 and 12 kpc

Figura 6.1

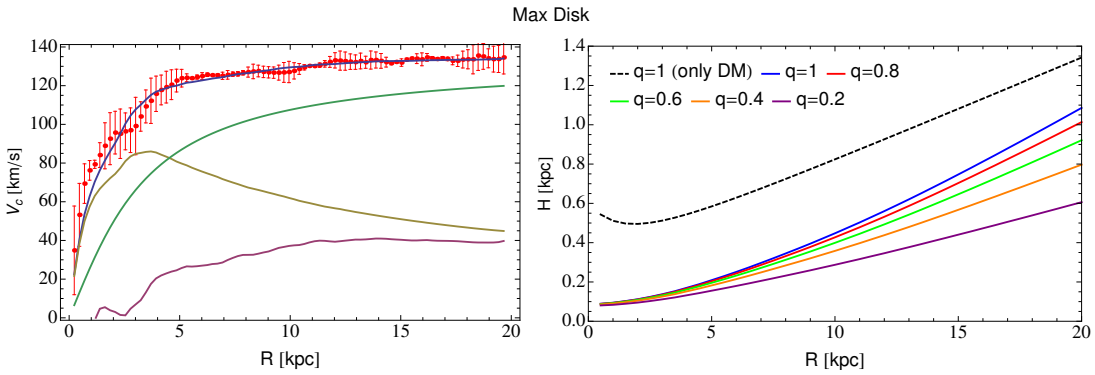


(a) Left: maximum disk best fit (blue curve) of the observed rotation curve (red points). The purple, yellow and green curves show respectively the contribution of the gas disk, stellar disk and DM halo. The error bars come from the difference between the evaluation on the approaching and receding side of the galaxy. Right: The colored curves show the expected HI scale heights for dynamic models that produce the rotation curve shown in the right panel but with different flattenings for the DM halo (see App. C). The dashed black curve show the case with only a spherical DM halo and it represents a strong upper limit for the HI thickness.

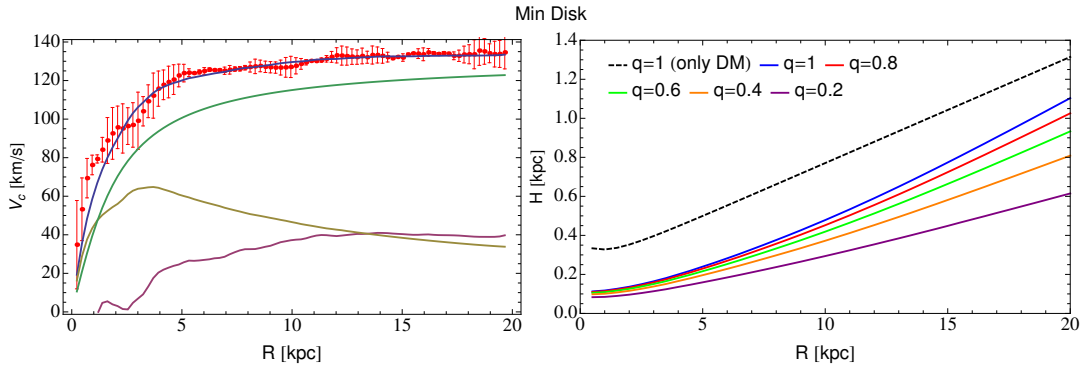


(b) Same as above for the minimum disk decomposition

Figura 6.2: Mass models and related theoretical HI scale-height. The upper and lower panels show the results respectively for the maximum and the minimum disk models (see text for further explanations)

where $\Upsilon_*$ is the mass to light ratio of the stellar disk. We calculated the velocity of the stellar and the gaseous disks using the functions in Casertano (1983) implemented in the task *Rotmod*. For the stellar disk we used the $3.6\mu$ data from Muñoz-Mateos et al. (2009) while for the gaseous disk we used the radial profile of fig. 6.1(a) multiplied by 1.4 to take in account the Helium.

Since we know the circular velocity of the baryonic matter, we can use the task *Rotmas* to evaluate the halo parameters fitting the observed rotation curve. The functions used for the DM velocity curves are eqs. 3.21 and 3.34, therefore the parameters to constrain are the halo central density and the halo scale length. Indeed, also the stellar mass to light ratio is unknown and it can be treated as a free parameter of the fit. It is common to define an upper and a lower limit for this value and fit only the halo parameters. For the lower limit we use the value of $\Upsilon_* = 0.21$ obtained by de Blok et al. (2008a) by study the stellar populations, while for the upper limit

we used $\Upsilon_* = 0.37$ that is the largest value that gives a reasonable fit for the observed rotation curve (maximum disk hypothesis). We used both a NFW and an isothermal density profile for the DM, the results are very similar, hence we reported here only the analysis for the isothermal halo. The results are shown in the left panels of fig. 6.2. We fitted only the case of a spherical halo, we can then extend the results to the flatted halos using eqs. C.2 and C.3.

We used the mass model just obtained to calculate the theoretical vertical scale height of the gas following the method explained in sec. 2.3. For the gas velocity dispersion we used the best fit function shown by the purple curve in fig. 6.1(b). We noted that both the beam smearing and the thickness of the HI layer can increase the value of the velocity dispersion (sec. 5.3.5). Therefore, our evaluation could be considered an upper limit of the intrinsic $\sigma$. As previously mentioned in this thesis, the numerical code *Galforces* calculates the potential only in disks with an exponential radial density distribution, however beyond 5-6 kpc the observed surface density falls nearly as an exponential as shown by the blue curve in fig. 6.1(a). We used this curve to model the HI disk in *Galforces*: it overestimates the surface density at small radii, but in these regions the gaseous surface density is more that ten times lower with respect to the stellar surface density and it has a very small effect on the gas vertical scale height. The resulting HI thickness is shown in the right panels of fig. 6.2 for various values of the halo flattening $q$. We also show a strong upper limit (black dashed curves) for the HI thickness using a mass model with only a DM spherical halo. The radial trend of H is very similar for the maximum and minimum disk models. The only differences are at small radii, where in the case of maximum disk model the stellar disk strongly dominates the potential and the vertical scale height are practically identical for each value of q.

### Comparison with the data

We extracted the azimuthal profiles of the emission following the method explained in sec. 5.2.3. The sampling elliptical segments have been set using the geometrical parameters shown in tab. 6.1 and with radial and azimuthal widths respectively of $15''$ and $3°$. The resultant profiles are shown for various radii in figs. 6.3 and 6.4.

We used the upper limit of the vertical scale height (dashed curve in fig.6.2(a)) and the radial profile of the gas in fig. 6.1(a) to build theoretical azimuthal profiles of the emission. They are shown in figs. 6.3 and 6.4 as blue curves. The expected oscillations are so low that they appear practically constant with respect of the observed emission. They are also several time lower than the data rms (error bars) calculated on the sampling segments. In conclusion, we confirm that the expected HI scale height of a galaxy like NGC 2403 is too low to give an appreciable effect on the observed emission. We found that the observed profiles can be fitted only by a model with a constant scale height. In particular, we found that the best fitting model predicts a HI thickness of about 3.2 kpc. The theoretical profiles of this model are

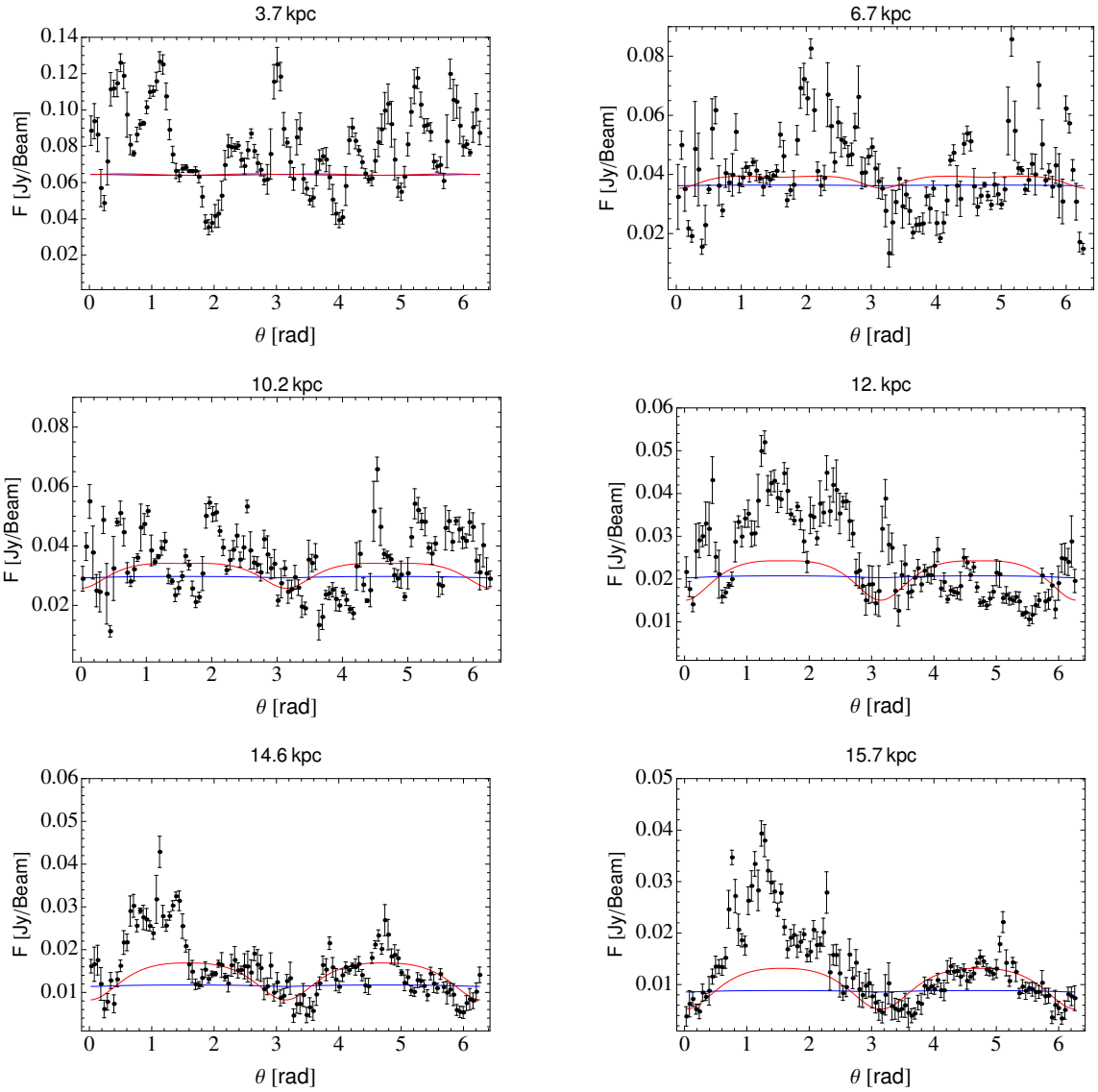


Figura 6.3: The black points represent the azimuthal profiles of emission calculated by *Ellint* (5.1.2) from the HI total map (right panels of fig. 6.1(a)), the error bar show the data rms calculated by *Ellint* on the sampling segments. The blue curves show the profiles expected for upper limit of the gas scale height shown in fig. 6.2(a). The red curves is referred to a model with a HI thickness fixed to 3.2 kpc.

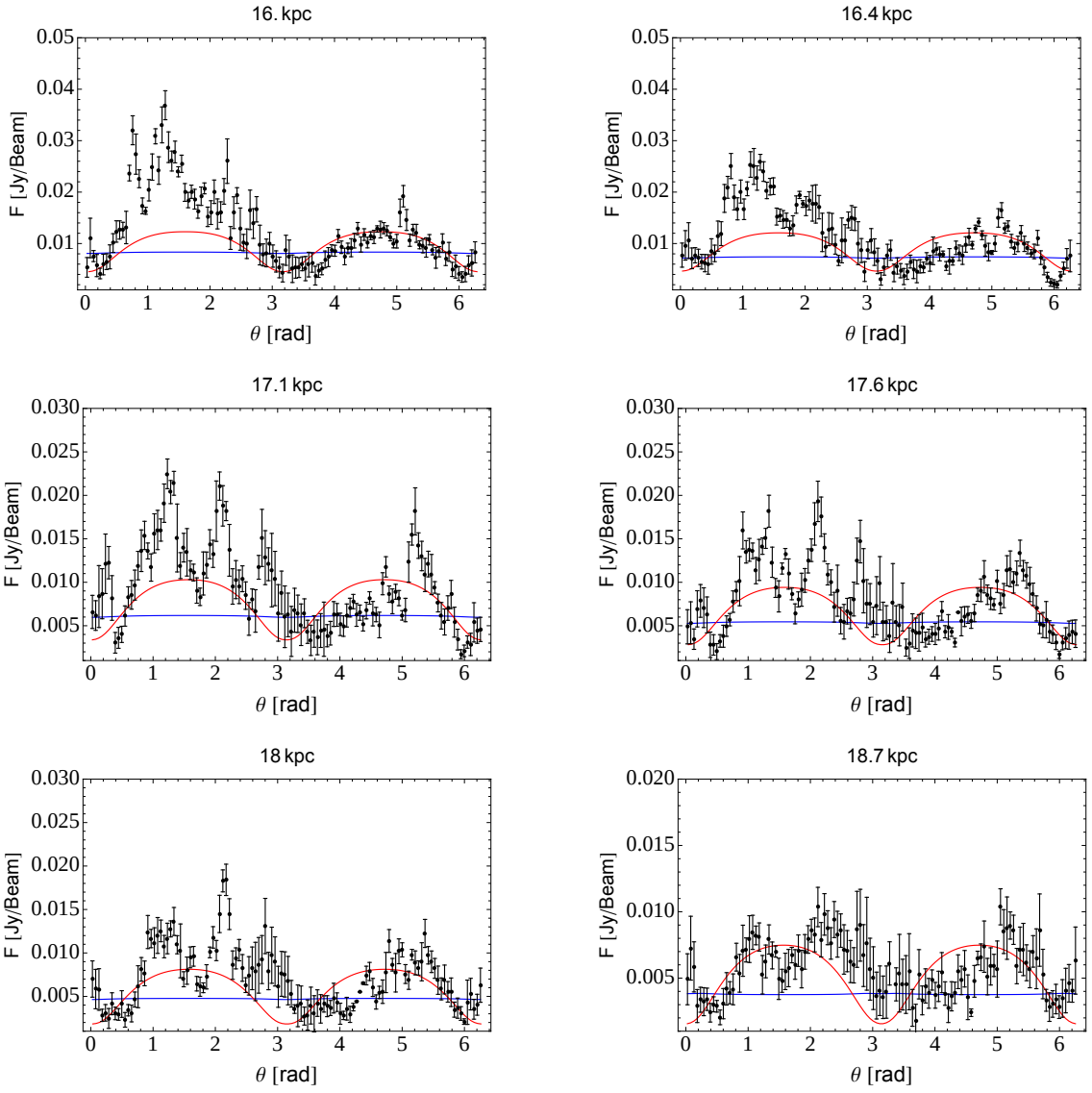


Figura 6.4: Same as fig. 6.3

shown by red curves in panels of figs. 6.3 and 6.4. The fit is not completely satisfactory, but especially at large radii it is able to produce oscillations on the signal of the same magnitude as the data. An HI disk with a constant thickness of 3.2 kpc is a very extreme model clearly not supported by our hydrostatic equilibrium analysis. Moreover it should produce relevant effects on the observed kinematics (sec. 5.3) that we do not see in this case. It is more probable that the prominent observed oscillation are due both to intrinsic asymmetries of the disk (e.g. the various spikes on the azimuthal profiles can be due to spiral arms) and for to wrong estimates of the galactic geometrical parameters. Indeed, in these profiles it is possible to identify some features highlighted in sec. 5.3.6. As a last note, it is intersting to note that the value of 3.2 kpc is very similar to the thickness estimated by Fraternali et al. (2002) for the gaseous halo of NGC 2403. It is probably only a chance, given that the emission from this halo should only contribute to 10% of the total, but it can be interesting in the future to extend our study considering also the contribution of the extra-planar gas.

## 6.3 Final remarks

The previuos section and the results of the last chapter (sec. 5.3.5) suggest that the method described in this thesis to estimate the vertical profile of the gas could not work if applied to real observations. Indeed, two cases can arise:

1. The thickness of the disk is very prominent and also the related signature on the observed total map will be clearly observable. In this case, the estimate of the inclination angle will be largely influenced by the thickness an it will be very hard to separate a real variation of $i$ from these spurious effects. Moreover, a wrong estimate of $i$ can heavily affect the subsequent fitting procedure to evaluate the vertical profile of the gas.

2. The disk has a modest thickness. In this case the signature on the total map can be totally lost due to the presence in the data of features like holes, disomogetis, spiral arms and so on.

Clearly between these two cases the first is preferable, indeed in this case the informations are only hidden and we can try to restore them using a deeper analysis of the emission and maybe a better fitting procedure (as the Monte Carlo Markov Chain). In the second case, instead, the signature of the vertical profile of the gas are lost. Unfortunately, the estimated vertical scale height of real galaxy models made in sec. 2 and the analysis of NGC 2403 (sec. 6.2) shows that probably the second case will be the most common.

However, given the linear increase of the scale height in the outer parts, galaxies with very extended disk could reach levels of the signal that can be analysed successfully. The search and

the study of these objects is beyond the scope of this thesis, but could be the subject of future work.

We can conclude that the proposed analysis of the azimuthal asymmetries of total map is not capable to give useful information about the vertical profile of non edge on galaxies. Since also the method proposed by Sicking (1997) does not give significative results, we can conclude that at this time it appears very difficult to study the vertical profiles of the gas in ordinary non edge-on disk galaxies.

# Appendice A

# Physical background: interaction of radiation with matter.

In this appendix we briefly recap the theoretical background about interactions between matter and radiation. The following concepts are the base to derive physical informations by the emission of astrophysical sources. In particular, we focus on the HI line emission from the gaseous layer of disk galaxies.

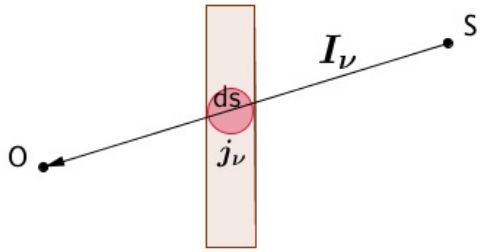


Figura A.1: A source $S$ emits a radiation with intensity $I_\nu$ crossing a portion of matter $ds$, with a proper intrinsic specific emission $j_\nu$, before reaching the observer $O$. The red spot is magnified in fig. A.2

We consider a portion of matter with a specific emission $j_\nu$ $[\frac{\text{erg}}{\text{cm}^3\text{arcsec}^2\ \text{s Hz}}]$ and a background radiation with Intensity $I_\nu$ $[\frac{\text{erg}}{\text{cm}^2\text{arsec}^2\ \text{s Hz}}]$ crossing it (fig. A.1). The total intensity seen by an observer $O$ will be:

$$dI_\nu = -\alpha_\nu I_\nu ds + j_\nu ds \qquad Transport\ equation \tag{A.1}$$

Where the first term on the r.h.s is the background intensity absorbed or scattered by the medium ($\alpha_\nu$ $[cm^{-1}]$ is the extinction coefficient of the crossed matter), and the second term is the cumulative emission of the medium.

## A.1 Extinction(Absorbtion and/or scattering)

We consider a medium with particle density n [$cm^{-3}$]. Any particle can absorb or scatter the radiation with a cross sections $\sigma_\nu$. We interpret the cross-section as the area of a circumference of radius $\sqrt{\frac{\sigma}{\pi}}$ within which the particles (the atoms of Hydrogen in our case) can interact with the incidente radiation. Considering a straight line of emission, we can build an infinitesimal

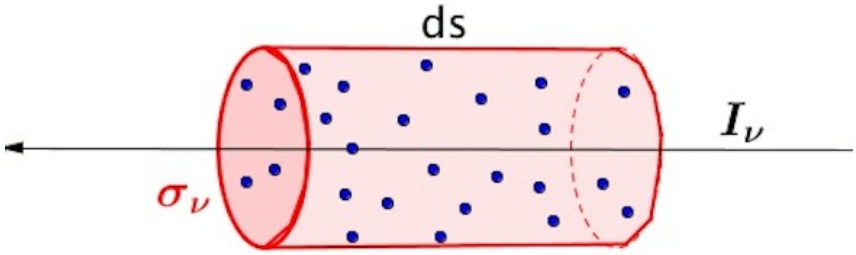


Figura A.2: The figure is a magnification of the red spot of fig. A.1. In a infinitesimal sheet with lengths ds, the intensity $I_\nu$ interacts with N centers of extinction (blue dots).

cylinder with base surface $\sigma_\nu$ and length ds (fig. A.2). The emission interacts with N=n$\sigma_\nu$ds centers of extinction, thus the intensity loss in the medium is:

$$dI = -I\sigma_\nu \mathrm{nds} \tag{A.2}$$

The cross section $\sigma_\nu$ takes in account both the probability to scatter or to absorb the radiation. We note that the absorption is a real loss of energy, while the scattering is a redistribution of intensity, so looking at a certain direction we can observe emission scattered from other areas of the emitting source. However, for the 21 cm emission the scattering is inefficient and it can be neglected in our treatment; hereafter $\sigma_\nu$ and $\alpha_\nu$ will be always implicitly referred to the absorption phenomena. Comparing eqs. A.1 and A.2 we can define the the optical depth as d$\tau$=$\alpha_\nu$ds=n$\sigma_\nu$ds, hence we can rewrite the transport equation as:

$$\frac{\mathrm{d}I}{\mathrm{d}\tau} = -I_\nu + S_\nu \tag{A.3}$$

where $S_\nu = j_\nu$ is called source function. We can multiply the r.h.s. and l.h.s. of eq. A.3 for the same factor $e^\tau$:

$$e^\tau \frac{dI}{d\tau} = -I_\tau e^\tau + S_\nu e^\tau \tag{A.4}$$

and defining $\Upsilon = I_\nu e^\tau$ and $\zeta = S_\nu e^\tau$, after some passages we obtain the following eqs.:

$$\begin{aligned} &\frac{d\Upsilon}{d\tau} = \zeta \\ &I_\nu(\tau)e^\tau = I_\nu(0) + \int_0^\tau S_\nu e^{\tau'} d\tau' \\ &I_\nu(\tau) = I(0)e^\tau + \int_0^\tau S_\nu e^{(\tau'-\tau)} d\tau' \end{aligned} \tag{A.5}$$

finally

$$I_\nu(\tau) = I_\nu(0)e^{-\tau} + S_\nu(1 - e^{-\tau}) \tag{A.6}$$

In the case of study (gaseous neutral disk) $S_\nu$ is the 21 cm line emission and $I_\nu$ may be a background emission (e.g. CMB, galaxy synchrotron).

### A.1.1 2-Level system

The HI line emission is due to an hyperfine transition from the upper level F=1 with multiplicity 3 (g=2F +1) to the ground level F=0 with multiplicity 1 (sec. 1.1). This is a simple 2-level system: the upper state ($u$) can be populated from collisional excitation (rate $\gamma_{lu}$ [$s^{-1}cm^3$]) or from radiative excitation (rate $B_{lu}\overline{J}$ [$s^{-1}$]); from the upper level, the hydrogen atoms can reach the ground state ($l$) through collisional de-excitation ($\gamma_{ul}$), spontaneous emission (rate $A_{ul}$) or induced emission ($B_{ul}\overline{J}$) where $\overline{J}$ is the mean intensity over the line profile (eq. A.8). Because of the uncertain principle every emission line has a natural quantum broadening. We can define the emission over the line profile as $\phi(\nu)$ and imposing normalization we can write:

$$\int_0^\infty \phi(\nu)d\nu = 1 \tag{A.7}$$

Thus,

$$\overline{J} = \int_0^\infty J(\nu)\phi(\nu)d\nu \tag{A.8}$$

The negative frequencies are unphysical values, but defining $\phi(\nu)$=0 for $\nu \leq 0$, we can write:

$$\overline{J} = \int_0^\infty J(\nu)\phi(\nu)d\nu = \int_{-\infty}^\infty J(\nu)\phi(\nu)d\nu \tag{A.9}$$

For 21 cm transition the emission lifetimes is very long ($10^7$ yr), thus for the uncertainty principle ($\Delta E \Delta t > \frac{h}{4\pi}$) the line broadening $\Delta E$ is very small such that:

$$\phi(\nu) \to \delta(\nu - \nu_{ul})$$

and

$$\overline{J} \to J_{ul}$$

Using the above relations and imposing statistical equilibrium between excitation and de-excitation, we can write:

$$nn_l\gamma_{lu} + n_lB_{lu}J_{ul} = n_uA_{ul} + nn_u\gamma_{ul} + n_uB_{ul}J_{ul} \tag{A.10}$$

where $n_l$ and $n_u$ are the number density of Hydrogen with F=0 and F=1. The ratio of these values can written as:

$$\frac{n_u}{n_l} = \frac{g_u}{g_l}e^{-\frac{E_{ul}}{KT_s}} \tag{A.11}$$

where $g$ is the multiplicity, thus $g_u = 3$ and $g_l = 1$. $T_s$ is the Spin Temperature, defined as the temperature at which the observed ratio $n_u/n_l$ would occur if the gas were in thermal equilibrium (Dickey et al., 2000). Therefore, for system in LTE (local thermal equilibrium) with a kinetic gas temperature $T_g$, $T_s = T_g$. In the following sections we will study eq. A.10 in two opposite situations: collisional systems (high density) and radiative systems (low density).

### Collisional system

We impose $J = 0$ (no radiation field) in the statistical equilibrium equation (A.10):

$$n n_l \gamma_{lu} = n_u A_{ul} + n_u n \gamma_{ul} \tag{A.12}$$

On can prove that $\gamma_u l$ and $\gamma_l u$ fulfill the following relation:

$$\gamma_{lu} = \frac{g_u}{g_l} \gamma_{ul} e^{-\frac{E_{ul}}{KT_g}} \tag{A.13}$$

where $T_g$ is the gas temperature. Using the relation A.13 in eq. A.12 we obtain:

$$\frac{n_u}{n_l} = \frac{g_u}{g_l} \frac{e^{-\frac{E_{ul}}{KT}}}{(1 + \frac{n_{\text{crit}}}{n})} \tag{A.14}$$

where $n_{\text{crit}} = \frac{A_{ul}}{\gamma_{ul}}$ is the discriminant value between collisional and non collisional systems. If $n >> n_{\text{crit}}$ the term inside bracket in equation A.14 tend to 1, accordingly, from A.11 $T_s$ tends to $T_g$. Considering the Einstein coefficient of the HI hyperfine transition and assuming all the collisions as neutral-neutral we can write (Tielens, 2005):

$$n_{\text{crit}} = 1.07 \cdot 10^{-5} \left( \frac{T_g}{80^{\circ}\text{K}} \right)^{-\frac{1}{2}} \tag{A.15}$$

Therefore, $\text{n}_{\text{crit}} \sim 10^{-5}$ for the CNM and $\text{n}_{\text{crit}} \simeq 1.26 \cdot 10^{-6}$ for the WNM. Since the number density of the ISM approximately ranges from 1 to 50 $\text{cm}^{-3}$ for CNM and from 0.01 to 0.2 $\text{cm}^{-3}$ for WNM. We conclude that the HI layers can be considered collisional systems.

### Radiative system

If the radiative transitions dominate the population of the quantic levels eq. A.10 becomes:

$$n_l B_{lu} J_{ul} = n_u A_{ul} + n_u B_{ul} J_{ul} \tag{A.16}$$

Thus, we can write the radiation field as:

$$J_{ul} = \frac{A_{ul}}{B_{ul}} \cdot \left( \frac{n_l}{n_u} \frac{B_{lu}}{B_{ul}} - 1 \right)^{-1} \tag{A.17}$$

considering the eq. A.11, we obtain:

$$J_{ul} = \frac{A_{ul}}{B_{ul}} \cdot \left( \frac{g_l}{g_u} \frac{B_{lu}}{B_{ul}} e^{\frac{E_{ul}}{KT_r}} - 1 \right)^{-1}$$

If we assume the system in thermal equilibrium and the radiation field as a Black-Body thermal radiation, we can write the above eq. as:

$$J_{ul} = 2\frac{E_{ul}^3}{h^2c^2} \left( e^{\frac{E_{ul}}{KT_r}} - 1 \right)^{-1} \tag{A.18}$$

Equating eqs. A.17 and A.18 one can obtain two important relations for the Einstein coefficient:

$$A_{ul} = \frac{2hv^3}{c^2} B_{ul} \tag{A.19a}$$

$$g_l B_{lu} = g_u B_{ul} \tag{A.19b}$$

Also if these relations come from the assumption of thermal equilibrium, they are independent from T, thus they must be fulfilled whether the system is in thermal equilibrium or not. We notice that substituting eqs. A.19 and A.18 in eq. A.16 we find the following level density ratio:

$$\frac{n_u}{n_l} = \frac{g_u}{g_l} e^{-\frac{E_{ul}}{kT_r}} \tag{A.20}$$

**Population of the quantic levels**

Comparing eqs. A.14 and A.20 we note that the radiation field starts to have an important role in increasing the population of the upper level only in very low density environments ($n_{\rm crit} >> n$) or when $T_r >> T_g$. The HI hyperfine transition occurs at very small energy ($E_{ul} = \mathrm{h}\nu_{ul} = 9.41 \cdot 10^{-18}$ erg) and the population density ratio is almost independent of the temperature and is nearly equal to the ratio of multiplicity. In the worst case with a very diffuse gas ($\mathrm{n}_{crit} >> \mathrm{n}$) and without a strong background radiation field, we note that the all Universe is in the thermal bath of the CMB at 3°. Therefore, using eq. A.20, we can define a lower limit of the population ratio:

$$\frac{n_u}{n_l} = \frac{g_u}{g_l} e^{-\frac{h\nu_{1420}}{kT_{cmb}}} \simeq 0.97 \frac{g_u}{g_l}$$

We can also calculate the upper limit when $n >> n_{crit}$ and/or $T_{gas}$ or $T_{rad}$ tends to $10^4$ and hydrogen becomes ionized. In these cases:

$$\frac{n_u}{n_l} = \frac{g_u}{g_l}$$

The small difference between the lower and upper limit leads us to conclude that for the Neutral Hydrogen the followings relations are always fulfilled:

$$n_u = \frac{3}{4} n \tag{A.21a}$$

$$n_l = \frac{1}{4} n \tag{A.21b}$$

where $n = n_u + n_l$ is the total number density of the HI.

## A.2 Spin temperature and thermal equilibrium

The population levels estimated in the previous section are based on the assumption of Local Thermal equilibrium. In this section we will enquire if it is a good approximation or an excessive simplification of the real physical condition. From eq. A.10 we can write the detailed balance as:

$$\frac{n_u}{n_l} = \frac{n\gamma_{lu} + B_{lu}J_{ul}}{n\gamma_{ul} + A_{ul} + B_{ul}J_{ul}} \tag{A.22}$$

We can explicit $\gamma$, $J_{ul}$ and the Einstein coefficients from eq. A.13, A.18 and A.19:

$$\frac{g_u}{g_l}e^{-\frac{E}{kT_s}} = \frac{g_u}{g_l}\frac{\left(\frac{n}{n_{\rm crit}}e^{\frac{-E}{kT_g}} + \left(e^{\frac{E}{kT_r}} - 1\right)^{-1}\right)}{\left(1 + \frac{n}{n_{\rm crit}} + \left(e^{\frac{E}{kT_r}} - 1\right)^{-1}\right)} \tag{A.23}$$

where $T_r$ is the brightness temperature, i.e., the temperature of a black body that emits have the energy at frequency $\nu_u = \frac{E}{h}$. Obviously, if the radiation field is from a BB $T_r$=$T_{\rm BB}$. In the case of the HI hyperfine transition $E << kT$ and we can express the exponential terms of eq. A.23 as Taylor series, thus we obtain:

$$1 - \frac{E}{kT_s} = \frac{\left(\frac{n}{n_{crit}}(1 - \frac{E}{kT\,g}) + \frac{kT_R}{E}\right)}{\left(1 + \frac{n}{n_{crit}} + \frac{kT_R}{E}\right)} \tag{A.24}$$

and finally,

$$T_s = \frac{T_g + \beta T_r}{1 + \beta} \tag{A.25}$$

where (considering the HI line emission):

$$\beta = \frac{KT_g}{E}\frac{n_{\rm crit}}{n} \simeq 1.28\ 10^{-2}\left(\frac{T_g}{80\ K}\right)^{\frac{1}{2}} n^{-1}$$

The Spin ($T_s$) temperature can be read as the weight average between the gas temperature and the brightness temperature of the background emission with weight $\beta$. In the case of emission line $T_g > T_r$, and if $T_g >> \beta T_R$ and $\beta << 1$ we restore the LTE. These two conditions lead to:

$$n >> \frac{KT_r}{E}n_{\rm crit} \tag{A.26a}$$

$$n >> \frac{KT_g}{E}n_{\rm crit} \tag{A.26b}$$

but $T_g > T_r$ so we can use only the last condition. In conclusion, using the detailed balance (eq. A.22) the density discriminant between collisional and non collisional system is larger of a factor $\frac{KT_g}{E}$ ($\simeq 14.9T_g$ for HI emission) with respect to the case with only collisional population of the quantic levels (eq. A.14). Panels of fig. A.3 show the value of $T_s$ (eq. A.25) under certain physical conditions. In A.3a we fixed the particle density of the medium: it is easily to

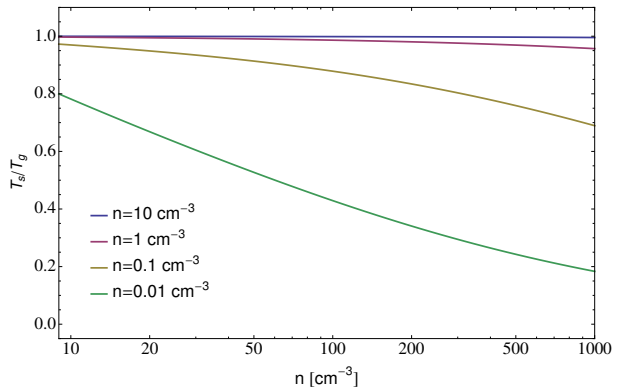


(a) fixed density

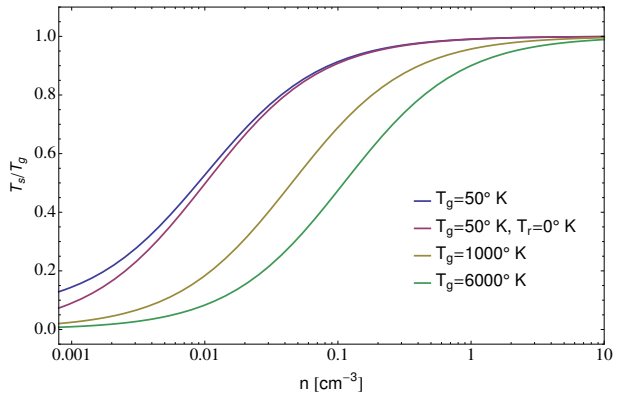


(b) fixed temperature

Figura A.3: Spin temperature and its dependence on number density and gas temperature. Where not otherwise specified $T_r$ is set to 3° K.

note that for n< 0.1 cm$^{-3}$ an increase in temperature causes a strong departure from LTE and brings the spin temperature to lower values than $T_g$. Panel A.3b shows that for particle density greater than 1cm$^3$ LTE is a good approximation for almost all the values of gas temperature. In both figures is clear that the background radiation influences the spin temperature only in the extreme conditions of low density and low gas temperature. In conclusion, in the CNM there are the physical condition to achieve LTE and $T_s = T_g$, while the WNM is too hot and diffuse and $T_s < T_g$. We can estimate a lower limit for $T_s$ using the average condition of WNM and without background radiation:

$$\beta \simeq 1.1$$

and from eq. A.25

$$T_s \sim \frac{T_g}{2.2} \sim 2729°\mathrm{K} \tag{A.27}$$

Theoretically, from eq. A.21 we would expect that in the WNM the upper state levels (F=1) of HI will be less populated than the CNM. In practice, the energy of the hyperfine transition is so small that despite the spin temperature, both WNM and CNM achieve the condition expressed in A.21.

# Appendice B

# Definitions of the vertical scale-height

Relying on the assumption of cylindrical symmetry the density of a gaseous disk $\rho$ can be divided in two contributors: a radial ($\epsilon$) and a vertical distribution ($f$). Thus, we can write:

$$\rho(R, Z) = C\epsilon(R)f(Z) \tag{B.1}$$

In this thesis we model the gas vertical distribution $f(Z)$ in three different way: gaussian, exponential and a hyperbolic secant squared:

- Exponential: $f_e(Z) = e^{-\frac{|Z|}{Z_e}}$
- Gaussian: $f_g(Z) = e^{-\frac{Z^2}{2\sigma^2}}$
- Hyperbolic sec. $f_s(Z) = \mathrm{sech}^2(Z/Z_s)$

There is not an univocal way to define a representative Z and to call it "scale height. In this appendix we briefly report some different definitions of vertical scale height for the HI layer in the disk galaxies.

- **Function scale height.** It is the natural scale parameter of each vertical distribution.

  Exponential: $Z_e$. It is the same scale length of the exponential scale ($h_e$) and of the Half equivalent width ($E_e$).

  Gaussian: $\sigma$. It represents the vertical density dispersion $Z_{0g}$.

  Hyperbolic Secant: $Z_s$. It represents the Half equivalent width $E_s$.

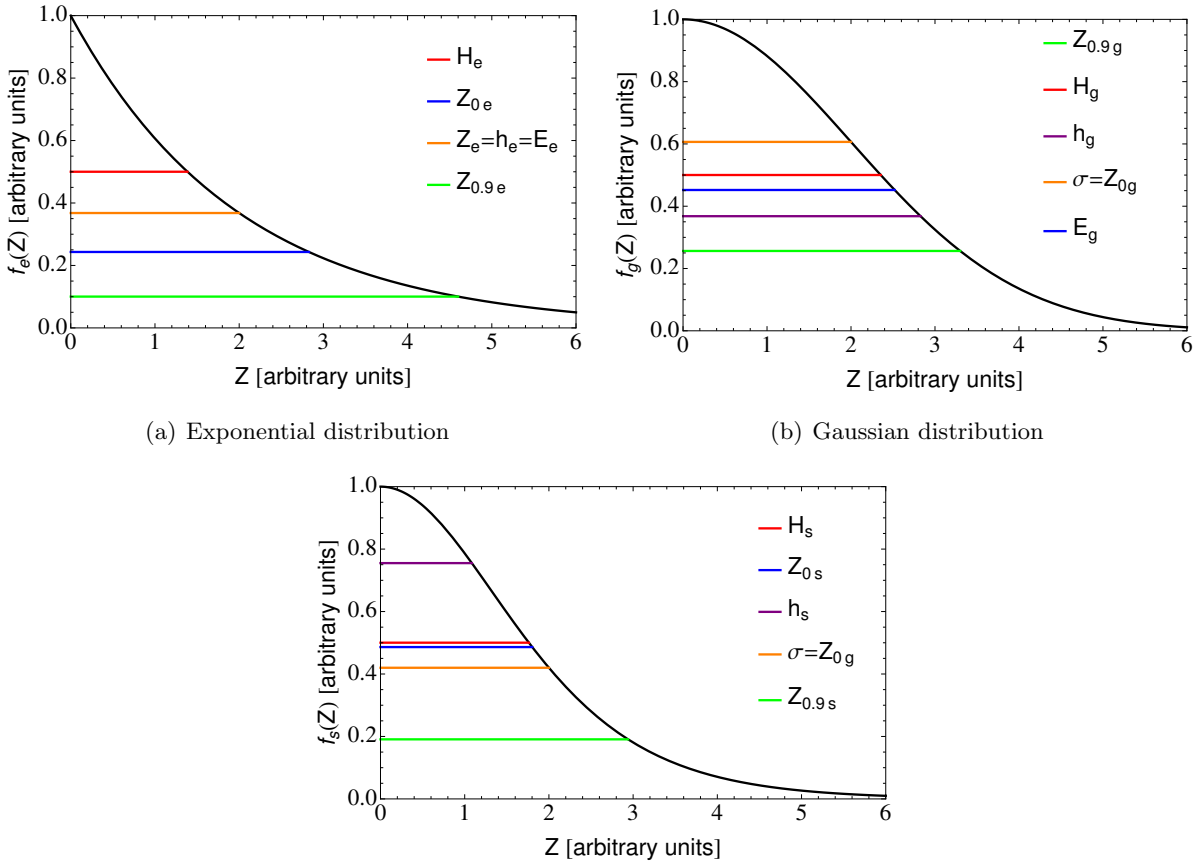


(a) Exponential distribution

(b) Gaussian distribution

(c) Hyperbolic secant squared distribution

Figura B.1: Various definitions of scale height for the three vertical density distributions discussed in the text. See text for further explanations.

- **Exponential scale height h.** It is the value of Z where the vertical density drops by a factor $e^{-1}$ with respect to its maximum,. It is the more direct way to define a scale height for an exponential (e.g. van der Kruit 1981; Kamphuis 2007).

  $h_e = Z_e$

  $h_g = \sigma_d\sqrt{2} = 1.414\sigma$

  $h_s = 1.085 Z_s$

- **Vertical Density dispersion $Z_0$.** It is the the normalized $2^{th}$ moment of a distribution:

$$Z_{0i}^2 = \frac{\int_{-\infty}^{\infty} Z^2 f_i(Z) dZ}{\int_{-\infty}^{\infty} f_i(Z) dZ}$$

  $Z_{0e} = Z_e\sqrt{2} = 1.414 Z_d$

  $Z_{0g} = \sigma$

  $Z_{0s} = Z_s \frac{\pi}{\sqrt{12}} = 0.901 Z_d$

It is commonly used in literature when a gaussian is assumed as vertical gas profile (e.g. Sicking 1997; Olling 1996).

- **HWHM (Half Width Half Maximum) H.** It is the positive value of Z where the functions reach the half of their maximum. It is commonly used to estimate the width of functions as gaussian or lorentzian.

  $H_e = Z_e ln(2) = 0.693 Z_d$

  $H_g = \sigma\sqrt{2\ln(2)} = 1.177\sigma_d$

  $H_s = Z_s \left( \text{asech}\left(\frac{1}{\sqrt{2}}\right)\right) = 0.881 Z_d$

  It is usually used in the study of flaring (e.g. Kalberla et al. 2007; O'Brian et al. 2010a).

- **Percentile Scale height $\mathbf{Z_p}$.** It is the Z which subtends the $100p$ % of the distribution area. It can be helpful to match models with different vertical distribution. We can obtain a general equation of $Z_p$ only for the exponential and hyperbolic distribution because the gaussian has not a general analytical solution for its integral.

  $Z_{pe} = Z_d \ln(\frac{1}{1-p})$

  $Z_{ps} = Z_d \text{atanh}(p)$

  For instance, we can choice a 90% percentile:

  $Z_{0.9e} = 2.30 Z_e$

  $Z_{0.9g} = 1.65\sigma$

  $Z_{0.9s} = 1.47 Z_s$

- **HEW(Half Equivalent Width) E.** This concept comes from the line spectral analysis where it is used to compare in a objective way the strength of an emission or an absorption line. Since the spectral lines are in first approximation similar to the functional forms we are considering , we can use the HEW to estimate the vertical widths of our distributions. In our particular case, the HEW is defined as

  $$2 \cdot \max[f(Z)] \cdot HEW = \int_{-\infty}^{\infty} f(Z) dZ$$

  From the initial definitions of the functions, we note that $\max[f(Z)] = 1$ for all the three distributions, thus we can write:

  $$HEW = \frac{\int_{-\infty}^{\infty} f(Z) dZ}{2}$$

  and

  $E_e = Z_e$

$$E_g = \sigma \frac{\sqrt{2\pi}}{2} = 1.26\sigma$$

$$E_a = Z_s$$

See fig. B.1 for a graphic interpretation of the different scale heights defined in this appendix.

In case of a gaseous disk with not constant thickness the vertical scale heights will depend on the galactic radius R, thus $f = f(R, Z)$. However, the definitions made in this appendix are still locally valid.

# Appendice C

# About the degeneracy of DM halos

## C.1 Flattening Degeneracy

The aim of this appendix is to study the relations between the parameters of the DM halos (either isothermal C.1.1 or NFW C.1.2) that produce the same rotation curve but have different flattenings ($q$).

### C.1.1 Isothermal

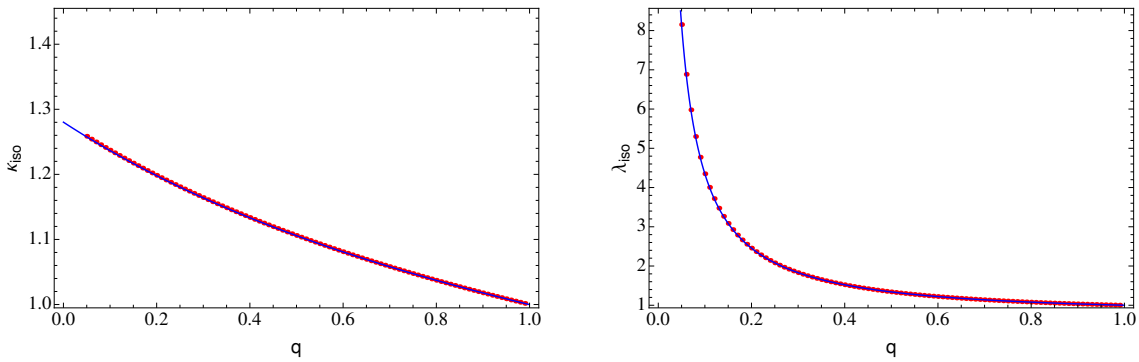


Figura C.1: Correction factors for the core radius $R_c$(left) and for the central density ($\rho_0$)(right) needed to reproduce the same velocity curve of a spherical isothermal halo. The blue curves are the best fitting functions (eq. C.2).

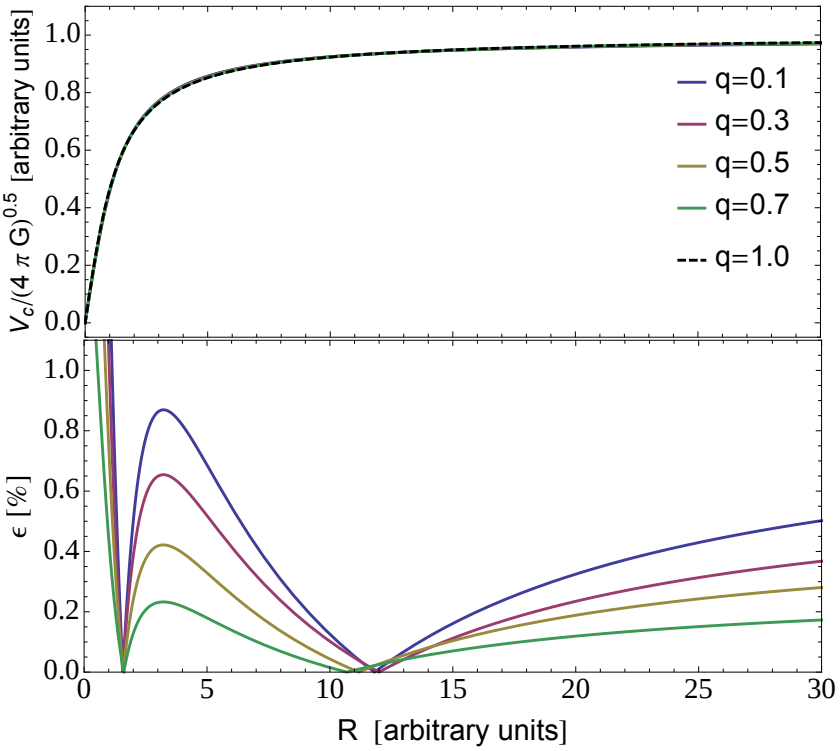


Figura C.2: RC produced by isothermal halos with various flattening q (upper panel) and the related relative differences $\epsilon$ with respect to the spherical case. The halo parameters come from eq. C.2.

We consider a spheroidal isothermal halo (eq. 3.15) with density parameters $R_c(1)$ (core radius), $\rho_0(1)$ (central density) that produces a rotation curve (RC) $V_c(1)$ (eq. 3.21). Our goal is to find the values of the parameters $R_c(q)$ and $\rho_0(q)$ of a flatten isothermal halo that produces the same RC of the spheroidal model. In practice, we need to solve the following:

$$V_c(R; R_c(q), \rho_0(q), q) = V_c(1) = V_c(R; R_c(1), \rho_0(1), 1) \tag{C.1}$$

This is a problem of 1 equation and 2 unknowns, thus there are no analytic solutions. We choose to obtain the two parameters through a fitting procedure.

First, we created a reference model of the RC (eq. 3.16) with the following settings:

$$q = 1, \quad R_c = 1, \quad \rho_0 = 1$$

Then, we set $R_c(q)$ and $\rho_0(q)$ as free parameters and we fitted the reference model with the analytic velocity curve of eq. 3.16: $V_{rot}(R; R_c(q), \rho_0(q), q)$. This procedure has been repeated for values of q in the interval 0.05-0.99 with step of $\Delta q = 0.01$. Since we set $R_c(1) = \rho_0(1) = 1$, the parameters obtained are the factor of conversion $\kappa(q)$ and $\lambda(q)$ such that:

$$R_c(q) = R_c(1)\kappa_{\rm iso}(q) \tag{C.2a}$$

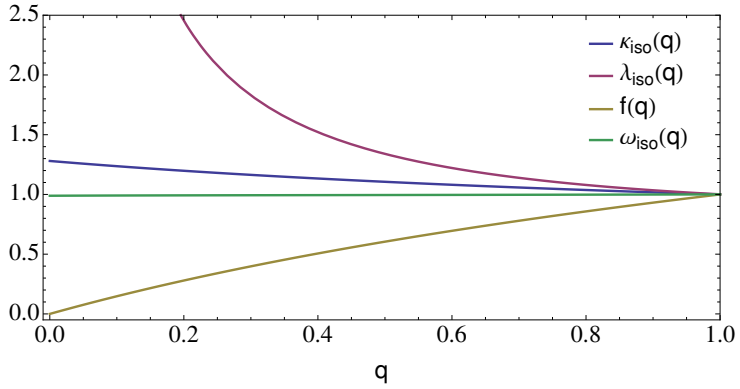


Figura C.3: Functional forms of the correction factors for the core radius ($\kappa_{\rm iso}$), for the central density ($\lambda_{\rm iso}$) and for the asymptotic velocity ($\omega_{\rm iso}$). $f$ is the function that represents the dependence of the rotational velocity on the flattening paramter q (eq. 3.21)

$$\rho_0(q) = \rho_0(1)\lambda_{\rm iso}(q) \tag{C.2b}$$

Fig. C.1 shows the corrections factor $\kappa_{\rm iso}$ and $\lambda_{\rm iso}$ that we obtained from the procedure described so far. Both the core radius and the central density of the halo increase with the halo flattening. The correction factor for the core radius is relatively small, it reaches at least 1.25 for very flat halo ($q \approx 0.1$). The correction $\lambda_{\rm iso}$ for the central density is similar to $\kappa_{\rm iso}$ out to $q \approx 0.3$, for flatter halo it diverges and the central density can become larger than 2 $\rho_0(1)$ ($\lambda_{\rm iso} \sim 4$ at q=0.1). We found that the trends of $\kappa_{\rm iso}$ and $\lambda_{\rm iso}$ are well described by the following functions:

$$\kappa_{iso}(q) = 0.598 + \frac{0.996}{q + 1.460} - 0.003q^3 \tag{C.3a}$$

$$\lambda_{iso}(q) = 0.538 + \frac{0.380}{q} + 0.083q \tag{C.3b}$$

Using the eqs. C.3 it is possible to obtain the same RC for every flattening parameter $q$ as shown in figure C.2. The resultant RCs clearly overlap and the relative differences (shown in the bottom panel) are always within 1 %, except for the inner radii. However, in these regions the galactic dynamics is dominated by the baryonic matter, thus the high relative errors are not a real problem. Using the definitions C.2 in eq. 3.17 we obtain:

$$V_\infty(q) = V_\infty(1)\kappa_{\rm iso}(q)\sqrt{\lambda_{\rm iso}(q)f(q)} = V_\infty(1)\omega_{\rm iso}(q)$$

The term $\omega_{\rm iso}(q)$ is the correction factor for the asymptotic velocity of the RC. It is plotted in fig. C.3: it is evident that $\kappa_{\rm iso}, \lambda_{\rm iso}$ and $f$ (eq. 3.18) conspire to make $\omega_{\rm iso}$ constant for every flattening parameter. Using eqs. 3.15 and C.2 in eq. 2.74 of Binney & Tremaine (2008) we can

evaluate the mass encircled in a isothermal halo with flattening $q$ and major axis $R$:

$$\begin{aligned} M_h(q)(R) &= 4\pi R_c(1)\rho_0(1)q\lambda_{\rm iso}(q)\kappa_{\rm iso}(q)\int_0^R (R_c^2(q)+x^2)^{-1}d(x^2) \\ &= m(q)\int_0^R (R_c^2(q)+x^2)^{-1}d(x^2) \\ &= m(q)\int_0^R g(q,x)d(x^2) \end{aligned} \tag{C.4}$$

Defining $\psi_{\rm iso}(q) = q\lambda_{\rm iso}(q)\kappa_{\rm iso}(q)$ and $m(1) = 4\pi R_c(1)\rho_0(1)$, we can write:

$$m(q) = m(1)\psi(q)$$

We consider two flattening parameters $q_1$ and $q_2$ with $q_1 < q_2$. One can show that $\psi_{\rm iso}(q)$ is a monotonic increasing function of q, therefore $m(q_1) < m(q_2) \leq m(1)$. Moreover, from eq. C.3a we know that $R_c(1) \leq R_c(q_2) < R_c(q_1)$, thus $g(1,x) \geq g(q_2,x) \geq g(q_1,x)$. Combining the above inequality chains with eq. C.4, we conclude that for every $q_1 < q_2$:

$$M_h(q_1) < M_h(q_2) \leq M_h(1)$$

In conclusion a given RC can be explained with a family of isothermal DM halo models with different flattenings: flatter halos will have higher central density $\rho_0$, larger radial core length $R_c$ but lower total mass $M_h$.

### C.1.2 NFW

We applied the approach described so far (sec. C.1.1) also to a NFW halo (sec 3.1.4). We want to find the correction factors ($\kappa_{NFW}(q)$, $\lambda_{NFW}(q)$) for both the radial scale length $R_s$ and for the central density $\rho_0$ to reproduce the RC of a spherical reference model (q=1,$R_s = 1$,$\rho_0 = 1$) for every value of the flattening parameter q.

In the case of a NFW halos we know the analytic functional form of $V_c$ only for q=1. Using eq. 3.32 in eq. 2.132 of Binney & Tremaine (2008) we can obtain the general form of the circular velocity:

$$V_c^2(R,q) = 4\pi\rho_0 R_s G q \int_0^R \frac{x}{(1+(x/R_s))^2}\frac{dx}{\sqrt{R^2-(1-q^2)x^2}} \tag{C.5}$$

As in the previous section we fitted the reference model with $V_c^2(R,q)$, but this time the fit function has to be numerically evaluated. In order to prevent numerical errors we performed a preliminary analysis: we compared the analytic and the numerical solution for the spherical case (q=1). The errors are of the order of machine precision ($10^{-16}$), hence we are confident not to introduce numerical biases in this analysis. Fig. C.4 shows the correction factors found for every value of q from 0 to 1. In analogy with the isothermal halo, the radial scale length shows

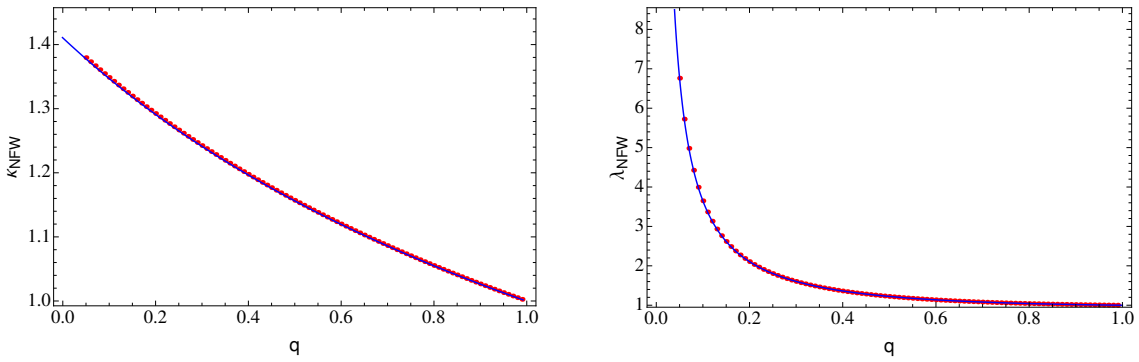


Figura C.4: Correction factors for the radius scale length $R_s$(left) and for the central density ($\rho_0$)(right) needed to reproduce the same RC of a spherical NFW halo. The black curves are the best fit functional forms.

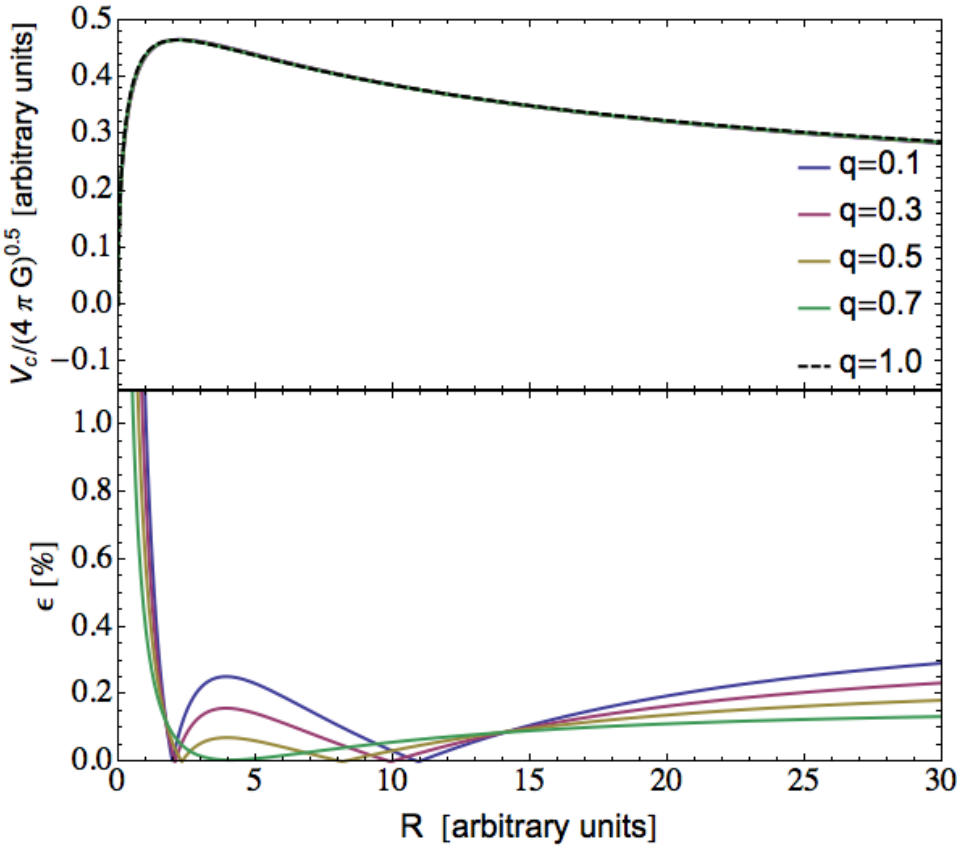


Figura C.5: Same as fig. C.2 but for NWH halo. The halo parameters are tuned with the factor of eq. C.6.

small variations while the central density can reach values several time larger with respect to the spherical case. The trends of $\kappa_{NFW}$ and $\lambda_{NFW}$ are well fitted by the following functions:

$$\kappa_{NFW}(q) = 0.549 + \frac{1.170}{1.367 + q} - 0.047q \tag{C.6a}$$

$$\lambda_{NFW}(q) = 0.510 + \frac{0.312}{q} + 0.178q \tag{C.6b}$$

Fig. C.5 (top panel) shows the RC produced by NFW halos with different flattening q and with the parameters: $R_s(q) = R_s(1)\kappa_{\rm NFW}(q)$ and $\rho_0(q) = \rho_0(1)\lambda_{\rm NFW}(q)$. It is clear that applying the correction factors the RC are practically coincident, indeed the relative differences are always under the value of 1%, except at small radii where they reach the value of 10% (fig. C.5, bottom panel).

In analogy with the isothermal halo, we can state that a given RC can be explained with a family of NFW DM halo models with different flattening: flatter halos will have higher central density $\rho_0$ (eq. C.6a) and larger radial scale length $R_s$ (eq. C.6b), but lower total mass $M_h$.

## C.2 Density Law Degeneracy

The observed RCs of disk galaxies are usually well fitted both by an isothermal DM halo and by a NFW DM halo. (de Blok et al., 2008a). The aim of this section is to find the correction factors ($\kappa_m$ and $\lambda_m$) for the parameters of an isothermal halo ($R_c$, $\rho_0^{iso}$) to reproduce the same velocity curve of a NFW halo of parameters $R_s$ and $\rho_0^{NFW}$. The RC produced by the two halo models have a different asymptotic behavior: the isothermal RC (eq. 3.21) tends to the finite value $V_\infty$, while the NFW one (eq. 3.34) goes to 0. In particular, beyond $R \sim 2R_s$ the NFW RC starts to decline, while the isothermal RC is always an increasing function of R. For this reason, to try to find an agreement of the two RCs on the whole radial dominion does not make sense. We choose to perform the analysis between 0 and 2 $R_s$. The result of this kind of analysis is independent of the halo flattening q, because of the flattening degeneracy outlined in the previous sections, hence we used two spherical halos. Firstly, we set the parameters of the NFW halo as follows:

$$R_s = 1 \qquad \rho_0^{NFW} = 1$$

After, we found the best fit value of $\kappa_m$ and $\lambda_m$ fitting the NFW RC to the isothermal RC of parameters:

$$R_c = R_s\kappa_m \qquad \rho_0^{iso} = \rho_0^{NFW}\lambda_m \tag{C.7}$$

The results are:

$$\kappa_m = 0.142 \qquad \lambda_m = 11.973 \tag{C.8}$$

The corrections are significant: both the radius scale length and the central density differ by one order of magnitude. Figure C.6 shows the results of the fit in terms of RC. The fit is slightly

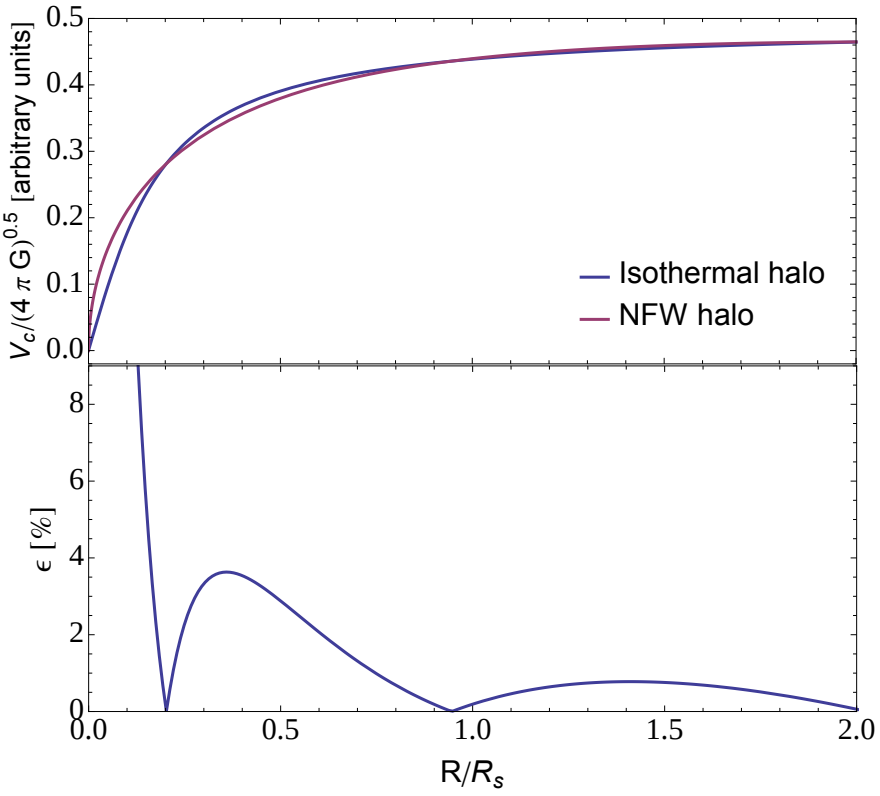


Figura C.6: RCs for two DM halos with different density law (Isothermal vs NFW) and the relative differences. The parameters of the NFW halo have been fixed to 1 while the halo parameters are corrected with the factors shown in C.8 (see eq. C.7) .

worse with respect to whar seen for the flattening degeneracy (fig. C.2 and C.5), indeed at the inner radii ($R < R_S$) the relative differences are greater that the 1 %. However, at large radii, the two curves matches well and the relative differences are very small.

# Appendice D

# A case of study: exponential disk with a constant scale height

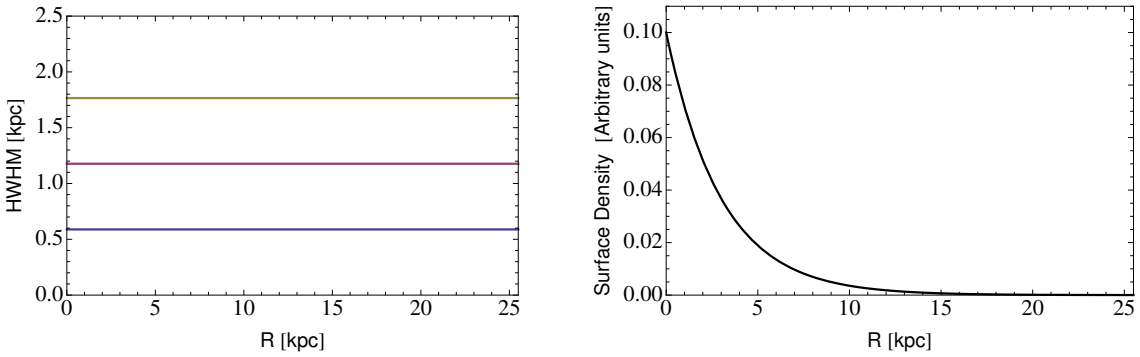


Figura D.1: Density distributions used to make the galactic models analyzed in this app.: the intrinsic surface density is shown in the right panel, while the vertical profiles are gaussian with constant scale heights shown in the left.

In this appendix we performed a similar analysis to one made in sec. 4.3 using a disk with an exponential surface density and a constant gaussian thickness. This galactic model can be a realistic approximation for a stellar disk (van der Kruit & Freeman, 2011). The vertical profile of a stellar disk is usually modeled by a hyperbolic secant squared, however we found that the patterns of the observed surface density turns out to be very similar to the one produced by a gaussian vertical profile. In particular, we found that if the scale height of the two functions are set to have the same 90 % percentile scale height (App. B) the observed surface density is practically the same. We built three galactic models with surface density of eq. 4.26 with $\alpha = 0$, $\Sigma_0 = 0.1$aU and $R_d = 3$ kpc (shown in the right panel of fig. D.1); the vertical profiles are modeled with a gaussian profile with dispersion set to 0.5, 1 and 1.5 kpc (the related HWHM are shown in the left panel of fig. D.1 with blue, purple and yellow curves). Then, we calculated

the observed surface density through eq. 4.19 setting the inclination angle to 60 degree and the disk border to 26 kpc: a sample of the observed azimuthal profiles are shown in fig. D.2, the radial trend of the related $\gamma$ (eq. 4.27) is plotted in fig. D.3 Panels in fig. D.2 show that for

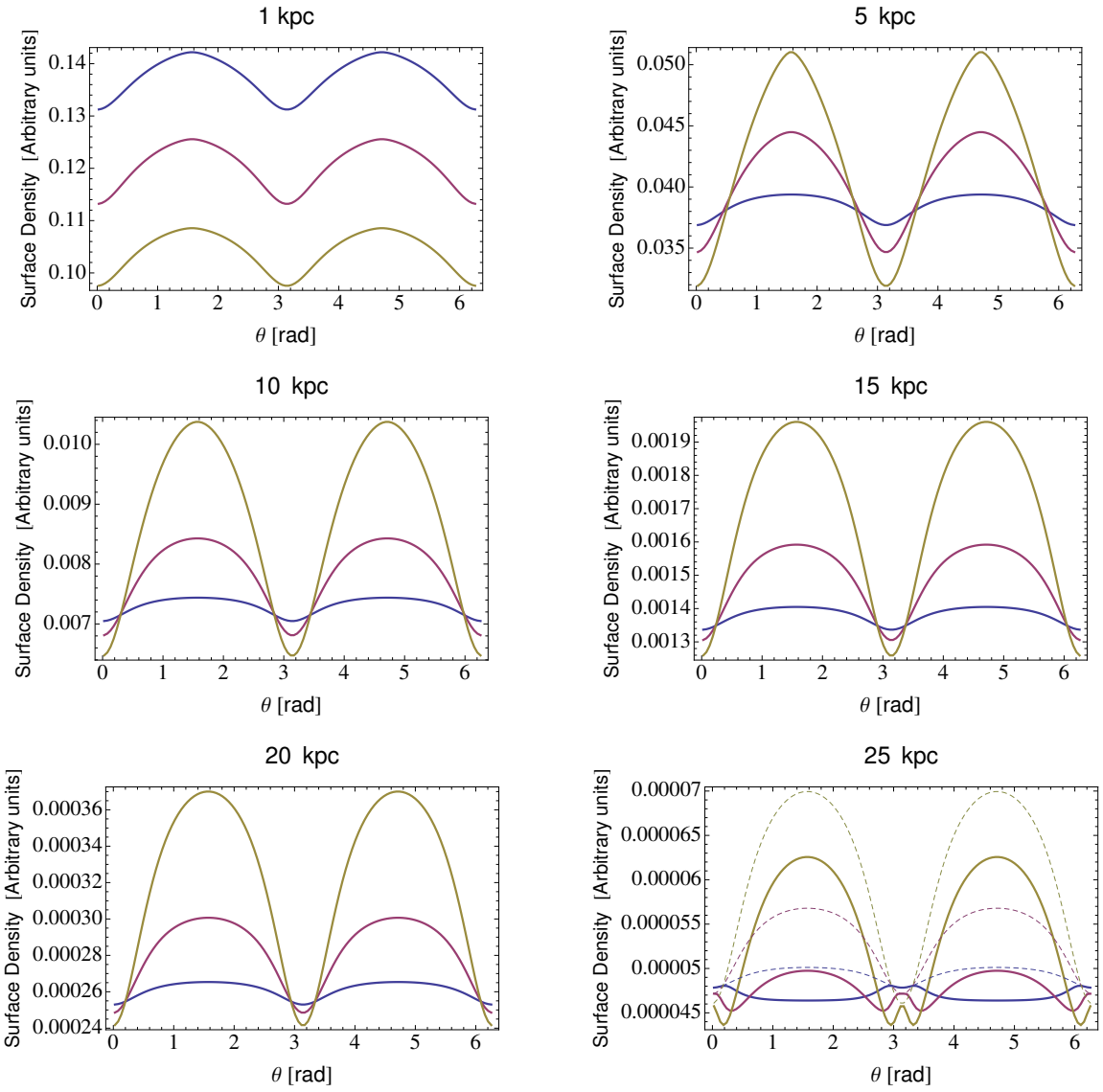


Figura D.2: Azimuthal profiles of the observed surface density for the galactic models of fig. D.1. The dashed curves in the last panel show the profile for the galactic models without border.

these galactic models the observed azimuthal profiles are very regular out to 24 kpc, very close to the end of the disk. They exhibit always oscillations with a peak around the major axis. The peaks become progressively sharper and more important (with respect to the mean signal value along the rings) with the increase of the vertical scale height.

The regularity of the observed azimuthal profiles is evident also in the $\gamma$ parameters plotted in fig. D.3. The radial trend of $\gamma$ is very similar among the three models: it exhibits a rapid increase until it reaches a maximum located at a radius depending on the thickness model: a

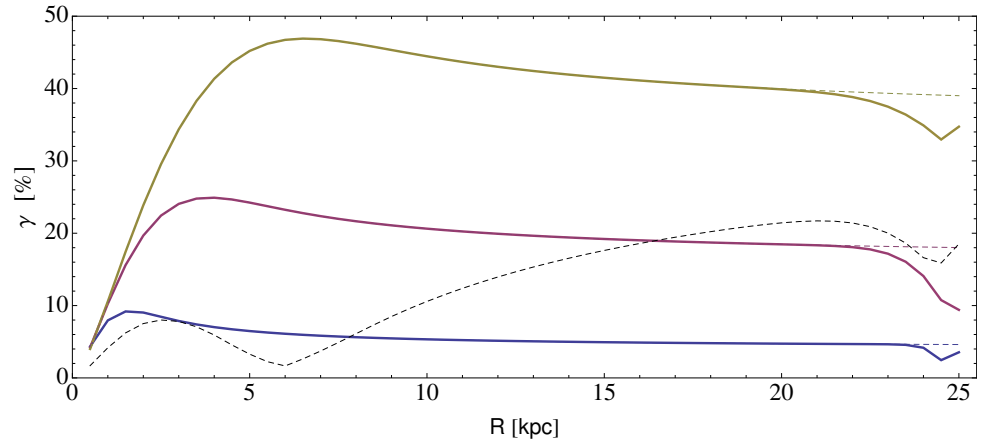


Figura D.3: Gamma parameter for the three models of fig. D.1. The full and the dashed colored curves represent respectively models with and without the border. The black dashed line shows the gamma for a model with the same vertical profile of the full yellow curve, but with the intrinsic surface density plotted in the right panel of fig. 4.6.

lower thicknesses tends to shift the maximum toward smaller radii. Beyond the maximum, $\gamma$ slowly decreases until it reaches the radius of influences (where the full and dashed curves of fig. D.3 start to diverge, eq. 4.30). An example of the differences between the azimuthal profiles produced by models with and without border is shown in the last panel of fig. D.2. The black dashed line in fig. D.3 shows the $\gamma$ for a galactic model with a constant scale height of 1.5 kpc (as for the yellow curve) but with the intrinsic surface density of fig. 4.6: its behavior is different with respect to the yellow model and it exhibits more features and a switch of peak at the inner disk. Moreover, it is evident that in the case of the exponential surface density the magnitude of the azimuthal patterns is two o more times greater with respect to the case of eq. 4.26 with $\alpha \neq 0$. One time again, we show that the radial distribution of the surface density has the same or even greater importance with respect to the vertical gas distribution in the making of the observed azimuthal features.

# Bibliografia


Battaner, E., & Florido, E. 2000, The Rotation curve of spiral galaxies and its cosmological implications

Begeman, K. 1987, PhD thesis, University of Groeningen

Binney, J., & Tremaine, S. 2008, Galactic dynamics (Princeton University Press)

Bosma, A. 1978, PhD thesis, PhD Thesis, Groningen Univ.

Boulanger, F., & Viallefond, F. 1992, A&A, 266, 37

Casertano, S. 1983, MNRAS, 203, 735

Corwin, Jr., H. G., Buta, R. J., & de Vaucouleurs, G. 1994, AJ, 108, 2128.2144

Cuddeford, P. 1993, MNRAS, 262, 1076

Cuddeford, P., & Binney, J. 1993, Nature, 365, 20

Davidge, T. J. 2003, AJ, 125, 3046

de Blok, W. J. G., Walter, F., Brinks, E., et al. 2008a, ApJ, 136, 2648

—. 2008b, The Astronomical Journal, 136, 2648

de Grijs, R., & Peletier, R. F. 1997, AA, 320

Dehnen, W., & Binney, J. 1998, MNRAS, 294

Dickey, J. M., Mebold, U., Stanimirovic, S., & Staveley-Smith, L. 2000, ApJ, 536, 756

Dove, B., & Shull, M. 1994, ApJ, 423, 196

Dubinski, J. 1994, ApJ, 431, 617

Field, G. B., Goldsmith, D. W., & Habing, H. J. 1969, ApJ, 155, L149

Fraternali, F., & Binney, J. 2006, 449, 449

Fraternali, F., van Moorsel, G., Sancisi, R., & Oosterloo, T. 2002, ApJ, 123, 3124

Freeman, K. 1970, ApJ, 160

Garcia-Ruiz, I., Sancisi, R., & Kuijken, K. 2002, AA, 394, 769

Gilmore, G., & Reid, N. 1983, MNRAS, 202, 1025

Gooch, R. 1996, Karma: a Visualization Test-Bed, Vol. 101

Gradshteyn, I., & Ryzhik, I. 1980, Table of Integrals, Series and Products, ed. A. P. Inc

Gunn, J. E., & Gott, III, J. R. 1972, ApJ, 176, 1

Jog, C. J., & Banerjee, A. 2008, ApJ, 685, 254

Joung, M. K. R., & Mac Low, M.-M. 2006, ApJ, 653, 1266

Kalberla, P. M. W., Dedes, L., Kerp, J., & Haud, U. 2007, A&A, 469, 511

Kamphuis, P. 2007, PhD thesis, Groeningen University

Kregel, M., van der Kruit, P. C., & de Grijs, R. 2002, MNRAS, 334

Malhotra, S. 1995, ApJ, 433, 687

Marasco, A., & Fraternali, F. 2011, AA, 525, A134

Marinacci, F., Fraternali, F., Ciotti, L., & Nipoti, C. 2010, MNRAS, 401

Markus Hohenwarter. 2002, Master's thesis, Paris Londron University, Salzburg, Austria

Marquardt, D. 1963, SIAM J. App. Math, 11

Matthews, L. D., & Wood, K. 2003, ApJ, 593, 721
Merrifield, M. R. 1992, AJ, 103, 1552
Mosenkov, A. V., Sotnikova, N. Y., & Reshetnikov, V. P. 2010, MNRAS, 401, 559
Muñoz-Mateos, J. C., de Paz, A. G., Boissier, S., et al. 2009, The Astrophysical Journal, 701, 1965
Narayan, C. A., Sha, K., & Jog, C. J. 2005, A&A, 440, 523
Navarro, J., Frenk, C., & White, S. 1996, ApJ, 563
Neto, A. F., Gao, L., Bett, P., et al. 2007, MNRAS, 381, 1450
O'Brian, J., Freeman, K., & van der Kruit, P. 2010a, AA, 515
—. 2010b, A&A, 515
Olling, R. 1995, AJ, 110, 591
Olling, R. 1996, AJ, 112, 481
Olling, R., & Merrifield, M. R. 2000, MNRAS, 311, 361
Oosterloo, T., Fraternali, F., & Sancisi, R. 2007, AJ, 134, 1019
Petric, A., & Rupen, M. P. 2007, Apj, 134, 1952
Piontek, R. A., & Ostriker, J. 2005, ApJ, 629, 849
Roberts, M. S., & Rots, A. H. 1973, AA, 26, 483
Ruiz-Granados, B., Rubiño-Martín, J. A., Florido, E., & Battaner, E. 2010, ApJ, 723, L44
Sackett, P., & Sparke, L. S. 1990, ApJ, 361
Sanchez-Salcedo, F. J., Saha, K., & Narayan, C. A. 2008, MNRAS, 385
Schneider, M. D., Frenk, C. S., & Cole, S. 2012, Jcap, 5, 30
Sellwood, J. A., & Balbus, S. A. 1999, ApJ, 511, 660
Sicking, F. 1997, PhD thesis, University of Groningen
Sofue, Y. 1997, PASJ, 49, 17
Swaters, R. A. 1999, PhD thesis, Rijksuniversiteit Groningen, (1999)
Swaters, R. A., Sancisi, R., & van der Hulst, J. 1997, ApJ, 491, 140
Tamburro, D., Rix, H., Leroy, A., et al. 2009, ApJ, 137, 4424
Tielens, A. 2005, The physics and chemistry of the interstellar medium, ed. Springer, Astronomy and astrophysics library
van der Hulst, J., Terlouw, J., Begeman, K., Zwitser, W., & Roelfsema, P. 1992, in , 131
van der Kruit, P. C. 1981, AA, 99, 298
van der Kruit, P. C., & Freeman, K. 2011, ARA&A, 49
van der Kruit, P. C., & Searle, L. 1981, AA, 116
—. 1982, AA, 110
Watson, W., & Deguchi, S. 1984, ApJ
Wolfire, M. G., Hollenbach, D., McKee, C. F., Tielens, A. G. G. M., & Bakes, E. L. O. 1995, ApJ, 443, 152
Zschaechner, L. K., Rand, R. J., Heald, G. H., Gentile, G., & Kamphuis, P. 2011, ApJ, 740